



HAL
open science

Comparative microscopic signatures of microbial and abiotic alteration of calcite

Luca Stigliano

► **To cite this version:**

Luca Stigliano. Comparative microscopic signatures of microbial and abiotic alteration of calcite. Earth and Planetary Astrophysics [astro-ph.EP]. Université Grenoble Alpes [2020-..], 2024. English. NNT : 2024GRALU004 . tel-04600456

HAL Id: tel-04600456

<https://theses.hal.science/tel-04600456>

Submitted on 4 Jun 2024

HAL is a multi-disciplinary open access archive for the deposit and dissemination of scientific research documents, whether they are published or not. The documents may come from teaching and research institutions in France or abroad, or from public or private research centers.

L'archive ouverte pluridisciplinaire **HAL**, est destinée au dépôt et à la diffusion de documents scientifiques de niveau recherche, publiés ou non, émanant des établissements d'enseignement et de recherche français ou étrangers, des laboratoires publics ou privés.

THÈSE

Pour obtenir le grade de

DOCTEUR DE L'UNIVERSITÉ GRENOBLE ALPES

École doctorale : STEP - Sciences de la Terre de l'Environnement et des Planètes

Spécialité : Sciences de la Terre et de l'Environnement

Unité de recherche : Institut des Sciences de la Terre

Signatures microscopiques comparées de l'altération microbienne et abiotique de la calcite

Comparative microscopic signatures of microbial and abiotic alteration of calcite

Présentée par :

Luca STIGLIANO

Direction de thèse :

Damien DAVAL

CHARGE DE RECHERCHE, Université Grenoble Alpes

Directeur de thèse

Rapporteurs :

Catherine NOIRIEL

MAITRESSE DE CONFERENCE HDR, Université Toulouse III - Paul Sabatier

Steve BONNEVILLE

FULL PROFESSOR, Université Libre de Bruxelles

Thèse soutenue publiquement le **15 janvier 2024**, devant le jury composé de :

Liane G. BENNING,

FULL PROFESSOR, German Research Centre for Geosciences

Présidente

Damien DAVAL,

CHARGE DE RECHERCHE HDR, CNRS délégation Alpes

Directeur de thèse

Karim BENZERARA,

DIRECTEUR DE RECHERCHE, CNRS délégation Paris Centre

Co-directeur de thèse

Catherine NOIRIEL,

MAITRESSE DE CONFERENCE HDR, Université Toulouse III - Paul Sabatier

Rapporteuse

Steve BONNEVILLE,

FULL PROFESSOR, Université Libre de Bruxelles

Rapporteur

Cornelius FISCHER,

SCIENTIST, Helmholtz-Zentrum Dresden-Rossendorf

Examineur

Isabelle DANIEL,

PROFESSEURE DES UNIVERSITES, Université Lyon 1 - Claude Bernard

Examinatrice

Laurent CHARLET,

PROFESSEUR DES UNIVERSITES, Université Grenoble Alpes

Examineur

Invités :

Roland Hellmann

DIRECTEUR DE RECHERCHE, ISTerre, Université Grenoble Alpes

Philippe Ackerer

DIRECTEUR DE RECHERCHE, Institut Terre & Environnement de Strasbourg, Université de Strasbourg



Comparative microscopic signatures of microbial and abiotic alteration of calcite

Ph.D. candidate :

Luca Stigliano

Ph.D. advisors :

Damien Daval

Philippe Ackerer

Karim Benzerara

Acknowledgments

To begin, I would like to express my gratitude to my PhD supervisors, Damien, Philippe, and Karim, for their invaluable mentorship, guidance, support, and encouragement throughout this journey.

First, I owe a big thank you to **Damien** for being the one person who first made me realize my passion for research, completely changing my life perspective. His genuine enthusiasm has been a constant source of inspiration for me since the very beginning, and his dedication has been an invaluable asset at every step of the process. Whether providing practical assistance with running experiments, offering insightful guidance in conceptualizing ideas, or simply being kind, extraordinarily present, and supportive, Damien has really embodied the ideal supervisor.

I am also deeply grateful to **Philippe** for believing in me from the very beginning and for readily offering insightful advice whenever I needed his expertise and guidance. I knew I could always count on Philippe whenever I found myself at a dead end, confident that he would come up with unconventional resolving ideas that I would have never thought of. His only shortcoming throughout this journey was his inability to persuade me to master French fluently.

Last but not least, I owe a huge thanks to **Karim** for conveying to me his passion towards the fascinating world of microbe-mineral interactions and for consistently being an extraordinary wellspring of ideas with his enthusiasm and boundless curiosity. Karim's multidisciplinary, creative, and committed approach has always been inspirational for me, profoundly shaping my broader approach to research in general.

A sincere thanks to each one of you for always being there, especially at the beginning of this journey, when I needed it the most. None of this would have ever been possible without all of you.

A huge thanks to all jury members (the reviewers: **Maîtresse de conférences Catherine Noiriel** and **Prof. Steve Bonneville**, the president of the jury: **Prof. Liane G. Benning**, and all examiners: **Prof. Cornelius Fischer**, **Prof. Isabelle Daniel**, **Prof. Laurent Charlet** and **Directeur de recherche Roland Hellman**) for evaluating this manuscript and for the fruitful discussions held during the defense, from which I have really learnt a lot.

On the same note, I extend my gratitude to the members of my thesis committee (i.e., Comité de Suivi Individuel), **Fabrice** and **Tanguy**, for their invaluable inputs and insights over these three years, which meaningfully contributed to improve this work.

I am also sincerely thankful to all the people that helped me in the lab(s) and with the various analytical characterizations necessary for this research work (**Simona**, **Delphine**, **Nathaniel**, **Rachel**, **Gilles**, **Nicolas**, ...). Additionally, a massive thank you to all lab-members from the Geochemistry team at ISTERre and the BIOMIN team at IMPMC, with a special thanks to **Fériel** and **Cynthia** for introducing me to the dynamics of working in a (geo-)microbiology lab, and to **Bastien** for the training and assistance with the VSI *in-situ* experiments.

Lastly, one final big thank you to all **ISTerre friends** (Alicia, Arpad, Benjamin, Carlos & Carlos, Diksha, Jafar, Juliette, Marievi, Mathilde, Robin, Roland *et al*), for the countless lunch & coffee breaks, for all climbing and ski sessions, and for simply being wonderful companions throughout this *Grenobloise wannabe* adventure.

Abstract

Studying the topography of altered rock surfaces represents a cornerstone for reconstructing past environmental conditions and for the identification of traces of life in the geological record, on Earth and beyond. Indeed, the surface microtopography of altered minerals has proven effective in retaining signatures of fluid-mineral interactions. For example, etch pits are among the commonly accepted signatures of interactions between a highly undersaturated aqueous fluid and a mineral surface. However, additional imprints of water-mineral interactions remain to be defined. On a similar note, weathering imprints supposedly left by microorganisms have been proposed as potential biosignatures. These include etching features and microchannels resembling microbes in ‘size, shape and distribution’. However, it has been shown that qualitatively similar surface features can also be reproduced through purely abiotic processes. Therefore, it becomes crucial to develop less ambiguous criteria to differentiate between abiotic and biotic weathering features. In this PhD thesis, these questions were addressed through a combination of experimental and modeling approaches. Calcite dissolution experiments were carried out at various saturation states, both under abiotic conditions and with a cyanobacteria biofilm covering the calcite surface. Time-resolved statistical analyses of the resulting surface topography acquired using vertical scanning interferometry were then conducted. The results suggested that the steady-state surface roughness resulting from dissolution can be used as a proxy to back-estimate the saturation state of the fluid. In this context, stochastic modeling of crystal dissolution helped defining the relaxation time that is required for the surface microtopography to switch from a given steady-state configuration to another, as a result of a change in the solution composition. This suggested that the microtopography of naturally weathered minerals may be representative of the fluid composition most recently visited. Furthermore, the experimental results showed that statistical characterizations of the surface microtopography of altered minerals can be used to quantitatively -thus less ambiguously- detect bio-weathering imprints. Specifically, at far-from-equilibrium conditions, biofilm-mediated dissolution led to the formation of high-elevation regions across the calcite surface, which could be quantitatively detected by semi-variogram analyses. Atomic-scale stochastic simulations of the dissolution process suggested that these bio-weathering features resulted from a local increase in fluid saturation state at the biofilm-mineral contact, leading to a localized reduction in dissolution rate. Altogether, this work provides novel, mechanistically-supported quantitative criteria that may help reconstruct past weathering conditions and identify mineral bio-weathering signatures in natural settings in a non-destructive and less ambiguous way.

Résumé

L'étude de la surface des minéraux altérés et, en particulier, de leur topographie, joue un rôle fondamental dans la reconstitution des conditions environnementales passées et dans la détection de traces de vie dans l'enregistrement géologique, sur Terre et au-delà. En effet, on sait que la microtopographie de surface des minéraux altérés peut conserver des signatures caractéristiques des conditions dans lesquelles leurs interactions avec des solutions aqueuses se sont déroulées. Par exemple, les puits de corrosion figurent parmi les signatures admises des interactions entre un fluide aqueux fortement sous-saturé et une surface minérale. Toutefois, d'autres empreintes d'interactions fluides-minéraux restent à définir. Dans le même ordre d'idées, des empreintes microtopographiques spécifiques ont déjà interprétées comme résultant de l'interaction entre micro-organismes et surfaces minérales : en particulier, il a été suggéré que les puits et microcanaux ressemblant à des micro-organismes en termes de 'taille, forme et distribution' pouvaient constituer des biosignatures. Cependant, il a été démontré que des caractéristiques de surface qualitativement similaires peuvent également être reproduites par des processus purement abiotiques. Il apparaît donc crucial de développer des critères plus univoques pour différencier les caractéristiques d'altération abiotiques et microbiennes. Dans le cadre de cette thèse, ces questions ont été abordées en combinant des approches expérimentales et de modélisation. Des expériences de dissolution de calcite ont été réalisées à divers états de saturation du fluide, à la fois dans des conditions abiotiques et avec un biofilm de cyanobactéries couvrant la surface de la calcite. Des analyses statistiques de la topographie de surface résultante, déterminée au cours du temps à l'aide d'un interféromètre à balayage vertical, ont ensuite été effectuées. Les résultats suggèrent que la rugosité de surface à l'état stationnaire résultant de la dissolution peut être utilisée comme un traceur caractéristique de l'état de saturation du fluide. Dans ce contexte, une modélisation stochastique de la dissolution de la calcite a permis de définir le temps de relaxation nécessaire pour que la microtopographie de surface passe d'une configuration d'équilibre à une autre, en réponse à un changement de composition de la solution. Les résultats suggèrent que la microtopographie des minéraux altérés dans le milieu naturel peut être représentative de la composition du dernier fluide en contact avec le minéral. En outre, les résultats expérimentaux ont montré que les caractérisations statistiques de la microtopographie de surface des minéraux altérés peuvent être utilisées pour détecter quantitativement – et donc de manière moins ambiguë – les empreintes de bio-altération. Plus précisément, dans des conditions loin de l'équilibre, la dissolution sous biofilm a conduit à la formation de régions surélevées de la surface de la calcite, mises en évidence par l'utilisation d'outils statistiques d'analyse de la rugosité tels que des

variogrammes. Des simulations stochastiques à l'échelle atomique du processus de dissolution suggèrent que ces caractéristiques d'altération biotique résultaient d'une augmentation locale de l'état de saturation du fluide au contact du biofilm avec le minéral, entraînant une réduction localisée de la vitesse de dissolution. Dans l'ensemble, ce travail introduit des critères quantitatifs et mécanistes novateurs pour reconstituer les conditions environnementales passées et pour identifier des biosignatures dans l'enregistrement géologique, sur Terre et au-delà, de manière plus univoque et à l'aide d'outils non-destructifs.

Table of Contents

Chapter 1 : Introduction	8
1.1 Chemical weathering: what are the challenges?	8
1.2 Mineral dissolution.....	11
1.2.1 Approaches to measure mineral dissolution rates.....	11
1.2.2 Relationship between saturation state and dissolution rate	13
1.2.3 Interplay between surface area and surface reactivity.....	16
1.2.4 Dissolution rate spectra and resulting surface roughness	18
1.2.5 Relationship between saturation state and surface topography resulting from dissolution.....	23
1.2.6 Impact of organic molecules and foreign ions on the mineral surface topography resulting from dissolution.....	25
1.3 Mineral surface roughness resulting from dissolution as a proxy for the reaction conditions	28
1.4 Microbial weathering of minerals: what are the challenges?	29
1.4.1 Mechanisms of microbial weathering	30
1.4.2 Signatures of microbial weathering.....	32
1.5 Surface topography techniques to study biofilm-mediated mineral dissolution	35
1.5.1 Atomic force microscopy (AFM) to image the topography, and mechanical, electrical and chemical properties of biofilm-mineral assemblages at the sub-nanometre scale.....	35
1.5.2 Vertical scanning interferometry (VSI) to quantify dissolution rates of mineral substrates covered by biofilms.....	39
1.6 Surface imprints resulting from bacterial weathering as potential biosignatures.....	44
1.7 Manuscript plan.....	46
Chapter 2 : Statistical methods to quantitatively detect fluid imprints and bio-weathering signatures	63
2.1 Frequency distribution of height values	63
2.2 Semi-variogram	67
2.3 Power spectral density (PSD).....	70
2.4 Complementary use of semi-variogram and PSD	73
Chapter 3 : Calcite surface roughness resulting from dissolution at close-to-equilibrium conditions	75
3.1 Introduction	80
3.2 Materials and Methods	82
3.3 Results	93
3.4 Discussion	101
3.5 Conclusions	106
Chapter 4 : Calcite surface roughness as a proxy for the reaction conditions	112
4.1 Introduction	116
4.2 Materials and methods.....	119
4.3 Results	129
4.4 Discussion	138
4.5 Conclusions	153
Chapter 5 : Surface imprints of microbial weathering as potential biosignatures	161

5.1 Imprints of microbial contribution to mineral weathering detected by statistical characterizations of surface microtopography.....	163
5.1.1 Introduction	165
5.1.2 Results	167
5.1.3 Discussion	172
5.1.4 Materials and methods.....	176
5.2 <i>In situ</i> VSI investigations of microbial weathering signatures.....	180
5.2.1 Introduction	180
5.2.2 Materials and methods.....	180
5.2.3 Results and discussion.....	182
5.2.4 Conclusions	190
Chapter 6 : Conclusions and perspectives.....	194
6.1 Key findings, limitations, and generalizability.....	194
6.1.1 Limitations.....	195
6.1.2 Generalizability	197
6.2 Applications to natural settings	198
6.2.1 Estimation of the fluid saturation state in natural environments	198
6.2.2 Determination of biosignatures on naturally weathered minerals	199
6.3 Future perspectives.....	199
6.3.1 Microbial weathering in-situ experiments.....	200
6.3.2 Incubation weathering experiments and field studies.....	202
6.4 Concluding remarks	203
Appendices	205
Appendix A	205
Appendix B	206
Appendix C	212

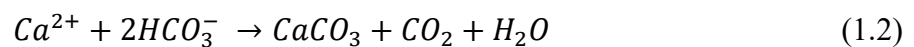
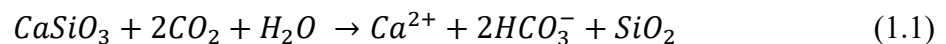
Chapter 1 : Introduction

1.1 Chemical weathering: what are the challenges?

Fluid–solid interactions and associated material fluxes play a significant role across various fields and applications, including the bio-geochemical cycle of elements (Schlesinger et al., 2011), (bio-)leaching (Rohwerder et al., 2003), material corrosion (Sanchez et al., 2015), vitrified nuclear waste disposal (Grambow, 2006), medical science (Wang et al., 2005), and the study of prehistoric rock art (Rousaki et al., 2018), to name a few.

In the Earth sciences, significant emphasis is placed on water-rock interactions occurring in the upper crust, particularly at or near the Earth's surface (Daval et al., 2009b). One of the key water-rock interactions in this context is the process known as ‘chemical weathering’, which involves the breakdown and alteration of mineral assemblages by the chemical action of aqueous solutions (Lasaga, 1984).

Chemical weathering holds a crucial role in reshaping the distribution of mass on Earth, as it participates in the formation of soils (Minasny and McBratney, 2001), releases nutrients for living organisms (Brantley et al., 2011), contributes to seafloor and continental weathering (Krissansen-Totton and Catling, 2017), and plays a role in the long-term regulation of atmospheric CO₂ levels (Berner et al., 1983). As an example, the weathering of silicates and consequent precipitation of carbonates, a natural process also denoted as carbonation of silicates, consumes one mol of CO₂ per mol of silicate, thus serving as a net sink of CO₂ in the overall carbon cycle. For instance:



In addition to its natural occurrence, chemical weathering processes can also be harnessed in various geo-engineering applications, including enhanced rock weathering for CO₂ removal from the atmosphere (Beerling et al., 2020), geothermal energy recovery (Alt-Epping et al., 2013) and CO₂ sequestration.

In order to model the material fluxes associated with chemical weathering, it is essential to determine the rate at which the individual components of rocks, i.e., single minerals, react in the presence of aqueous fluids (Daval et al., 2009b). Several empirical dissolution rate laws

have been developed to this end, according to the following general expression (Aagaard and Helgeson, 1982):

$$r = kA(\xi)e^{\left(-\frac{E_a}{RT}\right)} \prod_i [a_i]^{n_i} f(\Delta G_r) \quad (1.3)$$

where: r [mol/s] is the dissolution rate of a given mineral phase; t is time [s]; k is the rate constant; $A(\xi)$ is the mineral surface area in contact with the fluid [m²], which varies as a function of the extent of reaction, ξ [/]; E_a [J/mol] is the activation energy of the dissolution process, that is the minimum energy required to initiate the reaction; R is the universal gas constant [J/K/mol]; T is temperature [K]; a_i [/] is the activity (i.e., a function of the concentration) of the i^{th} species; ΔG_r [J/mol] is the Gibbs free energy of reaction, that is the energy change that drives the dissolution process.

Regardless of the specific formulation, the hypothesis underlying these rate laws is that the dissolution flux is proportional to the mineral surface area in contact with the fluid, which implies that the reactivity is uniform across the surface and does not change with time. Nonetheless, all rate laws based on this assumption systematically fail to reproduce the long-term and large-scale mineral dissolution rates observed in natural environments by several orders of magnitude (Bricker et al., 2003), making necessary to use the surface area as an adjustable parameter in geochemical reactive models (Aradóttir et al., 2012; Maher et al., 2009; Montes-H et al., 2005). It becomes therefore imperative to appropriately model the relationship between surface area and mineral reactivity.

Numerous studies showed that the heterogeneous nature of the surface reactivity appears as a universal feature of solid dissolution (Fischer et al., 2015; Fisk et al., 2013; Horlait et al., 2014; Nicoleau and Bertolim, 2015; Noiriél et al., 2020; Robin et al., 2018; Williams et al., 1985). This heterogeneity arises from variations in the surface energy (Figure 1.1), which reflects a distribution of different reactive sites and their corresponding reaction mechanisms and kinetics (Figure 1.2) (Fischer et al., 2012). Moreover, as the mineral surface area evolves over time due to dissolution, modifications in the surface reactive sites have a direct dynamic impact on its overall reactivity (Noiriél et al., 2009; Noiriél et al., 2019).

Consequently, developing alternative approaches to assess mineral reactivity, with a specific emphasis on the heterogeneous space–time dynamics of surface roughness, becomes crucial to achieve a more comprehensive understanding and accurate modeling of chemical weathering processes.

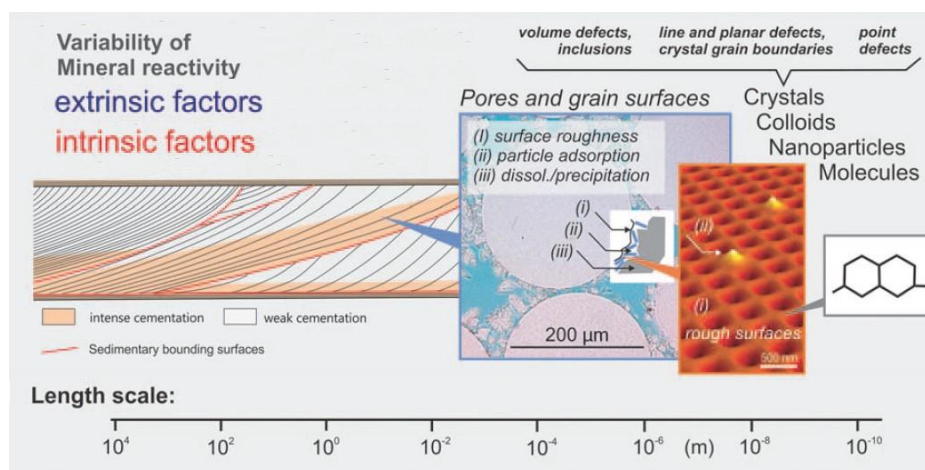


Figure 1.1 Illustration of the main intrinsic and extrinsic contributors to the variability of mineral reactivity, which explains the large uncertainty associated with predictions of mineral reaction rates in natural settings. Large scale extrinsic factors include grain-boundary distribution, mineral aggregation, pores-size, and bounding surfaces in rocks, whereas small scale extrinsic factors comprise molecules, nanoparticles, colloids, and newly precipitated surface films. On the other hand, intrinsic factors include mineral discontinuities and crystallographic defects. Collectively, both extrinsic and intrinsic factors lead to heterogeneities of surface energy over a broad span of length scales that ultimately result in large variabilities in the mineral dissolution rates measured in natural environments. Adapted from (Lüttge et al., 2013).

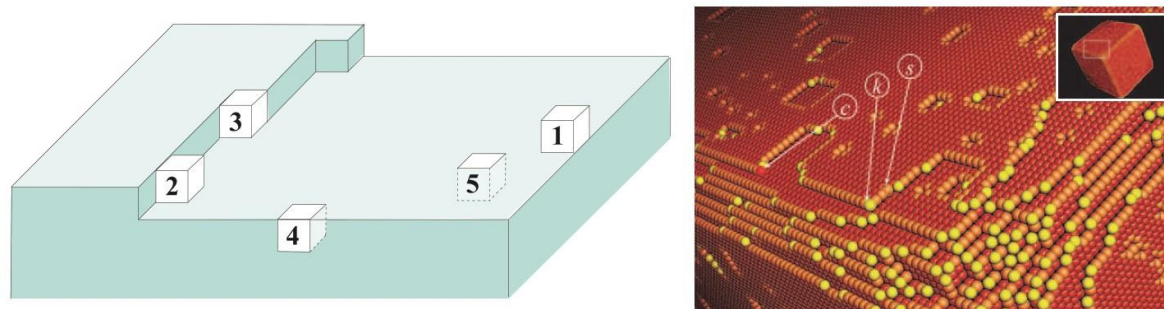


Figure 1.2 Schematic illustrations of a Kossel-cubic crystal, showing the different site types and corresponding number of neighbours, N , with adatom ($N=1$), step ($N=2$, 'c' and $N=4$, 's'), kink ($N=3$, 'k'), and terrace ($N=5$) sites. The illustration at the right-hand side, which was adapted from (Lüttge et al., 2013), shows the details of corners and edges of a 3-D Kossel-cubic crystal.

1.2 Mineral dissolution

In light of the broader context outlined earlier, it becomes crucial to delve deeper into the mechanisms underlying mineral dissolution. The following section is, therefore, dedicated to introducing the methods and techniques commonly employed to study mineral dissolution. Additionally, it offers an overview of the current state of knowledge, established practices, and recent advancements in the field.

1.2.1 Approaches to measure mineral dissolution rates

Mineral dissolution can be assessed using various methods, differing in approach and scales of observation. In laboratory studies, the experimental setups employed to determine mineral dissolution rates can be categorized as closed (batch) and open (fluidized bed reactors, continuously stirred flow-through reactors, column experiments, and variants thereof) systems (Lüttge et al., 2013).

The classical approach involves placing a mineral sample, either as powders or μm -to- mm size single crystals, into a reactor. The *bulk dissolution rate* is then estimated by measuring changes in solution composition, typically with ICP-OES (Inductively Coupled Plasma Optical Emission spectroscopy). In closed (batch) systems, applying a mass balance and assuming a stoichiometric reaction, the mineral dissolution (or precipitation) rate can be expressed according to the following equation:

$$r = \frac{|\Delta C_i|}{\Delta t} * \frac{V}{A} \quad (1.4)$$

where: r [$\text{mol}/\text{m}^2/\text{s}$] is the rate; Δt [s] is the time difference between the time of sampling, t , and the initial (or reference) time, t_0 ; ΔC_i [mol/m^3] is the difference in solution concentration of the i^{th} element composing the mineral, calculated between the time of sampling, t , and the initial time, t_0 (note that ΔC_i is positive for dissolution and negative for precipitation); V [m^3] is the volume of the fluid in the batch; A [m^2] is the surface area of the mineral.

Similarly, in open (flow-through) systems, the rate can be calculated when a hydrodynamic steady-state is reached following:

$$r = Q * \frac{|C_{i,outlet} - C_{i,inlet}|}{A} \quad (1.5)$$

where: Q [m^3/s] is the volumetric flow rate of the fluid; $C_{i,outlet}$ [mol/m^3] is the concentration of the i^{th} element composing the mineral, measured at the outlet of the reactor; $C_{i,inlet}$ [mol/m^3] is

the concentration of the i^{th} element composing the mineral, measured in the tank solution (note that $C_{i,outlet} > C_{i,inlet}$ for dissolution and $C_{i,outlet} < C_{i,inlet}$ for precipitation). Equations 1.4 and 1.5 implicitly assume that the average concentration effectively represents the concentration distribution throughout the volume, implying 'perfect homogenization' of the fluid.

Provided that the volume of the crystals is known, the mineral surface area, A , can be approximated to the geometrical surface area. This method involves calculating the surface area assuming ideal geometrical shapes, such as cubes, rhombohedrons, or spheres (in case of powders) (Lüttge, 2005). Alternatively, the surface area can be estimated based on the Brunauer-Emmett-Teller (BET) theory, which relates the amount of gas adsorbed onto the surface of solid materials to the total surface area available for adsorption (Brunauer et al., 1938).

Unlike the geometric surface area, the BET surface area accounts for all additional contributions arising from surface roughness, porosity, and other surface features, such as steps and etch pits (Anbeek, 1992). However, in practice, the BET method is only effective for minerals characterized by high surface area-to-volume ratios, such as fine-grained mineral powders or highly porous samples with open pores (Lüttge, 2005). Moreover, and more importantly, the BET method does not enable to differentiate between the various surface features (e.g., etch pits or fractures) that collectively contribute to the overall increase in the total surface area. Additionally, it cannot be applied to monitor the evolution of such features during dissolution and their relative contribution to the dissolution rate.

Overall, techniques for estimating dissolution rates based on changes in the solution composition can only yield a *bulk dissolution rate*, which does not provide any information regarding the specific locations on the surface from which the material fluxes are originated. Nevertheless, a prerequisite to the fundamental understanding of the dissolution mechanisms is the ability to measure the dissolution fluxes directly from the mineral surface and to monitor the evolution of the surface during the dissolution process. This became possible in recent decades with the advent of high-resolution surface topography techniques, such as atomic force microscopy (AFM) and vertical scanning interferometry (VSI). These techniques are presented in detail in Section 1.5.1 and 1.5.2, respectively.

The use of VSI allows to estimate the mineral dissolution (or precipitation) rate by directly evaluating the amount of material lost (or gained) by the mineral sample during the reaction. This requires measuring the height difference between a portion of the surface undergoing

dissolution (or precipitation) and a portion of the surface that remains unaltered and serves as a reference (Figure 1.12). To this end, the standard procedure involves covering several small spots on the pristine mineral surface with a high-temperature silicon rubber prior to the experiment. These masks are then removed at later stages of the experiment, exposing the unreacted portions of the surface (Lüttge et al., 1999). The dissolution (or precipitation) rate is thus given by:

$$r = \frac{|\langle \Delta h \rangle|}{V_m \Delta t} \quad (1.6)$$

where: $|\langle \Delta h \rangle|$ [m] is the average height difference between the reacted and the non-reacted area, denoted as ‘surface retreat’ in case of dissolution and as ‘surface advance’ in case of precipitation; V_m is the molar volume of the mineral; Δt [s] is the time difference between the acquisition time, t , (i.e., the time at which the experiments are stopped (or paused) to measure $|\langle \Delta h \rangle|$) and the initial (or reference) time, t_0 .

This approach is particularly useful to study the relationship between the crystallographic orientation of a given mineral face and the corresponding dissolution rate (Daval et al., 2013; Perez et al., 2019; Saldi et al., 2017). Moreover, it can be used to directly measure mineral dissolution rates in soil profiles through incubation experiments (Wild et al., 2019a; Wild et al., 2021).

In addition to measuring dissolution rates, both VSI and AFM can offer valuable insights into the underlying dissolution mechanisms. These techniques enable the tracking of spatial variations in dissolution processes across the surface and the identification of reactive sites, thereby shedding light on how changes in surface topography relate to changes in reactivity. These aspects are discussed in greater detail in Section 1.2.3.

Overall, accurately measuring mineral dissolution rates serves as a pre-requisite to better understand the link between mineral reactivity and a broad range of environmental conditions.

1.2.2 Relationship between saturation state and dissolution rate

In general, the dissolution rate of minerals depends on both physic-chemical parameters (e.g., temperature, pH, fluid saturation state) and mineral properties (e.g., crystal structure, chemical composition, surface area).

Focusing on fluid properties, a critical parameter influencing mineral dissolution / precipitation rates is the saturation state of the fluid with respect to a given mineral phase, which represents

the driving force of the reaction. The saturation state indeed provides a thermodynamic measure of the distance from equilibrium for a particular dissolution (or precipitation) reaction, providing a link between thermodynamics and kinetics.

The saturation state is defined as the ratio between the activity product of the ions in solution (i.e., the product of the ions concentrations raised to the power of their stoichiometric coefficients in the dissolution/precipitation reaction) and the solubility product constant for the mineral phase studied. For $\Omega < 1$ (i.e., undersaturated solution), dissolution is favoured; for $\Omega = 1$ (saturated solution), there is equilibrium between dissolution and precipitation; for $\Omega > 1$ (oversaturated solution), precipitation is favoured.

Since natural waters display a wide range of saturation states with respect to common rock-forming minerals (Opdyke and Wilkinson, 1993; Stefansson and Arnorsson, 2000), it is particularly important to understand the relationship between Ω (or, equivalently, Gibbs free energy of reaction, ΔG_r) and dissolution rate for various minerals. To this end, numerous theoretical (Bandstra and Brantley, 2008; Dove et al., 2005; Lasaga and Luttge, 2004; Luttge, 2006) and experimental studies (Arvidson and Luttge, 2010; Beig and Luttge, 2006; Bouissonnié et al., 2018; Hellmann and Tisserand, 2006; Smith et al., 2013; Xu et al., 2012) have been conducted to investigate this fundamental relationship.

Several experimental studies documented a sigmoidal relationship between dissolution rate and Gibbs free energy for a range of different minerals, including calcite (Xu et al., 2012) (Figure 1.3), albite (Hellmann and Tisserand, 2006), gibbsite (Nagy and Lasaga, 1992), kaolinite (Devidal et al., 1997), labradorite (Taylor et al., 2000), and smectite (Cama et al., 2000), among others. At conditions sufficiently far-from-equilibrium, the dissolution becomes independent of ΔG_r (thus reaching the so-called ‘dissolution plateau’). As conditions move closer to equilibrium, there is a sharp decrease in the dissolution rate over a narrow range of ΔG_r values. Ultimately, as equilibrium is approached, the curve becomes approximately linear, with rates gradually approaching zero along a gentle slope (Arvidson and Luttge, 2010).

Such non-linear behaviour can be explained by the existence of two different dissolution mechanisms, one occurring at far-from-equilibrium and the other occurring at close-to-equilibrium conditions. A description of these two different mechanisms is offered by the stepwave model (Lasaga and Luttge, 2001a), which builds upon the Burton-Cabrera-Frank (BCF) theory (Burton et al., 1951; Cabrera and Levine, 1956).

In brief, according to the BCF theory, dislocations with sufficiently large Burgers vectors will form hollow cores under any undersaturated solution ($\Delta G_r < 0$, $\Omega < 1$). However, these hollow cores only open up to form etch pits (i.e., nm- to μm -scale excavations forming at the mineral surface at line defects, such as screw dislocations) if a critical value of undersaturation is reached ($\Delta G_r < \Delta G_{r,\text{critical}}$, $\Omega < \Omega_{\text{critical}}$) (Cabrera et al., 1954). Subsequently, as per the stepwave theory, the walls of the etch pit serve as a constant source of dissolution stepwaves (i.e., monolayer steps) originated from the outskirts of the pit. These stepwaves then traverse the crystal surface, thus dissolving the crystal in a layer-by-layer fashion, while concomitantly deepening the pit. In contrast, when differences in Gibbs free energy of reaction are not sufficiently large to open hollow cores to form etch pits (i.e., close-to-equilibrium conditions), the constant source of dissolution stepwaves emanated from the pit walls is absent. As a consequence, at close-to-equilibrium conditions, dissolution is significantly slower than at far-from-equilibrium, as it is primarily driven by dissolution of point defects and pre-existing edges and corners, lacking the rate-enhancing contribution of the stepwaves emanated from the pits. Several experimental studies using AFM and VSI have offered substantial support for these two distinct dissolution mechanisms (Arvidson et al., 2003; Arvidson and Lutge, 2010; Cama et al., 2010; Teng, 2004).

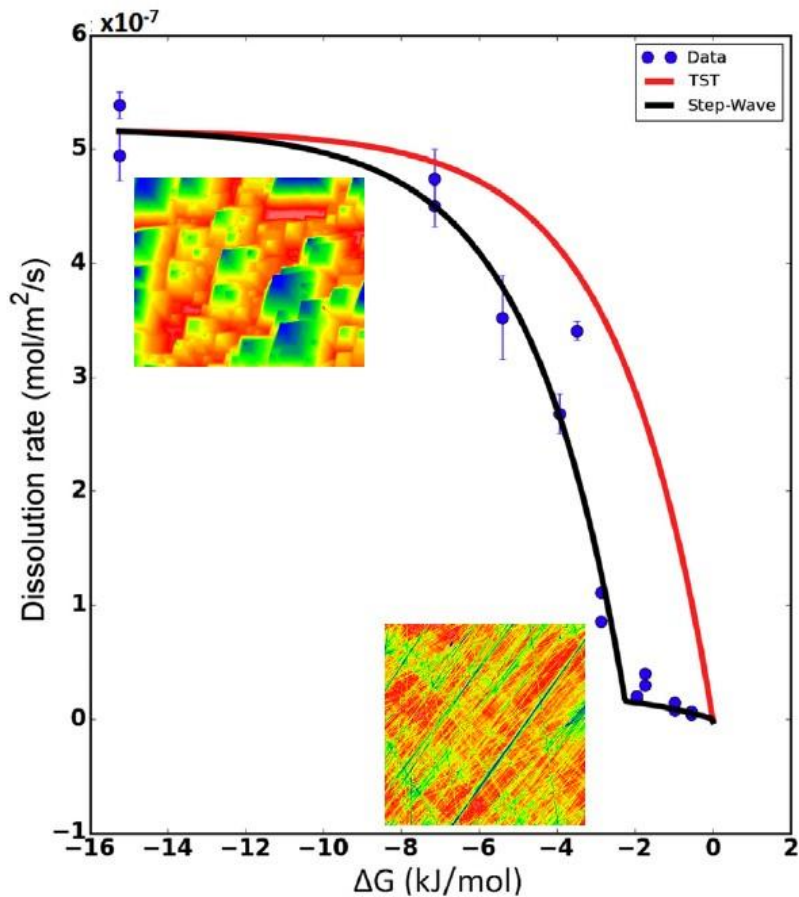


Figure 1.3 Sigmoidal relationship between calcite dissolution rate and Gibbs free energy of reaction, ΔG_r , showing two typical surface topographies resulting from dissolution at far-from-equilibrium and close-to-equilibrium conditions. The size of both topography images displayed is $400 \times 400 \mu\text{m}^2$. Adapted from (Bouissonnié et al., 2018).

1.2.3 Interplay between surface area and surface reactivity

The dissolution mechanisms discussed above implicitly demonstrate how certain areas on the surface exhibit higher reactivity compared to the rest of the surface. In general, certain locations at the surface, such as dislocation lines and point defects (Duckworth and Martin, 2004a), steps (Teng, 2004), and edges and corners (Noiriel et al., 2020), tend to dissolve preferentially.

The specific relationship between surface area and surface reactivity can be conceptualized by considering a Kossel crystal (Kossel, 1927a) (Figure 1.2). A Kossel crystal is a theoretical crystal made up of a stack of individual sites, which can be used to understand the fundamental mechanisms of crystal dissolution at the atomic scale. The faces of a Kossel crystal follow a TLK model (Kossel, 1927a; Stranski, 1928), also denoted as terrace-step-kink model (TSK) model, which means that a given surface is primarily constituted by three types of sites: terraces,

steps, and kinks. It is based on the idea that the reactivity of a given site on a crystal surface is determined by its bonding to neighbouring sites. The higher the number of neighbours (i.e., the higher the number of bonds), the lower the reactivity of that specific site. As so, terraces are less reactive than kinks and steps. The reactivity of all sites at the surface defines the surface reactivity.

It follows that the surface reactivity (and consequent dissolution events) determines changes in the surface area, and changes in the surface area lead to changes in the surface reactivity. This can be easily understood from Figure 1.2. Upon dissolution of specific sites at the surface, new sites with different configurations (i.e., characterized by a different number of neighbours, hence bonds) are revealed, which, as a result, change the overall surface energy. This dynamic interplay, combined with the heterogeneous distribution of structural defects, drives the heterogeneity of reaction rates observed at the mineral surface, as further discussed in the following subsection.

It becomes therefore particularly important to monitor the evolution of the surface area (or topography) of minerals as a function of the dissolution progress and the corresponding changes in reactivity. In other words, it is crucial to investigate the impact of the *reaction history* on mineral dissolution rates.

Numerous works emphasized that the reactivity of crystalline materials is partly inherited from the reaction history. This has been demonstrated both experimentally (Arvidson and Luttge, 2010; Beig and Luttge, 2006; Bose et al., 2008; Luttge, 2006) and from a modeling perspective (Bose et al., 2008; Fischer et al., 2018; Kurganskaya and Luttge, 2021).

One common aspect of all these studies is that the dissolution mechanism does not switch instantaneously from one mode to the other when the crystal experiences a sharp change in the saturation state of the solution. This is particularly evident when the change in saturation state occurs in the direction of increasing Ω (i.e., the solution moves closer to equilibrium conditions). Specifically, as demonstrated experimentally by Arvidson and Luttge (2010), when etch pits are already present on the surface (due to far-from-equilibrium conditions previously experienced), once the saturation state switches to close-to-equilibrium conditions, the (stepwave) dissolution mechanism *transiently* does not change. The stepwaves continue to propagate from the etch pit walls, thereby dissolving the surface layer-by-layer. This results in a *non-steady-state* dissolution rate significantly higher than the *steady-state* rate that would be observed on a pristine surface exposed to identical close-to-equilibrium conditions (Beig and

Luttge, 2006) (Figure 1.4). As dissolution goes on, the pre-existing etch pits grow in radius and become less deep over time, until they ultimately disappear. This is due to a combination of stepwave dissolution mechanism and of fluid conditions not sufficiently far-from-equilibrium to sustain etch pits at dislocation lines.

As a result, after a transient time (also denoted as topographic relaxation time (Bose et al., 2008)), the surface reaches a new configuration for which the *steady-state* dissolution rate, associated with the specific saturation state of the fluid investigated, is once more established.

Altogether, these considerations further highlight the importance of capturing the heterogeneity of reactive sites at the surface when modeling mineral reactivity. This aspect and its implications will be further explored in the upcoming sub-section.

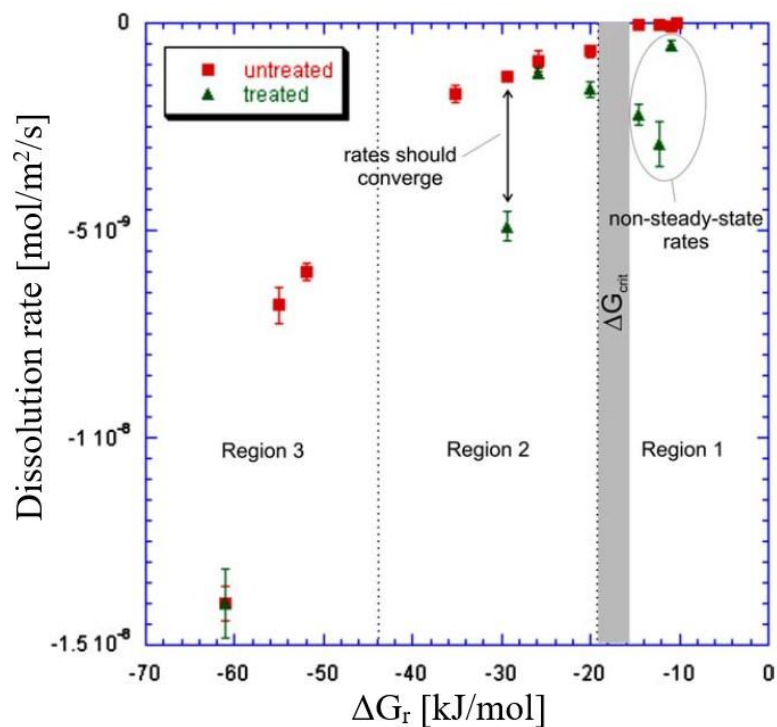


Figure 1.4 Albite dissolution rate vs Gibbs free energy of reaction, ΔG_r , showing the comparison between steady-state rates (obtained starting from pristine, untreated surfaces) and non-steady-state rates (obtained starting from treated, pre-etched surfaces). Adapted from (Beig and Luttge, 2006).

1.2.4 Dissolution rate spectra and resulting surface roughness

Mineral dissolution rates determined in field studies are commonly one to three orders of magnitude lower than rates determined in laboratory (Bricker et al., 2003). Such large

discrepancy can be attributed to both extrinsic and intrinsic factors (Fischer et al., 2014) (Figure 1.1).

The extrinsic factors represent all those factors that have an impact on the mineral dissolution rate but that are not directly related to the physicochemical properties of the mineral itself. This includes environmental conditions such as temperature, pH, and saturation state, differences in fluid-dynamics conditions (i.e., turbulent flow in laboratory vs slow laminar flow in the field (Uroz et al., 2009)), as well as the contribution of microorganisms (Uroz et al., 2009; Wild et al., 2022).

Examples of intrinsic factors include mineral anisotropy (Daval et al., 2013), surface aging (Daval et al., 2013; Wild et al., 2018), differences in the density of structural defects in minerals, and difficulties in quantifying surface area and wetted surface ((Bricker et al., 2003) and references therein).

However, numerous observations from laboratory studies (that controlled for most of these factors) showed that the measured *mean dissolution rates* remain highly variable, suggesting that an *intrinsic variability* in dissolution rates might exist (Fischer et al., 2014). In this context, Fischer et al. (2012) showed that the distribution of reaction rates across the mineral surface is highly heterogeneous, as quantified through the so-called ‘rate spectra’ (i.e., the frequency distribution of local rate values over a given domain). This heterogeneity closely mirrors the anisotropic distribution of surface energy. By comparing the dissolution of calcite to its polycrystalline counterpart (micrite), the authors showed that the resulting rate spectra significantly differ from each other, indicating fundamentally distinct distributions of reactive sites among the two mineral samples. Notably, this intrinsic variability in the distribution of reactive sites may, in part, explain the dispersion seen in the dissolution rates data within the literature (Fischer et al., 2014).

Numerous experimental observations revealed that mineral rate spectra are not normally distributed (Brand et al., 2017; Emmanuel, 2014; Feng et al., 2017; Fischer et al., 2012; Siena et al., 2023), indicating that mean values (and associated standard deviation) are not good descriptors of the actual rate distributions. Adopting a single-valued *mean rate* (or rate constant) as a function of environmental conditions is therefore unjustified (Fischer et al., 2014). Moreover, mean dissolution rates completely obscure all the information about the different contributors to the overall rate, which is instead preserved by the rate spectra (Figure 1.5).

The spatial variability in dissolution rates, captured by the rate spectra, stems from the heterogeneous distribution of reactive sites at the mineral surface and from the seemingly random distribution of crystallographic defects. These spatially variable dissolution rates, in turn, give rise to a surface topography that also exhibits spatial heterogeneity, as quantified through surface roughness characterizations.

As a consequence, both the ‘dissolution rate spectra’ and the ‘surface roughness arising from dissolution’ can be treated as random fields and interpreted through stochastic models ((Siena et al., 2023) and references therein).

For example, the generalized extreme value (GEV) model has proven effective in interpreting the dissolution rate spectra of dolostone (Emmanuel, 2014) and calcite (Brand et al., 2017) at far-from-equilibrium conditions, whereas the generalized-sub-gaussian model has been found to effectively capture the key statistical features of calcite surface roughness arising from close-to-equilibrium dissolution (Siena et al., 2020) and of the rate spectra associated with calcite dissolution at far-from-equilibrium conditions (Siena et al., 2021).

Alternatively, Fischer and Lutge (2007) proposed the use of the length-dependent convergence of surface roughness parameters (and corresponding graphs) as a tool to quantify the surface topography of altered minerals. As surface roughness is a scale-dependent quantity, unidimensional roughness parameters (e.g., average roughness parameter, R_a , root mean square roughness, R_q , etc.) scale as a function of the observation window size. Plotting roughness parameters as a function of the field of view can, thus, provide insights about the contributions of different ‘surface sections’ to the global surface roughness. Specifically, by looking at the convergence graph (i.e., roughness parameters as a function of the field of view), it is possible to identify the ‘regions of convergence’ as those field of views for which the roughness parameters remain locally constant. The converged roughness parameters evaluated over those regions can, therefore, be used to characterize various surface building blocks and to quantify the topography associated with those specific surface sections (Fischer et al., 2014). When employing this approach in conjunction with the rate spectra, it becomes possible to identify the contributions of the various surface sections to the overall reaction rate (Fischer et al., 2014).

A complementary method for quantifying the surface roughness across various scales is the so-called power spectral density (PSD), which is covered in-depth in a later section. This method finds extensive application in material engineering for evaluating surface quality (Duparré et al., 2002; Krolczyk et al., 2016). Conversely, in the field of Earth sciences, it is commonly

employed to characterize the roughness of rock fractures (Cardona et al., 2021), but it is only rarely applied to describe the evolution of the topography of minerals during dissolution (Mellott et al., 2002). Overall, the PSD is a powerful technique that allows to track the evolution of the different frequency components of surface roughness during dissolution.

An alternative approach to study the spatial heterogeneity of surface roughness arising from dissolution is given by the application of geostatistical techniques, which are usually applied at the km-scale (Liu et al., 2017), to topography data at the μm -scale. As an example, Pollet-Villard et al. (2016b) developed a numerical model of orthoclase dissolution able to reproduce the key statistical features of the surface area evolution observed experimentally under far-from-equilibrium conditions. In their study, semi-variogram analyses were employed to calibrate the model parameters, ensuring that the model outputs would display the same spatial autocorrelation observed experimentally. Semi-variogram and PSD techniques are described and discussed more in detail in Chapter 2.

From a stochastic modeling perspective (including kinetic Monte Carlo (kMC) modeling (Blum and Lasaga, 1987), which will be discussed in detail later in the manuscript), most of the studies have focused on the analysis of the number of sites that are involved in the reactions (Figure 1.6) and, thus, on the global material flux (e.g., (Ackerer et al., 2021) and references therein), without specifically looking at the evolution of surface roughness during dissolution (Fischer et al., 2014). Among the kMC studies that specifically placed emphasis on surface roughness, Hernández Creus et al. (1997) showed that, under chemically aggressive conditions, surface roughness strongly increases due to etching, until it eventually reaches a morphological steady-state configuration. Wehrli (1989) demonstrated that the steady-state surface roughness increases when the crystal bonds strength decreases (i.e., when the relative reactivity of all sites increases). More recently, de Assis and Aarão Reis (2018) investigated the dissolution of minerals with rough surfaces, showing how the evolution of the surface undergoing dissolution evolves in the direction of decreasing the surface energy, until the whole sample is ultimately flattened. Conversely, Carrasco et al. (2021) studied the dissolution of initially flat calcite surfaces, showing how, at high temperature, the surface roughness scales in time and size according to the Kardar–Parisi–Zhang equation of kinetic roughening.

Overall, kMC modeling and stochastic simulations are powerful tools to explore the evolution of surface roughness during dissolution. They can be particularly advantageous in situations where experimental endeavours are impractical or excessively time-consuming. Nevertheless, the primary limitation lies in the inability to predict in advance whether the model accurately

reproduces the outcomes that would be observed experimentally. Therefore, as a general strategy, it is recommended to employ numerical simulations in combination with experimental and analytical methods, consistently looking for cross-validations.

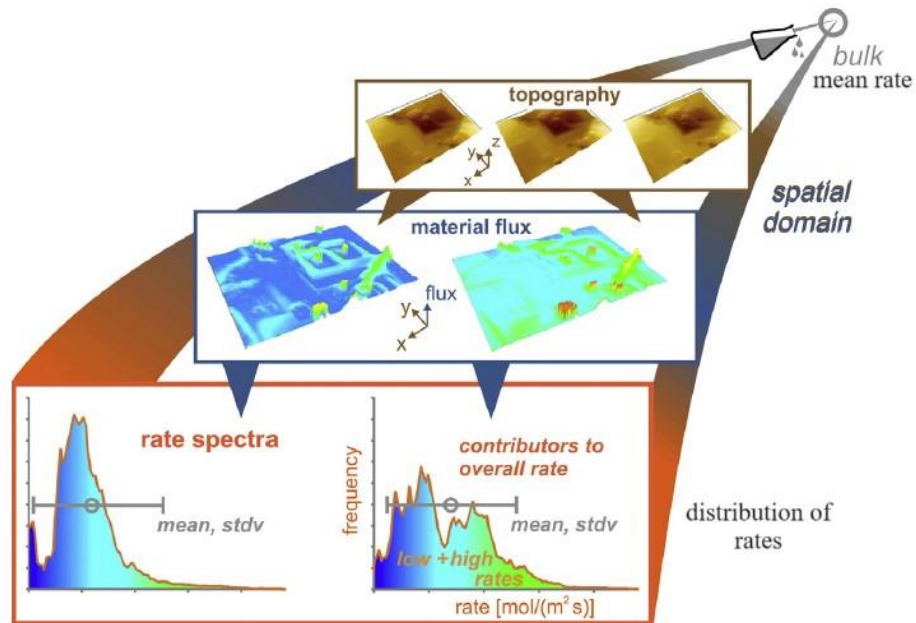


Figure 1.5 Schematic illustration depicting how rate spectra preserve critical information about reaction modes that are obscured by single-valued mean dissolution rates. Illustration adapted from (Fischer et al., 2014).

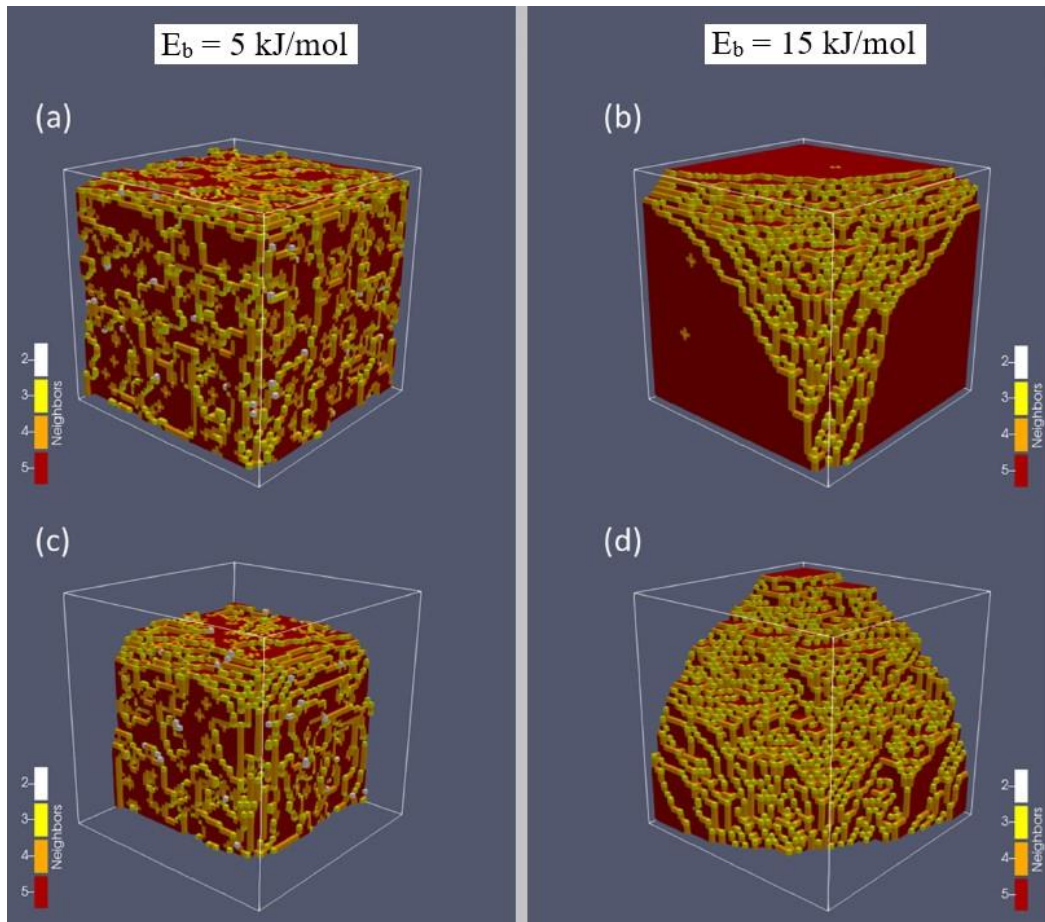


Figure 1.6 Evolution of a Kossel crystal during dissolution, simulated using kMC modeling with two different values of bond-breaking activation energy: $E_b = 5$ kJ/mol (a, c) and $E_b = 15$ kJ/mol (b, d). Images (a) and (b) correspond to a reaction extent of 10%, whereas images (c) and (d) represent a reaction extent of 50%. Only 1/8 of the crystal is displayed, and the white solid line represents the initial size of such a one eighth of the crystal. Adapted from (Ackerer et al., 2021).

1.2.5 Relationship between saturation state and surface topography resulting from dissolution

As discussed in section 1.2.2, several minerals exhibit a sigmoidal relationship between dissolution rate and Gibbs free energy, which can be explained by the existence of two distinct dissolution mechanisms. Arvidson and Mackenzie (2000) suggested that such relationship might be shared by all crystals that dissolve through the formation of etch pits formed at dislocation outcrops, which includes all crystals having a framework structure.

Due to the existence of two distinct dissolution mechanisms, far-from-equilibrium and close-to-equilibrium conditions lead to surface microtopographies that are markedly dissimilar from

each other. Specifically, while the ‘far-from-equilibrium microtopography’ is dominated by the presence of etch pits, the ‘close-to-equilibrium microtopography’ tends to preserve the largest pre-existing surface features, such as cleavage steps, over the relatively short timescales commonly investigated in laboratory studies (Teng, 2004; Xu et al., 2012).

Of note, the examples and discussions provided in this (and in the following) sub-section revolve around calcite, as it was chosen as a *model mineral* for this study, for the reasons that will be elaborated in section 1.7. Additionally, for calcite, the relationship between saturation state and resulting dissolution morphological features has been studied extensively (Bouissonnié et al., 2018; Gao et al., 2010; Kurganskaya and Lutge, 2021; Smith et al., 2013; Teng, 2004; Xu et al., 2012).

When it comes to dissolution of calcite {104} faces, the relationship between saturation state and surface topography extends beyond a simple differentiation based on the presence or absence of etch pits. At very far-from-equilibrium conditions ($\Omega \sim 0.00$), the etch pits typically have a rhombic shape, whereas, at slightly closer-to-equilibrium conditions ($\Omega \sim 0.02 - 0.20$), they tend to become more triangular (Figure 1.7) (Bouissonnié et al., 2018; Gao et al., 2010; Teng, 2004). Of note, the critical value of the saturation state (Ω_{critical}) above which the formation of microscopic etch pits is no longer observed experimentally is estimated at $\sim 0.31 - 0.45$ ((Bouissonnié et al., 2018) and references therein).

A mechanistic explanation for the etch pits morphology observed at far-from-equilibrium conditions is provided in (Gao et al., 2010). Their considerations are briefly summarized here. The rhombic shape observed at $\Omega \sim 0.00$ is a direct consequence of the rhombohedral symmetry of the calcite lattice, for which there are two inequivalent types of steps, with obtuse and acute orientations. The two acute (and the two obtuse) steps are crystallographically equivalent in the absence of chiral solutes (Orme et al., 2001). The acute steps create an overhang on the lower terrace, whereas the obtuse steps form a more open structure with respect to the lower terrace. At $\Omega \sim 0.02 - 0.20$, the etch pits develop a more triangular shape. While the obtuse steps intersect at a distinct point, forming a sharp corner, the acute steps form a curvilinear boundary.

This phenomenon can be fundamentally attributed to backward reactions (precipitation processes), which become increasingly frequent as the saturation state rises. According to the TLK model (Liang and Baer, 1997), precipitation occurs at single kink sites. Since acute steps have more single kink sites compared to obtuse steps, the net acute–acute kink detachment rate is thus significantly reduced compared to that of the obtuse–acute kink sites (Jordan et al.,

2001). This results in the accumulation of acute-acute kink sites at the acute steps, which ultimately produces the triangular shape of the (otherwise rhombohedral) etch pits.

Altogether, these considerations suggest that valuable information about the fluid saturation state might be *imprinted* in the altered calcite surface. This suggests the potential existence of a more general relationship between saturation state and surface topography arising from dissolution, as further discussed in a subsequent section.

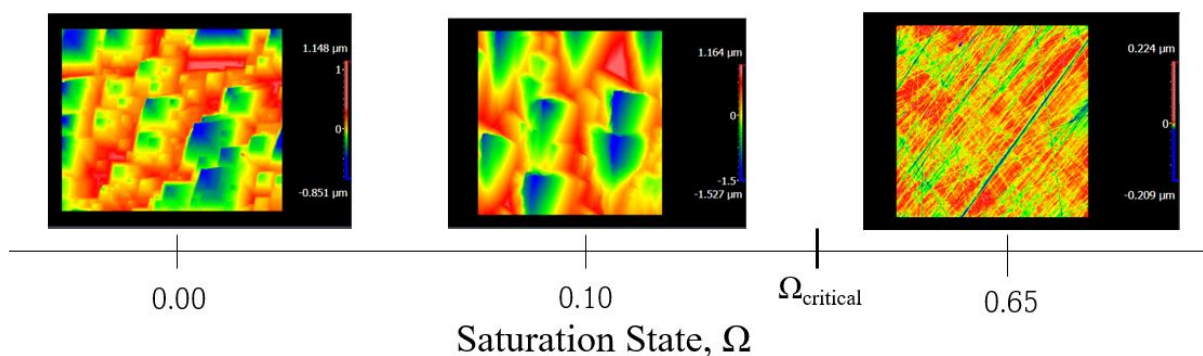


Figure 1.7 Calcite surface microtopography arising from dissolution as a function of the saturation state. Topography data were acquired with VSI at 50x magnification. The size of all windows is $400 \times 400 \mu\text{m}^2$. Topography data corresponding to $\Omega_{\text{calcite}} = 0.00$ and $\Omega_{\text{calcite}} = 0.65$ are unpublished data, whereas topography data corresponding to $\Omega_{\text{calcite}} = 0.10$ were published in (Stigliano et al., 2023b).

1.2.6 Impact of organic molecules and foreign ions on the mineral surface topography resulting from dissolution

It is worth noting that beside the saturation state, other factors can impact the surface microtopography that emerges from dissolution. In this regard, there is an extensive literature documenting how the presence of organic compounds (Oelkers et al., 2011; Teng and Dove, 1997; Wu et al., 2011; Yang et al., 2008) and foreign ions (Lea et al., 2001; Vinson et al., 2007) can alter the reaction mechanism (e.g., through inhibition of relative step velocities by selective binding), which, in turn, modifies the etch pits morphology.

The crucial role played by organics (e.g., polysaccharides) in biologically controlled mineralization of calcite is widely recognized (Arias and Fernández, 2008; Yang et al., 2008). However, organic molecules also play a role in mediating calcite dissolution, thus altering the resulting surface topography (Oelkers et al., 2011; Wu et al., 2011; Yang et al., 2008). For instance, (Teng and Dove, 1997) showed that, when exposed for a few minutes to aspartate solutions, the calcite surface develops triangular-shaped etch pits with sharp edges, which, after

two weeks of reaction, lead to the formation of well-oriented tetrahedral etch hillocks interconnected by triangular etch pits (Figure 1.8).

Clear modifications in calcite etch pits morphology can also be observed in presence of foreign ions, i.e., ions that are not normally part of the calcite structure and that may come from the surrounding environment or from impurities within the crystal itself. The interaction of calcite surfaces with foreign ions has a significant impact on its overall reactivity and resulting surface topography. Several studies showed that the presence of Mg^{2+} in carbonated solutions can significantly alter the morphology of calcite etch pits by selective step pinning through adsorption of Mg^{2+} (Arvidson et al., 2006; Gao et al., 2010; Ruiz-Agudo et al., 2009). Modifications in step velocity ratio and resulting changes in etch pits morphology due to site-specific pinning or adsorption was also observed in presence of Mn^{2+} (Vinson et al., 2007), Sr^{2+} (Vinson and Lüttge, 2005), Li^+ (Ruiz-Agudo et al., 2010) and Cd^{2+} (Pérez-Garrido et al., 2007). Furthermore, (Ruiz-Agudo et al., 2010) documented changes in etch pit morphology from rhombohedral to pseudo-hexagonal and elliptical during calcite dissolution in solutions containing F^- . Additionally, (Klasa et al., 2013) showed how, in phosphate-bearing solutions, the rhombohedral etch pits gradually changed morphology as the phosphate concentration increased, starting with the rounding of acute steps, progressing to pseudo-triangular shapes, and ultimately resulting in the appearance of heart-shaped, tear-shaped, or distorted rhombohedra. In general, the mechanisms responsible for the observed alterations in the etch pits morphology primarily involved the selective inhibition of specific sites within the etch pit steps.

Altogether, these observations highlight how the mineral surface topography arising from dissolution can be informative about the solution chemistry to which the mineral was exposed. However, these studies also show that some of the non-rhombohedral etch pits morphologies (e.g., pseudo-triangular and rounding of acute steps) can occur under a range of chemical conditions very distant from each other. This suggests that qualitative descriptions of surface morphology alone may not be adequate to differentiate between the various chemical factors (e.g., saturation state, foreign ions, or organic mediation) that might have led to their formation. This aspect poses significant challenges for potential applications in environmental reconstruction, as discussed in the following section.

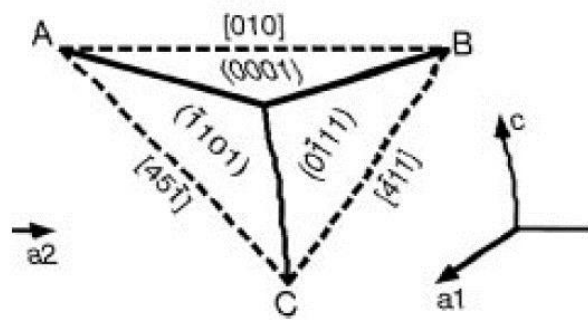
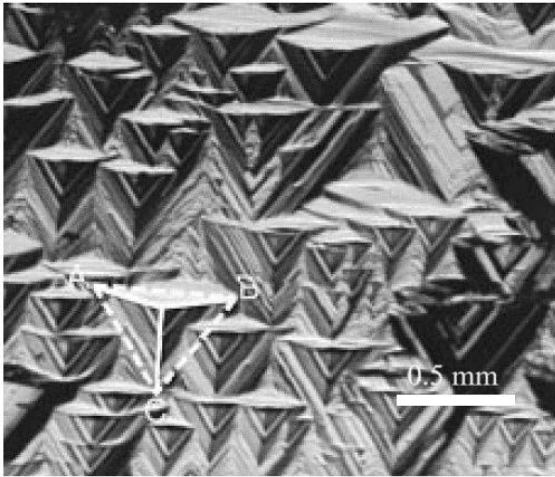


Figure 1.8 Digital image of etch hillock features (i.e., well-oriented tetrahedral etch hillocks that are interconnected by triangular etch pits) developed on the calcite $\{104\}$ face after dissolution in an aspartate solution for two weeks. The image includes labels indicating the orientations of the three constituent faces of the tetrahedrons and the orientations of the individual layers that make up the hillocks. The corresponding crystallographic axes associated with these features are also included. Adapted from (Teng and Dove, 1997).

1.3 Mineral surface roughness resulting from dissolution as a proxy for the reaction conditions

As discussed in sub-section 1.2.5, qualitative comparisons of the calcite surface topographies resulting from dissolution at different saturation states indicate that a more general Ω - surface topography relationship might exist. If such a relationship *does* exist, several minimum requirements must be fulfilled to make it a reliable proxy to back-estimate the fluid saturation state: 1. the relationship must be quantitative, hence the microtopography main features must be somehow quantified; 2. the surface topography arising from dissolution must reach a steady-state configuration, as quantified by the metrics adopted; 3. the steady-state configurations resulting from different Ω must be sufficiently distinguishable from each other; 4. the steady-state configurations resulting from different Ω must be sufficiently distinguishable from the surface topographies originated by other factors (e.g., organics or foreign ions).

All these conditions need to be verified experimentally. However, central to the development of this relationship (and its potential use as a proxy) is the *quantification* of the surface topography, which can be done through surface roughness characterizations, as discussed in detail in Chapter 2. In this way, the informative content of the surface microtopography is summarized into the main statistical traits captured by the surface roughness characterization. As so, the surface microtopographies resulting from dissolution at different saturation states can be quantitatively compared through the corresponding surface roughness characterizations, thus establishing the Ω - surface topography relationship.

1.4 Microbial weathering of minerals: what are the challenges?

The chemical weathering of rock-forming minerals was initially conceptualized in terms of abiotic reactions alone (Smits et al., 2009). Nevertheless, over the last decades, there has been a growing recognition of the role that living organisms play in this process (Burford et al., 2003; Hoffland et al., 2004; Smits et al., 2009; Wild et al., 2022). Various living organisms have been shown to influence (either promoting or inhibiting) mineral weathering rates, including bacteria (Uroz et al., 2015), archaea (Bai et al., 2021), algae (Coombes, 2014), fungi (Gadd and Petrology, 2017), plants (Bonneville et al., 2009), and animals (Dorn, 2014), both individually and through symbiotic cooperations. The processes by which living organisms influence mineral weathering are commonly referred to as *bioweathering*.

Plants and microbes play a significant role in mineral bioweathering. Specifically, the contribution of plants, including their roots and associated microbial symbionts, has been extensively studied and tentatively modelled ((Wild et al., 2022) and references therein). Current evidence suggest that plants globally accelerate rock weathering through a variety of chemical and physical mechanisms (Dontsova et al., 2020; Porder, 2019). These include: (i) carbon acid production and exudation of organic ligands; (ii) selective uptake of macronutrients, such as base cations (Ca^{2+} , K^+ , Mg^{2+}) and phosphorous; (iii) modifications of the soil hydrology; (iv) physical breakdown of rocks caused by the growth of roots, which, in turn, exposes new mineral surface area to chemical weathering (Dontsova et al., 2020).

Conversely, the specific contribution of microbes to mineral bioweathering (also denoted as *microbial weathering*) has often been overlooked, despite several factors indicating its potential significant impact (Wild et al., 2022). Microorganisms, which include prokaryotes (bacteria and archaea) and μm -size eukaryotes (fungi, algae and protozoa), inhabit a wide array of environments on Earth, including the most extreme habitats (e.g., deserts, geothermal soils, hot springs, hypersaline habitats, and the deep sub-surface) ((Burford et al., 2003) and references therein). In all these environments, microbes constantly interact with minerals, e.g., by using them as substrates to sustain biofilm growth (Gorbushina, 2007), by inducing their dissolution for nutrients uptake (Ahmed and Holmström, 2014), or by inducing their formation for energy storage or pH regulation functions (Cosmidis and Benzerara, 2022). Moreover, it has been shown that the crystallographic properties of the mineral substrates (i.e., chemical composition and structure) can influence the diversity of soil bacterial communities, suggesting that the minerals create true ecological niches (Gleeson et al., 2006; Uroz et al., 2012).

Overall, these observations indicate that microbial weathering *does contribute* to mineral weathering. However, this prompts several questions: What are the mechanisms underlying microbial weathering? Is microbial contribution quantitatively significant? How can microbial weathering be differentiated from other forms of (bio-)weathering? What are the signatures of microbial weathering?

1.4.1 Mechanisms of microbial weathering

Microbes can both promote and inhibit (also denoted as *bioprotection*) mineral weathering, according to different mechanisms. For instance, acidolysis reactions (e.g., resulting from the excretion of H^+ , organic acids and other metabolites, and / or by the formation of carbonic acid due to respiration) lead to a decrease in pH, which tends to favour mineral dissolution (Gadd, 2010). Conversely, CO_2 fixation carried out by some autotrophic (e.g., photosynthetic, chemosynthetic) microorganisms leads to an increase in pH, which tends to favour mineral precipitation (Dittrich and Sibling, 2010). Microbes can also promote dissolution of primary metals-bearing minerals by excreting organic ligands, which can form chelate complexes with metal ions at the crystal surface, thus promoting its dissolution (i.e., the organic ligand wraps around the metal ion, creating a stable complex in which the metal ion is effectively sequestered and solubilized). For example, it is widely recognized that microbial siderophores (Fe-chelating ligands) can increase the dissolution rate of Fe-silicates (olivines, pyroxenes, hornblendes, and biotite) in soils ((Buss et al., 2007) and references therein).

Certain microorganisms, specifically fungi, have the capability to enhance weathering through mechanical processes similar to those previously described for plant roots. The combination of turgor pressure forces within fungal appressoria (structures utilized to penetrate host organisms), which can reach up to 8 MPa, along with the pulsatile, apical growth of hyphae and the strong adhesive forces that anchor fungi to mineral surfaces, can play a role in the creation of shallow ‘trenches’ of ~ 100 nm in depth on the surfaces of biotite and chlorite basal planes ((Wild et al., 2022) and references therein). This distinctive growth pattern facilitates the displacement and fragmentation of the uppermost material, leading to the generation of new mineral surface area on an otherwise relatively unreactive basal plane (Bonneville et al., 2016).

When studying microbe-mineral interactions (including microbial weathering) in natural environments, it is crucial to differentiate between planktonic (i.e., free-floating) and biofilm-forming (i.e., adhering to surfaces) microbes. Biofilms are complex communities of sessile (i.e., immobile) prokaryotic and / or eukaryotic microbes adhering to each other through a self-produced extracellular matrix (Figure 1.9), primarily made of extracellular polymeric

substances (EPS), which mostly consist of exopolysaccharides, DNA, and/or proteins (Costerton et al., 1995). Water constitutes ~ 97% of the total mass of a biofilm (Zhang et al., 1998), while a substantial portion of the organic content, ranging from 50% to 90%, is composed of EPS (Flemming and Wuertz, 2019).

While planktonic microbes can also indirectly interact with minerals in their vicinity by inducing (and by responding to) changes in the bulk solution chemistry, biofilm lifestyles generally enable a more effective exchange of elements with the mineral substrates (e.g., (Ahmed and Holmström, 2014)). Of note, in natural environments, planktonic microbial communities are generally taxonomically and metabolically very different from microbial communities within biofilms (Iniesto et al., 2022).

A key advantage of biofilms is the ability to generate at the fluid-mineral interface *confined microenvironments* with chemical conditions that locally diverge from those of the surrounding bulk solution. In these microenvironments, microbes can locally regulate chemical (e.g., pH, chemical potential of specific elements) and environmental (e.g., moisture content) conditions to protect themselves from adverse conditions (e.g., droughts, fluctuations in solution compositions) ((Wild et al., 2022) and references therein). As so, in the context of bioweathering, biofilms can establish at the fluid-mineral interface weathering conditions (in terms of, e.g., pH, fluid saturation state, local concentration of chelating agents and redox conditions (Liu et al., 2002; Newman and Kolter, 2000)) that are highly different from the weathering conditions of the bulk fluid, thus significantly impacting the overall mineral weathering rate.

Finally, it is worth emphasizing that when the conditions within the biofilm microenvironment favour mineral precipitation, biofilms can serve as *protection* against weathering. Such bioprotection mechanism can be achieved through the passivating impact of mineral precipitation and EPS covering the mineral substrate (Jroundi et al., 2017).

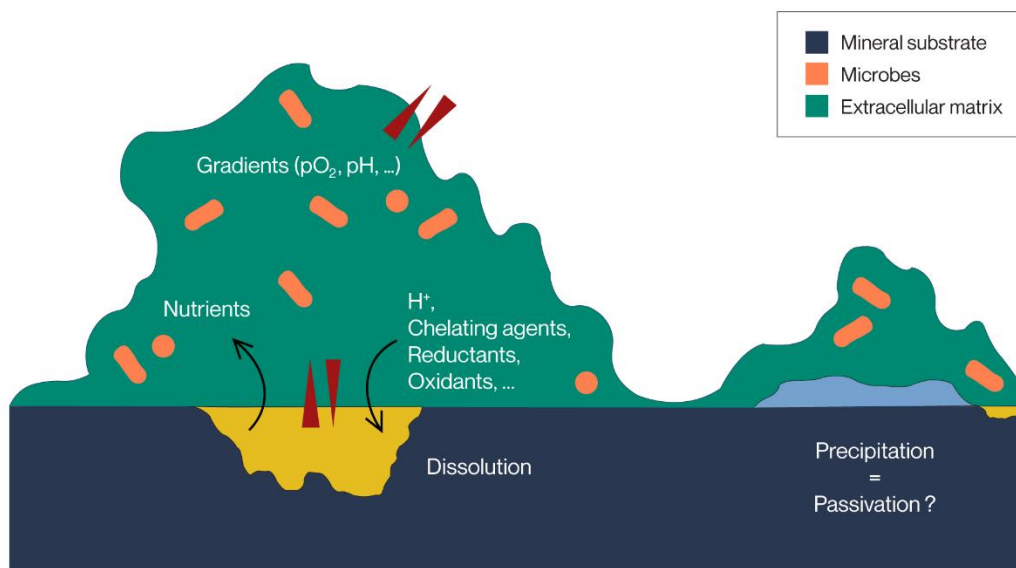


Figure 1.9 Sketch of biofilm-mineral interactions. Minerals can be dissolved. Dissolution can be enhanced or slowed down by the production of protons, chelating agents, reductants, oxidants by microbes. Microbes can also attach to high-energy sites. Dissolution in turn releases nutrients and drives the onset of chemical gradients (double arrows in red) at the base of the biofilm. Minerals can be precipitated (light blue) within biofilms, which can lead to passivation of the mineral substrate surface underneath the biofilm. Passivation refers to the formation of minerals on top of the mineral substrate (yellow) surface that makes the substrate surface less prone to alteration, reducing its dissolution rate. Sketch and corresponding captions from Fig.1 in (Stigliano et al., 2023a).

1.4.2 Signatures of microbial weathering

As outlined in the previous subsection, microbes have the potential for both enhancing and inhibiting mineral weathering. Assessments of the microbial impact on weathering rates for specific microbe-mineral interactions, as quantified by the ‘acceleration factor’ (i.e., microbially enhanced rate / abiotic rate), can vary significantly, ranging from as low as 0.1 (indicating bioprotection) to more than 8 (indicating enhancement) ((Wild et al., 2022) and references therein). Nevertheless, the quantitative global net contribution of microbial weathering to the overall weathering rate remains an open question.

Due to several challenges associated with measuring chemical weathering rates in natural environments, most of the studies attempting to estimate the intrinsic contribution of microbes to weathering fluxes relied on laboratory experiments involving axenic (i.e., single strain) cultures (e.g., (Santelli et al., 2001)). While these studies provided valuable insights into the

mechanisms by which microbes affect dissolution rates (Bray et al., 2015; Cama and Ganor, 2006), they have several limitations in terms of relevance with respect to natural settings. First, they are restricted to microorganisms that can be cultured in the laboratory. Second, they do not consider the complex interactions that occur within microbial communities in the field, where multiple species coexist, sometimes in symbiotic cooperations. Then, it is not possible to precisely replicate the actual environmental conditions within laboratory settings. Lastly, these experiments often employ fresh mineral surfaces, from which elements are much more readily accessible than in natural settings, in which natural samples are subject to ‘surface aging’ (Eggleston et al., 1989).

Higher degrees of relevance and accuracy have been reached over the years both in field (e.g., incubation experiments) and laboratory (e.g., microcosms experiments) settings ((Wild et al., 2022) and references therein). However, beyond the question of microbial weathering rates, it is crucial to understand the mechanisms by which microbes affect the dissolution fluxes.

To this end, high-resolution surface topography techniques, such as VSI, have recently proven successful in providing insights about the link between bacterial and/or fungal attachment and mineral surface dynamics (Davis and Lüttge, 2005; Quirk et al., 2015; Wild et al., 2021). For instance, Wild et al. (2021) used VSI topography measurements to deconvolute the weathering flux distinctively due to the fungal hyphae of *Verticillium* sp. from the solution-related flux from olivine samples incubated in a soil profile of a temperate forested area. The authors concluded that the contribution of olivine-colonizing fungi in a Mg-deficient forest soil accounted for up to 16% of the weathering flux after 9 months of incubation. Such enhancing contribution was highly localized and limited to the location where the hypha attached to the mineral, resulting in a depression of the surface. Similar imprints of localized enhanced mineral weathering due to hyphae attachment were also documented in other studies (Bonneville et al., 2009; Quirk et al., 2015) and can be explained by a combination of mechanical forcing that weakens the crystal structure at early stages (during attachment) and chemical alteration of the mineral substrate at later stages (Bonneville et al., 2009).

Overall, these observations indicate that the surface topography resulting from microbial weathering can retain distinct signatures of the microbial contribution, suggesting that the *surface imprints* left behind by microbes during weathering may serve as potential *biosignatures*.

In this context, micron-scale morphological features, such as tubular microchannels or etch pits developed in altered glass or mineral samples, have often been interpreted as imprints of bioweathering left by microorganisms (Bennett et al., 1996; Benzerara et al., 2005; Fisk et al., 1998; Jongmans et al., 1997; McLoughlin et al., 2007; Thorseth et al., 1995). Specifically, etching features resembling microorganisms in ‘size, shape and distribution’ are among the conventional criteria used to suggest past or ongoing interactions between microbial cells and minerals (Fisk et al., 1998; Thorseth et al., 1995). However, the identification of biosignatures based on the microtopography of naturally weathered samples has often proven elusive, as etch pits and tubular features could equally be formed abiotically (Benzerara et al., 2007; Fisk et al., 2013; Santelli et al., 2001).

This requires, on the one hand, to better understand the mechanisms behind the formation of various weathering features under a broad range of biotic and abiotic conditions, which would allow to evaluate the likelihood of different potential explanations. On the other hand, this also requires to be able to detect the subtle differences in the fine morphology of weathering features, which could be key to differentiate between abiotic and biotic processes (Welch et al., 2002). To these ends, high-resolution surface topography techniques are particularly useful, as discussed in the following section.

1.5 Surface topography techniques to study biofilm-mediated mineral dissolution

High-resolution surface topography techniques can offer valuable insights into the mechanisms underlying microbial weathering of minerals and the subsequent formation of bioweathering features. As previously discussed, mineral-colonizing microbes, especially those forming biofilms, can interact effectively with minerals, due to their close proximity. As so, studying biofilm-mineral interactions with high-resolution surface topography techniques can be particularly informative in this regard.

This section includes two paragraphs of the book chapter ‘Micro- and nanoscale techniques for studying biofilm-mineral interactions’ that was recently published in *Methods in Microbiology* (Stigliano et al., 2023a). These segments focus on two high-resolution surface topography techniques (AFM and VSI) that show great potential in elucidating the mechanisms behind microbial weathering and in distinguishing subtle variations within the fine structure of (bio-)weathering features.

1.5.1 Atomic force microscopy (AFM) to image the topography, and mechanical, electrical and chemical properties of biofilm-mineral assemblages at the sub-nanometre scale

Atomic Force Microscopy (AFM) is a very-high-resolution scanning probe microscopy technique for surface analysis. It essentially consists of: (i) a flexible cantilever with a sharp tip scanning over the sample surface; (ii) a piezoelectric scanner controlling lateral and vertical position of the AFM probe relative to the surface under study; (iii) a laser beam reflected from the back side of the cantilever and directed onto a photodiode detector; (iv) a feedback loop system (Figure 1.10). As the tip scans over the studied surface, attractive or repulsive forces between the tip and the sample cause a deflection of the cantilever. The deflection is measured with the laser reflected from the back side of the cantilever onto the detector. The deflection signal recorded on the photodiode detector, combined with the information about the distance between the cantilever and the surface as controlled by the piezoelectric scanner, are finally converted into a topographic map.

AFM is actually a broad term encompassing several different operating modes, ranging from topography measurements to mechanical, electrical and chemical surface characterizations at the nanoscale. The different topographic modes can be classified based on the specific operating modes such as: (i) ‘contact mode’, in which the tip is continuously in contact with the surface

when raster-scanned across the sample, (ii) ‘intermittent contact mode’, better known as ‘tapping mode’, in which the tip continuously oscillates close to the studied surface and perpendicularly to it, intermittently touching it, and (iii) ‘non-contact mode’, in which the tip oscillates as in ‘tapping mode’ but without ever getting in direct contact with the surface (Figure 1.10). Generally, ‘contact mode’ is optimal for hard and regular samples, whereas ‘intermittent’ or ‘non-contact modes’ are preferable for softer and less regular samples (e.g., biofilm). AFM allows to obtain topography images with 1 Å vertical resolution, 30 nm lateral resolution, 10 µm vertical scanning range and 100 µm² field of view. For the study of biofilm-mineral assemblages, the ‘force mapping’, a non-topographic mode, also appears particularly interesting. In this mode, the force between the AFM tip and the studied surface is measured, providing information about mechanical properties, such as adhesion forces. An extensive description of all AFM operating modes can be found in (Eaton and West, 2010).

Applying AFM to the study of mineral dissolution and growth has become increasingly popular over the years (Daval et al., 2013; Li et al., 2021; Nagy et al., 1999; Pollet-Villard et al., 2016a). Mineral samples can be imaged under wet conditions, without any sample preparation, allowing the study of the surface dynamics of minerals undergoing dissolution-precipitation processes in situ (Pimentel et al., 2013; Siena et al., 2021; Wang and Putnis, 2020). Meanwhile, AFM has proven to be an equally essential tool for the analysis of microbial systems (Dufrêne, 2002; Wright et al., 2010). However, proper AFM imaging and force mapping of live cells under physiologically relevant conditions are technically challenging. In fact, since the cells are only weakly bonded to the substrate, the interaction with the scanning tip may provoke cell detachment or damage (Wright et al., 2010). Nevertheless, great progress has been achieved in this respect over the past two decades (Evans et al., 2021; Hu et al., 2020). Additionally, AFM has been extensively applied to monitor biofilm development (Kamaeva et al., 2014; Oh et al., 2007; Oh et al., 2009) and biofilm-EPS properties (Breitenbach et al., 2018).

Overall, AFM has great potential in characterizing biofilm-mineral interactions. Recently, (Wang et al., 2022) documented how *Vibrio harveyi* J4, an extreme halophilic bacterium, could initiate the calcite-to-protodolomite transformation in Mg-containing solutions. AFM was used in the ‘contact mode’, over observation areas of 5 µm² and 500 nm². This revealed nano-spheroids-hemispheroids (interpreted as protodolomite) over the calcite surface after 3 months of incubation. They suggested that the numerous carboxyl groups with negative charges present in the bacterial EPS may attract Ca²⁺ and Mg²⁺ ions, promoting the precipitation of protodolomite.

AFM has been especially used to investigate biofilm-mediated dissolution of minerals. These studies have been conducted from various experimental perspectives, ranging from ex situ observations of incubation experiments ((Kirtzel et al., 2020; Saccone et al., 2012)) to in situ imaging of batch and flow-through systems (Pokrovsky et al., 2021). To investigate the impact of fungal biofilm on different mineral surfaces (hornblende, biotite and chlorite) after 6 months of incubation, (Saccone et al., 2012) adopted AFM imaging and ‘force mapping’ before and after the removal of the biofilm. The biofilm comprises globular features measuring 10–80 nm in diameter, as shown by images acquired in ‘tapping mode’, and its morphology differed from mineral to mineral. AFM ‘force mapping’ revealed the hydrophobic nature of the hypha (compared with the AFM tip), and of the biofilm to a lesser extent. Additionally, the biofilm altered the hornblende surface underneath, which made the mineral surface significantly more mechanically fragile than a cleaved surface, pointing at the key role that fungal biofilm might play in enhancing silicate weathering. In contrast, in situ AFM imaging was also used to show the potential of biofilms to inhibit mineral weathering, with possible applications in stone heritage protection and consolidation (Jroundi et al., 2017).

Another area where AFM offers considerable insights is bioleaching, i.e., solubilization of metals from insoluble ores mediated by bacteria and archaea. Since bioleaching requires attachment (Bellenberg et al., 2014), AFM in the ‘force mapping’ mode was used to investigate how to favour early microbial attachment and biofilm formation. As an example, (Su et al., 2021) showed how the presence of a surfactant increased the mean adhesion forces between *Acidianus manzaensis* YN-25 and chalcopyrite, supposedly by changing the Lewis acid-base interaction and electrostatic force (Su et al., 2021). Finally, the spatial correlation of AFM imaging in ‘topographic mode’ with epifluorescence microscopy (EFM) and CLSM, can provide great insights about bioleaching, including the ability to thoroughly investigate cell distribution, biofilm formation and EPS production (Zhang et al., 2014; Zhang et al., 2019). As an example, by correlating AFM and EFM, (Zhang et al., 2014) showed that *F. acidiphilum* cells attach to pyrite substrates preferentially along cracks and macro-steps, with subsequent formation of a monolayer biofilm.

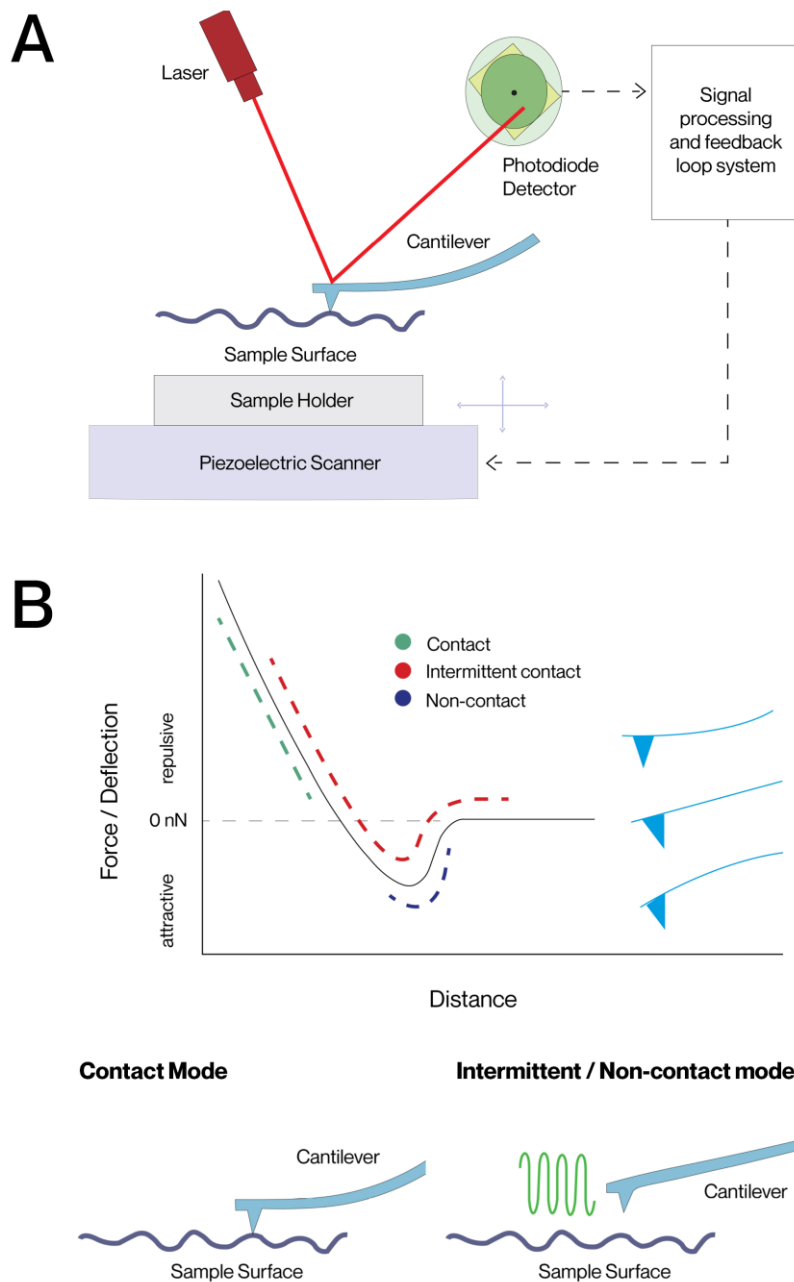


Figure 1.10 Principle of AFM. (A) Working principle (in constant force mode, i.e. constant deflection). The sharp tip at the end of the cantilever feels the (attractive or repulsive) force from the sample surface and deflects accordingly, causing the laser beam to deviate its path to the photodetector, reaching a point different than the ‘setpoint’, i.e., the point on the photodetector corresponding to no deflection of the cantilever. The error signal is sent to a

feedback loop system that responds by adjusting the cantilever height, through vertical adjustment of the piezoelectric scanner, to move it back to the no deflection configuration. The height adjustment of the piezoelectric scanner is converted into a surface height measurement. The scanner then moves horizontally in the plane to scan other points on the surface. (B) Different topographic operating modes. In ‘contact mode’, the sharp tip continuously touches the surface while scanning and is therefore always in the repulsive force regime (green dot line). In contrast, in ‘non-contact mode’, the sharp tip continuously oscillates vertically while moving along the surface and is therefore always in the attractive force regime (blue dot line). Lastly, in ‘intermittent contact mode’, the sharp tip oscillates and moves along the surface as in ‘non-contact mode’, but it constantly ranges from one force regime to the other (red dot line). Force/Deflection graph adapted from (Eaton and West, 2010). Atomic force microscopy. Oxford University Press.

1.5.2 Vertical scanning interferometry (VSI) to quantify dissolution rates of mineral substrates covered by biofilms

Biofilms can positively and/or negatively impact the dissolution rates of the mineral substrates on which they grow. However, this effect remains to be properly quantified and the parameters controlling the impact type (i.e. enhancement or inhibition of dissolution) and magnitude of this effect to be determined. Like AFM, white light vertical scanning interferometry (WL-VSI, commonly known as VSI) proves as a particularly interesting tool for this purpose. VSI is an interference microscopy technique using the low coherence of white light to obtain areal surface topography measurements. In brief, a beam emitted from a white light source is split into two parts with a beam splitter: one beam is reflected by a fixed reference mirror, the other by the surface under examination. The two beams are recombined by the beam splitter to interfere with each other on a detector. A CCD sensor detects the resulting interference fringe pattern, and the corresponding signal is digitized to generate a topography map of the surface investigated (Figure 1.11). State-of-the-art VSI allows to obtain topography images with a sub nanometric vertical resolution, a 360 nm lateral resolution, a 1 mm vertical scanning range and a 1 mm² field of view (extendable up to 1 cm² in ‘stitching mode’). More details regarding VSI basic principles are provided elsewhere (Wyant, 2002).

VSI is widely used in mineral reactivity studies in order to (i) quantify crystal dissolution (or growth) rates through direct measurements of the surface normal retreat (or advance), as well as (ii) characterize the resulting surface morphology (Lüttge et al., 1999). In this regard, VSI is also suitable for studying microbially-mediated alteration of minerals, as it allows to localize

the biofilm forming microbes, while quantifying any changes in surface topography (Davis and Lüttge, 2005) (Figure 1.12).

When compared to AFM (topographic mode), VSI offers a larger field of view, which makes it more appropriate for studying the spatial heterogeneity of biofilm mineral interactions. In contrast, due to the limited lateral resolution, VSI cannot detect the nanometric surface features that can be resolved with AFM. The complementary use of VSI and AFM is therefore particularly advised for the quantitative characterization of scale-dependent phenomena (e.g. mineral surface roughness and biofilm spatial distribution). Additionally, the higher vertical scanning range of VSI allows to study crystal macro-steps, inaccessible with AFM. It is crucial to investigate such surface macro-features as they provide high-energy sites that might favour microbial attachment (Davis and Lüttge, 2005). Lastly, AFM may be detrimental to the biofilms because of the invasive nature of the tip it uses to probe the sample. By contrast, VSI is non-invasive and non-destructive. In return, since VSI is optimized for non-biological opaque and/or thick (relatively to vertical scanning range) samples, great care must be taken in some specific cases, when interpreting potential microbe-mineral interactions. For example, (Waters et al., 2009) used VSI to study the attachment of *Shewanella* MR1 on different substrates and showed how an optical artifact was generated when reflective surfaces were used, with the bacteria appearing as rod-shaped pits instead of cells attached on the surface (Waters et al., 2009). The authors interpreted such artifacts as the result of conflicting interferometric information between the light reflected from the top of the transparent bacterium and the light reflected from the surface underneath the cell. Interestingly, they suggested that, by modifying the VSI software recognition program, it may be possible to acquire separate heights data from the top of the cells and from the substrate underneath them. In principle, this would allow to directly track the dissolution of the substrate underneath the cells, without having to physically remove the cells. While this phenomenon could represent an opportunity, in other cases, the generation of such optical artifacts might lead to misinterpretations of the VSI output. Therefore, in the case of ambiguous results, validation of the final interpretations with AFM is recommended.

All so-far published geomicrobiology studies using VSI addressed mineral bio-dissolution and not bio-precipitation, although the latter should also be feasible. Regarding bio-dissolution, VSI was used to compare the effects on Fe-silicate dissolution of: (i) siderophores-only (high-affinity iron-chelating organic molecules); (ii) EPS-only; (iii) *Bacillus* sp., a siderophore- and EPS-producing microorganism, which necessitates Fe only as a micronutrient (Buss et al., 2007). The authors documented an increase in surface roughness whenever siderophores were

present, alone or in *Bacillus* sp. biofilms. This was attributed to etch-pit growth, resulting from siderophore-promoted dissolution. Hence, it was concluded that the etch-pits formed in the presence of *Bacillus* sp. cells may be caused by siderophores concentrated in biofilms. Similarly, VSI was applied to assess the impact of *Shewanella oneidensis* MR-1 surface colonization on the dissolution of different carbonate phases (calcite-CaCO₃ vs dolomite-(Ca,Mg)CO₃) through surface retreat measurements (Davis et al., 2007). The presence of *S. oneidensis* MR-1 cells was found to influence carbonate dissolution via two pathways with competing effects: (i) inhibition of dissolution and etch-pits growth through covering of mineral reactive sites by the cells; (ii) enhancement of dissolution through carbonate material excavation during irreversible attachment of the cells to the mineral surface. For calcite substrates, which are more soluble and faster-dissolving than dolomite substrates, inhibition prevailed, resulting in a biotic dissolution rate 40–70% lower than in the corresponding abiotic case. For dolomite, the enhancement due to carbonate material excavation by the cells during surface colonization prevailed, which led to an overall higher dissolution rate compared with the abiotic control. More recently, (Wild et al., 2021) used VSI to estimate fungal contribution to silicate weathering rates in natural soils by measuring local depressions of the mineral surface right underneath the hyphae. In this case, they showed a local increase in olivine weathering, which they attributed to fungal hyphae of *Verticillium* sp.

The main current limitation in the application of VSI to biofilm-mineral interaction studies, is the requirement of a dry environment during acquisition of topography images, i.e., *ex situ* characterizations. In fact, the presence of any fluid other than air in between the objective and the sample would affect the optical path of the beam reflected from the sample surface. However, this limitation may be overcome by adding a 'compensating filter' in the path of the beam reflected from the reference mirror. This filter needs to be ad-hoc designed with a refractive index and a thickness that could compensate for the presence of an aqueous solution and a reactor cap in the path of the beam reflected from the sample surface (Larimer et al., 2019; Larimer et al., 2016). Such technical modification, although technically challenging, would make VSI *in situ* observations of biofilm-mineral interactions feasible.

A



B

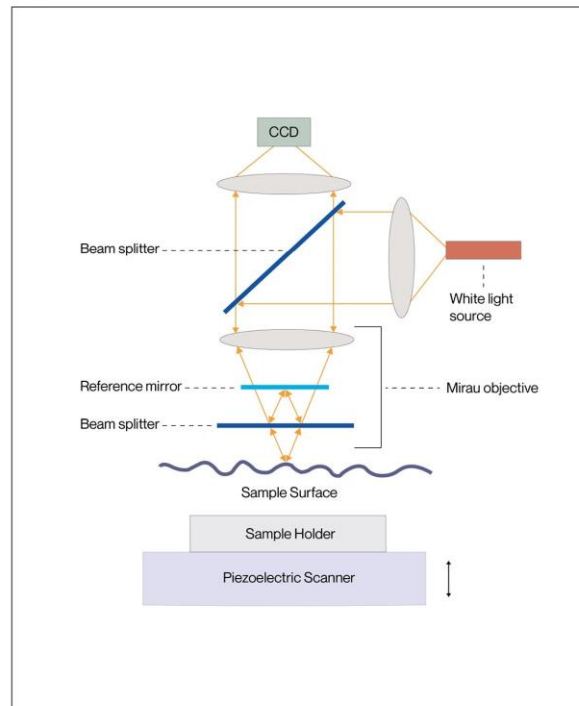


Figure 1.11 (A) VSI apparatus, showing two Mirau objectives (10x, 50x) Samples have to be placed on the working table aligned with the selected objective. The objective remains fixed, while the working table can move horizontally to find the desired location on the sample surface and vertically to find fringes on the surface, as controlled by the piezoelectric scanner. (B) Simplified scheme of VSI working principle with a Mirau objective. In this configuration, a beam is split into two beams, one reflected by a reference mirror built in the Mirau objective, the other reflected by the sample surface. Both beams are reflected back and will interfere with each other, producing an interferogram, which can be converted into a surface topography map. Panel B: Adapted from (Wu et al., 2021). Performance analysis of surface reconstruction algorithms in vertical scanning interferometry based on coherence envelope detection. *Micromachines*, 12(2), Art. 2. doi: 10.3390/mi12020164.

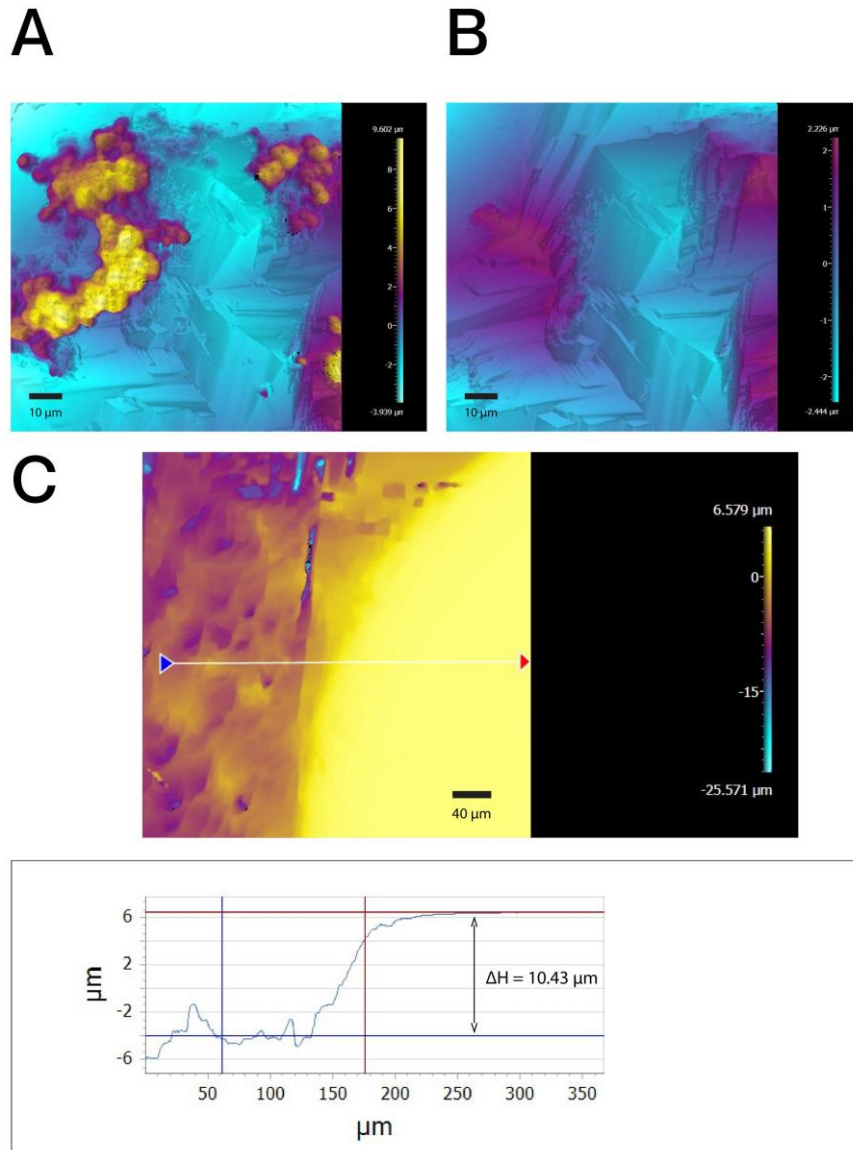


Figure 1.12 Example of VSI application to microbe-mineral interaction studies: topography data of a calcite surface colonized by a biofilm of *Chroococcidiopsis thermalis* PCC 7203 cells after dissolution under alkaline conditions, before (A) vs after (B) physical removal of the cells. These experiments will be further addressed in Chapter 5. (A) Topography data of the calcite surface partially covered by the cells. The highest height values (i.e., mostly in the yellow colour range) and arranged in circular shapes refer to the cells, whereas the lowest height values (i.e., mostly in the blue colour range) refer to the calcite substrate surface. (B) Topography data of the calcite surface after physical removal of the cells. (C) Corresponding calcite surface normal retreat, ΔH , measured as the relative height difference between an unreacted (reference) area (displayed in light yellow) and a dissolved area.

1.6 Surface imprints resulting from bacterial weathering as potential biosignatures

As discussed in the previous sections, altered minerals can be indicative, to different degrees, of ongoing and past microbe-mineral interactions.

For instance, *rock-eating fungi*, as denoted by Jongmans et al. (1997), can penetrate minerals through the hyphae along points of weakness, or by direct tunnelling or boring, leading to the formation of micro tunnels (Gadd, 2017; van Schöll et al., 2008). After the degradation of the fungal hyphae, the micro tunnels formed by the hyphae are left within the minerals (and, sometimes, later filled by precipitated minerals), leaving behind traces of past bioweathering activity (Gadd, 2017). These micro tunnels are often characterized by parallel-oriented walls with constant diameter (typically corresponding to that of the original hypha) and rounded ends, which help to distinguish these micro tunnels from coalesced etch pits and cracks that might have been caused by abiotic processes (van Schöll et al., 2008).

Notably, micro tunnels are also commonly formed by microorganisms within calcareous and calco-phosphatic substrates in marine and freshwater settings (Campbell, 1983). This involves a variety of filamentous or pseudo filamentous microbes (denoted as carbonate borers), which includes eukaryotes (fungi, green and red algae) and prokaryotes (cyanobacteria) (Garcia-Pichel, 2006). Among these, euendolithic (i.e., true boring endoliths) cyanobacteria represent a geochemical paradox, as photoautotrophic metabolism is usually considered to induce carbonate precipitation rather than dissolution. Nonetheless, the chemical excavation into carbonates is made possible by the microbial active uptake of Ca^{2+} at the boring front, which locally decreases the saturation state with respect to CaCO_3 , thereby making dissolution thermodynamically favoured (Garcia-Pichel et al., 2010). Interestingly, it has been shown that these filamentous euendolithic cyanobacteria can create micro tunnels as deep as several 100s of μm , which extend significantly beyond the length of the individual microorganisms.

In general, micro tunnels and similar volumetric signatures of bioweathering can readily be interpreted as biosignatures when detected in natural settings, primarily due to their large size and because fewer plausible processes have been proposed to explain the formation of these features abiotically. However, this type of weathering features is limited to a small sub-set of multicellular (and relatively complex) microbes. Since the predominant form of microbial life on Earth is single-celled organisms, in order to search for more *universal* signatures of microbial bioweathering, it becomes necessary to examine the impact of single-celled microbes.

Comparative studies of the surface microtopography resulting from abiotic and abiotic weathering carried out to date suffer from the limitations discussed in section 1.4.2, which mainly include the intrinsic ambiguity associated with biogenic criteria based on qualitative (thus subjective) comparisons (Rouillard et al., 2020). Shifting towards biogenic criteria based on *quantitative approaches* appears therefore necessary. Ultimately, these quantitative approaches need to be versatile enough to capture the full spectrum of potential imprints that might be left at the surface by microbes, which may go far beyond the presence of etch pits resembling cells in ‘size, shape and distribution’.

1.7 Manuscript plan

The central aim of this manuscript is to investigate the informative content that is retained within weathered mineral surfaces, addressing the following fundamental questions:

1. Can the microtopography of naturally-weathered minerals serve as a proxy to back-estimate the fluid saturation state?
2. Does microbial weathering result in specific imprints at the mineral surface that could be quantitatively attributable to the action of life?

These questions are addressed through a combination of flow-through dissolution experiments and numerical modeling employing various stochastic methods, ranging from empirical approaches to kMC and Ising modeling. The detailed descriptions of the experimental and numerical approaches employed will be provided in the upcoming chapters. However, the general experimental approach involved conducting calcite dissolution experiments at various saturation states, both under sterile conditions and with a biofilm of cyanobacteria *Chroococcidiopsis thermalis* PCC 7203 covering the calcite surface. Ex-situ and in-situ time-resolved analyses of the resulting surface topography were conducted using VSI. The statistical analyses of the surface topography involved a combination of descriptive statistics and spatial statistical metrics, such as semi-variogram and PSD.

Calcite was selected as a model mineral because of its widespread availability on Earth, as it constitutes the principal rock-forming constituents in limestone. Calcium carbonate minerals have also been detected on other planetary environments, such as Mars, making them potentially relevant for the search for biosignatures on other planets. Furthermore, the relatively fast reactivity of calcite makes it a suitable candidate for attaining a surface steady-state configuration in relatively short time scales. As previously discussed, the achievement of a steady-state configuration of the surface resulting from dissolution is indeed a prerequisite to use mineral surface roughness as a proxy for the reaction conditions. On the other hand, the cyanobacteria *Chroococcidiopsis thermalis* PCC 7203 was chosen as a model bacteria strain because it is particularly targeted as a model strain in astrobiology research and because several *Chroococcidiopsis* strains have been shown to be endolithic and to inhabit calcite rocks. Additionally, the PCC 7203 strain revealed to adhere effectively to calcite substrates, making it an ideal candidate for studying the localized effects of microbial weathering on mineral surfaces.

Chapter 2 provides an overview of the surface roughness descriptors employed in this manuscript to quantify the key statistical features of surface microtopography data and provides some illustrative conceptual examples of their application.

Chapter 3 and 4 are focused on the question of the fluid imprints that are left on mineral surfaces after abiotic dissolution at various saturation states, aiming to develop a quantitative link between a statistical characterization of the surface roughness resulting from dissolution and the fluid saturation state. Chapter 5 focuses instead on the question of signatures of microbial weathering that are left on mineral surfaces after biofilm-mediated dissolution, aiming to provide a novel approach to quantitatively differentiate between abiotically and biotically weathered mineral surfaces.

Chapter 3 and 4 contain two articles that were published in the framework of this PhD. Chapter 5 is divided in two sub-sections. Sub-section 5.1 contains the final draft of an article in its final version before submission, whereas sub-section 5.2 presents novel experimental results involving the in-situ monitoring of calcite dissolution mediated by biofilm-forming cyanobacteria using VSI, made possible through the parallel development of a specific reaction cell developed by a postdoctoral scholar (Dr. Bastien Wild) involved in the same project that funded most of the work gathered in the present manuscript (ERC Mobidic).

Each chapter is preceded by a general introduction, serving the purpose of connecting the various articles together. The manuscript ends with a final chapter dedicated to conclusions and perspectives, exploring limitations and generalizability of this study, and presenting the prospects of experimental and field studies designed to explore the potential application of the laboratory-based findings of this work to natural environments.

References

Aagaard, P., Helgeson, H.C., 1982. THERMODYNAMIC AND KINETIC CONSTRAINTS ON REACTION-RATES AMONG MINERALS AND AQUEOUS-SOLUTIONS. 1. THEORETICAL CONSIDERATIONS. *American Journal of Science*, 282(3): 237-285.

Ackerer, P., Bouissonié, A., di Chiara Roupert, R., Daval, D., 2021. Estimating the activation energy of bond hydrolysis by time-resolved weighing of dissolving crystals. *npj Materials Degradation*, 5(1): 48.

Ahmed, E., Holmström, S.J.J.M.b., 2014. Siderophores in environmental research: roles and applications. 7(3): 196-208.

- Alt-Epping, P., Waber, H.N., Diamond, L., Eichinger, L., 2013. Reactive transport modeling of the geothermal system at Bad Blumau, Austria: Implications of the combined extraction of heat and CO₂. *Geothermics*, 45: 18–30.
- Anbeek, C., 1992. Surface roughness of minerals and implications for dissolution studies. *Geochimica et Cosmochimica Acta*, 56(4): 1461-1469.
- Aradóttir, E., Sonnenthal, E., Björnsson, G., Jónsson, H., 2012. Multidimensional reactive transport modeling of CO₂ mineral sequestration in basalts at the Hellisheidi geothermal field, Iceland. *International Journal of Greenhouse Gas Control*, 9: 24-40.
- Arias, J.L., Fernández, M.S., 2008. Polysaccharides and Proteoglycans in Calcium Carbonate-based Biomineralization. *Chemical Reviews*, 108(11): 4475-4482.
- Arvidson, R.S. et al., 2006. Magnesium inhibition of calcite dissolution kinetics. *Geochimica et Cosmochimica Acta*, 70: 583-594.
- Arvidson, R.S., Ertan, I.E., Amonette, J.E., Luttge, A., 2003. Variation in calcite dissolution rates. *Geochimica Et Cosmochimica Acta*, 67(9): 1623-1634.
- Arvidson, R.S., Luttge, A., 2010. Mineral dissolution kinetics as a function of distance from equilibrium - New experimental results. *Chemical Geology*, 269(1-2): 79-88.
- Arvidson, R.S., Mackenzie, F.T., 2000. Temperature Dependence of Mineral Precipitation Rates Along the CaCO₃–MgCO₃ Join. *Aquatic Geochemistry*, 6: 249-256.
- Bai, F.-Y. et al., 2021. Microbial biofilms on a giant monolithic statue of Buddha: The symbiosis of microorganisms and mosses and implications for bioweathering. *International Biodeterioration & Biodegradation*, 156: 105106.
- Bandstra, J.Z., Brantley, S.L., 2008. Surface evolution of dissolving minerals investigated with a kinetic Ising model. *Geochimica Et Cosmochimica Acta*, 72(11): 2587-2600.
- Berling, D.J. et al., 2020. Potential for large-scale CO₂ removal via enhanced rock weathering with croplands. *Nature*, 583(7815): 242-248.
- Beig, M.S., Luttge, A., 2006. Albite dissolution kinetics as a function of distance from equilibrium: Implications for natural feldspar weathering. *Geochimica et Cosmochimica Acta*, 70: 1402-1420.
- Bellenberg, S. et al., 2014. Biofilm formation, communication and interactions of leaching bacteria during colonization of pyrite and sulfur surfaces. *Research in Microbiology*, 165(9): 773-781.
- Bennett, P.C., Hiebert, F.K., Choi, W.J., 1996. Microbial colonization and weathering of silicates in a petroleum-contaminated groundwater. *Chemical Geology*, 132(1): 45-53.
- Benzerara, K. et al., 2007. Alteration of submarine basaltic glass from the Ontong Java Plateau: A STXM and TEM study. *Earth and Planetary Science Letters*, 260(1-2): 187-200.
- Benzerara, K., Menguy, N., Guyot, F., Vanni, C., Gillet, P., 2005. TEM study of a silicate-carbonate-microbe interface prepared by focused ion beam milling. *Geochimica Et Cosmochimica Acta*, 69(6): 1413-1422.
- Berner, R.A., Lasaga, A.C., Garrels, R.M., 1983. The carbonate-silicate cycle and its effect on atmospheric carbon dioxide over the past 100 millions years. *American Journal of Science*, 284: 641-683.

- Berner, R.A., Sjöberg, E.L., Velbel, M.A., Krom, M.D., 1980. Dissolution of pyroxenes and amphiboles during weathering. *Science*, 207(4436): 1205-1206.
- Billi, D. et al., 2011. Damage Escape and Repair in Dried *Chroococcidiopsis* spp. from Hot and Cold Deserts Exposed to Simulated Space and Martian Conditions. *Astrobiology*, 11(1): 65-73.
- Blum, A.E., Lasaga, A.C., 1987. Monte Carlo Simulations of Surface Reaction Rate Laws. In: *Sons, J.W.a. (Ed.), Aquatic Surface Chemistry: Chemical Processes at the Particle-Water Interface*, New York, pp. 255-292.
- Bonneville, S., Bray, A.W., Benning, L.G., 2016. Structural Fe(II) Oxidation in Biotite by an Ectomycorrhizal Fungi Drives Mechanical Forcing. *Environmental Science & Technology*, 50(11): 5589-5596.
- Bonneville, S. et al., 2009. Plant-driven fungal weathering: Early stages of mineral alteration at the nanometer scale. *Geology*, 37(7): 615-618.
- Bose, S., Hu, X.M., Higgins, S.R., 2008. Dissolution kinetics and topographic relaxation on celestite (001) surfaces: The effect of solution saturation state studied using Atomic Force Microscopy. *Geochimica Et Cosmochimica Acta*, 72(3): 759-770.
- Bouissonnié, A., Daval, D., Ackerer, P., 2020a. Dissolution Anisotropy of Pyroxenes: A Surrogate Model for Steady-State Enstatite Dissolution Resulting from Stochastic Simulations of the Hydrolysis Process. *The Journal of Physical Chemistry C*, 124(24): 13113-13126.
- Bouissonnié, A., Daval, D., Guyot, F., Ackerer, P., 2020b. The Dissolution Anisotropy of Pyroxenes: Experimental Validation of a Stochastic Dissolution Model Based on Enstatite Dissolution. *The Journal of Physical Chemistry C*, 124(5): 3122-3140.
- Bouissonnié, A., Daval, D., Marinoni, M., Ackerer, P., 2018. From mixed flow reactor to column experiments and modeling: Upscaling of calcite dissolution rate. *Chemical Geology*, 487: 63-75.
- Brand, A.S., Feng, P., Bullard, J.W., 2017. Calcite dissolution rate spectra measured by in situ digital holographic microscopy. *Geochimica et Cosmochimica Acta*, 213: 317-329.
- Brantley, S. et al., 2011. Twelve testable hypotheses on the geobiology of weathering. *Geobiology*, 9(2): 140-165.
- Brantley, S.L., Crane, S.R., Crerar, D.A., Hellmann, R., Stallard, R., 1986. Dissolution at dislocation etch pits in quartz. *Geochimica et Cosmochimica Acta*, 50(10): 2349-2361.
- Brantley, S.L., Olsen, A.A., 2014. 7.3 - Reaction Kinetics of Primary Rock-Forming Minerals under Ambient Conditions A2 - Holland, Heinrich D. In: *Turekian, K.K. (Ed.), Treatise on Geochemistry (Second Edition)*. Elsevier, Oxford, pp. 69-113.
- Bray, A.W. et al., 2015. The effect of pH, grain size, and organic ligands on biotite weathering rates. *Geochimica et Cosmochimica Acta*, 164: 127-145.
- Breitenbach, R. et al., 2018. Corrosive extracellular polysaccharides of the rock-inhabiting model fungus *Knufia petricola*. *Extremophiles*, 22(2): 165-175.
- Bricker, O.P., Jones, B.F., Bowser, C.J., 2003. 5.04 - Mass-balance Approach to Interpreting Weathering Reactions in Watershed Systems. In: *Holland, H.D., Turekian, K.K. (Eds.), Treatise on Geochemistry*. Pergamon, Oxford, pp. 119-132.

- Briese, L., Arvidson, R.S., Luttge, A., 2017. The effect of crystal size variation on the rate of dissolution – A kinetic Monte Carlo study. *Geochimica Et Cosmochimica Acta*, 212: 167-175.
- Brunauer, S., Emmet, P.H., Teller, E., 1938. Adsorption of gases in multimolecular layers. *Journal of the American Chemical Society*, 60: 309-319.
- Burford, E.P., Fomina, M., Gadd, G.M., 2003. Fungal involvement in bioweathering and biotransformation of rocks and minerals. *Mineralogical Magazine*, 67(6): 1127-1155.
- Burton, W.-K., Cabrera, N., Frank, F., 1951. The growth of crystals and the equilibrium structure of their surfaces. *Phil. Trans. R. Soc. Lond. A*, 243(866): 299-358.
- Buss, H.L., Lüttge, A., Brantley, S.L., 2007. Etch pit formation on iron silicate surfaces during siderophore-promoted dissolution. *Chemical Geology*, 240(3): 326-342.
- Cabrera, N., Levine, M.M., 1956. XLV. On the dislocation theory of evaporation of crystals. *The Philosophical Magazine: A Journal of Theoretical Experimental and Applied Physics*, 1(5): 450-458.
- Cabrera, N., Levine, M.M., Plaskett, J.S., 1954. Hollow Dislocations and Etch Pits. *Physical Review*, 96(4): 1153-1153.
- Cama, J., Ganor, J., 2006. The effects of organic acids on the dissolution of silicate minerals: A case study of oxalate catalysis of kaolinite dissolution. *Geochimica et Cosmochimica Acta*, 70(9): 2191-2209.
- Cama, J., Ganor, J., Ayora, C., Lasaga, A.C., 2000. Smectite dissolution kinetics at 80°C and pH 8.8. *Geochimica et Cosmochimica Acta*, 64(15): 2701-2717.
- Cama, J. et al., 2010. Fluorite dissolution at acidic pH: In situ AFM and ex situ VSI experiments and Monte Carlo simulations. *Geochimica Et Cosmochimica Acta*, 74(15): 4298-4311.
- Campbell, S.E., 1983. The Modern Distribution and Geological History of Calcium Carbonate Boring Microorganisms. In: Westbroek, P., de Jong, E.W. (Eds.), *Biomineralization and Biological Metal Accumulation: Biological and Geological Perspectives Papers presented at the Fourth International Symposium on Biomineralization, Renesse, The Netherlands, June 2–5, 1982*. Springer Netherlands, Dordrecht, pp. 99-104.
- Cardona, A., Finkbeiner, T., Santamarina, J.C., 2021. Natural Rock Fractures: From Aperture to Fluid Flow. *Rock Mechanics and Rock Engineering*, 54(11): 5827-5844.
- Carrasco, I.S.S., Aarão Reis, F.D.A., 2021. Modeling the kinetics of calcite dissolution in neutral and alkaline solutions. *Geochimica et Cosmochimica Acta*, 292: 271-284.
- Carrasco, I.S.S., Machado, E.A., Reis, F.D.A.A., 2021. Simulations of Dissolution of Initially Flat Calcite Surfaces: Retreat Velocity Control and Surface Roughness Scaling. *ACS Earth and Space Chemistry*, 5(10): 2755-2767.
- Casero, M.C., Ascaso, C., Quesada, A., Mazur-Marzec, H., Wierzchos, J., 2021. Response of Endolithic Chroococciopsis Strains From the Polyextreme Atacama Desert to Light Radiation. 11.
- Coombes, M.A.J.G.S., London, Memoirs, 2014. Chapter 5 The rock coast of the British Isles: weathering and biogenic processes. 40(1): 57-76.
- Cosmidis, J., Benzerara, K., 2022. Why do microbes make minerals? %J *Comptes Rendus. Géoscience*. 354: 1-39.

- Costerton, J.W., Lewandowski, Z., Caldwell, D.E., Korber, D.R., Lappin-Scott, H.M., 1995. MICROBIAL BIOFILMS. 49(1): 711-745.
- Daval, D., Calvaruso, C., Guyot, F., Turpault, M.-P., 2018. Time-dependent feldspar dissolution rates resulting from surface passivation: Experimental evidence and geochemical implications. *Earth and Planetary Science Letters*, 498: 226-236.
- Daval, D., Hellmann, R., Saldi, G.D., Wirth, R., Knauss, K.G., 2013. Linking nm-scale measurements of the anisotropy of silicate surface reactivity to macroscopic dissolution rate laws: New insights based on diopside. *Geochimica Et Cosmochimica Acta*, 107(0): 121-134.
- Daval, D. et al., 2009. Mechanism of wollastonite carbonation deduced from micro- to nanometer length scale observations. *American Mineralogist*, 94(11-12): 1707-1726.
- Daval, D. et al., 2010. The effect of silica coatings on the weathering rates of wollastonite (CaSiO₃) and forsterite (Mg₂SiO₄): an apparent paradox.
- Daval, D. et al., 2011. Influence of amorphous silica layer formation on the dissolution rate of olivine at 90 degrees C and elevated pCO₂. *Chemical Geology*, 284(1-2): 193-209.
- Davis, K., Lüttge, A., 2005. Quantifying the relationship between microbial attachment and mineral surface dynamics using vertical scanning interferometry (VSI). *American Journal of Science*, 305(6-8): 727-751.
- Davis, K., Neelson, K., Lüttge, A., 2007. Calcite and dolomite dissolution rates in the context of microbe–mineral surface interactions. *Geobiology*, 5(2): 191-205.
- Davit, Y. et al., 2013. Hydrodynamic dispersion within porous biofilms. *Physical Review E*, 87(1): 012718.
- de Assis, T.A., Aarão Reis, F.D.A., 2018. Dissolution of minerals with rough surfaces. *Geochimica Et Cosmochimica Acta*, 228: 27-41.
- Devidal, J.-L., Schott, J., Dandurand, J.-L., 1997. An experimental study of kaolinite dissolution and precipitation kinetics as a function of chemical affinity and solution composition at 150°C, 40 bars, and pH 2, 6.8, and 7.8. *Geochimica et Cosmochimica Acta*, 61: 5165-5186.
- Dittrich, M., Sibling, S.J.G.S., London, Special Publications, 2010. Calcium carbonate precipitation by cyanobacterial polysaccharides. 336(1): 51-63.
- Dontsova, K., Balogh-Brunstad, Z., Chorover, J., 2020. Plants as Drivers of Rock Weathering, *Biogeochemical Cycles*, pp. 33-58.
- Dorn, R.I., 2014. Ants as a powerful biotic agent of olivine and plagioclase dissolution. *Geology*, 42(9): 771-774.
- Dove, P.M., Han, N.Z., De Yoreo, J.J., 2005. Mechanisms of classical crystal growth theory explain quartz and silicate dissolution behavior. *Proceedings of the National Academy of Sciences of the United States of America*, 102(43): 15357-15362.
- Duckworth, O.W., Martin, S.T., 2004a. Dissolution rates and pit morphologies of rhombohedral carbonate minerals. *American Mineralogist*, 89(4): 554-563.
- Duckworth, O.W., Martin, S.T., 2004b. Role of molecular oxygen in the dissolution of siderite and rhodochrosite. *Geochimica et Cosmochimica Acta*, 68(3): 607-621.

- Dufrêne, Y.F., 2002. Atomic force microscopy, a powerful tool in microbiology. *J Bacteriol*, 184(19): 5205-13.
- Duparré, A. et al., 2002. Surface characterization techniques for determining the root-mean-square roughness and power spectral densities of optical components. *Appl Opt*, 41(1): 154-71.
- Eaton, P., West, P., 2010. Atomic force microscopy. Oxford university press.
- Eggleston, C.M., Hochella, M.F., Parks, G.A., 1989. Sample Preparation and Aging Effects on the Dissolution Rate and Surface-Composition of Diopside. *Geochimica Et Cosmochimica Acta*, 53(4): 797-804.
- Emmanuel, S., 2014. Mechanisms influencing micron and nanometer-scale reaction rate patterns during dolostone dissolution. *Chemical Geology*, 363: 262-269.
- Evans, C.T. et al., 2021. A non-destructive, tuneable method to isolate live cells for high-speed AFM analysis. 9(4): 680.
- Feng, P., Brand, A.S., Chen, L., Bullard, J.W., 2017. In situ nanoscale observations of gypsum dissolution by digital holographic microscopy. *Chem Geol*, 460: 25-36.
- Fischer, C., Arvidson, R.S., Lüttge, A., 2012. How predictable are dissolution rates of crystalline material? *Geochimica Et Cosmochimica Acta*, 98(0): 177-185.
- Fischer, C., Finkeldei, S., Brandt, F., Bosbach, D., Luttge, A., 2015. Direct Measurement of Surface Dissolution Rates in Potential Nuclear Waste Forms: The Example of Pyrochlore. *ACS Applied Materials & Interfaces*, 7(32): 17857-17865.
- Fischer, C., Kurganskaya, I., Luttge, A., 2018. Inherited control of crystal surface reactivity. *Applied Geochemistry*, 91: 140-148.
- Fischer, C., Kurganskaya, I., Schäfer, T., Lüttge, A., 2014. Variability of crystal surface reactivity: What do we know? *Applied Geochemistry*, 43(0): 132-157.
- Fischer, C., Luttge, A., 2007. Converged Surface Roughness Parameters – A New Tool to Quantify Rock Surface Morphology and Reactive Alteration. *American Journal of Science*, 307.
- Fisk, M.R., Crovisier, J.-L., Honnorez, J., 2013. Experimental abiotic alteration of igneous and manufactured glasses. *Comptes Rendus Geoscience*, 345(4): 176-184.
- Fisk, M.R., Giovannoni, S.J., Thorseth, I.H., 1998. Alteration of Oceanic Volcanic Glass: Textural Evidence of Microbial Activity. *Science*, 281(5379): 978-980.
- Flemming, H.-C., Wuertz, S., 2019. Bacteria and archaea on Earth and their abundance in biofilms. *Nature reviews microbiology*, 17(4): 247-260.
- Gadd, G.M., 2010. Metals, minerals and microbes: geomicrobiology and bioremediation. *Microbiology*, 156(3): 609-643.
- Gadd, G.M.J.E.A.I.M.o.M., *Geochemistry,, Petrology*, 2017. Fungi, rocks, and minerals. 13(3): 171-176.
- Gao, P. et al., 2010. In situ TEM studies of oxygen vacancy migration for electrically induced resistance change effect in cerium oxides. *Micron*, 41(4): 301-305.
- Garcia-Pichel, F., 2006. Plausible mechanisms for the boring on carbonates by microbial phototrophs. *Sedimentary Geology*, 185(3): 205-213.

- Garcia-Pichel, F., Ramírez-Reinat, E., Gao, Q.J.P.o.t.N.A.o.S., 2010. Microbial excavation of solid carbonates powered by P-type ATPase-mediated transcellular Ca²⁺ transport. *107(50)*: 21749-21754.
- Gautier, J.M., Oelkers, E.H., Schott, J., 2001. Are quartz dissolution rates proportional to BET surface areas? *Geochimica Et Cosmochimica Acta*, *65(7)*: 1059-1070.
- Gilmer, G.H., 1980. Computer Models of Crystal Growth. *208(4442)*: 355-363.
- Gilmer, G.H., Bennema, P., 1972. Simulation of Crystal Growth with Surface Diffusion. *43*: 1347-1360.
- Gleeson, D.B. et al., 2006. Characterization of bacterial community structure on a weathered pegmatitic granite. *Microb Ecol*, *51(4)*: 526-34.
- Godinho, J.R.A., Piazzolo, S., Balic-Zunic, T., 2014. Importance of surface structure on dissolution of fluorite: Implications for surface dynamics and dissolution rates. *Geochimica Et Cosmochimica Acta*, *126*: 398-410.
- Gong, Y., Misture, S.T., Gao, P., Mellott, N.P., 2016. Surface Roughness Measurements Using Power Spectrum Density Analysis with Enhanced Spatial Correlation Length. *The Journal of Physical Chemistry C*, *120(39)*: 22358-22364.
- Gorbushina, A.A.J.E.m., 2007. Life on the rocks. *9(7)*: 1613-1631.
- Grambow, B., 2006. Nuclear Waste Glasses - How Durable? *Elements*, *2(6)*: 357-364.
- Gringarten, E., Deutsch, C.V., 2001. Teacher's Aide Variogram Interpretation and Modeling. *Mathematical Geology*, *33(4)*: 507-534.
- Guinoiseau, D. et al., 2021. Tropical Weathering History Recorded in the Silicon Isotopes of Lateritic Weathering Profiles. *48(19)*: e2021GL092957.
- Hellmann, R., Tisserand, D., 2006. Dissolution kinetics as a function of the Gibbs free energy of reaction: An experimental study based on albite feldspar. *Geochimica et Cosmochimica Acta*, *70*: 364-383.
- Hellmann, R. et al., 2012. Unifying natural and laboratory chemical weathering with interfacial dissolution–reprecipitation: A study based on the nanometer-scale chemistry of fluid–silicate interfaces. *Chemical Geology*, *294–295(0)*: 203-216.
- Hernández Creus, A., Carro, P., Salvarezza, R.C., Arvia, A.J., 1997. Three-Dimensional Monte Carlo Simulations of Roughness Development from Different Mechanisms Applicable to the Dissolution of a Pure Solid. *Langmuir*, *13(4)*: 833-841.
- Hoffland, E. et al., 2004. The role of fungi in weathering. *2(5)*: 258-264.
- Horlait, D. et al., 2014. Environmental SEM monitoring of Ce_{1-x}Ln_xO_{2-x/2} mixed-oxide microstructural evolution during dissolution. *Journal of Materials Chemistry A*, *2(15)*: 5193-5203.
- Hu, J. et al., 2020. Global mapping of live cell mechanical features using PeakForce QNM AFM. *6*: 9-18.
- Iniesto, M. et al., 2022. Planktonic microbial communities from microbialite-bearing lakes sampled along a salinity-alkalinity gradient. *67(12)*: 2718-2733.

- Jacobs, T.D.B., Junge, T., Pastewka, L., 2017. Quantitative characterization of surface topography using spectral analysis. *Surface Topography: Metrology and Properties*, 5(1): 013001.
- Jongmans, A.G. et al., 1997. Rock-eating fungi. *Nature*, 389: 682.
- Jordan, G., Higgins, S.R., Eggleston, C.M., Knauss, K.G., Schmahl, W.W., 2001. Dissolution kinetics of magnesite in acidic aqueous solution, a hydrothermal atomic force microscopy (HAFM) study: step orientation and kink dynamics. *Geochimica Et Cosmochimica Acta*, 65(23): 4257-4266.
- Jordan, G. et al., 1999. Acidic dissolution of plagioclase: In-situ observations by hydrothermal atomic force microscopy. *Geochimica Et Cosmochimica Acta*, 63(19-20): 3183-3191.
- Jroundi, F. et al., 2017. Protection and consolidation of stone heritage by self-inoculation with indigenous carbonatogenic bacterial communities. *Nature Communications*, 8(1): 279.
- Kamaeva, A.A., Vasilchenko, A.S., Deryabin, D.G., 2014. Atomic Force Microscopy Reveals a Morphological Differentiation of *Chromobacterium violaceum* Cells Associated with Biofilm Development and Directed by N-Hexanoyl-L-Homoserine Lactone. *PLOS ONE*, 9(8): e103741.
- Kampman, N., Bickle, M., Wigley, M., Dubacq, B., 2014. Fluid flow and CO₂-fluid-mineral interactions during CO₂-storage in sedimentary basins. *Chemical Geology*, 369(0): 22-50.
- Kanafi, M.M., 2020. Surface generator: artificial randomly rough surfaces, MATLAB Central Forum (<https://www.mathworks.com/matlabcentral/fileexchange/60817-surfacegenerator--artificial-randomly-rough-surfaces>).
- Kirtzel, J. et al., 2020. Organic acids, siderophores, enzymes and mechanical pressure for black slate bioweathering with the basidiomycete *Schizophyllum commune*. 22(4): 1535-1546.
- Klasa, J. et al., 2013. An atomic force microscopy study of the dissolution of calcite in the presence of phosphate ions. *Geochimica et Cosmochimica Acta*, 117: 115-128.
- Köhler, S.J., Bosbach, D., Oelkers, E.H., 2005. Do clay mineral dissolution rates reach steady state? *Geochimica et Cosmochimica Acta*, 69(8): 1997-2006.
- Kontakiotis, G., Mortyn, P.G., Antonarakou, A., Martínez-Botí, M.A., Triantaphyllou, M.V., 2011. Field-based validation of a diagenetic effect on *G. ruber* Mg/Ca paleothermometry: Core top results from the Aegean Sea (eastern Mediterranean). 12(9).
- Kossel, W., 1927a. Zur Theorie des Kristallwachstums. *Nachrichten von der Gesellschaft der Wissenschaften zu Göttingen, Mathematisch-Ph* 135–406 (1927).
- Kossel, W.J.N.v.d.G.d.W.z.G., Mathematisch-Physikalische Klasse, 1927b. Zur theorie des kristallwachstums. 1927: 135-143.
- Krissansen-Totton, J., Catling, D.C., 2017. Constraining climate sensitivity and continental versus seafloor weathering using an inverse geological carbon cycle model. *Nature Communications*, 8(1): 15423.
- Krolczyk, G.M., Maruda, R.W., Nieslony, P., Wieczorowski, M., 2016. Surface morphology analysis of Duplex Stainless Steel (DSS) in Clean Production using the Power Spectral Density. *Measurement*, 94: 464-470.

- Kurganskaya, I., Luttge, A., 2013. A comprehensive stochastic model of phyllosilicate dissolution: Structure and kinematics of etch pits formed on muscovite basal face. *Geochimica Et Cosmochimica Acta*, 120(0): 545-560.
- Kurganskaya, I., Luttge, A., 2016. Kinetic Monte Carlo Approach To Study Carbonate Dissolution. *The Journal of Physical Chemistry C*, 120(12): 6482-6492.
- Kurganskaya, I., Luttge, A., 2021. Mineral Dissolution Kinetics: Pathways to Equilibrium. *ACS Earth and Space Chemistry*, 5(7): 1657-1673.
- Larimer, C. et al., 2019. Rapid nondestructive measurement of bacterial cultures with 3D interferometric imaging. *Scientific Reports*, 9(1): 8055.
- Larimer, C., Suter, J.D., Bonheyo, G., Addleman, R.S., 2016. In situ non-destructive measurement of biofilm thickness and topology in an interferometric optical microscope. 9(6): 656-666.
- Lasaga, A.C., 1984. Chemical kinetics of water-rock interactions. 89(B6): 4009-4025.
- Lasaga, A.C., Blum, A.E., 1986. Surface chemistry, etch pits and mineral-water reactions. *Geochimica et Cosmochimica Acta*, 50(10): 2363-2379.
- Lasaga, A.C., Luttge, A., 2001a. Variation of Crystal Dissolution Rate Based on a Dissolution Stepwave Model. *Science*, 291: 2400-2404.
- Lasaga, A.C., Luttge, A., 2001b. Variation of Crystal Dissolution Rate Based on a Dissolution Stepwave Model. 291(5512): 2400-2404.
- Lasaga, A.C., Luttge, A., 2004. Mineralogical approaches to fundamental crystal dissolution kinetics. *American Mineralogist*, 89(4): 527-540.
- Lea, A.S., Amonette, J.E., Baer, D.R., Liang, Y., Colton, N.G., 2001. Microscopic effects of carbonate, manganese, and strontium ions on calcite dissolution. *Geochimica et Cosmochimica Acta*, 65(3): 369-379.
- Lemarchand, D., Cividini, D., Turpault, M.P., Chabaux, F., 2012. Boron isotopes in different grain size fractions: Exploring past and present water–rock interactions from two soil profiles (Strengbach, Vosges Mountains). *Geochimica et Cosmochimica Acta*, 98: 78-93.
- Li, X., Wang, Q., Shen, X., Pedrosa, E.T., Luttge, A., 2021. Multiscale investigation of olivine (010) face dissolution from a surface control perspective. *Applied Surface Science*, 549: 149317.
- Liang, Y., Baer, D.R., 1997. Anisotropic dissolution at the $\text{CaCO}_3(101\bar{1}0)$ –water interface. *Surface Science*, 373(2): 275-287.
- Liu, C., Gorby, Y.A., Zachara, J.M., Fredrickson, J.K., Brown, C.F., 2002. Reduction kinetics of Fe(III), Co(III), U(VI), Cr(VI), and Tc(VII) in cultures of dissimilatory metal-reducing bacteria. *Biotechnol Bioeng*, 80(6): 637-49.
- Liu, Y., Bi, J., Lv, J., Ma, Z., Wang, C., 2017. Spatial multi-scale relationships of ecosystem services: A case study using a geostatistical methodology. *Scientific Reports*, 7(1): 9486.
- Loan, C.V., 1992. Computational frameworks for the fast Fourier transform. Society for Industrial and Applied Mathematics.

- Lüttge, A., 2006. Crystal dissolution kinetics and Gibbs free energy. *Journal of Electron Spectroscopy and Related Phenomena*, 150(2-3): 248-259.
- Lüttge, A., Arvidson, R.S., Fischer, C., 2013. A Stochastic Treatment of Crystal Dissolution Kinetics. *Elements*, 9(3): 183-188.
- Lüttge, A., Arvidson, R.S., Fischer, C., Kurganskaya, I., 2019. Kinetic concepts for quantitative prediction of fluid-solid interactions. *Chemical Geology*, 504: 216-235.
- Lüttge, A., Bolton, E.W., Lasaga, A.C., 1999. An interferometric study of the dissolution kinetics of anorthite; the role of reactive surface area. *American Journal of Science*, 299(7-9): 652-678.
- Lüttge, A.J.A.M., 2005. Etch pit coalescence, surface area, and overall mineral dissolution rates. 90(11-12): 1776-1783.
- MacInnis, I.N., Brantley, S.L., 1992. The role of dislocations and surface morphology in calcite dissolution. *Geochimica et Cosmochimica Acta*, 56(3): 1113-1126.
- Maher, K., DePaolo, D.J., Lin, J.C.F., 2004. Rates of silicate dissolution in deep-sea sediment: In situ measurement using U-234/U-238 of pore fluids. *Geochimica Et Cosmochimica Acta*, 68(22): 4629-4648.
- Maher, K., Steefel, C.I., White, A.F., Stonestrom, D.A., 2009. The role of reaction affinity and secondary minerals in regulating chemical weathering rates at the Santa Cruz Soil Chronosequence, California. *Geochimica Et Cosmochimica Acta*, 73(10): 2804-2831.
- Martin, P., Gaitero, J.J., Dolado, J.S., Manzano, H., 2020. KIMERA: A Kinetic Montecarlo Code for Mineral Dissolution. 10(9): 825.
- Martin, P., Manzano, H., Dolado, J.S., 2019. Mechanisms and Dynamics of Mineral Dissolution: A New Kinetic Monte Carlo Model. 2(10): 1900114.
- McCave, I.N., Hall, I.R., 2006. Size sorting in marine muds: Processes, pitfalls, and prospects for paleoflow-speed proxies. 7(10).
- McLoughlin, N., Brasier, M.D., Wacey, D., Green, O.R., Perry, R.S., 2007. On biogenicity criteria for endolithic microborings on early Earth and beyond. *Astrobiology*, 7(1): 10-26.
- Meakin, P., Rosso, K.M., 2008. Simple kinetic Monte Carlo models for dissolution pitting induced by crystal defects. *The Journal of Chemical Physics*, 129(20): 204106.
- Mellott, N.P., Brantley, S.L., Pantano, C.G., 2002. Topography of polished plates of albite crystal and glass during dissolution.
- Minasny, B., McBratney, A.B., 2001. A rudimentary mechanistic model for soil formation and landscape development: II. A two-dimensional model incorporating chemical weathering. *Geoderma*, 103(1): 161-179.
- Montes-H, G., Fritz, B., Clement, A., Michau, N., 2005. Modelling of geochemical reactions and experimental cation exchange in MX80 bentonite. *Journal of Environmental Management*, 77(1): 35-46.
- Morse, J.W., Arvidson, R.S., A., L., 2007. Calcium carbonate formation and dissolution. *Chemical Reviews*, 107(2): 342-381.

- Murik, O. et al., 2017. What distinguishes cyanobacteria able to revive after desiccation from those that cannot: the genome aspect. *19(2)*: 535-550.
- Mutaftschiev, B., 2001. The atomistic nature of crystal growth.
- Nagy, K.L., Cygan, R.T., Hanchar, J.M., Sturchio, N.C., 1999. Gibbsite growth kinetics on gibbsite, kaolinite, and muscovite substrates: atomic force microscopy evidence for epitaxy and an assessment of reactive surface area. *63*: 2337-2351.
- Nagy, K.L., Lasaga, A.C., 1992. Dissolution and precipitation kinetics of gibbsite at 80°C and pH 3: The dependence on solution saturation state. *Geochimica et Cosmochimica Acta*, *56(8)*: 3093-3111.
- Naviaux, J.D. et al., 2019. Calcite dissolution rates in seawater: Lab vs. in-situ measurements and inhibition by organic matter. *Marine Chemistry*, *215*: 103684.
- Newman, D.K., Kolter, R., 2000. A role for excreted quinones in extracellular electron transfer. *Nature*, *405(6782)*: 94-7.
- Nicoleau, L., Bertolim, M.A., 2015. Analytical model for the alite (C3S) dissolution topography. *Journal of the American Ceramic Society*.
- Noiriel, C. et al., 2009. Changes in reactive surface area during limestone dissolution: An experimental and modelling study. *Chemical Geology*, *265(1)*: 160-170.
- Noiriel, C., Oursin, M., Daval, D., 2020. Examination of crystal dissolution in 3D: A way to reconcile dissolution rates in the laboratory? *Geochimica Et Cosmochimica Acta*, *273*: 1-25.
- Noiriel, C., Oursin, M., Saldi, G., Haberthür, D., 2019. Direct Determination of Dissolution Rates at Crystal Surfaces Using 3D X-ray Microtomography. *ACS Earth and Space Chemistry*, *3(1)*: 100-108.
- Nugent, M.A., Brantley, S.L., Pantano, C.G., Maurice, P.A., 1998. The influence of natural mineral coatings on feldspar weathering. *Nature*, *395(6702)*: 588-591.
- Oelkers, E.H., Golubev, S.V., Pokrovsky, O.S., Bénézech, P., 2011. Do organic ligands affect calcite dissolution rates? *Geochimica Et Cosmochimica Acta*, *75(7)*: 1799-1813.
- Oh, Y., Jo, W., Yang, Y., Park, S.J.U., 2007. Influence of culture conditions on Escherichia coli O157: H7 biofilm formation by atomic force microscopy. *107(10-11)*: 869-874.
- Oh, Y., Lee, N., Jo, W., Jung, W., Lim, J.J.U., 2009. Effects of substrates on biofilm formation observed by atomic force microscopy. *109(8)*: 874-880.
- Opdyke, B.N., Wilkinson, B.H.J.A.J.o.S., 1993. Carbonate mineral saturation state and cratonic limestone accumulation. *293(3)*: 217-234.
- Orme, C.A. et al., 2001. Formation of chiral morphologies through selective binding of amino acids to calcite surface steps. *Nature*, *411(6839)*: 775-9.
- Pérez-Garrido, C., Fernández-Díaz, L., Pina, C.M., Prieto, M., 2007. In situ AFM observations of the interaction between calcite (101⁻⁴) surfaces and Cd-bearing aqueous solutions. *Surface Science*, *601(23)*: 5499-5509.
- Perez, A. et al., 2019. Comparing the reactivity of glasses with their crystalline equivalents: The case study of plagioclase feldspar. *Geochimica Et Cosmochimica Acta*, *254*: 122-141.

- Persson, B.N.J., Albohr, O., Tartaglino, U., Volokitin, A.I., Tosatti, E., 2005. On the nature of surface roughness with application to contact mechanics, sealing, rubber friction and adhesion. *Journal of Physics: Condensed Matter*, 17(1): R1.
- Phillips-Lander, C.M., Legett, C., Madden, A.S.E., Madden, M.E.E., 2017. Can we use pyroxene weathering textures to interpret aqueous alteration conditions? Yes and No. 102(9): 1915-1921.
- Pimentel, C., Pina, C.M., Gnecco, E., 2013. Epitaxial Growth of Calcite Crystals on Dolomite and Kutnahorite (104) Surfaces. *Crystal Growth & Design*, 13(6): 2557-2563.
- Pokrovsky, O.S., Shirokova, L.S., Zabelina, S.A., Jordan, G., Bénézech, P.J.n.M.D., 2021. Weak impact of microorganisms on Ca, Mg-bearing silicate weathering. 5(1): 51.
- Pollet-Villard, M. et al., 2016a. Does crystallographic anisotropy prevent the conventional treatment of aqueous mineral reactivity? A case study based on K-feldspar dissolution kinetics. *Geochimica Et Cosmochimica Acta*, 190: 294-308.
- Pollet-Villard, M. et al., 2016b. Influence of etch pit development on the surface area and dissolution kinetics of the orthoclase (001) surface. *Chemical Geology*, 447: 79-92.
- Porder, S., 2019. How Plants Enhance Weathering and How Weathering is Important to Plants. *Elements*, 15(4): 241-246.
- Quirk, J. et al., 2015. Constraining the role of early land plants in Palaeozoic weathering and global cooling. *Proceedings of the Royal Society B: Biological Sciences*, 282(1813): 20151115.
- Rippka, R., Deruelles, J., Waterbury, J.B., Herdman, M., Stanier, R.Y., 1979. Generic Assignments, Strain Histories and Properties of Pure Cultures of Cyanobacteria. 111(1): 1-61.
- Robin, V. et al., 2018. Experimental study and numerical simulation of the dissolution anisotropy of tricalcium silicate. *Chemical Geology*, 497: 64-73.
- Rohwerder, T., Gehrke, T., Kinzler, K., Sand, W., 2003. Bioleaching review part A. *Applied Microbiology and Biotechnology*, 63(3): 239-248.
- Rouillard, J., van Zuilen, M., Pisapia, C., Garcia-Ruiz, J.-M., 2020. An Alternative Approach for Assessing Biogenicity. *Astrobiology*, 21(2): 151-164.
- Rousaki, A. et al., 2018. On-field Raman spectroscopy of Patagonian prehistoric rock art: Pigments, alteration products and substrata. *TrAC Trends in Analytical Chemistry*, 105: 338-351.
- Ruiz-Agudo, E., Kowacz, M., Putnis, C.V., Putnis, A., 2010. The role of background electrolytes on the kinetics and mechanism of calcite dissolution. *Geochimica et Cosmochimica Acta*, 74(4): 1256-1267.
- Ruiz-Agudo, E., Putnis, C., Jiménez-López, C., Rodríguez-Navarro, C., 2009. An atomic force microscopy study of calcite dissolution in saline solutions: The role of magnesium ions. *Geochimica Et Cosmochimica Acta*, 73(11): 3201-3217.
- Saccone, L. et al., 2012. High resolution characterization of ectomycorrhizal fungal-mineral interactions in axenic microcosm experiments. 111: 411-425.
- Saldi, G.D., Voltolini, M., Knauss, K.G., 2017. Effects of surface orientation, fluid chemistry and mechanical polishing on the variability of dolomite dissolution rates. *Geochimica Et Cosmochimica Acta*, 206: 94-111.

- Sanchez, A.H.M., Luthringer, B.J.C., Feyerabend, F., Willumeit, R., 2015. Mg and Mg alloys: How comparable are in vitro and in vivo corrosion rates? A review. *Acta Biomaterialia*, 13: 16-31.
- Santelli, C.M., Welch, S.A., Westrich, H.R., Banfield, J.F., 2001. The effect of Fe-oxidizing bacteria on Fe-silicate mineral dissolution. *Chemical Geology*, 180(1-4): 99-115.
- Schlesinger, W.H., Cole, J.J., Finzi, A.C., Holland, E.A., 2011. Introduction to coupled biogeochemical cycles. 9(1): 5-8.
- Sheldon, N.D., Tabor, N.J., 2009. Quantitative paleoenvironmental and paleoclimatic reconstruction using paleosols. *Earth-Science Reviews*, 95(1): 1-52.
- Siena, M. et al., 2021. Statistical Characterization of Heterogeneous Dissolution Rates of Calcite from In situ and Real-Time AFM Imaging. *Transport in Porous Media*, 140(1): 291-312.
- Siena, M. et al., 2020. Generalized Sub-Gaussian Processes: Theory and Application to Hydrogeological and Geochemical Data. *Water Resources Research*, 56(8): e2020WR027436.
- Siena, M., Recalcati, C., Guadagnini, A., Riva, M., 2023. A Gaussian-Mixture based stochastic framework for the interpretation of spatial heterogeneity in multimodal fields. *Journal of Hydrology*, 617: 128849.
- Sjoberg, E.L., Rickard, D.T.J.C.G., 1984. Calcite dissolution kinetics: surface speciation and the origin of the variable pH dependence. 42(1-4): 119-136.
- Smith, M.E., Knauss, K.G., Higgins, S.R., 2013. Effects of crystal orientation on the dissolution of calcite by chemical and microscopic analysis. *Chemical Geology*, 360–361(0): 10-21.
- Smits, M.M. et al., 2009. The fungal–mineral interface: challenges and considerations of micro-analytical developments. *Fungal Biology Reviews*, 23(4): 122-131.
- Stefansson, A., Arnorsson, S., 2000. Feldspar saturation state in natural waters. *Geochimica Et Cosmochimica Acta*, 64(15): 2567-2584.
- Stigliano, L., Caumartin, J., Benzerara, K., 2023a. Micro-and nanoscale techniques for studying biofilm-mineral interactions.
- Stigliano, L., Ackerer, P., Benzerara, K., Daval, D., 2023b. Linking calcite surface roughness resulting from dissolution to the saturation state of the bulk solution. *Chemical Geology*, 637: 121680.
- Stranski, I.N.J.Z.f.p.C., 1928. Zur theorie des kristallwachstums. 136(1): 259-278.
- Su, G. et al., 2021. Low concentration of Tween-20 enhanced the adhesion and biofilm formation of *Acidianus manzaensis* YN-25 on chalcopyrite surface. 284: 131403.
- Taylor, A.S., Blum, J.D., Lasaga, A.C., 2000. The dependence of labradorite dissolution and Sr isotope release rates on solution saturation state. *Geochimica et Cosmochimica Acta*, 64(14): 2389-2400.
- Teng, H.H., 2004. Controls by saturation state on etch pit formation during calcite dissolution. *Geochimica Et Cosmochimica Acta*, 68(2): 253-262.
- Teng, H.H., Dove, P.M., 1997. Surface site-specific interactions of aspartate with calcite during dissolution: Implications for biomineralization. *American Mineralogist*, 82(9-10): 878-887.

- Thorseth, I.H., Furnes, H., Tumyr, O., 1995. Textural and chemical effects of bacterial activity on basaltic glass: an experimental approach. *Chemical Geology*, 119(1): 139-160.
- Uroz, S., Calvaruso, C., Turpault, M.-P., Frey-Klett, P., 2009. Mineral weathering by bacteria: ecology, actors and mechanisms. *Trends in Microbiology*, 17(8): 378-387.
- Uroz, S., Kelly, L.C., Turpault, M.-P., Lepleux, C., Frey-Klett, P., 2015. The mineralosphere concept: mineralogical control of the distribution and function of mineral-associated bacterial communities. *Trends in Microbiology*, 23(12): 751-762.
- Uroz, S. et al., 2012. Minerals affect the specific diversity of forest soil bacterial communities. *Geomicrobiology Journal*, 29(1): 88-98.
- van der Lee, J., De Windt, L., 2002. *CHESSTutorial and Cookbook*. Updated for version 3.0., Manual Nr. LHM/RD/02/13, Paris, 116 pp.
- van Schöll, L. et al., 2008. Rock-eating mycorrhizas: their role in plant nutrition and biogeochemical cycles. *Plant and Soil*, 303(1-2): 35-47.
- Vance, D., Teagle, D.A.H., Foster, G.L., 2009. Variable Quaternary chemical weathering fluxes and imbalances in marine geochemical budgets. *Nature*, 458(7237): 493-496.
- Velbel, M.A., Losiak, A.I., 2010. Denticles on Chain Silicate Grain Surfaces and Their Utility as Indicators of Weathering Conditions on Earth and Mars. *Journal of Sedimentary Research*, 80(9): 771-780.
- Vinson, M.D., Arvidson, R.S., Lüttge, A.J.J.o.C.G., 2007. Kinetic inhibition of calcite (1 0 4) dissolution by aqueous manganese (II). 307(1): 116-125.
- Vinson, M.D., Lüttge, A.J.A.J.o.S., 2005. Multiple length-scale kinetics: an integrated study of calcite dissolution rates and strontium inhibition. 305(2): 119-146.
- Wang, J. et al., 2022. Extreme halophilic bacteria promote the surface dolomitization of calcite crystals in solutions with various magnesium concentrations. 606: 120998.
- Wang, L., Putnis, C.V., 2020. Dissolution and Precipitation Dynamics at Environmental Mineral Interfaces Imaged by In Situ Atomic Force Microscopy. *Accounts of Chemical Research*, 53(6): 1196-1205.
- Wang, L. et al., 2005. A new model for nanoscale enamel dissolution. 109(2): 999-1005.
- Waterbury, J.B., Stanier, R.Y., 1978. Patterns of growth and development in pleurocapsalean cyanobacteria. *Microbiol Rev*, 42(1): 2-44.
- Waters, M.S. et al., 2009. Simultaneous Interferometric Measurement of Corrosive or Demineralizing Bacteria and Their Mineral Interfaces. 75(5): 1445-1449.
- Wehrli, B., 1989. Monte Carlo simulations of surface morphologies during mineral dissolution. *Journal of Colloid and Interface Science*, 132(1): 230-242.
- Weissbart, E.J., Rimstidt, D.J., 2000. Wollastonite: Incongruent dissolution and leached layer formation. *Geochimica Et Cosmochimica Acta*, 64(23): 4007-4016.
- Welch, S., Taunton, A., Banfield, J., 2002. Effect of microorganisms and microbial metabolites on apatite dissolution. *Geomicrobiology Journal*, 19(3): 343-367.
- White, A.F., Brantley, S.L., 2003. The effect of time on the weathering of silicate minerals: why do weathering rates differ in the laboratory and field? *Chemical Geology*, 202(3-4): 479-506.

- Wierzchos, J., Casero, M.C., Artieda, O., Ascaso, C., 2018. Endolithic microbial habitats as refuges for life in polyextreme environment of the Atacama Desert. *Curr Opin Microbiol*, 43: 124-131.
- Wild, B. et al., 2019a. In-situ dissolution rates of silicate minerals and associated bacterial communities in the critical zone (Strengbach catchment, France). *Geochimica Et Cosmochimica Acta*, 249: 95-120.
- Wild, B. et al., 2016. pH-dependent control of feldspar dissolution rate by altered surface layers. *Chemical Geology*, 442: 148-159.
- Wild, B. et al., 2019b. Physical Properties of Interfacial Layers Developed on Weathered Silicates: A Case Study Based on Labradorite Feldspar. *The Journal of Physical Chemistry C*, 123(40): 24520-24532.
- Wild, B., Gerrits, R., Bonneville, S., 2022. The contribution of living organisms to rock weathering in the critical zone. *npj Materials Degradation*, 6(1): 98.
- Wild, B., Imfeld, G., Daval, D., 2021. Direct measurement of fungal contribution to silicate weathering rates in soil. *Geology*.
- Wild, B., Imfeld, G., Guyot, F., Daval, D., 2018. Early stages of bacterial community adaptation to silicate aging. *Geology*, 46(6): 555-558.
- Wilkin, R.T., Barnes, H.L., Brantley, S.L., 1996. The size distribution of framboidal pyrite in modern sediments: An indicator of redox conditions. *Geochimica et Cosmochimica Acta*, 60(20): 3897-3912.
- Wille, M. et al., 2018. Silicon and chromium stable isotopic systematics during basalt weathering and lateritisation: A comparison of variably weathered basalt profiles in the Deccan Traps, India. *Geoderma*, 314: 190-204.
- Williams, D., Westcott, C., Fleischmann, M.J.J.o.t.E.S., 1985. Stochastic models of pitting corrosion of stainless steels: I. Modeling of the initiation and growth of pits at constant potential. *Corrosion*, 35(8): 1796.
- Wright, C.J., Shah, M.K., Powell, L.C., Armstrong, I.J.S., 2010. Application of AFM from microbial cell to biofilm. *Langmuir*, 26(3): 134-149.
- Wu, C. et al., 2011. Molecular modulation of calcite dissolution by organic acids. *Langmuir*, 27(7): 3153-3162.
- Wu, D., Liang, F., Kang, C., Fang, F., 2021. Performance Analysis of Surface Reconstruction Algorithms in Vertical Scanning Interferometry Based on Coherence Envelope Detection. *Optics*, 12(2): 164.
- Wyant, J., 2002. White light interferometry. *AeroSense 2002*, 4737. SPIE.
- Xu, J., Fan, C., Teng, H.H., 2012. Calcite dissolution kinetics in view of Gibbs free energy, dislocation density, and pCO₂. *Chemical Geology*, 322-323: 11-18.
- Yang, M., Stipp, S.L.S., Harding, J., 2008. Biological Control on Calcite Crystallization by Polysaccharides. *Crystal Growth & Design*, 8(11): 4066-4074.
- Zhang, R. et al., 2014. Colonization and biofilm formation of the extremely acidophilic archaeon *Ferroplasma acidiphilum*. *Microb Drug Resist*, 150: 245-252.

Zhang, R., Neu, T.R., Blanchard, V., Vera, M., Sand, W.J.N.b., 2019. Biofilm dynamics and EPS production of a thermoacidophilic bioleaching archaeon. 51: 21-30.

Zhang, X., Bishop, P.L., Kupferle, M.J., 1998. Measurement of polysaccharides and proteins in biofilm extracellular polymers. *Water Science and Technology*, 37(4-5): 345-348.

Zhu, C., Veblen, D.R., Blum, A.E., Chipera, S.J., 2006. Naturally weathered feldspar surfaces in the Navajo Sandstone aquifer, Black Mesa, Arizona: Electron microscopic characterization. *Geochimica Et Cosmochimica Acta*, 70(18): 4600-4616.

Chapter 2 : Statistical methods to quantitatively detect fluid imprints and bio-weathering signatures

As discussed in the previous chapter, the present thesis work revolves around the informative content that is retained within weathered mineral surfaces, encompassing both fluid imprints and signatures of microbial weathering. In this context, it becomes crucial to shift from subjective, qualitative (thus debated) assessments to quantitative (thus less ambiguous) criteria, based on surface roughness characterizations.

To this end, the general approach adopted involves summarizing the key statistical features of the surface topography into surface roughness descriptors. This enables to compare quantitatively different surfaces by comparing the corresponding roughness descriptors. As so, a new question arises: which surface roughness descriptors are most appropriate for characterizing mineral surfaces resulting from dissolution?

The following chapter is dedicated to introducing and providing illustrative examples of the main statistical techniques employed in this study. These methods are used to quantitatively detect fluid imprints resulting from dissolution at different saturation states and bio-weathering signatures resulting from microbially-mediated dissolution, through surface roughness characterizations.

A comprehensive collection of the various techniques employed in surface metrology for quantifying roughness can be found in (Whitehouse, 1994). In brief, these can range from simple unidimensional descriptors of the roughness amplitude, such as R_a (i.e., arithmetic average of height deviations from the mean plane) and R_q (i.e., root mean square of height deviations from the mean plane), to evaluations of the frequency distribution of surface height values and/or the corresponding spatial patterns.

2.1 Frequency distribution of height values

The specific shape of the frequency distribution of the height values of a surface holds significant information. For instance, if the distribution closely follows a Gaussian (normal) distribution, wherein the majority of the height values gather around the mean and the height values are equally likely to be above or below the mean, it suggests that there is no systematic bias or trends in the surface's elevation data. Alternatively, distributions that deviate from the bell-shaped curve can reveal information about particular height values that are more or less

frequent on the surface, potentially providing valuable insights into the underlying dissolution process.

A broad range of descriptive statistics tools can be used for characterizing the particular shape of a given frequency distribution. Here, the focus will be directed towards two specific parameters—skewness and kurtosis—that hold particular significance in describing the surface roughness resulting from dissolution.

The skewness and kurtosis of the frequency distribution of heights values evaluated over a given observation window of $N*M$ data points are defined as:

$$skewness = \frac{\sum_i^N (Z_i - \langle Z \rangle)^3}{(N*M-1)s^3} \quad (2.1)$$

$$kurtosis = \frac{\sum_i^N (Z_i - \langle Z \rangle)^4}{(N*M-1)s^4} \quad (2.2)$$

where: Z_i is the i^{th} value of the surface topography, Z , over the area investigated, $\langle Z \rangle$ is the surface heights mean value, and s is the corresponding surface heights standard deviation. Skewness is a measure of the degree of asymmetry of a given distribution, whereas kurtosis is a measure of the relative weight of the tails compared to the rest of the distribution. A Gaussian distribution is characterized by skewness and kurtosis equal to 0 and 3, respectively. A skewness value lower or higher than 0 indicates a left-skewed or right-skewed distribution, respectively, whereas a kurtosis lower or higher than 3 denotes a distribution with tails that are respectively thinner or heavier compared to a Gaussian distribution.

Figure 2.1 and 2.2 provide visual representations that help illustrate the concepts of skewness and kurtosis when applied to surface height values. Overall, applying these two parameters to surfaces resulting from dissolution can provide insights into whether (and to what degree) the dissolution process skews the height values towards either tail of the distribution, and to what extent the tailedness of the distribution is consequently affected.

Nonetheless, while descriptors of the frequency distribution, such as skewness and kurtosis, can effectively provide information about the prevalent height values within the surface, they do not take into account the spatial distribution of these values across the surface. Consequently, surfaces that share an identical frequency distribution of height values can exhibit substantial differences in terms of their spatial distribution, as exemplified in Figure 2.3. There is a need for the complementary application of statistical tools focused on characterizing the spatial distribution of the height values.

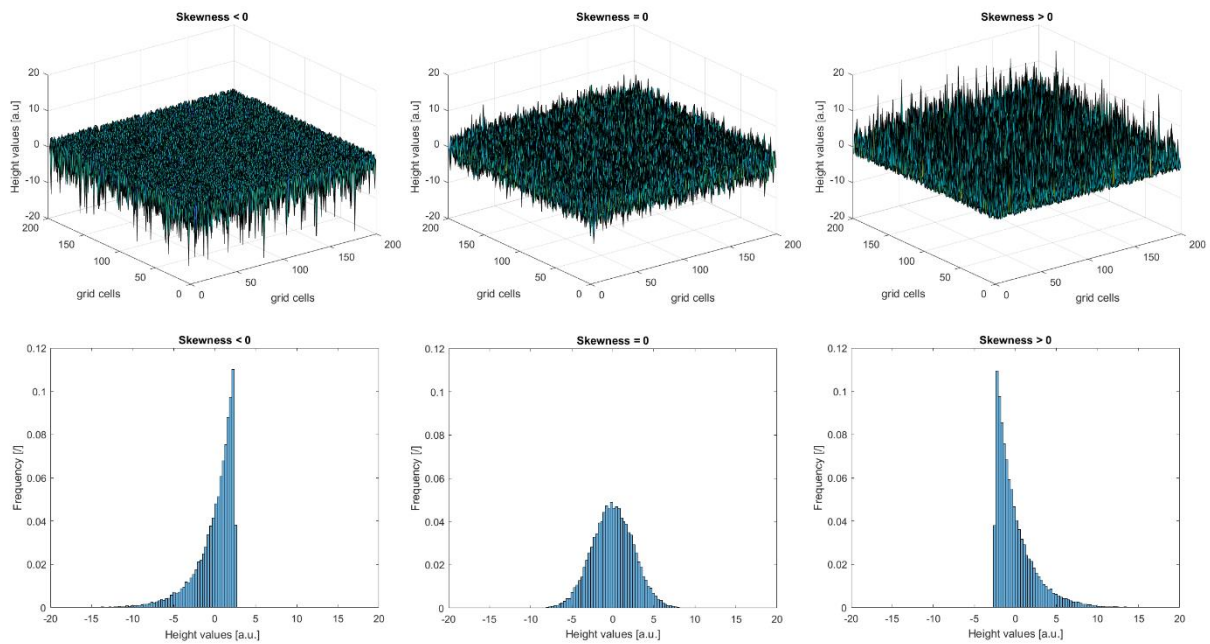


Figure 2.1 Visual representation of three surfaces sharing the same variance but characterized by different skewness values (top row) and corresponding histograms (bottom row). These include left-skewed (skewness < 0), symmetric (gaussian, skewness $= 0$) and right-skewed (skewness > 0) distributions, respectively. This visualization illustrates how a left-skewed distribution, characterized by long tails towards lower height values, indicates the presence of 'spikes' that prominently stand out from the overall texture of the surface towards lower height values. In contrast, for right-skewed distributions, which are characterized by long tails towards higher height values, the 'spikes' stand out from the overall surface texture towards higher height values.

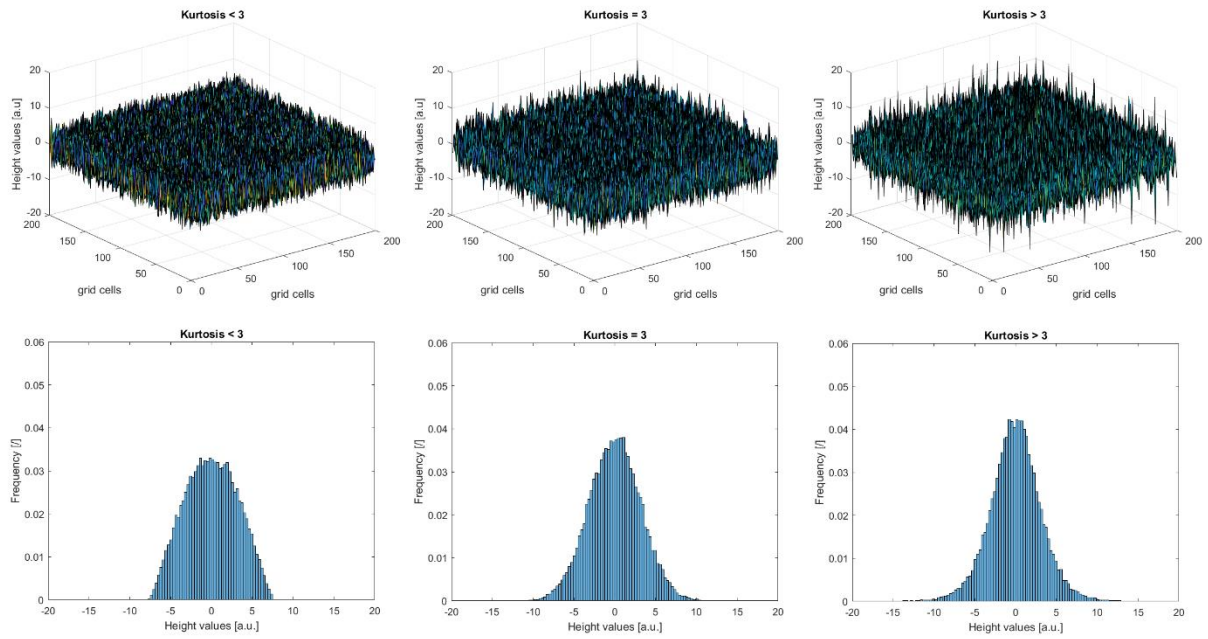


Figure 2.2 Visual representation of three surfaces sharing the same variance but characterized by different kurtosis values (top row) and corresponding histograms (bottom row). These include platykurtic (kurtosis < 3), gaussian (kurtosis $= 3$) and leptokurtic (kurtosis > 3) distributions, respectively. This visualization illustrates how a platykurtic distribution, characterized by lighter tails compared to a gaussian distribution with the same variance, indicates height values that are more compacted around the surface mean plane. In contrast, for leptokurtic distributions, which are characterized by heavier tails compared to a gaussian distribution with the same variance, the height values are less tightly clustered around the surface mean plane, displaying ‘spikes’ standing out from the overall surface texture both towards higher and lower height values.

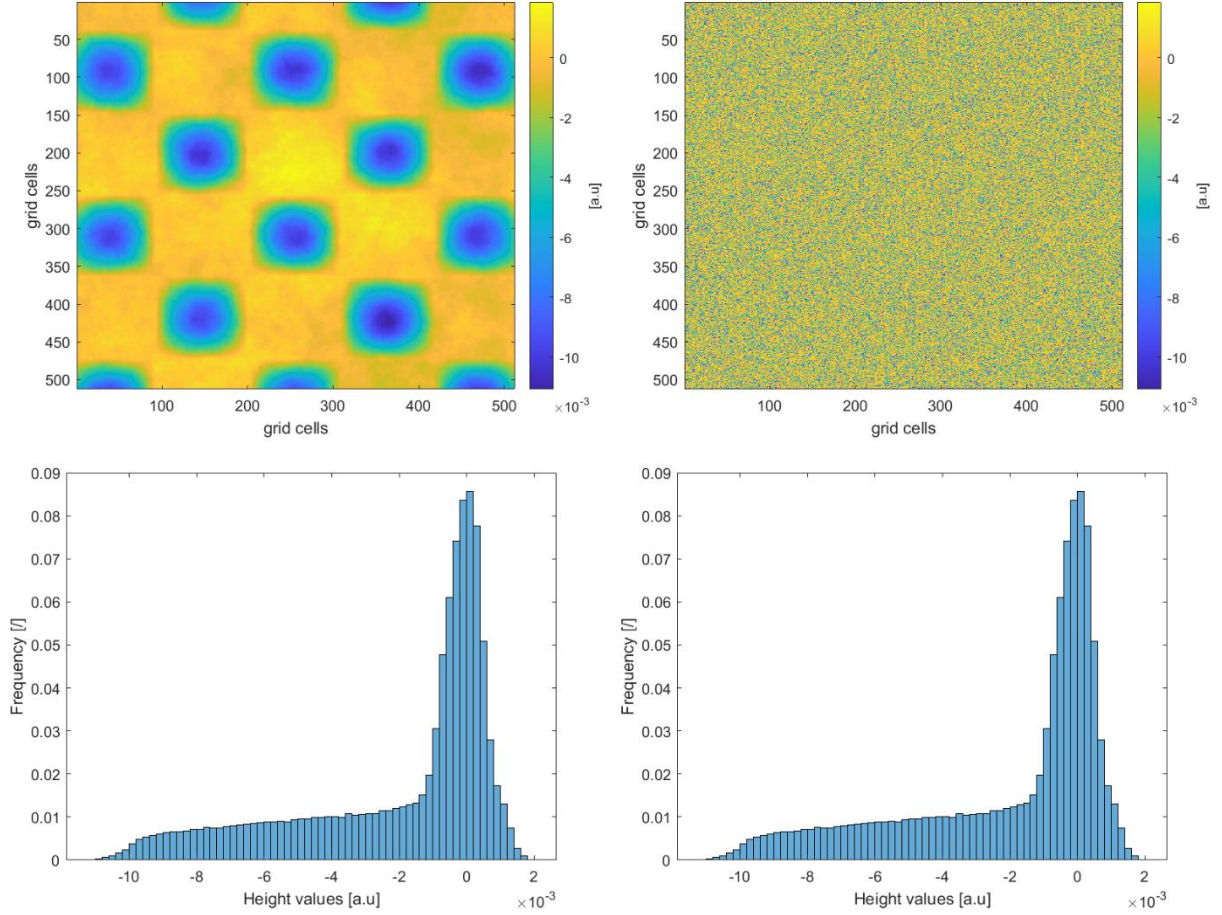


Figure 2.3 Visual representation of two surfaces sharing the same histogram of height values (bottom row) but different spatial distribution of the height values across the surface.

2.2 Semi-variogram

A statistical method specifically aimed at characterizing the spatial distribution of surface height values is the semi-variogram, which, indeed, provides a measure of the degree of spatial correlation of the height values (Jacobs et al., 2017).

The experimental semi-variogram, $\gamma(s)$, is defined as:

$$\gamma(s) = \frac{1}{2n(s)} \sum_{i=1}^{n(s)} [Z(u_i) - Z(u_i + s)]^2 \quad (2.3)$$

where: $n(s)$ is the total number of data (i.e., height values) pairs separated by a given distance s (evaluated along all directions), and $Z(u_i)$ is the height value evaluated on the i^{th} position on the grid, \mathbf{u} .

Conceptually, the experimental semi-variogram quantifies the notion that, for surfaces exhibiting a certain degree of spatial dependency, closer data pairs tend to be more similar than

more distant ones. As a consequence, the experimental semi-variogram, which in practice measures the ‘spatial dissimilarity’ of height values, shows lower values at short lags and increasingly higher values as the separation distance increases (Figure 2.4).

Different theoretical semi-variogram models can be used to interpret the semi-variogram computed on experimental data. Fitting experimental semi-variograms with theoretical models enables to summarize all the information regarding the degree of spatial correlation within the model parameters alone. The general expression for a theoretical semi-variogram is:

$$\gamma(s) = \gamma(s = 0) + f(\text{total sill}, \text{correlation length}) \quad (2.4)$$

where: $\gamma(s=0)$ is the nugget, a parameter that accounts for the short scale variability that is due to measurement errors and uncontrolled environmental oscillations; the *total sill*, which is the ‘plateau value’ exhibited by the semi-variogram under stationary conditions; the *correlation length*, which is the value of the separation distance at which the plateau value is reached.

Conceptually, the total sill measures how much the height values are spread around the surface mean plane, as it can be seen by comparing two surfaces with the same spatial pattern but different variance (see ‘Surface A’ and ‘Surface C’ in Figure 2.5). On the other hand, the correlation length measures the separation distance above which the height values are no longer spatially correlated. By comparing two surfaces with the same variance but different spatial pattern, it can be observed how larger surface features result in larger correlation length values (see ‘Surface A’ and ‘Surface B’ in Figure 2.5).

Altogether, these examples show how topography maps exhibiting different spatial patterns are characterized by different degrees of spatial correlation and thus by different experimental semi-variogram curves. It is therefore possible to use semi-variograms to quantitatively compare mineral surfaces resulting from dissolution at different (abiotic and biotic) conditions.

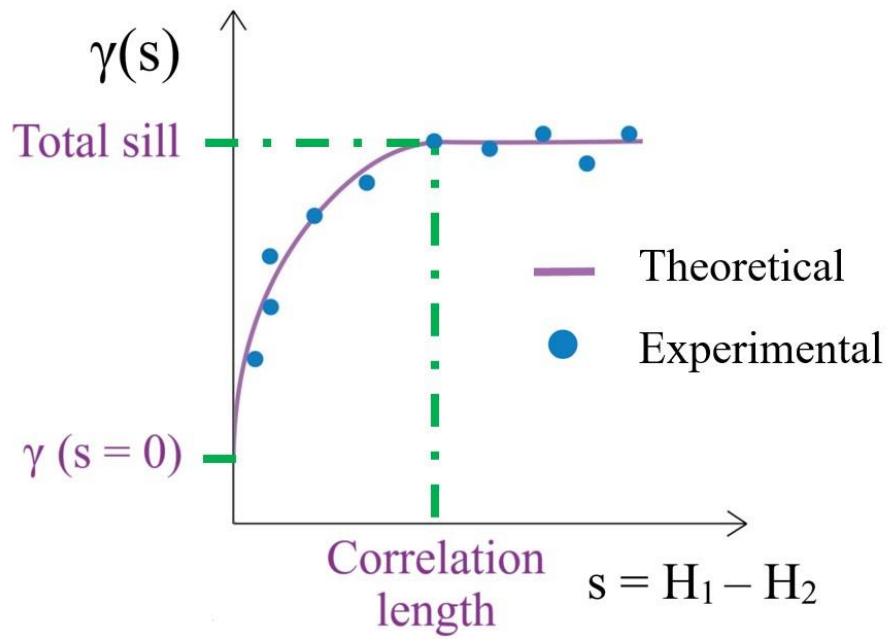


Figure 2.4 Figure showing the graphical relationships between experimental and theoretical semi-variogram, including model parameters: nugget, total sill and correlation length.

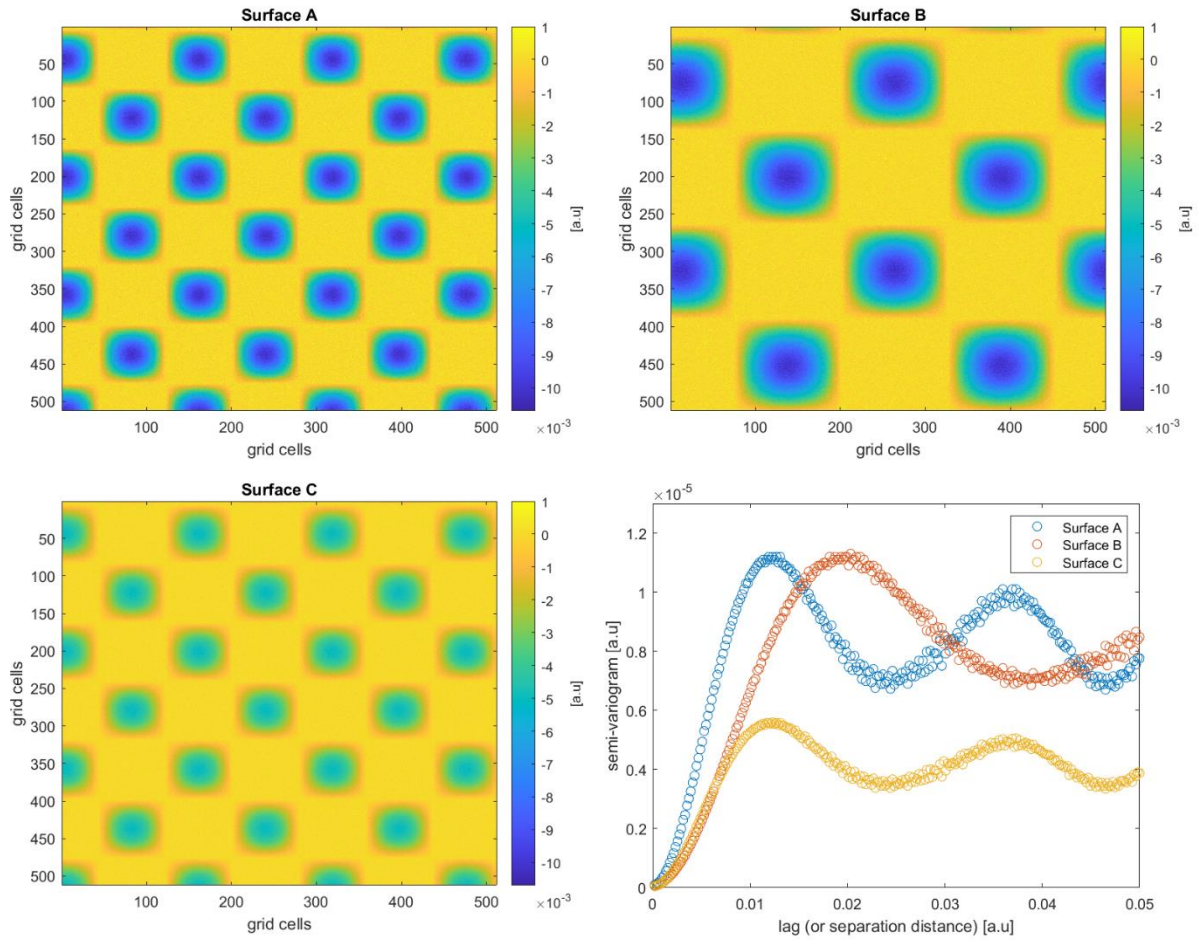


Figure 2.5 Visual representation of three surfaces characterized by different degrees of spatial autocorrelation. ‘Surface A’ and ‘Surface B’ have the same variance, but different spatial patterns. As a result, the larger surface features of ‘Surface B’ lead the variogram to shift to the right, thereby increasing the correlation length, while the average plateau value remains unaffected. On the other hand, ‘Surface A’ and ‘Surface C’ have the same spatial patterns, but different variance. As so, variogram associated with ‘Surface C’ exhibits a shift towards lower values, thereby decreasing the total sill, while the correlation length remains unaffected. Grid cell width = $2 \cdot 10^{-4}$ a.u.

2.3 Power spectral density (PSD)

An alternative method to assess the spatial distribution of the height values across the surface is given by the power spectral density (PSD), which, indeed, provides a measure of surface roughness at different length-scales. The mathematical definition of the PSD is detailed in (Jacobs et al., 2017). In brief, this involves a transformation of the surface topography, $Z(x,y)$, from the spatial domain to the frequency domain, through the 2D Fourier transform:

$$\tilde{Z}_{q_x q_y} = \int_A Z(x, y) e^{-i(q_x x + q_y y)} dx dy \quad (2.5)$$

where: q_x and q_y are the corresponding wavevectors.

However, in practice, the surface topography, $Z(x, y)$, is not a well-defined continuous function as it can be measured only at discrete sites on a regular rectangular grid with “pixel” size $l_x \times l_y$. As so, the discrete 2D Fourier transform, which is commonly computed through the FFT (Fast Fourier transform) algorithm (Loan, 1992), becomes:

$$\tilde{Z}_{q_x q_y} = l_x l_y \sum_{x, y} Z_{x, y} e^{-i(q_x x + q_y y)} \quad (2.6)$$

where: $Z_{x, y}$ is the actual topography matrix.

The 2D PSD can thus be defined as:

$$C_{q_x, q_y}^{2D} = \frac{1}{U} \left| \tilde{Z}_{q_x, q_y} \right|^2 \quad (2.7)$$

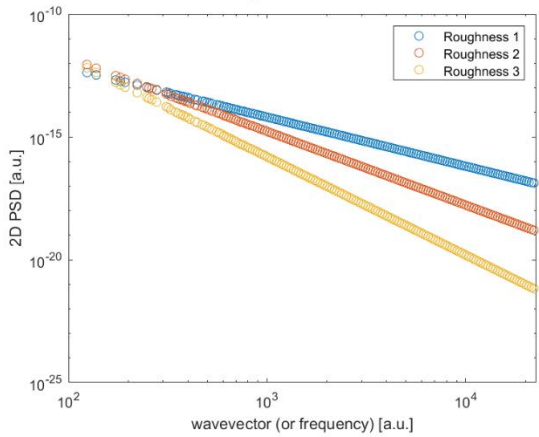
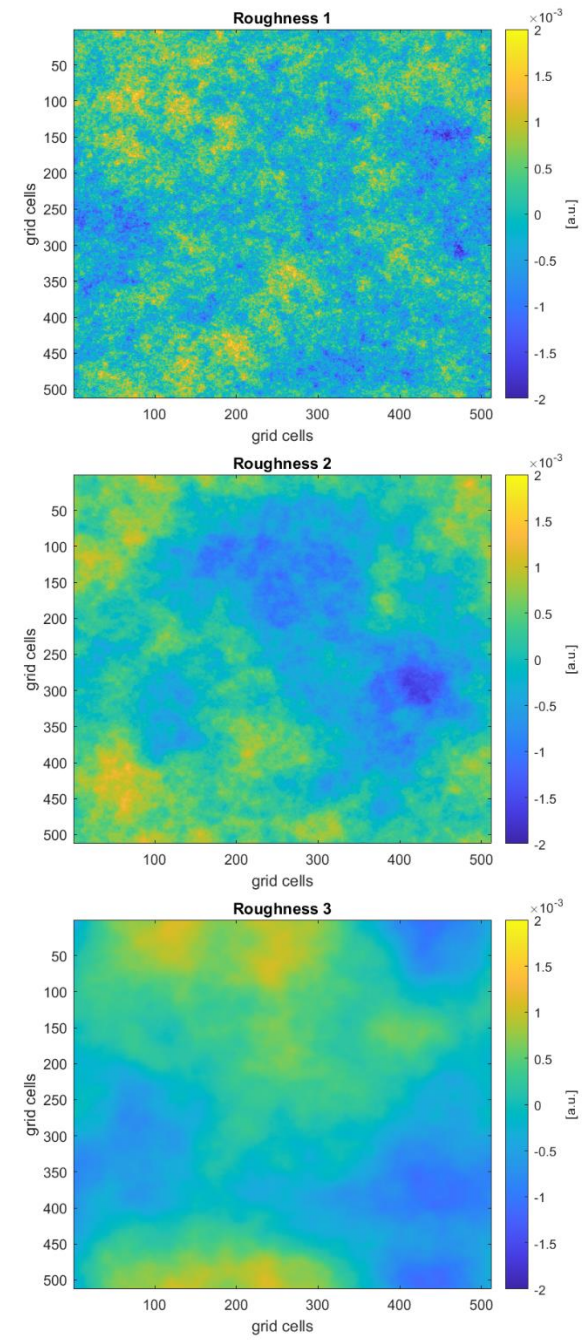
where: U is a scaling factor that makes the PSD independent of sample size.

Note that the magnitude operation removes all phase information from the discrete 2D Fourier transform but retains its amplitude. The 2D PSD values obtained can then be averaged over the radial direction, providing an effective quantification of the contribution of the different frequency components to the overall surface roughness.

Figure 2.6 provides examples of the application of the radially averaged 2D PSD to surfaces exhibiting different degrees of roughness at different length-scales, showing how the PSD can detect (and quantify) variations in the roughness amplitude at specific frequency components.

Overall, these examples show how the PSD is able to effectively differentiate between surfaces displaying different degrees of surface roughness at different length-scales. As so, it becomes possible to use PSD analyses in conjunction with semi-variogram analyses to quantitatively compare mineral surfaces resulting from dissolution at different (abiotic and biotic) conditions.

Different roughness scaling Same variance



Same roughness scaling Different variance

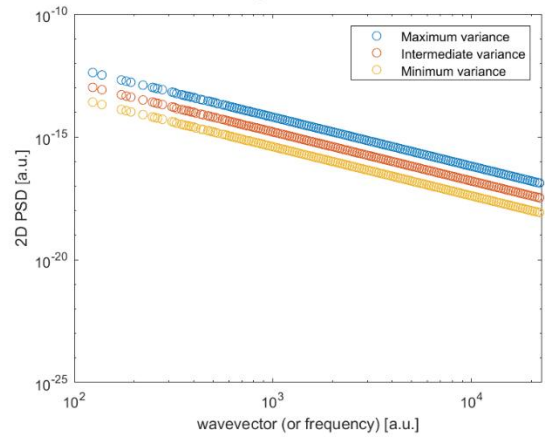
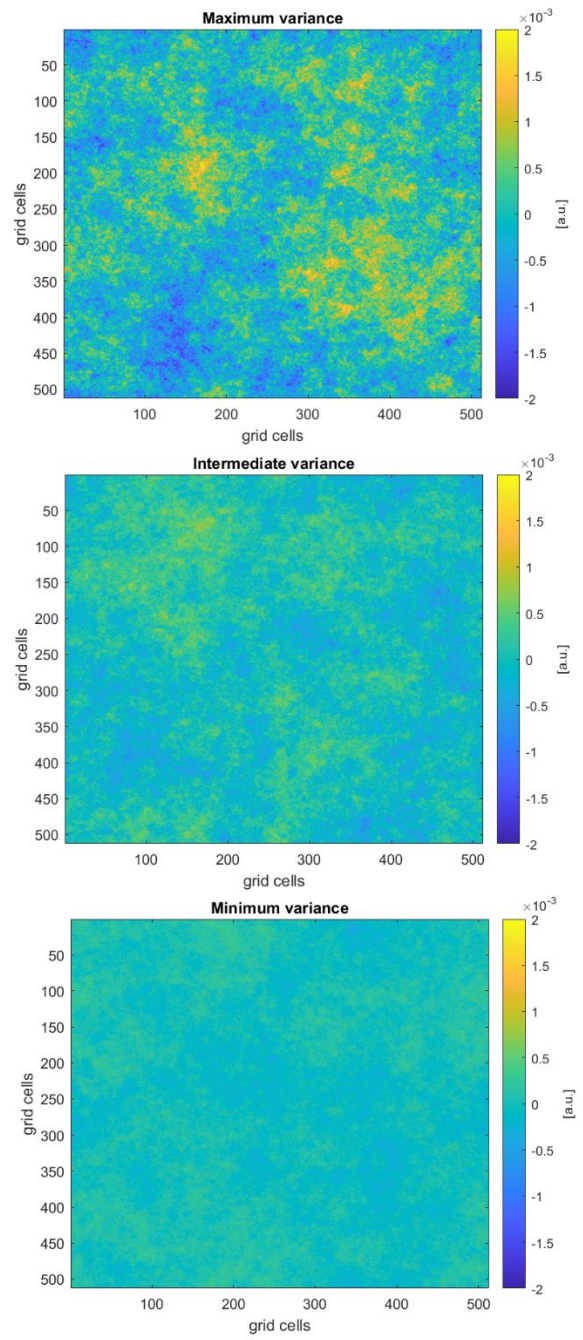


Figure 2.6 Visual representation of three surfaces characterized by different degrees of roughness scaling (i.e., how surface roughness changes as a function of window size) but same variance (left-hand side column) and three surfaces with the same roughness scaling but different variance (right-hand side column) and corresponding radially averaged 2D PSD plots. PSD analyses can effectively differentiate between these surfaces. For instance, the left-hand column illustrates how the PSD effectively captures the reduction in high-frequency surface roughness components when transitioning from 'Roughness 1' to 'Roughness 3'. Conversely, the right-hand side column illustrates how changes in the variance of the height values, while keeping the roughness scaling constant, lead to a shift in the PSD towards lower values. The different surfaces were generated by using an open-source code in MATLAB (Kanafi, 2020). Grid cell width = $2 \cdot 10^{-4}$ a.u.

2.4 Complementary use of semi-variogram and PSD

Both the semi-variogram and PSD are methods aimed at characterizing the spatial distribution of height values. However, they can provide complementary information. In particular, semi-variogram analyses are better suited to identify variations in surfaces with relatively prominent surface features, whereas the PSD is more effective at detecting variations in mid-to-high-frequency components of surface roughness. Figure 2.7 provides a clear illustration of this distinction.

Therefore, the combined application of both semi-variogram and PSD analyses emerges as a valuable approach for capturing the key statistical characteristics of any given surface, thereby serving as a valuable asset for comparing the mineral surface roughness resulting from dissolution under a wide spectrum of different conditions.

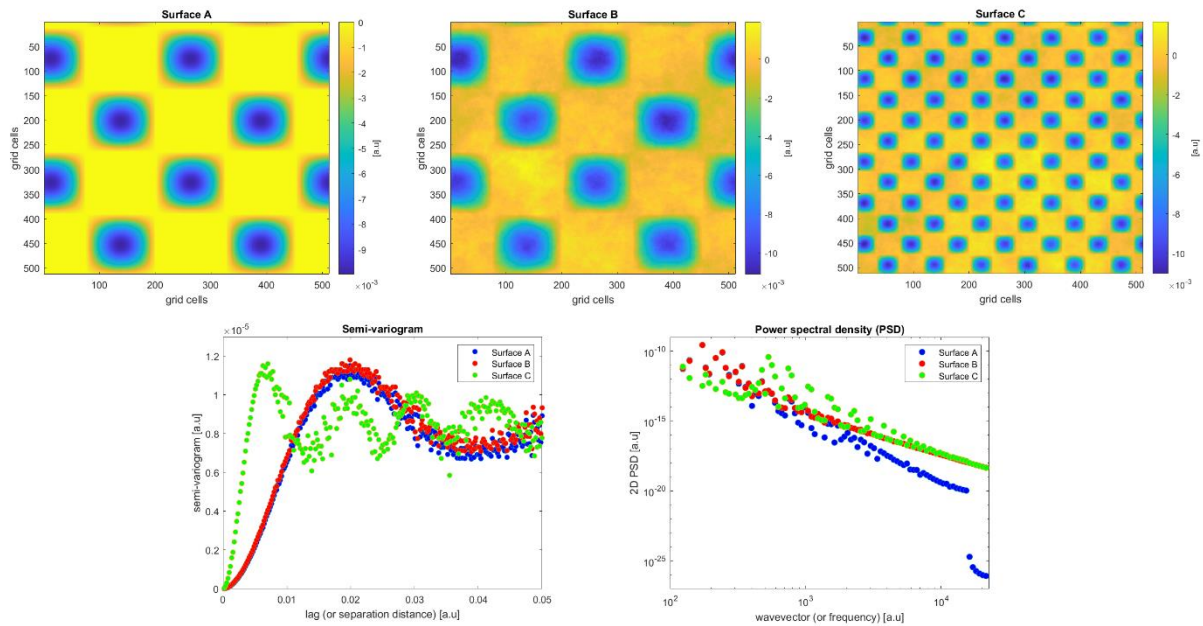


Figure 2.7 Visual representation of three surfaces exhibiting different spatial statistical traits. These surfaces were generated to illustrate the specific traits that are better captured by either the semi-variogram or the PSD. ‘Surface B’ was generated adding to ‘Surface A’ additional surface roughness, which was characterized by the same degree of roughness scaling as ‘Roughness 2’ in Figure 2.6. ‘Surface C’ was generated as ‘Surface B’, but with smaller and more frequent well-defined surface features. Overall, the semi-variogram fails to differentiate between ‘Surface A’ and ‘Surface B’, whereas it effectively differentiates both of them from ‘Surface C’. Conversely, the PSD is poorly effective at distinguishing between ‘Surface B’ and ‘Surface C’, whereas it effectively differentiates both of them from ‘Surface A’, especially in the high-frequency region. Grid cell width = $2 \cdot 10^{-4}$ a.u.

References

- Jacobs, T.D.B., Junge, T., Pastewka, L., 2017. Quantitative characterization of surface topography using spectral analysis. *Surface Topography: Metrology and Properties*, 5(1): 013001.
- Journel, A. G., and Huijbregts, C. (1978), *Mining Geostatistics*, Academic Press, 600 pp
- Kanafi, M.M., 2020. Surface generator: artificial randomly rough surfaces, MATLAB Central Forum (<https://www.mathworks.com/matlabcentral/fileexchange/60817-surfacegenerator--artificial-randomly-rough-surfaces>).
- Loan, C.V., 1992. *Computational frameworks for the fast Fourier transform*. Society for Industrial and Applied Mathematics.
- Whitehouse, D.J., 1994. *Handbook of surface metrology*. CRC Press.

Chapter 3 : Calcite surface roughness resulting from dissolution at close-to-equilibrium conditions

Introduction

The following chapter begins to address the question related to the quantitative detection of fluid imprints that are left on calcite surfaces upon dissolution at different saturation states. In particular, this first study focuses on the evolution of the calcite surface microtopography resulting from close-to-equilibrium dissolution at a given saturation state, $\Omega = 0.6$, as quantified through statistical characterizations of the resulting surface roughness. Flow-through dissolution experiments were conducted at $T = 22\text{ }^{\circ}\text{C}$ and $\text{pH} = 8$, with a mechanically-polished calcite crystal, for a total duration of ~ 8 days. Time-resolved surface topography data of a $\{104\}$ face exposed to dissolution were acquired *ex situ* with VSI at $50\times$ (lateral resolution, $dl = 0.22\text{ }\mu\text{m}$). The resulting surface topography data were analysed employing a statistical characterization that involved a combination of evaluations of the frequency distribution of the height values (variance, skewness, and kurtosis) and corresponding spatial distribution analyses (semi-variogram), calculated over subregions of size $33 \times 33\text{ }\mu\text{m}^2$.

The main experimental results showed that, at $\Omega = 0.6$, a steady-state configuration of the reacting calcite surface was attained after a relaxation time of ~ 2 days, as reflected by the temporal stabilization of the key statistics and semi-variogram of the resulting surface topography. As discussed in the general introduction, the achievement of a steady-state configuration of the surface represents a prerequisite for using surface roughness as a proxy to back-estimate the fluid saturation state. The other key requirement is that the statistical characterizations of the steady-state configurations of the surface obtained after dissolution at different saturation states are sufficiently distinguishable from each other.

To this end, an original empirical model based on stochastic approaches was developed and implemented. The model, which is based on the concept that the areas most exposed to the fluid are prone to preferential dissolution, revealed able to reproduce the space–time evolution of the key statistical descriptors of the surface topography observed experimentally. Furthermore, the empirical model suggested that a steady-state configuration of the surface is also achieved at different Ω values and that the corresponding surface roughness characterizations can be statistically differentiated, hinting at the potential existence of a bijective Ω – roughness relationship.

This chapter consists of a research article that was published in *ACS Earth and Space Chemistry* in 2021 (Stigliano et al., 2021).

Stigliano, L., Siena, M., Ackerer, P., Guadagnini, A., Daval, D., 2021. Statistical description of calcite surface roughness resulting from dissolution at close-to-equilibrium conditions. *ACS Earth Space Chem.* 5 (11), 3115–3129.

Statistical Description of Calcite Surface Roughness Resulting from Dissolution at Close-to-Equilibrium Conditions

Luca Stigliano^{1,2,3,*}, Martina Siena², Philippe Ackerer¹, Alberto Guadagnini², Damien Daval^{1,3}

¹ Université de Strasbourg / CNRS / ENGEES, Institut Terre et Environnement de Strasbourg,
UMR 7063. 1 Rue Blessig, 67084 Strasbourg, France

² Dipartimento di Ingegneria Civile e Ambientale, Politecnico di Milano, Piazza L. Da Vinci
32, 20133 Milano, Italy

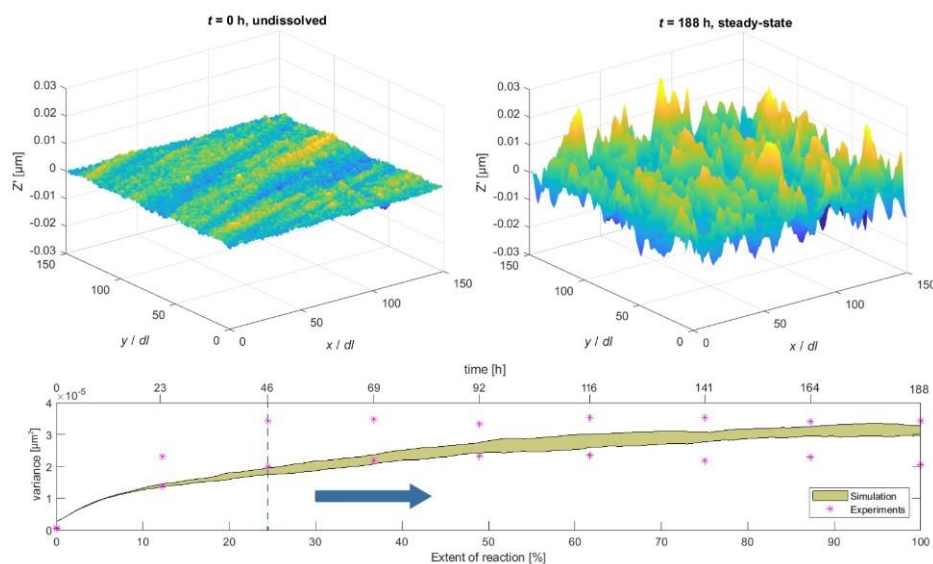
³ Univ. Grenoble Alpes, Univ. Savoie Mont Blanc, CNRS, IRD, IFSTTAR, ISTerre, Grenoble,
France

* Corresponding author: Luca Stigliano

Abstract

Linking the evolution of the surface area (as quantified, e.g., through its spatial roughness) of minerals to their dissolution rate is a key aspect of mineral reactivity. Unraveling the nature of their main features requires relying on approaches yielding a quantitative characterization of the temporal evolution of surface topography/roughness. Here, a mechanically polished {104} calcite surface was dissolved at room temperature and at close-to-equilibrium conditions ($\Omega = 0.6$) with an alkaline solution (pH = 8) across a temporal window of 8 days. Surface topography images were acquired daily using vertical scanning interferometry, the ensuing topography data being then embedded within a statistical analysis framework aimed at describing comprehensively the surface roughness evolution. The strongest system variations were observed after 1 day: the probability density function of surface roughness was observed to transition from being approximately Gaussian to being left-skewed and leptokurtic, exhibiting a dramatic increase in the variance and a significant change in the semi-variogram structure. After a relaxation time of approximately 2 days, the reacting surface appeared to attain a steady-state configuration, being characterized by the values of the statistical moments characterizing surface roughness that become virtually independent of time. Attempting to unravel the underlying dissolution mechanism, an original numerical model able to reproduce satisfactorily the statistical behavior observed experimentally was developed and tested. Our results suggest that under the investigated conditions, dissolution may be characterized as a spatially correlated random process, with the areas most exposed to the flowing fluid being prone to preferential dissolution. The numerical model was also used to obtain insights into the influences of the initial surface roughness and of the fluid composition on the steady-state statistical characterization of the surface roughness. Our results suggest that the influence of the initial surface roughness is limited. The present study suggests that potential empirical relations linking the surface roughness of the reacted crystals to the saturation state at which they dissolved may be developed, which would allow to back-estimate the reacting conditions only based on topography data. Linking the evolution of the surface area (as quantified, e.g., through its spatial roughness) of minerals to their dissolution rate is a key aspect of mineral reactivity. Unraveling the nature of their main features requires relying on approaches yielding a quantitative characterization of the temporal evolution of surface topography/roughness. Here, a mechanically polished {104} calcite surface was dissolved at room temperature and at close-to-equilibrium conditions ($\Omega = 0.6$) with an alkaline solution (pH = 8) across a temporal window of 8 days. Surface topography images were acquired daily using vertical scanning

interferometry, the ensuing topography data being then embedded within a statistical analysis framework aimed at describing comprehensively the surface roughness evolution. The strongest system variations were observed after 1 day: the probability density function of surface roughness was observed to transition from being approximately Gaussian to being left-skewed and leptokurtic, exhibiting a dramatic increase in the variance and a significant change in the semi-variogram structure. After a relaxation time of approximately 2 days, the reacting surface appeared to attain a steady-state configuration, being characterized by the values of the statistical moments characterizing surface roughness that become virtually independent of time. Attempting to unravel the underlying dissolution mechanism, an original numerical model able to reproduce satisfactorily the statistical behavior observed experimentally was developed and tested. Our results suggest that under the investigated conditions, dissolution may be characterized as a spatially correlated random process, with the areas most exposed to the flowing fluid being prone to preferential dissolution. The numerical model was also used to obtain insights into the influences of the initial surface roughness and of the fluid composition on the steady-state statistical characterization of the surface roughness. Our results suggest that the influence of the initial surface roughness is limited. The present study suggests that potential empirical relations linking the surface roughness of the reacted crystals to the saturation state at which they dissolved may be developed, which would allow to back-estimate the reacting conditions only based on topography data.



Keywords : calcite, near-equilibrium dissolution, surface roughness, spatial statistics, dissolution models

3.1 Introduction

Chemical weathering is a central part of the Earth system as it is one of the key processes that contributes to the redistribution of mass on Earth. The dissolution of rockforming minerals controls the formation of soil and supplies nutrients to sustain ecosystems¹, is responsible for atmospheric CO₂ drawdown, regulating the long-term climate of the Earth², and is involved in various geoen지니어ed strategies such as enhanced rock weathering for carbon dioxide removal from the atmosphere³, radioactive waste storage⁴, geothermal energy recovery⁵, or CO₂ sequestration⁶. The development of rate laws describing the dissolution kinetics of minerals is critical as an effective strategy for upscaling of mineral reactivity, with the ultimate goal of modeling fluxes associated with chemical weathering across a variety of space and time scales. The classical hypothesis underlying the rate laws that are employed to interpret mineral reactivity (through modeling frameworks based on either a bottom-up (e.g., ref 7) or a top-down (e.g., ref 8) approach) rests on a conceptual picture according to which the dissolution flux is proportional to the contact surface area between the fluid and the solid.

While such a simplification rests on the assumption that reactivity is immutable in time and homogeneous at the surface of the minerals, the heterogeneous nature of the surface reactivity appears as a universal feature of solid dissolution, as documented through a variety of material degradation studies ranging from the corrosion of metals^{9–11}, glasses¹², and ceramics^{13–16} to the weathering of rocks and minerals (e.g., refs 17–28). At the heart of the heterogeneous nature of surface reactivity is the concept of surface energy and its distribution in space and time throughout the evolution of the dissolution process (e.g., refs 15, 29), which is then mirrored by the gradual development of surface roughness. The heterogeneous distribution of structural defects and the seemingly random occurrence of hydrolysis events at the mineral surface drive the variability of surface reactivity, the latter possibly varying by two orders of magnitude for a single mineral (e.g., refs 15, 29). These observations thus support the need and opportunity for the development of an alternative approach for the assessment of mineral reactivity focused on the heterogeneous space–time dynamics of surface roughness.

As an example, the rate spectra approach²⁰ is based on the evaluation of the probability density function of the dissolution rates at each given location of the mineral surface. From a practical standpoint, spatially resolved dissolution rates at the surface of a given material can be quantified by monitoring the time-resolved evolution of surface topography resulting from dissolution (e.g., refs 15, 20, 22, 27, 29–33). One of the most promising aspects of the rate

spectra approach is that the deconvolution of a rate spectrum provides information about the modes (i.e., the main contributors to the overall rates), which can then be compared against outputs of atomic-scale simulations such as kinetic Monte Carlo modeling, and refines our knowledge of the corresponding reaction mechanisms (e.g., refs 34, 35).

A notable limitation of the rate spectra approach is that determining the distribution of dissolution rates at the mineral surface requires analyzing across time a laterally fixed and motionless surface. Such measurements can only be achieved under well-controlled laboratory conditions using techniques such as in situ atomic force microscopy (AFM) conducted in a fluid reaction cell (e.g., ref 30) or vertical scanning interferometry (VSI) with a reaction cell fixed to the VSI stage (e.g., refs 32, 36 and references therein), so that a given dissolution rate can be assigned to each pixel (or group of pixels) depicting the topography data collected for a given field of view. When considering crystals subject to weathering in the field (e.g., ref 37) or samples with a low reactivity (which makes them incompatible with measurements of the dissolution progress at room temperature over short time periods), obtaining insights into the temporal evolution of the key statistics of the overall roughness of a given surface is of significant interest. As documented by Fischer et al.¹⁹, the investigation of surface roughness evolution could provide information about the reaction history across the dissolution process. As such, time-resolved statistical analyses of dissolving mineral surfaces are of critical importance as they underpin the development of empirical and/or theoretically supported relationships between surface topography and the extent of reaction or between the surface topography and the reaction conditions.

Pollet-Villard et al.³⁸ showed that a statistical treatment of etch pit nucleation and growth monitored by AFM could be used to successfully develop a model accounting for the longterm evolution of the (001) surface of a dissolving K-feldspar at far-from-equilibrium conditions. By tuning the model parameters based on the comparison between the statistics of modeled and measured surface topographies at the early stage of dissolution, these authors could forecast the subsequent retreat rate of the surface as well as evaluate, through a sensitivity analysis, the impact of defect density (i.e., screw dislocation) on K-feldspar dissolution rates. To the best of our knowledge, a detailed analysis combining statistical approaches and process models to characterize the evolution of the surface roughness of a crystal dissolved at close-to-equilibrium conditions, where the nucleation of etch pits is no longer spontaneous, is still lacking. The present study aims at bridging this gap by providing a detailed statistic-based analysis of the topography evolution of a calcite surface dissolved at close-to-equilibrium conditions. In their

preliminary study, Siena et al.³⁹ demonstrated that single snapshots of the spatial distribution of surface topography of calcite under such conditions can be successfully characterized by jointly modeling the probability distribution functions of surface heights and their spatial increments as a generalized sub-Gaussian random field. Since single snapshots of surface roughness are not sufficient to predict or reconstruct reaction rates during dissolution (see, e.g., ref 22), the present study extends their work by providing a time-resolved analysis of the evolution of surface topography. We then assess the ability of three empirical numerical models of dissolution to reproduce the observed behavior of the key statistical descriptors associated with the experimental data. The model that is most successful for reproducing the observed statistical description of the system is then employed to assess the relative impact of initial surface roughness and fluid composition on the statistical evolution of the surface. The outputs of the simulations suggest that a bijective relationship might exist between the saturation state and the steady-state statistics of the surface topography data.

3.2 Materials and Methods

3.2.1 Materials and experimental methods

3.2.1.1 Sample preparation

The fragment used in the present study was obtained from an optically transparent calcite sample originating from the Massif des Écrins (Alps, France). The chemical composition of the sample was determined, as in the study of Bouissonnié et al.²⁵, from 3 g of calcite by loss on ignition and alkaline fusion, and only very few impurities (0.2 wt % MgO, 0.008% MnO, and trace amounts of Sr) were revealed. The calcite sample was cleaved along the natural {104} calcite plane to obtain a $3 \times 5 \text{ mm}^2$ size fragment (Figure 3.1). The crystal was then embedded in epoxy resin to be subjected to multistep abrasive grinding (the finest grit size being $8.4 \mu\text{m}$) to establish an initially flat surface and to remove the effects of sample cutting followed by a polishing sequence (the finest grit size being $0.25 \mu\text{m}$) using an aqueous solution saturated with respect to calcite as a lubricant to avoid etching of the surface. More details are provided in the Supporting Information (Table A1). After polishing, the crystallographic orientation of the sample was determined for the entire surface by electron backscatter diffraction (EBSD) using a TESCAN VEGA II scanning electron microscope (SEM). The sample was analyzed as it was (i.e., without carbon coating), and no grain boundaries were observed. The resin was then removed using a precision saw, and the crystal surface was cleaned with ethanol. Finally, a small portion ($\sim 1\text{--}2 \text{ mm}^2$) of the surface of the crystal was masked with RTV glue spots (Figure

1) to provide a nonreacting reference surface to enable one to measure the height difference (i.e., surface retreat) between the reference and the unmasked portions using VSI (see Section 3.3.1). The average roughness (R_a) for a given observation window is defined as:

$$R_a = \frac{1}{N} \sum_{i=1}^N |Z_i(\mathbf{x}) - \langle Z \rangle| \quad (3.1)$$

where $Z(\mathbf{x})$ corresponds to the height (evaluated with respect to a given reference) of the cell whose centroid is associated with vector position \mathbf{x} , $\langle Z \rangle$ is the average height (evaluated with respect to the same reference), and N is the total number of the sampled height data. Based on the VSI data ($50\times$ magnification) collected over $100 \times 100 \mu\text{m}^2$ areas and following a second-order degree surface detrending, which was required to minimize biases stemming from the tilt caused by the VSI acquisition and from the waviness of the sample resulting from polishing (see Section 3.2.1.5), values of R_a were found to range between 1.0 and 1.3 nm.

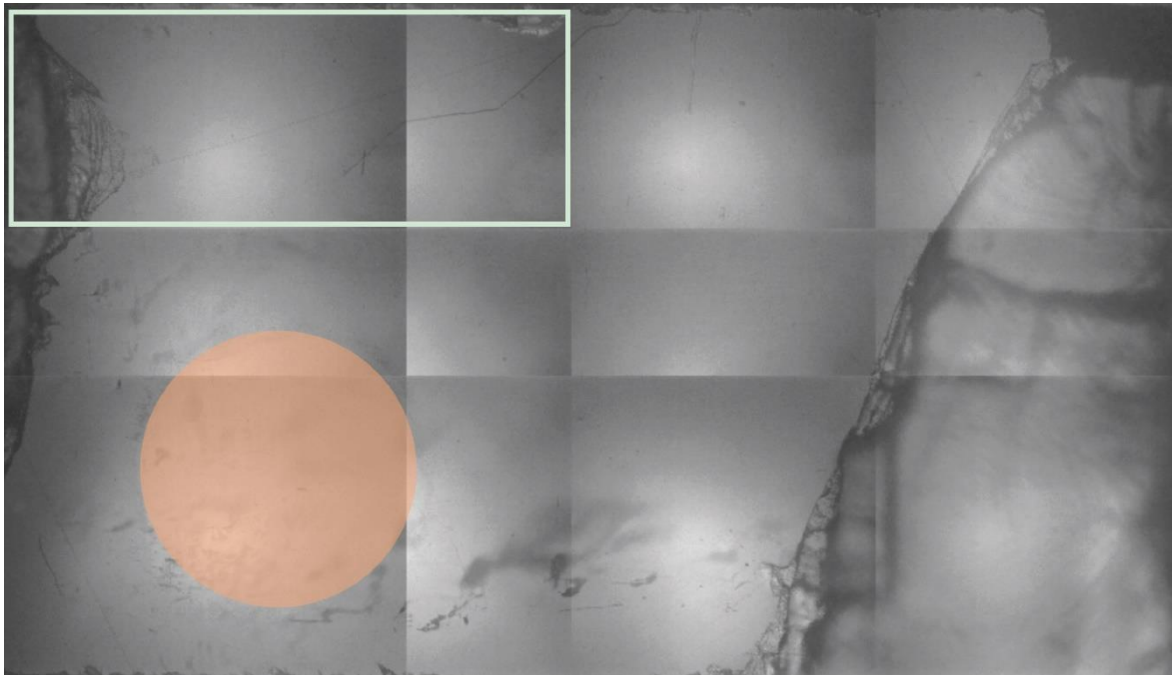


Figure 3.1 Intensity map of the polished $3 \times 5 \text{ mm}^2$ size fragment employed in the experiment as imaged by VSI at $5\times$ magnification (corresponding to the lateral resolution $dl = 2.2 \mu\text{m}$) after 188 h of dissolution. The orange area indicates where the mask was placed during the experiment before its removal. The highlighted rectangle corresponds to the region where VSI data were acquired also at $50\times$ magnification (corresponding to the lateral resolution $dl = 0.22 \mu\text{m}$; see also Figure 3.2).

3.2.1.2 Aqueous Solution Preparation

Reagent-grade NaCl, NaHCO₃, and CaCl₂ were added to ultrapure water (18 MΩ·cm) equilibrated with atmospheric CO₂ at concentrations similar to those documented in previous studies (refs 40, 25) to provide a baseline for the analysis of rate data. The concentration of NaCl was set to 5.85 g/L to yield an ionic strength of approximately 0.1 molal and that of NaHCO₃ was set to 0.095 g/L to fix the alkalinity. The measured pH of the resulting solution was 8.0 ± 0.1. The concentration of CaCl₂ was adjusted to maintain a constant saturation index of the solution with respect to calcite (Ω_{calcite}), which is defined as:

$$\Omega_{\text{calcite}} = \frac{a_{\text{Ca}^{2+}} a_{\text{CO}_3^{2-}}}{K_{\text{sp, calcite}}} \quad (3.2)$$

where $a_{\text{Ca}^{2+}}$ and $a_{\text{CO}_3^{2-}}$ are calcium and carbonate ion activities, respectively, and $K_{\text{sp, calcite}}$ is the solubility product of calcite. Since the nucleation of etch pits on the {104} calcite faces is no longer spontaneous for $\Omega > 0.45^{25}$, the experiment was conducted at a saturation index of 0.60 ($[\text{Ca}^{2+}] = 0.00135$ molal).

3.2.1.3 Experimental Approach

The experimental setup was analogous to the one used in the study by Bouissonni et al.²⁵. In brief, the experiment was conducted in a mixed-flow reactor setup at room temperature ($T = 22 \pm 1$ °C). A calcite fragment of size ~ 10 mm³ (which is small in comparison with the volume of the fluid in the reactor, i.e., ~ 100 mL) was used to maintain a negligible concentration of Ca released throughout calcite dissolution compared to the background concentration in the inlet solution, thus maintaining a nearly constant saturation index across the reaction progress. The experiment was conducted at a constant flow rate (0.25 mL/min) for a total duration of 188 h (~ 8 days). The peristaltic pump was periodically stopped (every ~ 23 h) to recover the calcite fragment, clean it with ethanol, and analyze the evolution of surface roughness as a function of time by VSI. After each analysis, the sample was placed back into the reactor and the pump was restarted for additional 23 h cycles until the experiment was ultimately stopped. The aqueous solution was also regularly sampled (once a day) to evaluate the pH and the Ca concentration, the latter being measured with an inductively coupled plasma–atomic emission spectroscope (ICP-AES, Thermo iCAP 6000 Series). Based on these fluid analyses, the saturation index was evaluated to be 0.58 ± 0.01 over the duration of the experiment. Details on ICP-AES analyses are given in the Supporting Information (Table A2).

3.2.1.4 VSI analyses

As emphasized by Fischer et al.¹⁹, a robust statistical analysis of surface roughness requires relying on an experimental method that yields a sufficiently high vertical resolution (similar to that provided by AFM) together with a large field of view (e.g., comparable to that provided by light optical microscopy). The technical specifications of VSI, for which the vertical resolution can range between 0.5 and 2 nm and fields of view can be as large as several tens of mm² in stitching mode, are fully compatible with this goal. Measurements of the surface topography, $Z(x, y)$, (x, y) being the spatial coordinates in the horizontal plane, were collected using a Zygo NewView 7300 VSI. As roughness is a scale-dependent quantity¹⁹, all data were acquired and processed at a fixed magnification (50 \times) over a collection of nine regions (see Figure 3.2), each associated with the same planar area and with lateral resolution $dl = 0.22 \mu\text{m}$. In addition, topography measurements acquired at 5 \times across the whole crystal surface were used to evaluate the overall dissolution rate of calcite over the duration of the experiment according to (see, e.g., ref 41):

$$r = \frac{\Delta h}{\Delta t V_m} \quad (3.3)$$

where r (mol/m²/s) is the overall dissolution rate, Δh (m) is the spatially averaged height difference (i.e., surface retreat) between the unreacted reference surface and the reacted mineral surface, Δt (s) is the time interval over which the height difference is evaluated, and V_m (m³/mol) is the molar volume of calcite.

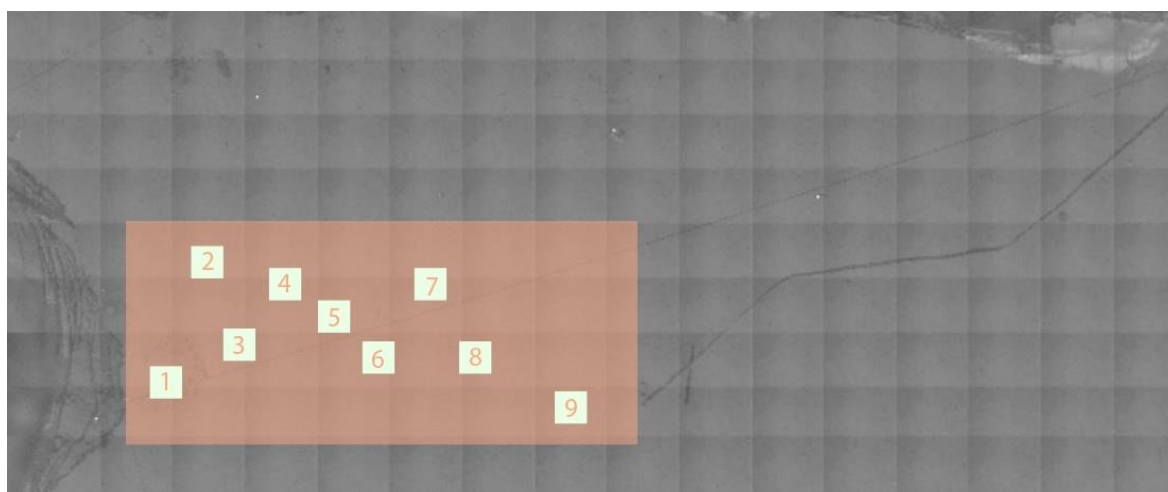


Figure 3.2 Intensity map of the portion of the crystal surface imaged at 50 \times magnification (depicted in Figure 3.1). The 710 \times 325 μm^2 area delineated in the figure (orange color box) represents the region identified as most suitable for the study and contains the 9 square sub-

regions ($33 \times 33 \mu\text{m}^2$) investigated across time during dissolution. The initial average surface roughness was evaluated (at $50\times$ magnification) to range between 0.6 and 0.8 nm across the 9 sampling windows.

3.2.1.5 Topography Data Processing

The analysis of topography data is focused on the $710 \times 325 \mu\text{m}^2$ area delineated in Figure 3.2. This region has been identified as the most suitable for this study as it has the lowest density of surface defects (such as macrosteps or cracks), which may lead to optical artifacts that would strongly affect the statistical analyses. Thus, the only features characterizing the initial surface in the selected region were polishing scratches. Nine subregions of size $33 \times 33 \mu\text{m}^2$ have been selected to provide a representative statistical description of the roughness of this area while attempting to avoid most of the VSI-related artifacts (e.g., artificial spikes arising as a result of a sharp (subvertical) height transition between two adjacent locations), which would lead to an overestimation of the average surface roughness parameter Ra^{42} . As such, for all the nine sampled regions, and at all available times, the total amount of “dead pixels” (i.e., pixels for which the VSI was not able to acquire a height value) and VSI-related artifacts was negligible ($<0.1\%$) compared to the total number of data. Each of these “dead pixels” and VSI-related artifacts was replaced by the arithmetic mean of the height values of the eight neighboring pixels. If one (or more) neighboring pixel was either a “dead pixel” or a VSI-related artifact, then these were excluded from the calculation of the mean value. The following two criteria have been considered for the selection of the sample window size: (i) convergence of the average surface roughness parameter Ra^{19} , which was observed to remain approximately constant within windows ranging from 25×25 to $35 \times 35 \mu\text{m}^2$ and (ii) the presence of a sufficient number of data for a statistical analysis.

We note that the raw topography data in the sampled regions could not be analyzed as acquired. Identification of the actual surface roughness required separating the effects of (i) the waviness generated by the polishing process and (ii) the tilt of the sample support applied during the acquisition phase to adjust the alignment between the sample surface and the VSI microscope objective. For this purpose, the topography data of each sample window at each observation time have been detrended by removing the best-fitting second-order degree surface from all data points (Figure 3.3). Otherwise, polishing scratches have been considered as part of the initial surface roughness (and hence were not removed with data processing) to be able to observe their influence on the surface roughness evolution.

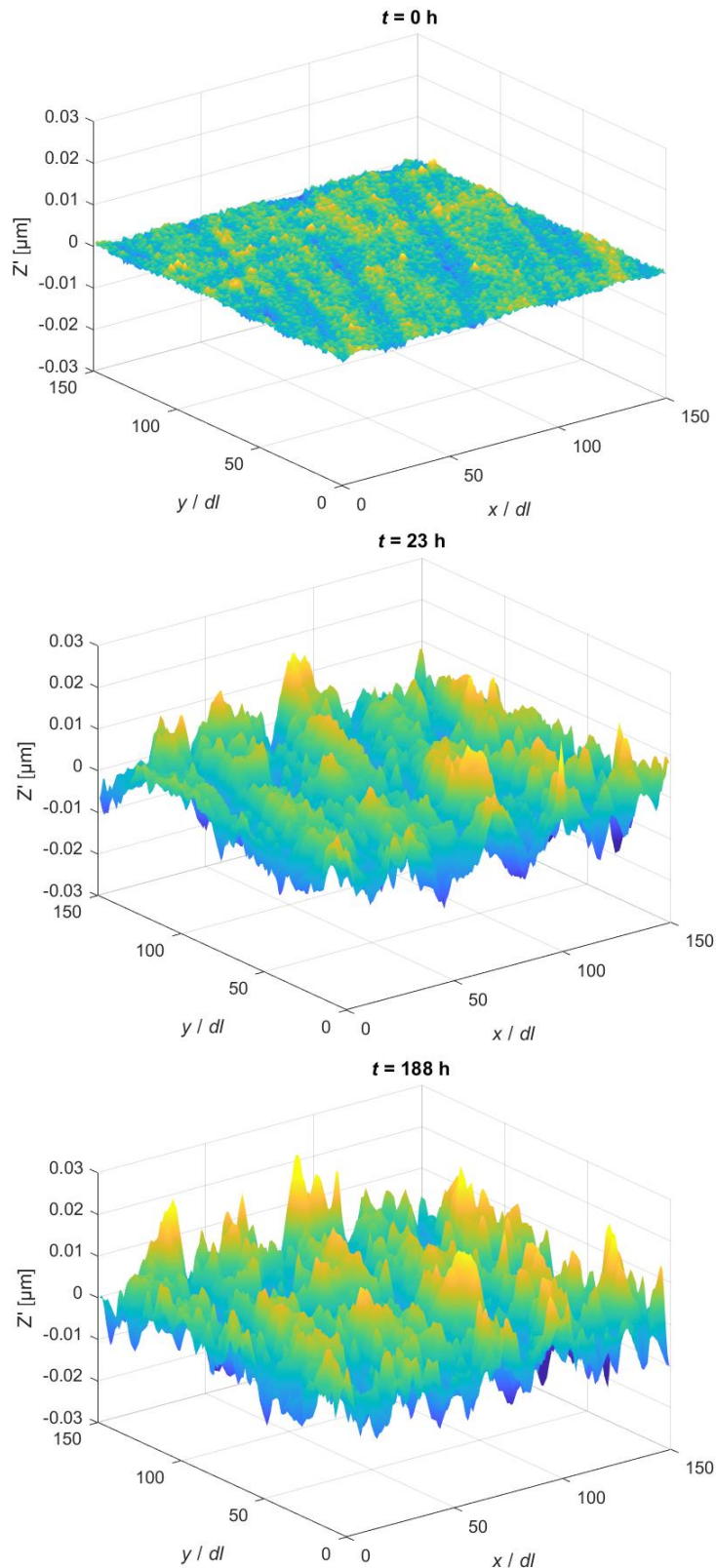


Figure 3.3 Exemplary three-dimensional (3D) representation of the mean-removed topography data, Z' , (see Section 3.2.2) associated with a selected sample window, after replacement of ‘dead pixels’ and VSI-related artifacts (see Section 3.2.1.5), and second order degree de-trending at observation times $t = 0, 23$, and 188 hours.

3.2.2 Statistical Approaches

A statistical characterization confined to the univariate analysis of the frequency distribution of heights shadows the information associated with the degree of spatial correlation of the data. We rely on statistical tools to characterize the degree of spatial correlation of surface topography by (i) interpreting the investigated random field, $Z(x)$, as the sum of an ensemble mean, $\langle Z \rangle$, and a zero-mean fluctuation, $Z'(x)$ and (ii) evaluating the key statistical features of both $Z'(x)$ and spatial increments, $\Delta Z(h) = Z(x) - Z(x + h)$, h being the separation distance (or lag).

We characterize the temporal evolution of the sample probability density functions of Z' (Figure 3.4) through the time-resolved analysis of the corresponding sample variance, skewness (eq 3.4), and kurtosis (eq 3.5). We quantify the temporal variation of the degree of spatial correlation of the roughness field through the analysis of the experimental semi-variogram (eq 3.6).

We recall that the skewness and the kurtosis of a probability density function are defined as:

$$\text{skew} = \frac{\sum_i^M (Z_i - \langle Z \rangle)^3}{(M-1) s^3} \quad (3.4)$$

$$\text{kurt} = \frac{\sum_i^M (Z_i - \langle Z \rangle)^4}{(M-1) s^4} \quad (3.5)$$

where z_i is the i th observed value of Z , $\langle Z \rangle$ is the ensemble average, M is the number of available observations of Z , and s is the standard deviation of Z . We recall that skewness is a measure of the degree of asymmetry of a probability distribution, whereas kurtosis gives the combined weight of the tails relative to the rest of the distribution. We recall that a Gaussian distribution is characterized by skewness and kurtosis equal to 0 and 3, respectively. A negative skewness indicates a left-skewed distribution; a kurtosis lower or higher than 3 denotes a distribution with tails that are respectively thinner or heavier than Gaussian.

The experimental semi-variogram is defined as half of the sample variance of the spatial increments, that is,

$$\gamma(h) = \frac{1}{2 n(h)} \sum_{i=1}^{n(h)} [Z(x_i) - Z(x_i + h)]^2 \quad (3.6)$$

where $n(h)$ is the number of data pairs separated by a given omnidirectional lag $h = |h|$. As stated above, it is a measure of the spatial dependency of Z .

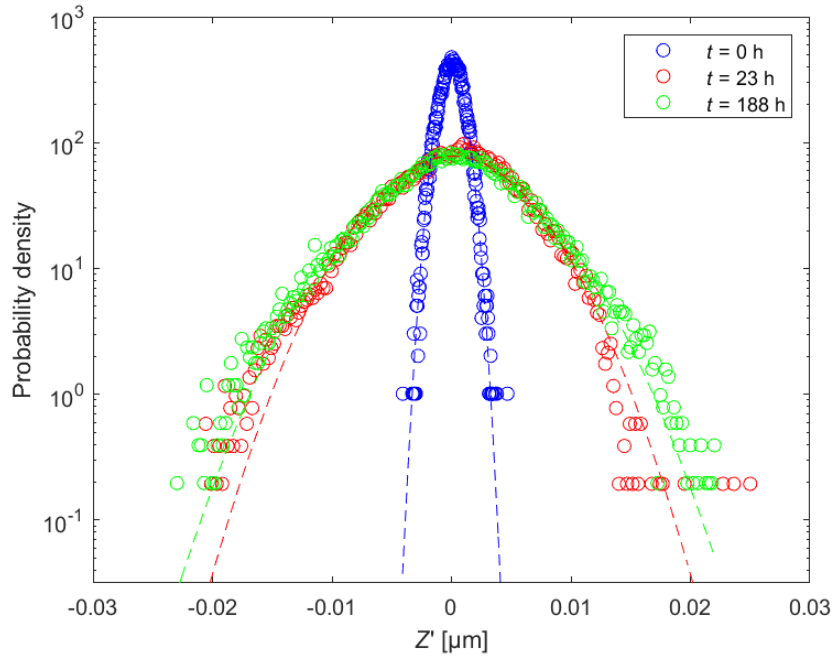


Figure 3.4 Comparison of the sample distributions probability densities of the variable Z' at observation times $t = 0, 23,$ and 188 hours (open circles) with Gaussian distributions densities (dashed lines) characterized by the same mean and standard deviation of Z' . The distribution of Z' appears to be symmetric at $t = 0$ hours and slightly asymmetric (left-skewed) at longer times.

3.2.3 Numerical Modeling

3.2.3.1 Numerical Approach

In addition to providing a statistical description of the evolution of the surface roughness resulting from dissolution, we also aim at comparing such depiction to results associated with three dissolution models, as described in the following. The objective of the development of these models is twofold: (i) demonstrating that a statistical characterization of surface roughness evolution may help to rule out some of the existing models describing the mechanisms of mineral dissolution and (ii) providing a qualitative assessment of the impact of input parameters such as initial surface topography and fluid composition on the calculated statistical descriptors. Each of the three dissolution models we analyze is characterized by a given mathematical rendering of dissolution processes, which are viewed in a probabilistic context. The parameters of each of these models (see Section 3.2.3.2) were adjusted to assess whether spatial statistics based on modeling results was compatible with the corresponding statistics based on the experimentally observed temporal evolution of calcite roughness. The models considered differ in the way one assigns the probability that dissolution takes place at a given location on the

simulated surface, as described in the following (additional details are provided in Section 3.2.3.2):

(i) Uniform and spatially independent dissolution probability (hereafter termed *Model 1*): the occurrence of dissolution at each location of the simulated crystal surface and at each time is associated with a given probability, the latter being uniformly distributed across the system, independent of the location. Initiation of dissolution at a given location is therefore unpredictable and independent of the neighborhood. Such a conceptual framework is typically common for pitting corrosion models^{9,10}.

(ii) Equiprobable dissolution with the presence of volume defects dissolving preferentially (hereafter termed *Model 2*). At close-to-equilibrium conditions, the strain field of a dislocation does not open up hollow cores to form etch pits (e.g., ref 43) and dissolution is driven by point defects, pre-existing edges, and corners³⁶. As such, whereas the dissolution taking place at defect-free zones is considered to be equally likely, locations termed as “defects” are associated with a higher probability to dissolve, this being intended to simulate such highly localized point defects.

(iii) Dissolution probability of individual locations in the (x, y) plane controlled by fluid accessibility (hereafter termed *Model 3*). The model is based on a conceptual picture according to which dissolution is locally proportional to the contact surface between the crystal and the fluid,⁴⁴ thus rendering the sites that are more accessible to the fluid more likely to be dissolved.

3.2.3.2 Details of the Numerical Models

For all models, the simulated crystal can be interpreted as a 3D collection of voxels, each with the lateral length equal to the VSI lateral resolution ($dl = 0.22 \mu\text{m}$) and their vertical size being assigned a value of $dv = 2 \text{ nm}$, consistent with the VSI vertical resolution range (0.5–2 nm; note that we selected the largest value to reduce the computational time).

To ensure that the outputs of the numerical simulations were representative of the experimental scenarios, several settings were considered for all models: (i) the size of the simulation window was taken equal to the size of a single experimental sample window (150×150 in terms of pixels, corresponding to a crystal surface area of $33 \times 33 \mu\text{m}^2$); (ii) model evaluations were stopped when the simulated surface retreat, averaged over the whole surface, was equal to its experimental counterpart at the end of the experiment (at $5\times$ magnification); and (iii) the initial topography employed in the simulations coincided with one of the experimental sample windows at $t = 0 \text{ h}$ (as the sample windows were characterized by similar initial average surface

roughness R_a , as described in Section 3.2.1.5). Finally, the outputs of the simulations were compared with the experimental data in terms of the statistics of Z' and of the associated semi-variogram function to identify the numerical model, which was most compatible with the statistical results stemming from the experimental observations.

The simulation of the dissolution process at a given time is based on the generation of a random number sampled from a uniform distribution at each (x, y) location of the simulated solid matrix. Such a number was then compared to the probability value assigned to the corresponding voxel: if the generated number was lower than the corresponding probability, the voxel was released from the crystal volume; otherwise, it remained in place.

Model 1 involved the presence of five types of surface voxels assigned at the beginning of the simulation, each one associated with a given probability of dissolution, being randomly distributed over the entire simulated crystal volume (i.e., the frequency of each voxel type was 20% and they were distributed without any spatial dependency; see Figure 3.5a).

Model 2 was initiated upon assigning to the whole crystal volume the same probability of dissolution (P_{\min}). Then, a given number of voxel defects (characterized by a given probability $P_{\max} > P_{\min}$) were randomly and uniformly distributed over the whole crystal volume. Each of these defects was associated with a degree of spatial influence, that is, all neighboring voxels up to a given distance (L , which is intended as an adjustable model parameter) were characterized by a probability of dissolution ($P_{\min} < P < P_{\max}$, P decreasing linearly with distance from the voxel defect until the nondisturbed region was reached; see Figure 3.5b for an example of a voxel defect).

Model 3 was characterized by two parameters (here denoted as P_1 and P_1^*) and is based on the concept that the voxels having the largest number of faces exposed to the fluid are the most reactive ones. All voxels having only their top faces exposed to the fluid are characterized by a probability of dissolution P_1^* . All voxels having also one or more lateral faces exposed to the fluid are characterized by a higher probability of being associated with dissolution: the higher the number of faces exposed to the fluid, the higher the probability that dissolution takes place at that voxel. The model parameter P_1 corresponds to the probability of dissolution of a single voxel given by a single lateral face exposed to the fluid. Hence, the probability of dissolution linked to a voxel having j lateral faces in contact with the fluid is $P_1 \times j$. This model also includes the possibility that various voxels which are superimposed (henceforth termed voxel spines, see Figure 3.5c) dissolve simultaneously. Consistently, the larger the voxel spine lateral area in

contact with the fluid, the higher the probability that one or more voxels are dissolved: for a given voxel within a voxel spine, the probability that the voxel considered is dissolved along with all the upper voxels is $\sum_{j=1}^4 j \times n_j + P_1^*$, where n_j is the number of lower voxels (the one considered being included) having j faces exposed to the fluid and P_1^* is nonzero only when considering the top voxel (see Figure 3.5c for a schematic example).

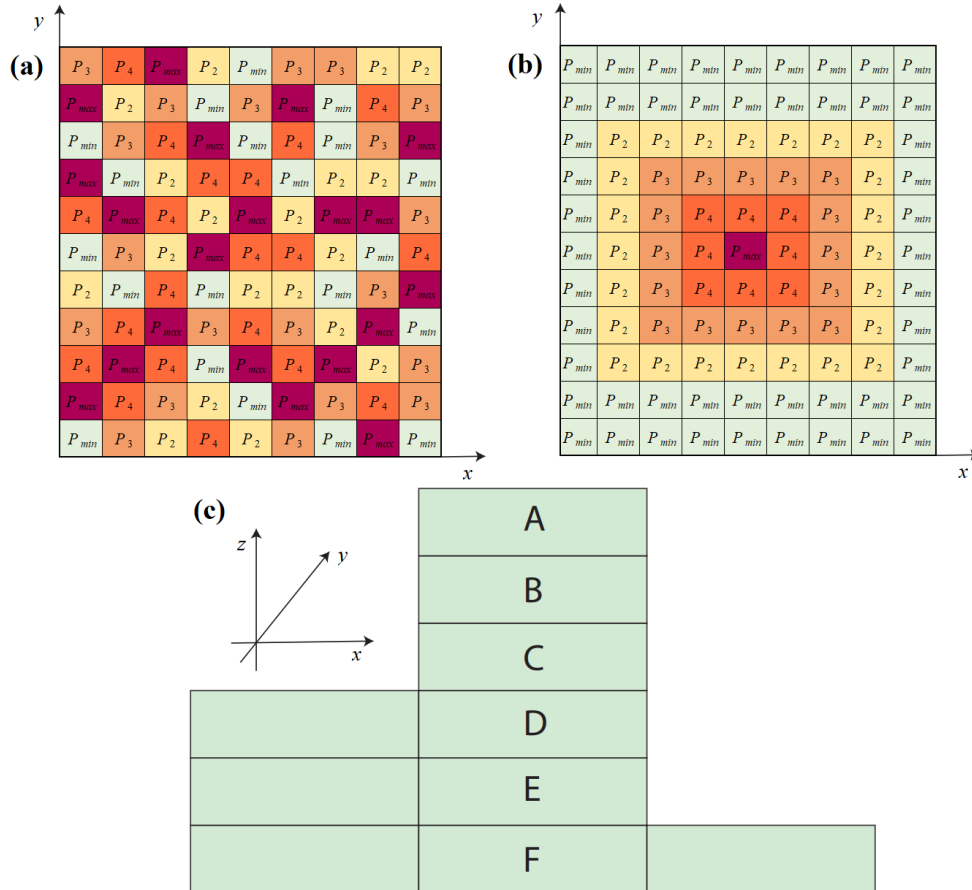


Figure 3.5 (a-b) Conceptual representation of the main features of *Model 1* (a) and *Model 2* (b) in a horizontal section. In these examples, values of dissolution probabilities are represented as $P_{\min} < P_2 < P_3 < P_4 < P_{\max}$. (c) Schematic representation of a voxel spine in a vertical section. As an example, the probability $P_{A+B+C+D+E+F}$ that voxels *A*, *B*, *C*, *D*, *E*, and *F* are all subject to dissolution (and hence are released from the solid matrix) at the same time is zero, as it is given by the probability P_F of voxel *F* (with no lateral faces exposed to the fluid) to be released, which is null (note that the configuration of the voxel layers along the *y*-axis is the same as the one here depicted). Following a similar reasoning: $P_{A+B+C+D+E} = P_{A+B+C+D+E+F} + P_E = 0 + P_1 \times 1$; $P_{A+B+C+D} = P_{A+B+C+D+E} + P_D = P_1 \times 1 + P_1 \times 1$; $P_{A+B+C} = P_{A+B+C+D} + P_C = P_1 \times 2 + P_1 \times 2$; $P_{A+B} = P_{A+B+C} + P_B = P_1 \times 4 + P_1 \times 2$; $P_A = P_1 \times 6 + P_1 \times 2 + P_1^*$.

3.3 Results

3.3.1 Calcite Dissolution Rate

The average surface retreat (Δh) measured after 188 h of dissolution at $\Omega = 0.60$ was determined to be $(0.20 \pm 0.01) \mu\text{m}$ (mean value \pm standard deviation), which resulted in an estimate of the {104} overall dissolution rate equal to $(8.0 \pm 0.4) \times 10^{-9} \text{ mol m}^{-2} \text{ s}^{-1}$. We note that this value is in good agreement with the close-to-equilibrium values documented in previous studies (refs 40, 25) using similar experimental and analytical protocols (these values range from $1.8 \times 10^{-8} \text{ mol m}^{-2} \text{ s}^{-1}$ at $\Omega = 0.45$ to $5.6 \times 10^{-9} \text{ mol m}^{-2} \text{ s}^{-1}$ at $\Omega = 0.80$). This gives us the confidence that the desired close-to-equilibrium thermodynamic conditions were attained in our experimental setting.

3.3.2 Statistical Analyses

3.3.2.1 Time-Resolved Statistical Analysis of Surface Roughness

The key results of the timeresolved statistical analysis of the mean-removed surface topography (Z') are shown in Figure 3.6, which depicts the temporal dependence of variance (Figure 3.6a), skewness (Figure 3.6b), and kurtosis (Figure 3.6c) of Z' , as obtained upon averaging the corresponding quantities evaluated for each of the nine samples analyzed. Intervals of width equal to ± 1 standard deviation are also shown to provide an appraisal of the variability of such statistical moments among the samples. These plots reveal that temporal variations of the main statistics of the surface topography take place mostly at early times (reaction times shorter than 46 h). All of the investigated statistical moments are seen to exhibit a plateau after such a relaxation time. Figure 3.6a clearly shows a steep increase of the variance for time $t < 46$ h until an asymptotic value of $(2.85 \pm 0.6) \times 10^{-5} \mu\text{m}^2$ is attained. The sharp variation observed at the very beginning of the experiment is possibly related to the initial condition rendered by the polishing process, which might have locally weakened the surface. Polishing-resulting scratches are likely to induce the formation of surface defects, which are in turn prone to preferential dissolution (see, e.g., refs 29, 32). Attainment of constant values of these statistical moments suggests that the rate at which the surface topography dissolves tends to become spatially constant as time progresses. Analyses of the third and fourth moments (i.e., skewness and kurtosis) of Z' reveal that the initial surface configuration is characterized by an approximately Gaussian probability density function, whereas the surface configuration at late times emerges as left-skewed (skew < 0) and leptokurtic (kurt > 3). Figure 3.6b shows a transition from a Gaussian pattern (skew ≈ 0) to an asymptotic negative value (skew ≈ -0.2), displaying a minimum value at early times ($t \approx 23$ h). Similarly, Figure 3.6c illustrates a

deviation from values typical of a Gaussian distribution at $t = 0$ h to a leptokurtic behavior at later times. This implies that dissolution leads to the formation of more pronounced peaks and valleys as the reactions starts, the valleys being predominant. This behavior may also provide a quantitative criterion to distinguish, at steady-state, between reacted and unreacted (mechanically polished) calcite surfaces based only on surface topography measurements. Consistent with the observation of Siena et al.³⁹, (mechanically polished) dissolved calcite surfaces are characterized, at late times, by left-skewed topography distributions. As such, while the probability distribution of the surface roughness across the mechanically polished unreacted surface is symmetric, reaction is seen to be associated with a larger frequency of low rather than high height values, implying that dissolution was very active in the majority of the area. As long as initial symmetric unreacted surfaces are concerned, the asymmetry of Z' distributions can then be considered a distinctive feature of dissolution, being also consistent with the right-skewed rate spectra observed in several studies related to a variety of minerals altered through various dissolution regimes (e.g., ref 20, 30). Furthermore, the decrease in skewness and the increase in kurtosis as the reaction starts may provide some insights into surface reactivity. Correspondingly, (i) a skewness value that decreases from 0 at $t = 0$ h to a negative value at $t = 23$ h might be the result of a nonuniform distribution of dissolution rates and (ii) a kurtosis value that increases from 3 at $t = 0$ h to a larger value at $t = 23$ h might be related to dissolution rates that are, respectively, extremely lower and extremely higher with respect to the average dissolution rate.

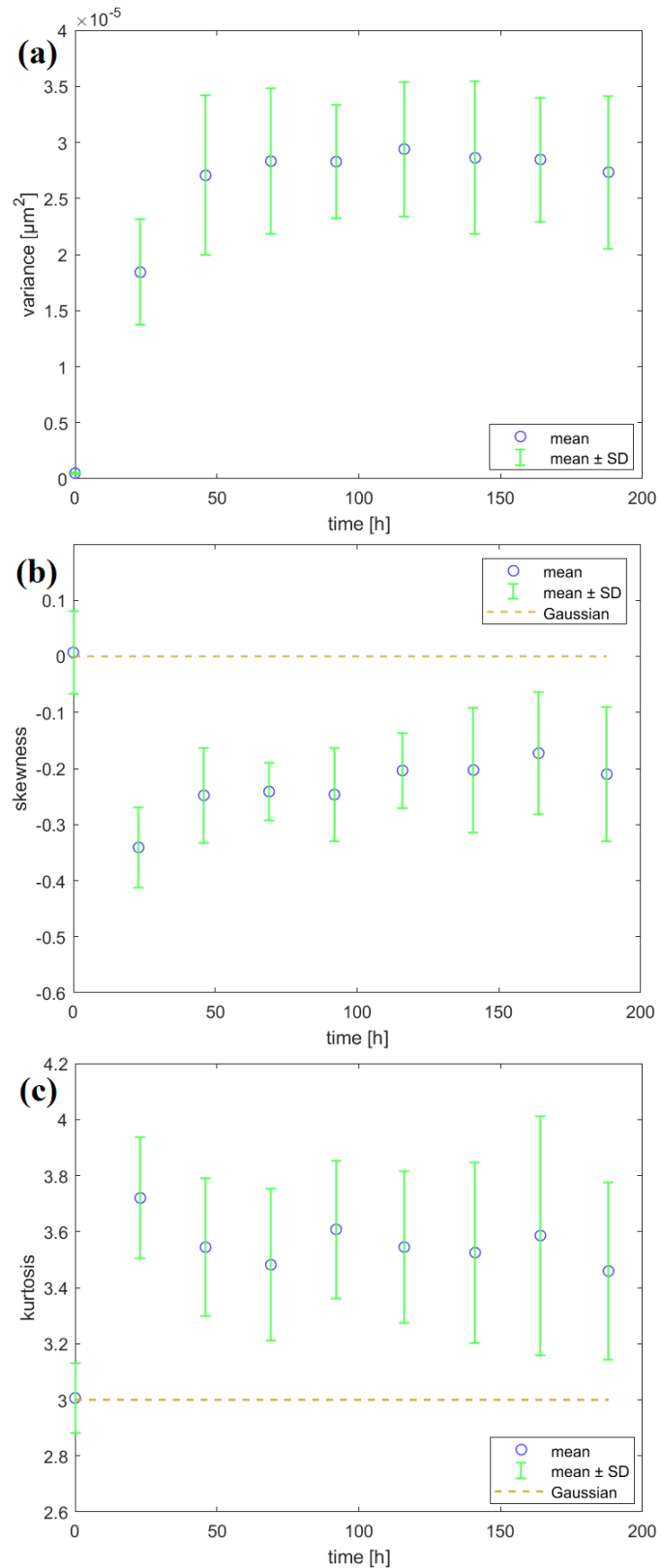


Figure 3.6 Temporal evolution of the key higher-order statistics of Z' , i.e., variance (a), skewness (b) and kurtosis (c). The figure depicts mean values (circles) evaluated across the 9 sample windows identified in Figure 3.2 and intervals of width corresponding to \pm one standard deviation (SD).

3.3.2.2 Time-Resolved Semi-Variogram Analyses

Figure 3.7 shows the sample omnidirectional semi-variograms of surface roughness evaluated as a function of time across a selected observation window, the results associated with the remaining windows being qualitatively similar.

Consistent with the results of Section 3.3.2.1, the most pronounced variations take place at early times. Three regimes can be identified. The first regime (corresponding to $0 \text{ h} \leq t \leq 23 \text{ h}$) is characterized by a strong increase of the experimental semi-variogram sill with time, consistent with the sample variance rise (Figures 3.6a and 3.7a). The semi-variogram at $t = 0 \text{ h}$ exhibits higher values at short lags and a more persistent spatial correlation than its counterpart at $t = 23 \text{ h}$ (Figure 3.7b). This feature, combined with the (previously discussed) observation that the distributions of Z' are left-skewed, may be employed to quantitatively distinguish between reacted and unreacted surfaces. Semi-variograms evaluated at $23 \text{ h} < t \leq 69 \text{ h}$ are characterized by a mild temporal increase of their sill (see also Figure 3.6a) and a virtually constant level of spatial correlation across time (Figure 3.7c). Our results show that differences between semi-variograms evaluated at subsequent times tend to diminish as time increases (see also Figure 3.7d), consistent with the observation that the system tends to attain a certain degree of steady state, in terms of the statistical characterization of surface roughness.

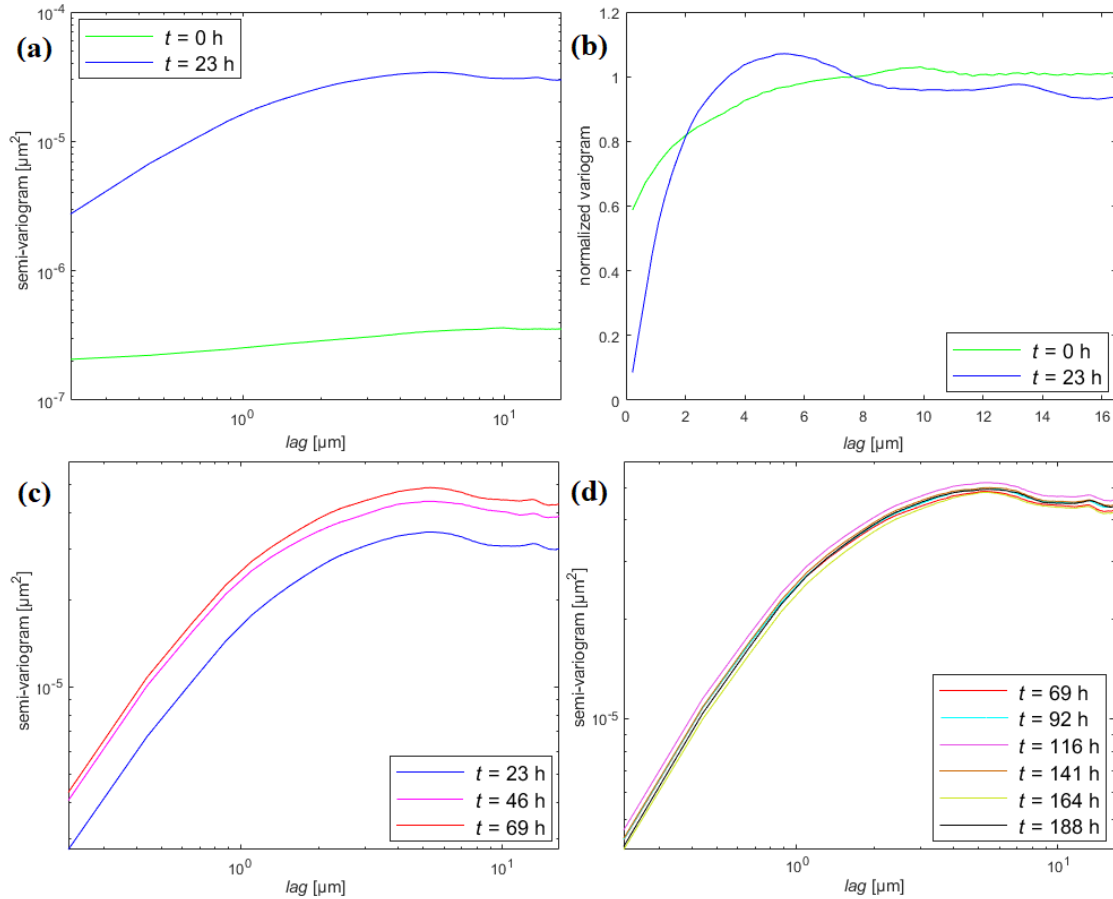


Figure 3.7 Evolution of experimental semi-variogram in time for a selected sample window (data associated with the remaining windows exhibit a qualitatively similar behavior). (a) Experimental semi-variogram (log-log scale) at observation time $t = 0$ h and 23 h; (b) Normal scored transformed variogram (i.e., semi-variogram normalized to the sample variance) at 0 and 23 hours. The main advantage of this visualization is that it makes it possible to compare the structure of semi-variograms characterized by strongly different sample variances; (c) Experimental semi-variograms for $23 \text{ h} \leq t \leq 69 \text{ h}$; (d) Experimental semi-variograms for $69 \text{ h} \leq t \leq 188 \text{ h}$.

3.3.2.3 Numerical Model Selection

As discussed in Section 3.2.3.1, model parameters are tuned until the best possible agreement with the statistics of the experimental data is attained. The least stringent condition to be met to this end was the constraint on the observed average surface retreat.

Optimal parameter values correspond to minimization of the mean square error (MSE) between (i) the average variance values depicted in Figure 3.6a and their model-based counterparts and (ii) the late-time model-based semi-variogram and the corresponding averaged experimental

semi-variogram. We recall that for a stationary random field, as $Z'(x)$ is, the semivariogram sill corresponds to the variance.

Model-based results correspond to averages across a collection of 100 simulation runs for each set of parameters tested. Figure 3.8a shows the behavior of the variance of surface roughness associated with (i) the experimental observations (obtained upon averaging the results associated with all of the spatial subregions investigated) and (ii) their model-based counterparts corresponding to the optimal parameter value sets versus the extent of reaction (i.e., the fraction of total iterations, equivalent to time). Figure 3.8b shows the corresponding depiction of sample semi-variograms associated with the longest observation time ($t = 188$ h, corresponding to 100% extent of the reaction).

Results from *Model 1* were deemed as not consistent with the documented experimental evidence because the modelbased semi-variogram shown in Figure 3.8b displayed a lack of spatial correlation, in line with the nature of the underlying physical model. A large number of parameter value combinations have been investigated for *Model 2*. It was found that even though the model does imprint a certain degree of correlation to the spatial field of roughness, none of the analyzed parameter sets allowed attaining a variance plateau over time. The latter result is related to the observation that the considered dissolution mechanism implied the variance to continuously increase with time. Otherwise, results from *Model 3* are consistent with the experimental observations with reference to both the attainment of the variance plateau at long times (see Figure 3.8a) as well as the ability to reproduce the semi-variogram structure after 188 h of dissolution (see Figure 3.8b). As an additional advantage, we note that *Model 3* requires only two model parameters. All of these features contribute to identify *Model 3* as the most successful, in terms of consistency with the experimental results, across the collection of models tested.

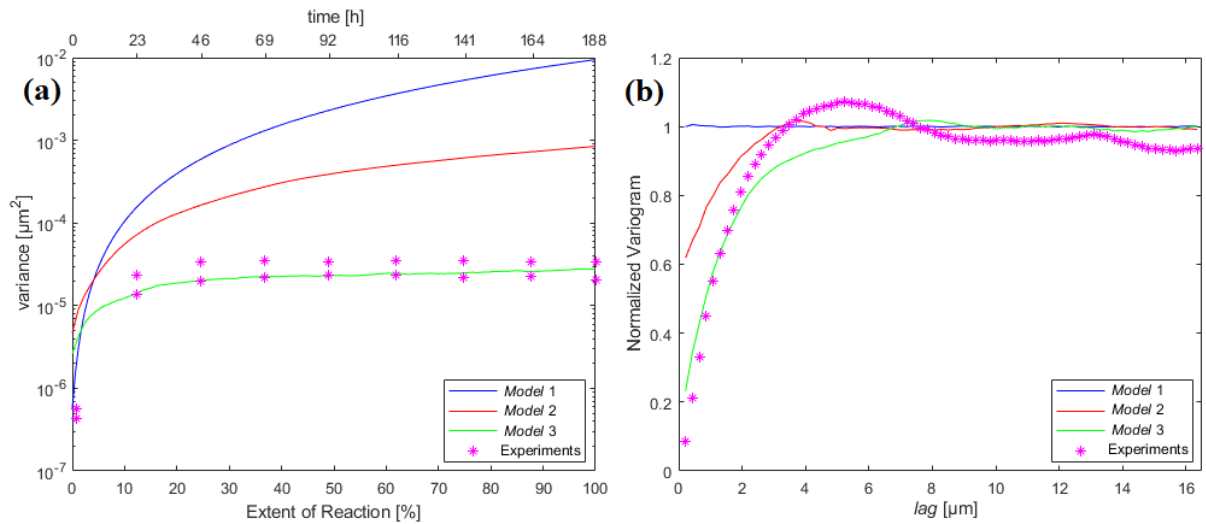


Figure 3.8 (a) Variance of surface roughness (Z^2) associated with (i) the experimental observations (symbols; \pm standard deviation evaluated across the 9 spatial sub-regions investigated) and (ii) their model-based counterparts corresponding to the optimal parameter value sets (solid lines) versus the extent of reaction (i.e., the fraction of total iterations, equivalent to time). (b) Experimental and numerically-based sample semi-variograms associated with the longest observation time ($t = 188$ h, corresponding to 100% extent of the reaction).

3.3.2.4 Parametrization and Validation of the Selected Model

The set of parameters for *Model 3* that results in the best match (based on the minimization of MSE, as described in Section 3.3.2.3) between numerical and experimental data is $P_1=0.05$ and $P_1^*=0.1$.

This model is able to capture the observed behavior of the variance as it causes the variance to steeply increase at early times through the generation of areas dissolving preferentially until a plateau is reached as these areas merge at long times, while the average retreat increases linearly. The implementation of the dissolution mechanism associated with *Model 3* imprints a certain degree of spatial correlation due to the assumption that the voxels associated with a larger number of faces exposed to the fluid are more reactive (i.e., more likely to be dissolved). As a consequence, the simulated dissolution process advances through time by propagating a number of randomly generated valleys (i.e., areas resulting from dissolution being locally more active than in the remaining portions of the surface). The temporal evolution of the simulated surface is probabilistically related to the locations where these valleys are randomly generated at early iterations.

As a result, diverse simulation runs may lead to moderately different statistical evolutions of the simulated surface. We investigate this aspect by performing 100 runs of *Model 3* with the optimal parameter set. Figure 3.9 shows a comparison of Z' statistics between \pm SD resulting from 100 simulation runs of *Model 3* and \pm SD evaluated across the nine subregions investigated.

We observe that the steady-state model-based values of Z' variance are in good agreement with their experimental counterparts (see Figure 3.9a), whereas mild discrepancies can be observed as the order of the statistical moments considered increases (see Figure 3.9b,c). The main differences in the behavior of the variance of Z' are detected at early times, the model plateau being attained later than the experimental one. Although the early time system variation observed experimentally is very sharp (and possibly enhanced by the weakening effect of polishing scratches), numerical results show that merging of areas dissolving preferentially is more gradual. Nevertheless, the main temporal trend of the modeling results is satisfactorily consistent with the experimental observations, thus supporting the selection of *Model 3* as capable of embedding the main statistical traits associated with the observed system dynamics.

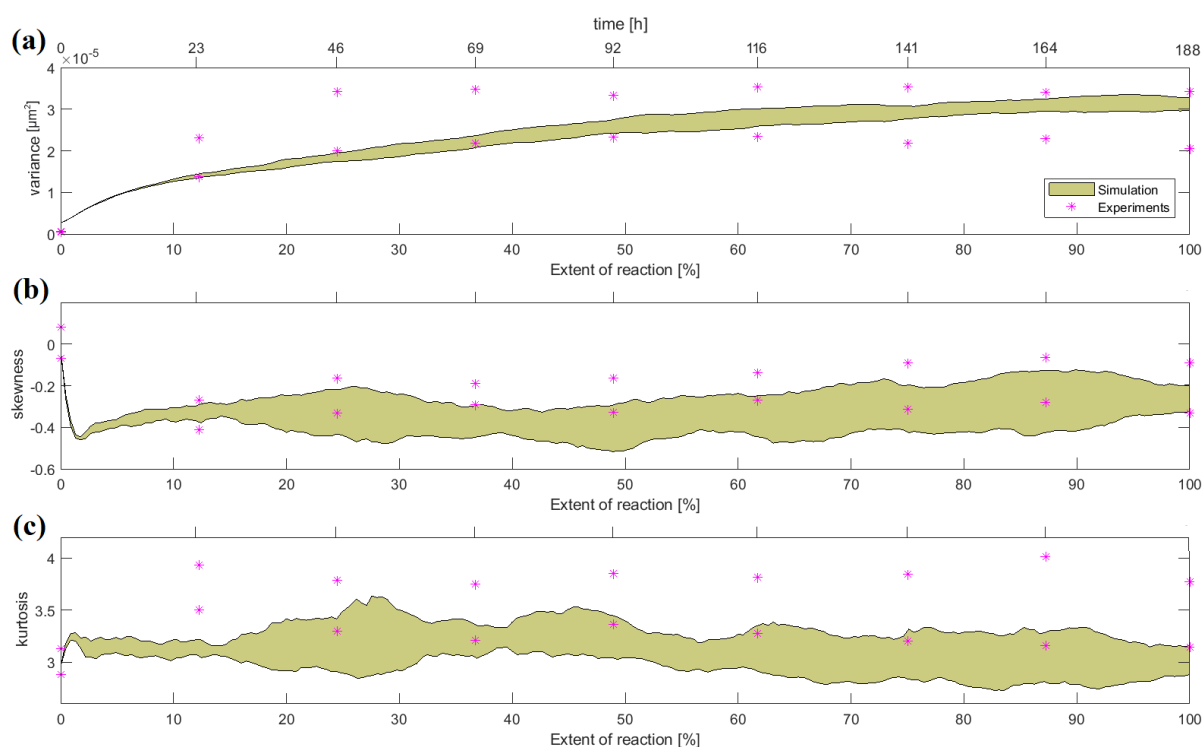


Figure 3.9 Temporal evolution of the key statistics of Z' evaluated over 100 realizations of *Model 3*. Envelopes of width equal to \pm one standard deviation around the corresponding mean are depicted (shaded areas). Symbols denote the corresponding intervals associated with the experimental data monitored across the 9 sample windows investigated.

3.4 Discussion

3.4.1 Applicability of a Statistical Approach to Surface Topography of Dissolved Mineral Surfaces

Attempting to take into account the spatial heterogeneity of mineral dissolution, Fischer et al.²⁰ suggested the rate spectra approach, which was then largely applied in several subsequent studies (e.g., refs 15, 20, 22, 27, 29–33). This strategy has opened up the possibility for new developments in the field of mineral reactivity as the deconvolution of rate spectra allows for the determination of the main contributors to a given rate distribution and can shed some light on our ability to identify dissolution mechanisms^{34, 35, 45} or the specific contribution of microbes to chemical weathering³³. However, this approach suffers from two main limitations: (i) it requires the presence of a laterally fixed (motionless through time) surface and/or reference points at the crystal surface, which may not be compatible with a number of field applications and (ii) it does not contain information about the spatial correlation of the surface roughness distribution as the evolution of dissolved surfaces characterized by diverse extents of spatial correlation might be associated with the same rate spectra.

Our statistic-based approach targeting close-to-equilibrium conditions (which are characteristic of most natural settings) can be seen as complementary to the rate spectra approach.

Our observations that the initial surface configuration of a mechanically polished calcite sample is characterized by a Gaussian probability density function, whereas the surface equilibrium configuration is left-skewed and leptokurtic, may provide a quantitative criterion to distinguish between the reacted and unreacted (mechanically polished) calcite surfaces based only on surface topography measurements. More specifically, the left-skewness of dissolved calcite surfaces (already observed by Siena et al.³⁹), which intrinsically implies that the surface is characterized by a larger number of low height values rather than high height values, could be viewed as a specific feature of dissolution as it results in a right-skewed rate spectrum consistent with the observations of numerous studies related to various minerals altered through various dissolution regimes (e.g., ref 20, 30).

3.4.2 Insights into Surface Dynamics of Calcite Dissolved at Close-to-Equilibrium Conditions

Our results show that the surface roughness variance increases with time until a plateau is reached, indicating the achievement of a steady-state surface configuration, as supported by the attainment of a virtually invariant semi-variogram. We note that the numerical simulations and

scanning tunneling microscopy observations of silver electro dissolution by Hernández et al.⁴⁶ yielded similar trends. A qualitatively similar behavior was also observed in previous studies (refs 23, 47) at far-from-equilibrium conditions for fluorite, where the authors noted that the value of the variance plateau may be specific to the considered crystallographic orientation.

With the aim of obtaining further insights into the underlying dissolution mechanism, three diverse numerical models have been examined (see Section 3.2.3). *Model 3* (i.e., dynamic dissolution probability based on fluid accessibility) has been identified as the one that best captures the results of our statistical analyses on the evolution of the surface topography. *Model 1* (i.e., uniform and spatially independent dissolution probability similar to pitting corrosion models) failed to account for the spatial correlation, whereas *Model 2* led to a monotonous temporal increase of the variance of the surface topography and the formation of geometric etch pits, these features being incompatible with dissolution at close-to-equilibrium conditions. Otherwise, the results of *Model 3* (i.e., equiprobable dissolution with the presence of volume defects dissolving preferentially), by involving a dynamic set of dissolution probabilities, were fully consistent with the main statistics and the semi-variogram structure of surface roughness.

Pollet-Villard et al.³⁸ developed a model accounting for the long-term evolution of the (001) surface of a dissolving K-feldspar at far-from-equilibrium conditions based on the correspondence between modeling and experimentally based statistical behaviors. Similarly, the results of our study enable us to conclude that the dissolution of a {104} calcite surface at close-to-equilibrium conditions progresses in a way which is consistent with a mechanism based on random generation of a number of valleys, which tend to increase with time and grow until they finally merge to attain a steady-state surface area. We note that while the temporal evolution of the roughness variance reaches a plateau, the average retreat increases according to a linear trend, which is also consistent with other studies (e.g., ref 38).

One should emphasize that our results are not intended to imply that *Model 3* can be considered a universal descriptor of mineral dissolution that would apply to any mineral reacted at close-to-equilibrium conditions. As opposed to mechanistic models such as kinetic Monte Carlo simulations (e.g., refs 26, 28, 48), *Model 3* is essentially phenomenological and its parameters need to be estimated against experimental observations. Nonetheless, and more importantly, the development and analysis of these various models underlined the need to consider some key elements that have to be implemented into any future model to ensure its ability to capture major features of the statistics of surface roughness, as described in the following:

(i) The dissolution probability of a given voxel is dynamic as it depends on its immediate neighboring environment. Interestingly, this feature is also observed at a smaller (i.e., atomic) scale (e.g., refs 26, 48–51) although in this latter case, the relationship that links the dissolution probability of an atom to its environment corresponds to the product of the probabilities to break the bonds linking the atom to the surface (thus resulting in the hydrolysis of all bonds simultaneously). Applying the exact same rule also at the nanometer scale would most likely be unreasonable without the development of upscaling laws as the detachment of a nm-scale voxel already involves the dissolution of hundreds of thousands of atoms. Here, we show that the detachment of a voxel is related, in a statistical sense, to the number of faces of the voxel exposed to the solution, consistent with the macroscopic description of the dissolution process where the dissolution rate is scaled to the surface area in contact with the solution.

(ii) Specific features that are shown to be consistent with the observation that the variance of the surface roughness reaches a plateau include (a) considering that columns of voxels (i.e., voxel spines) can dissolve at the same time and (b) assigning a higher dissolution probability to voxels located at the top of a given column (see Section 3.2.3.2). Interestingly, such a condition is similar to that implemented in one of the models developed to describe the dissolution of silver⁴⁶, where a given probability is assigned to each voxel depending on its distance to the basal plane.

(iii) Finally, we showed that the strength of the spatial correlation associated with the semi-variogram for late times is not necessarily related to a specific distance between pre-existing defects in the simulated crystal (as in *Model 2* or in the study by Pollet-Villard et al.³⁸) and can be otherwise associated with the specific choice of a dynamic set of dissolution probabilities.

3.4.3 Statistical Characterizations of Surface Topography as a Metric for Identification of Reacting Conditions

Dissolution at far-from-equilibrium conditions results in a final topography that is markedly different from the steady-state surface observed in our study at close-to-equilibrium conditions^{38,52,53}. As suggested by Godinho et al.²³, the temporal evolution of the surface topography may be associated with decreasing dissolution rates. This opens up the possibility that the observed steady-state surface topography is closely related to the fluid composition. The experimental investigation of such a conceptual element remains the focus of ongoing research.

The calibrated numerical model developed in this study, which has been shown to satisfactorily reproduce the experimentally observed statistical behavior at given conditions of initial roughness and fluid composition (i.e., *Model 3*), is then employed to explore additional scenarios with the aim of discriminating the contribution to the surface equilibrium configuration given by the initial roughness from that resulting from the fluid composition.

The results obtained considering various initial topographies in the absence of macrofeatures suggest that the initial surface roughness has only a negligible impact on the simulated steady-state surface. Our simulation results obtained upon considering the effect of a random noise associated with the initial surface document that there are no significant variations in the fluid–mineral contact surface (and hence in preferential dissolution), whereas considering the presence of surface macrofeatures (e.g., cracks or fractures) would possibly lead to different results. As an example, Figure 3.10a,b shows the temporal evolutions of variance and the steady-state semivariograms resulting from four different initial surface topographies: (i) a perfectly flat surface, (ii) the experimental topography measured at $t = 0$ h for one of the sample windows, and (iii + iv) the topography associated with (ii) which is then corrupted through a white noise with SD equal to: (iii) 1 SD and (iv) 2 times the SD of the experimental topography considered. If supported by experimental data, these results would enable one to rule out the starting topography as a major parameter controlling the steady-state variance of the surface topography resulting from mineral dissolution.

Conversely, differences in “fluid compositions” were shown to have a major impact on the steady-state topography. The impact of fluid composition was simulated based on the observation that P_1 and P_1^* are proportional to the dissolution rates and hence inversely proportional to the saturation state. Here, we limit our analysis to conditions where no etch pits would actually be observed so that only dissolution rates corresponding to saturation states ranging between $\Omega = 0.45$ and $\Omega = 0.8$ are simulated²⁵. As an example, Figure 3.10c,d illustrates the variance temporal evolutions and the steady-state semi-variograms related to three different simulated saturation states (and hence different surface retreats Δh after $t = 188$ h): starting from the values of the model parameters, which were found to best interpret the experimental conditions ($P_1 = 0.05$ and $P_1^* = 0.1$), the saturation state of the solution was simulated by increasing ($P_1 = 0.08$ and $P_1^* = 0.13$) and decreasing ($P_1 = 0.02$ and $P_1^* = 0.07$) the values of the model parameters, which resulted, respectively, in higher ($\Delta h = 0.26 \mu\text{m}$) and lower ($\Delta h = 0.14 \mu\text{m}$) surface retreats. The model results suggest that higher saturation states (i.e., closer-to-equilibrium conditions) result in higher values of the variance plateau due to the delayed

merging of the areas subject to preferential dissolution. This observation may seem counterintuitive: Fischer et al.²² showed that the kink site density at the atomic scale is positively correlated with an increase in surface roughness, the latter being in turn strongly correlated with the dissolution rate (see Figure 3.6). On the other hand, nm-scale experimental and modeling results of previous relevant studies (refs 23, 47) showed that an increase in roughness can be associated with decreasing dissolution rates, which would be in close agreement with our overall analysis.

We note that the results from our simulations, albeit constrained to the available experimental settings, suggest that the steady-state variance of the topography and the fluid composition may be related. From a practical aspect, generalizing this result would be based on the assumption that a steady-state surface configuration would be achieved also at saturation states differing from the one here investigated: if supported through additional experimental observations, direct measurements of surface roughness would allow to unambiguously distinguish surfaces that have reacted from surfaces that have not, while possibly providing insights into the saturation state of the fluid at which dissolution took place. This justifies the need for further experimental investigation on the relationship between the mineral dissolution rate and surface roughness to enhance the ability of our model to characterize these processes. While further experimental studies are required to explore the behavior seen in our numerical simulations, our results suggest that the reacting conditions could be back-estimated through a simple statistical characterization of topography data of a reacted surface, paving the way to the development of empirical transfer functions linking saturation states and reacted surface topographies.

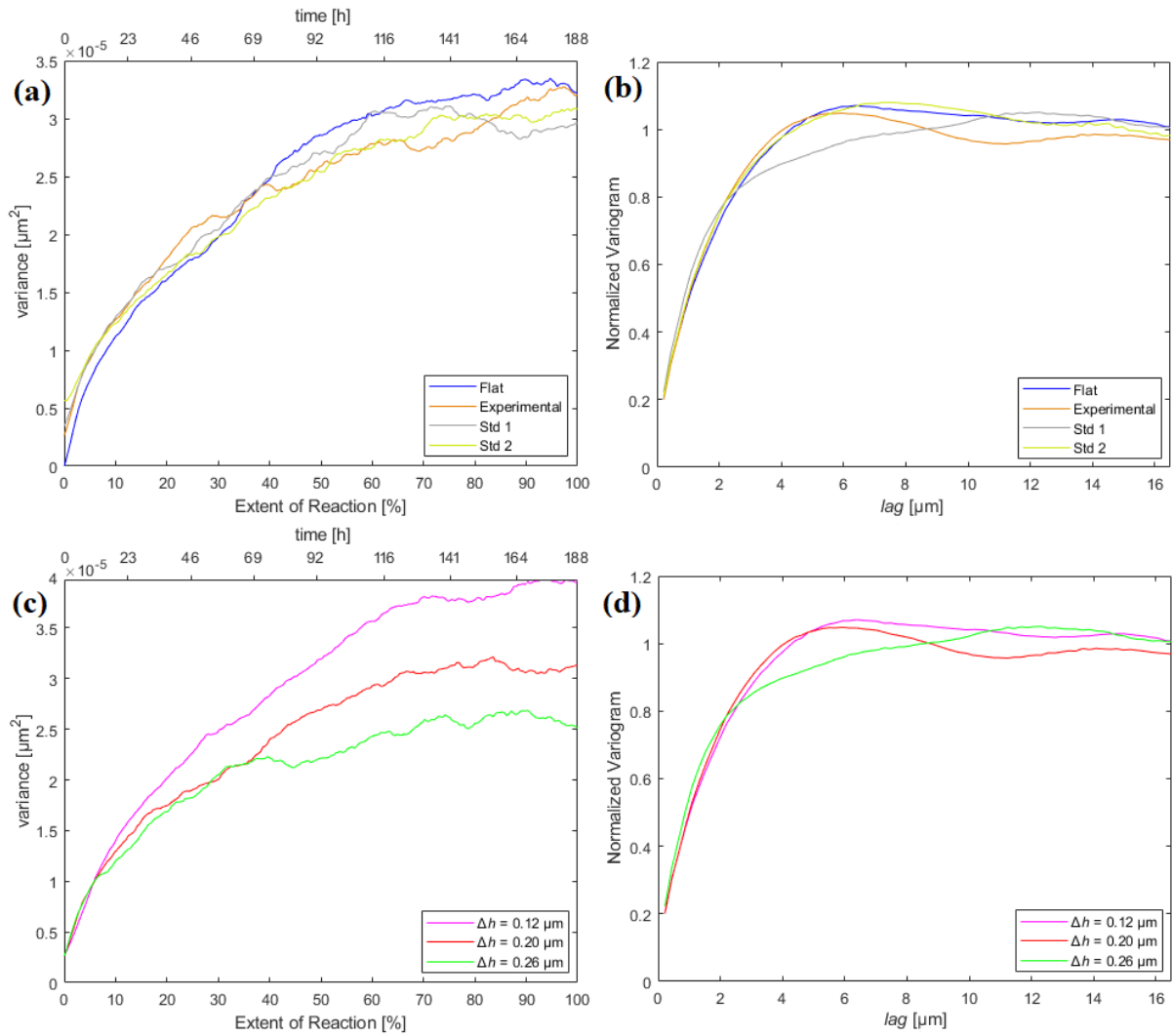


Figure 3.10 Temporal evolution of the variance of surface roughness as a function of the initial surface roughness (a) and of the fluid composition (i.e., saturation state) (c) resulting from numerical simulations associated with *Model 3*. Corresponding results for the normal scored transformed experimental semi-variogram evaluated at the last observation time (b, d) are also included. No significant variation in the semi-variogram was observed in both cases, suggesting that the semi-variogram structure may significantly change only at far from equilibrium conditions regardless of the initial surface roughness.

3.5 Conclusions

Time-resolved statistical analyses of a mechanically polished calcite surface reacting at close-to-equilibrium conditions were demonstrated to be a powerful tool to assess the attainment of a steady-state configuration for the reacting surface. This is reflected through the temporal dynamics of the key statistics and spatial semi-variograms of surface roughness, which tend to stabilize after a given relaxation time (approximately 2 days in our experiments). Our approach

can be used as a quantitative reference to compare (i) differently polished (or unpolished, e.g., cleavage) calcite surfaces reacting at the same physicochemical conditions or (ii) mechanically polished calcite surfaces reacting at different physicochemical conditions. In both cases, a spatial analysis of semi-variogram functions can provide a quantitative appraisal of the strength of the space–time correlation of surface roughness as it evolves subject to the progress of the reaction. In this context, additional investigations may contribute to possibly distinguish between the individual contributions given by the initial surface roughness and the reacting conditions to the plateau values of the statistical moments characterizing the dissolving surface area at steady state. As a consequence, a thorough characterization and understanding of the statistical evolution of the surface roughness could possibly be a key to backestimate the reacting conditions (e.g., saturation state of the solution) by simply measuring the topography of the reacted surface after attainment of the steady state.

We developed and implemented an original conceptual model that enabled us to reproduce the experimentally observed space–time evolution of the key statistical descriptors of surface topography. The documented consistency between modeling and experimentally based statistical analyses may imply that under the investigated conditions, the dissolution mechanism is characterized by an overall space–time organization, as reflected by the semi-variogram structure, with the areas most exposed to the fluid being prone to preferential dissolution. The results of our statistical analyses document that such a dissolution mode is fully compatible with the achievement of a steady-state surface area observed through the experiments in this study.

An ongoing study is geared toward analyzing whether this model, while being conceptually and mathematically simple, can be a viable tool to reliably predict the statistical evolution of calcite surface roughness as a function of the fluid composition.

References

- (1) Beaulieu, E.; Pierret, M.-C.; Legout, A.; Chabaux, F.; Godd ris, Y.; Viville, D.; Herrmann, A. J. E. M. Response of a forested catchment over the last 25 years to past acid deposition assessed by biogeochemical cycle modeling (Strengbach, France). 2020, 430,109124, DOI: 10.1016/j.ecolmodel.2020.109124.
- (2) Berner, R. A.; Lasaga, A. C.; Garrels, R. M. The carbonatesilicate cycle and its effect on atmospheric carbon dioxide over the past 100 millions years. *Am. J. Sci.* 1983, 284, 641–683.
- (3) Beerling, D. J.; Kantzas, E. P.; Lomas, M. R.; Wade, P.; Eufrazio, R. M.; Renforth, P.; Sarkar, B.; Andrews, M. G.; James, R. H.; Pearce, C. R.; Mercure, J.-F.; Pollitt, H.; Holden, P. B.; Edwards, N. R.; Khanna, M.; Koh, L.; Quegan, S.; Pidgeon, N. F.; Janssens, I. A.; Hansen, J.;

Banwart, S. A. Potential for large-scale CO₂ removal via enhanced rock weathering with croplands. *Nature* 2020, 583, 242–248.

(4) Frugier, P.; Gin, S.; Minet, Y.; Chave, T.; Bonin, B.; Godon, N.; Lartigue, J. E.; Jollivet, P.; Ayrat, A.; De Windt, L.; Santarini, G. SON68 nuclear glass dissolution kinetics: Current state of knowledge and basis of the new GRAAL model. *J. Nucl. Mater.* 2008, 380, 8–21.

(5) Alt-Epping, P.; Waber, H. N.; Diamond, L.; Eichinger, L. Reactive transport modeling of the geothermal system at Bad Blumau, Austria: Implications of the combined extraction of heat and CO₂. *Geothermics* 2013, 45, 18–30.

(6) Daval, D. Carbon dioxide sequestration through silicate degradation and carbon mineralisation: promises and uncertainties. *npj Mater. Degrad.* 2018, 2, 11.

(7) Beaulieu, E.; Godderis, Y.; Donnadieu, Y.; Labat, D.; Roelandt, C. High sensitivity of the continental-weathering carbon dioxide sink to future climate change. *Nat. Clim. Change* 2012, 2, 346–349.

(8) Berner, R. A. A Model for Atmospheric CO₂ over Phanerozoic Time. *Am. J. Sci.* 1991, 291, 339–376.

(9) Williams, D.; Westcott, C.; Fleischmann, M. Stochastic models of pitting corrosion of stainless steels: I. Modeling of the initiation and growth of pits at constant potential. 1985, 132 (8), 1796, DOI: 10.1149/1.2114220.

(10) Ryan, M. P.; Williams, D. E.; Chater, R. J.; Hutton, B. M.; McPhail, D. S. J. N. Why stainless steel corrodes. 2002, 415 (6873), 770–774, DOI: 10.1038/415770a.

(11) Mundhenk, N.; Huttenloch, P.; Sanjuan, B.; Kohl, T.; Steger, H.; Zorn, R. Corrosion and scaling as interrelated phenomena in an operating geothermal power plant. *Corros. Sci.* 2013, 70, 17–28.

(12) Fisk, M. R.; Crovisier, J.-L.; Honnorez, J. Experimental abiotic alteration of igneous and manufactured glasses. *Cr Geosci* 2013, 345, 176–184.

(13) Horlait, D.; Claparede, L.; Tocino, F.; Clavier, N.; Ravaux, J.; Szenknect, S.; Podor, R.; Dacheux, N. Environmental SEM monitoring of Ce_{1-x}Ln_xO_{2-x/2} mixed-oxide microstructural evolution during dissolution. *J. Mater. Chem. A* 2014, 2, 5193–5203.

(14) Nicoleau, L.; Bertolim, M. A. Analytical model for the alite (C₃S) dissolution topography. *J. Am. Ceram. Soc.* 2015, 99, 773–786.

(15) Fischer, C.; Finkeldei, S.; Brandt, F.; Bosbach, D.; Luttge, A. Direct Measurement of Surface Dissolution Rates in Potential Nuclear Waste Forms: The Example of Pyrochlore. *ACS Appl. Mater. Interfaces* 2015, 7, 17857–17865.

(16) Robin, V.; Wild, B.; Daval, D.; Pollet-Villard, M.; Nonat, A.; Nicoleau, L. Experimental study and numerical simulation of the dissolution anisotropy of tricalcium silicate. *Chem. Geol.* 2018, 497, 64–73.

(17) Gratz, A. J.; Manne, S.; Hansma, P. K. Atomic Force Microscopy of Atomic-Scale Ledges and Etch Pits Formed During Dissolution of Quartz. *Science* 1991, 251, 1343–1346.

(18) Arvidson, R. S.; Ertan, I. E.; Amonette, J. E.; Luttge, A. Variation in calcite dissolution rates: A fundamental problem? *Geochim. Cosmochim. Acta* 2003, 67, 1623–1634.

- (19) Fischer, C.; Luttge, A. Converged Surface Roughness Parameters – A New Tool to Quantify Rock Surface Morphology and Reactive Alteration. *Am. J. Sci.* 2007, 307, 955–973.
- (20) Fischer, C.; Arvidson, R. S.; Lüttge, A. How predictable are dissolution rates of crystalline material? *Geochim. Cosmochim. Acta* 2012, 98, 177–185.
- (21) Noiriél, C.; Luquot, L.; Madé, B.; Raimbault, L.; Gouze, P.; van der Lee, J. Changes in reactive surface area during limestone dissolution: An experimental and modelling study. *Chem. Geol.* 2009, 265, 160–170.
- (22) Fischer, C.; Kurganskaya, I.; Schäfer, T.; Lüttge, A. Variability of crystal surface reactivity: What do we know? *Appl. Geochem.* 2014, 43, 132–157.
- (23) Godinho, J. R. A.; Piazzolo, S.; Balic-Zunic, T. Importance of surface structure on dissolution of fluorite: Implications for surface dynamics and dissolution rates. *Geochim. Cosmochim. Acta* 2014, 126, 398–410.
- (24) Emmanuel, S. Short Communication: Evidence for non-Gaussian distribution of rock weathering rates. *Earth Surf. Dyn. Discuss.* 2015, 3, 561–575.
- (25) Bouissonnié, A.; Daval, D.; Marinoni, M.; Ackerer, P. From mixed flow reactor to column experiments and modeling: Upscaling of calcite dissolution rate. *Chem. Geol.* 2018, 487, 63–75.
- (26) Bouissonnié, A.; Daval, D.; Ackerer, P. Dissolution Anisotropy of Pyroxenes: A Surrogate Model for Steady-State Enstatite Dissolution Resulting from Stochastic Simulations of the Hydrolysis Process. *J. Phys. Chem. C* 2020, 124, 13113–13126.
- (27) Noiriél, C.; Oursin, M.; Daval, D. Examination of crystal dissolution in 3D: A way to reconcile dissolution rates in the laboratory? *Geochim. Cosmochim. Acta* 2020, 273, 1–25.
- (28) Kurganskaya, I.; Luttge, A. Mineral Dissolution Kinetics: Pathways to Equilibrium. *ACS Earth Space Chem.* 2021, 5, 1657–1673.
- (29) Perez, A.; Daval, D.; Fournier, M.; Vital, M.; Delaye, J.-M.; Gin, S. Comparing the reactivity of glasses with their crystalline equivalents: The case study of plagioclase feldspar. *Geochim. Cosmochim. Acta* 2019, 254, 122–141.
- (30) Emmanuel, S. Mechanisms influencing micron and nanometerscale reaction rate patterns during dolostone dissolution. *Chem. Geol.* 2014, 363, 262–269.
- (31) Fischer, C.; Kurganskaya, I.; Luttge, A. Inherited control of crystal surface reactivity. *Appl. Geochem.* 2018, 91, 140–148.
- (32) Trindade Pedrosa, E.; Kurganskaya, I.; Fischer, C.; Luttge, A. A Statistical Approach for Analysis of Dissolution Rates Including Surface Morphology. 2019, 9 (8), 458, DOI: 10.3390/min9080458.
- (33) Wild, B.; Imfeld, G.; Daval, D. Direct measurement of fungal contribution to silicate weathering rates in soil. *Geology* 2021, 49, 1055–1058.
- (34) Fischer, C.; Luttge, A. Beyond the conventional understanding of water–rock reactivity. *Earth Planet. Sci. Lett.* 2017, 457, 100–105.
- (35) Luttge, A.; Arvidson, R. S.; Fischer, C.; Kurganskaya, I. Kinetic concepts for quantitative prediction of fluid–solid interactions. *Chem. Geol.* 2019, 504, 216–235.

- (36) Arvidson, R. S.; Luttge, A. Mineral dissolution kinetics as a function of distance from equilibrium - New experimental results. *Chem. Geol.* 2010, 269, 79–88.
- (37) Wild, B.; Daval, D.; Beaulieu, E.; Pierret, M.-C.; Viville, D.; Imfeld, G. In-situ dissolution rates of silicate minerals and associated bacterial communities in the critical zone (Strengbach catchment, France). *Geochim. Cosmochim. Acta* 2019, 249, 95–120.
- (38) Pollet-Villard, M.; Daval, D.; Fritz, B.; Knauss, K. G.; Schäfer, G.; Ackerer, P. Influence of etch pit development on the surface area and dissolution kinetics of the orthoclase (001) surface. *Chem. Geol.* 2016, 447, 79–92.
- (39) Siena, M.; Guadagnini, A.; Bouissonnié, A.; Ackerer, P.; Daval, D.; Riva, M. Generalized Sub-Gaussian Processes: Theory and Application to Hydrogeological and Geochemical Data. *Water Resour. Res.* 2020, 56, No. e2020WR027436.
- (40) Smith, M. E.; Knauss, K. G.; Higgins, S. R. Effects of crystal orientation on the dissolution of calcite by chemical and microscopic analysis. *Chem. Geol.* 2013, 360–361, 10–21.
- (41) Lüttge, A.; Bolton, E. W.; Lasaga, A. C. An interferometric study of the dissolution kinetics of anorthite; the role of reactive surface area. *Am. J. Sci.* 1999, 299, 652–678.
- (42) Spencer, A.; Dobryden, I.; Almqvist, N.; Almqvist, A.; Larsson, R. The influence of AFM and VSI techniques on the accurate calculation of tribological surface roughness parameters. *Tribol. Int.* 2013, 57, 242–250.
- (43) Lasaga, A. C.; Luttge, A. Variation of Crystal Dissolution Rate Based on a Dissolution Stepwave Model. *Science* 2001, 291, 2400–2404.
- (44) Jeschke, A. A.; Dreybrodt, W. Dissolution rates of minerals and their relation to surface morphology. *Geochim. Cosmochim. Acta* 2002, 66, 3055–3062.
- (45) Emmanuel, S.; Levenson, Y. Limestone weathering rates accelerated by micron-scale grain detachment. *Geology* 2014, 42, 751–754.
- (46) Hernández Creus, A.; Carro, P.; Salvarezza, R. C.; Arvia, A. J. Three-Dimensional Monte Carlo Simulations of Roughness Development from Different Mechanisms Applicable to the Dissolution of a Pure Solid. *Langmuir* 1997, 13, 833–841.
- (47) Godinho, J. R.; Piazzolo, S.; Evans, L. Simulation of surface dynamics during dissolution as a function of the surface orientation: Implications for non-constant dissolution rates. *Earth Planet. Sci. Lett.* 2014, 408, 163–170.
- (48) Kurganskaya, I.; Luttge, A. A comprehensive stochastic model of phyllosilicate dissolution: Structure and kinematics of etch pits formed on muscovite basal face. *Geochim. Cosmochim. Acta* 2013, 120, 545–560.
- (49) Cailleateau, C.; Angeli, F.; Devreux, F.; Gin, S.; Jestin, J.; Jollivet, P.; Spalla, O. Insight into silicate-glass corrosion mechanisms. *Nat. Mater.* 2008, 7, 978–983.
- (50) Kurganskaya, I.; Luttge, A. Kinetic Monte Carlo Approach To Study Carbonate Dissolution. *J. Phys. Chem. C* 2016, 120, 6482–6492.
- (51) Bouissonnié, A.; Daval, D.; Ackerer, P. Dissolution Anisotropy of Pyroxenes: Role of Edges and Corners Inferred from Stochastic Simulations of Enstatite Dissolution. *J. Phys. Chem. C* 2021, 125, 7658–7674.

(52) Beig, M. S.; Luttge, A. Albite dissolution kinetics as a function of distance from equilibrium: Implications for natural feldspar weathering. *Geochim. Cosmochim. Acta* 2006, 70, 1402–1420.

(53) Bandstra, J. Z.; Brantley, S. L. Surface evolution of dissolving minerals investigated with a kinetic Ising model. *Geochim. Cosmochim. Acta* 2008, 72, 2587–2600.

Chapter 4 : Calcite surface roughness as a proxy for the reaction conditions

Introduction

In the previous chapter, it was shown that under close-to-equilibrium conditions, at a given saturation state, $\Omega = 0.6$, the calcite surface roughness resulting from dissolution reached a steady-state configuration, as quantified through key statistics and semi-variogram analyses. Furthermore, an empirical model that successfully reproduced the space-time dynamics of the surface topography observed experimentally, suggested that a bijective Ω – roughness relationship might exist. This question was addressed experimentally in the following study. Flow-through dissolution experiments were conducted at $T = 22$ °C and $\text{pH} = 7.9$, at various saturation states ($\Omega = 0.00, 0.10, 0.30, 0.55, 0.65, 0.80$), with mechanically-polished calcite crystals, for a total duration of ~ 11 days. Time-resolved surface topography data of $\{104\}$ faces exposed to dissolution at different Ω were acquired *ex situ* with VSI at $50\times$ (lateral resolution, $dl = 0.17$ μm). Of note, the lateral resolution changed compared to the previous study due to the use of an upgraded VSI instrument (Zygo NewView 9000 instead of Zygo NewView 7300 used in the previous study), which was then used for the rest of the PhD work. The surface topography data resulting from dissolution at different saturation states were analysed employing a comprehensive statistical approach. This approach involved the use of the unidimensional descriptor R_a , evaluated over subregions of 80×80 μm^2 , and spatial statistics metrics, which included semi-variogram and power spectral density (PSD) analyses, evaluated over subregions of 400×400 μm^2 . In comparison to the previous study, larger subregions were adopted to be able to capture the presence of larger surface features, such as etch pits, that were absent at $\Omega = 0.6$. Moreover, skewness and kurtosis analyses were not included in this study because they did not exhibit any distinctive pattern in relation to Ω .

The main experimental results showed that a steady-state configuration of the reacting surface was achieved for all saturation states investigated within ~ 4 days, and that the corresponding statistical characterizations of the resulting surface topography are quantitatively distinguishable, according to a seemingly bijective Ω -roughness relationship. Notably, in contrast to the behaviour predicted by the empirical model developed in the previous study, the experiments showed that larger surface roughness evaluations corresponded to lower Ω values.

Moreover, we found that Ising modelling of the dissolution of a Kossel crystal successfully reproduced the Ω -roughness relationship observed experimentally. The Ising modelling was

then used to investigate the impact of the initial surface topography and of Ω fluctuations on the steady-state configuration of the crystal surface. We showed that, in a timeframe negligible compared to geological timescales (i.e., \sim in the order of months at most), the crystal surface reaches a new steady-state configuration that only depends on the fluid saturation state most recently visited. This suggests that the impact of the reaction history on the Ω -roughness relationship is *transient*.

Overall, this study indicates that, for calcite, under the investigated conditions, a bijective relationship between the saturation state of the fluid and the steady-state surface roughness *does* exist. This suggests that calcite surface roughness can potentially be used as a proxy to reconstruct past weathering conditions.

This chapter consists of a research article that was published in *Chemical Geology* in 2023 (Stigliano et al., 2023).

Stigliano, L., Ackerer, P., Benzerara, K., Daval, D., 2023b. Linking calcite surface roughness resulting from dissolution to the saturation state of the bulk solution. *Chemical Geology*, 637: 121680.

Linking calcite surface roughness resulting from dissolution to the saturation state of the bulk solution

Luca Stigliano^{1,2,3,*}, Philippe Ackerer², Karim Benzerara³, Damien Daval¹

¹ ISTerre Institut des Sciences de la Terre – CNRS/Université Grenoble Alpes 38000 Grenoble, France

² ITES Institut Terre et Environnement de Strasbourg - CNRS/Université de Strasbourg, 5 rue Descartes, 67000 Strasbourg, France

³ Sorbonne Université, Museum National d'Histoire Naturelle, UMR CNRS 7590, Institut de Minéralogie, de Physique des Matériaux et de Cosmochimie (IMPMC), 75005 Paris, France

* Corresponding author: Luca Stigliano

Abstract

It has long been supposed that mineral dissolution results in surface microtopography features that may be related to the weathering conditions. Detection of etch pits on weathered mineral surfaces is indicative of far-from-equilibrium conditions ($\Omega \rightarrow 0$), whereas their absence points towards close-to-equilibrium conditions ($\Omega \rightarrow 1$). However, surface microtopography characterizations limited solely to qualitative comparisons may conceal the potential of reconstructing intermediate saturation conditions. To investigate this prospect, we performed flow-through dissolution experiments at room temperature and atmospheric $p\text{CO}_2$, on mechanically-polished $\{104\}$ calcite surfaces reacting at different saturation states with respect to calcite ($0 \leq \Omega \leq 0.8$), under alkaline conditions ($\text{pH} = 7.9$). Time-resolved topography data of the dissolved calcite surface were acquired *ex situ* using vertical scanning interferometry (VSI). Quantitative comparisons of the ensuing surface topography data relied on surface roughness characterizations, based on a combination of unidimensional descriptors (R_a) and spatial statistics metrics (power spectral density, or PSD, and semi-variogram). Time-resolved surface roughness analyses suggested a temporal stabilization of the calcite surfaces undergoing dissolution for all targeted saturation states, and that the steady-state surface roughness evaluations corresponding to different Ω values are statistically distinguishable, with larger roughness values corresponding to lower Ω values, according to a seemingly bijective relationship. We then investigated the atomic-scale mechanisms that might partially explain the empirical Ω -roughness relationship derived experimentally at the VSI-scale through kMC and Ising dissolution modeling of a Kossel crystal. We found that the Ising model successfully reproduced the Ω -roughness behaviour observed experimentally, and we discussed the features that interpretative stochastic models need to satisfy to agree with the experimental findings. Overall, the present study suggests that, under the investigated conditions, the steady-state calcite surface roughness resulting from dissolution can be used as a proxy to back-estimate the saturation state of the fluid under which the reaction occurred for samples reacted under unknown conditions.

Keywords: calcite dissolution, saturation state, surface roughness, kMC modeling, Ising modeling

4.1 Introduction

The reconstruction of the evolution of environmental conditions that prevailed at the Earth's surface through geological time essentially relies on the use of geochemical proxies related to the isotopic, the chemical, and/or the crystallographic properties of minerals found in the geologic record. In particular, some properties of secondary phases are supposed to reflect the specific physicochemical conditions that prevailed at the time of their formation. A large variety of environmental parameters such as temperature, precipitations, sea level, atmospheric composition, and weathering conditions are commonly back-estimated following this approach (Sheldon and Tabor, 2009). Regarding chemical weathering in particular, the development of non-traditional stable isotopes measurements (e.g., $\delta^{29}\text{Si}$, $\delta^{53}\text{Cr}$, $\delta^{11}\text{B}$) has greatly contributed to constrain the conditions under which water-rock interactions occurred. Some non-exhaustive examples include: (i) the determination of the hydrologic regime and intensity of successive weathering episodes that occurred during pedogenesis (Guinoiseau et al., 2021), (ii) the estimation of redox conditions of chemical weathering (Wille et al., 2018), (iii) the ability to distinguish between hydrothermal and supergene weathering events (Lemarchand et al., 2012). In addition, morphological observations of minerals at the microscale, such as characterizations of grains shape and size, or crystal overgrowth, can provide useful complementary information about the conditions under which they were deposited and/or formed (Kontakiotis et al., 2011; McCave and Hall, 2006; Wilkin et al., 1996).

Conversely, whether specific imprints left at the surface of altered primary minerals can be unambiguously used as proxies to infer the conditions under which water-rock interactions occurred is more controversial. As an example, it has long been documented that the chemical weathering of silicates results in the development of submicron-thick amorphous silica-rich surface layers (ASSLs), both in the field and in laboratory experiments ((Daval et al., 2018; Hellmann et al., 2012; Nugent et al., 1998) and references therein). However, linking their physicochemical properties to the fluid composition proved challenging. Indeed, the thickness of ASSLs is a complex parameter that is equally impacted by the intrinsic crystallographic orientation of the parent silicate mineral (e.g., (Bouissonnié et al., 2020b; Daval et al., 2013)) and extrinsic parameters such as the concentration of aqueous silica (Wild et al.). Conversely, other physical parameters characterizing the ASSLs, such as their density, may represent a more promising proxy as it may be intimately linked to the pH of the aqueous fluid that weathered the primary silicates (Wild et al., 2019b). However, knowledge of the pH-ASSL density

relationships remains in its infancy at present. Another feature possibly easier to characterize and that has been investigated for decades is the surface microtopography of minerals, which might be informative of past chemical weathering conditions in natural settings (Nugent et al., 1998; Phillips-Lander et al., 2017). As an example, the presence of etch pits on mineral surfaces has been historically used to suggest that chemical weathering in the field is a surface-controlled process, which operates following mechanisms comparable to those evidenced in laboratory experiments (Berner et al., 1980). The pioneering works of Lasaga et al. (1986) and Brantley et al. (1986) have further refined the use of this criterion, demonstrating that the presence of etch pits is indicative of reactions taking place under far-from-equilibrium conditions (i.e., high values of fluid undersaturation), whereas their absence points towards (close-to-) equilibrium conditions (i.e., low to null values of fluid undersaturation), as a result of a switch in the dominant dissolution mechanism ((Brantley et al., 1986; Lasaga and Blum, 1986)). Detection of etch pits on weathered oceanic volcanic glass has also been used as textural evidence of microbial activity (Fisk et al., 1998).

However, the information content of mineral surface microtopography goes beyond simply differentiating between the presence and absence of etch pits. For instance, the specific shape of etch pits on calcite can be informative of the saturation state of the fluid: at low saturation states (i.e., far from equilibrium), etch pits are typically rhombohedral, whereas, at gradually higher saturation states, they tend to become more triangular, as re-precipitation processes become more important (Bouissonnié et al., 2018; Teng, 2004). Bouissonnié et al. (2018) also observed how, within rhombohedral etch pits, the morphology of the pits changed from rhombohedral at the top to triangular at the bottom, suggesting that this could be an indication of the development of a chemical gradient in the fluid along the etch pit depth, and hence of a local variation of the saturation state (Bouissonnié et al., 2018). Likewise, Duckworth and Martin (2004) suggested that the morphology of etch pits nucleated on Fe-, Mg- and Zn-carbonates could be used to provide information on the pH at which fluid-mineral reactions occurred ((Duckworth and Martin, 2004b)). Finally, several studies showed that the presence of Mg^{2+} in carbonated solutions can significantly alter the morphology of calcite etch pits by selective step pinning through adsorption of Mg^{2+} impurities ((Arvidson et al., 2006; Gao et al., 2010; Ruiz-Agudo et al., 2009)). More generally, the fine description of dissolution textures at mineral surface, which may be preserved in spite of particle transport and sedimentation (see, e.g., (Velbel and Losiak, 2010)), shows promise as a means to provide constraints on the contact time, the fluid composition and/or temperature of fluid-rock interactions.

Such observations also motivated the need to thoroughly characterize the space-time evolution of the surface microtopography of minerals undergoing dissolution over a broad range of controlled chemical conditions. Surface area and surface reactivity are, in fact, fundamentally related. The heterogeneous distribution of reactive sites at the mineral surface and the seemingly random distribution of crystallographic defects are reflected in a corresponding non-uniform distribution of ‘dissolution rates’ at the fluid-mineral interface, as quantified through the ‘rate spectra’ approach (Fischer et al., 2012). This, in turn, results in a non-uniform spatial evolution of the surface area, as quantified through surface roughness characterizations (Fischer and Luttge, 2007). The spatial variability displayed by both the ‘dissolution rate spectra’ and the ‘surface roughness resulting from dissolution’ shows traits typical of stochastic processes and can, therefore, be quantified through corresponding approaches (Siena et al., 2021). For instance, (Emmanuel, 2014) applied the generalized extreme value (GEV) model to interpret rate spectra data of dolostone dissolution. More recently, a generalized sub-gaussian (GSG) model has proven successful to capture the key statistical features of calcite surface roughness resulting from dissolution at close-to-equilibrium (Siena et al., 2020), and to interpret the rate spectra associated with calcite dissolution at far-from-equilibrium (Siena et al., 2021). Alternatively, Fischer and Luttge (2007) proposed the convergence of surface roughness parameters as a tool to quantify the surface topography of altered minerals (Fischer and Luttge, 2007). The evolution of the surface area and surface reactivity of dissolving crystals has also been extensively investigated through kinetic Monte Carlo (kMC) modeling (Ackerer et al., 2021; Kurganskaya and Luttge, 2016; Lasaga and Blum, 1986). In particular, Kurganskaya et al. (2021) investigated numerically the relationship between calcite surface reactivity and fluid undersaturation, showing how, by gradually changing the saturation state from far-from-equilibrium to equilibrium conditions, different kinetic pathways could be generated for systems with different type and density of crystallographic defects (Kurganskaya and Luttge, 2021). In addition, Carrasco et al. (2021) specifically focused on characterizing the calcite surface roughness resulting from kMC dissolution at room and high temperature, showing that, for the latter conditions, the scaling of the surface roughness in time and size is the same as in the Kardar–Parisi–Zhang equation of kinetic roughening (Carrasco et al., 2021).

Despite being a key step in defining an unambiguous proxy of weathering conditions, to date, a comprehensive analysis combining statistical characterizations of experimental microtopography data and numerical modeling to describe the temporal evolution of the mineral surface roughness resulting from dissolution at different saturation states, is still lacking. In our

previous study (Stigliano et al., 2021), we showed how, at close-to-equilibrium conditions ($\Omega=0.6$), a steady-state configuration of the calcite surface roughness resulting from dissolution was achieved. In addition, we developed an empirical model based on experimental observations that suggests that a statistical characterization of the steady-state surface roughness could be used to differentiate between surfaces reacted at different saturation states. Here, we investigated to what extent statistical characterizations of the calcite surface roughness resulting from dissolution at different saturation states can be used as a proxy for the reaction conditions, under controlled laboratory conditions. Then, we conducted numerical modeling based on stochastic approaches. This allowed us to identify some of the atomic-scale mechanisms that could contribute to explain the different evolution of surface roughness as a function of the saturation state that we observe experimentally with vertical scanning interferometry (VSI). Lastly, we discussed generality and implications of our findings.

4.2 Materials and methods

4.2.1 Materials and experimental methods

4.2.1.1 Calcite samples and aqueous solutions preparation

All the crystals used in the present study were obtained from the same natural calcite sample employed in our preliminary study (Stigliano et al., 2021). Chemical composition analysis of the original natural sample revealed very few impurities: 0.2 wt % MgO, 0.008% MnO, and trace amounts of Sr. Starting from the original sample, six smaller pieces ($\sim 100 \text{ mm}^3$) were obtained through cleavage along the natural $\{104\}$ calcite plane, as verified with X-Ray diffraction (XRD) and electron backscatter diffraction (EBSD). For each piece, one of the resulting $\{104\}$ faces was then mechanically-polished in order to get initial surface topographies with comparable surface roughness for all the crystals employed in the experiments. EBSD characterizations of the resulting polished faces ensured that the outermost atomic layers were crystalline prior to the start of the experiments. The finest grit size of the polishing sequence was $0.25 \mu\text{m}$. Absolute ethanol (as a replacement for water-based solutions) was used as lubricant for each polishing step to avoid surface etching. The polishing process yielded comparable initial surface roughness across various locations on a given crystal and among the different crystals. For all the samples, the average surface roughness, R_a , (Equation 4.1) ranged between 0.6 and 0.8 nm. It was evaluated over $80 \times 80 \mu\text{m}^2$ areas of the polished surfaces, based on VSI data collected at 50x magnification. The chemical composition of the

dissolving aqueous solution chosen in the present study was similar to that used in previous works on calcite dissolution under slightly alkaline conditions (Bouissonnié et al., 2018; Smith et al., 2013; Stigliano et al., 2021). As so, NaCl, NaHCO₃ and CaCl₂·2H₂O were added to Milli-Q water (18 MΩ·cm). The concentrations of NaCl and NaHCO₃ were set to 99.25 mmol/kg and 1.02 mmol/kg, respectively, whereas CaCl₂·2H₂O was added in different amounts for each experiment (i.e., 0 mmol/kg, 0.33 mmol/kg, 0.97 mmol/kg, 1.83 mmol/kg, 2.18 mmol/kg, 2.75 mmol/kg) to target six different saturation indexes of the solution with respect to calcite (i.e., $\Omega = 0.00, 0.10, 0.30, 0.55, 0.65, 0.80$). The ionic strength was approximately constant throughout all the different experiments. Saturation Index calculations have been performed using CHES (van der Lee and De Windt, 2002).

4.2.1.2 Experimental setup

All experiments were conducted using the exact same setup as described in Bouissonnié et al. (2018) (see their Figure 1A, (Bouissonnié et al., 2018)) All the experiments were conducted for a total duration of ~ 11 days in perfluoroalkoxy alkane (PFA) reactors placed in an incubator set at $T = 22.0 \pm 0.1$ °C. The pCO₂ of the room was constantly monitored over time and found to be 500 ± 50 ppm, and the tank reservoir containing the inlet solution was left open to the atmosphere. For each experiment, a calcite chip was placed inside the reactor on a Teflon tripod with the polished face as top face. The solution inside the reactor was continuously stirred to maintain homogeneous chemical conditions. A flow-through system was adopted (with a flow rate of ~ 0.15 mL/min set by a peristaltic pump) aiming to roughly maintain the same saturation index inside the reactor as in the inlet solution. In this regard, we employed a reactor volume of ~ 100 mL, which is significantly larger than the calcite chips (~ 100 mm³) subject to dissolution. Chemical analyses conducted by inductively coupled plasma atomic emission spectroscopy (ICP-AES, Varian 720ES) of the Ca²⁺ concentration in the inlet vs outlet solutions showed no significant increase in the outlet solutions as a result of calcite dissolution (Table B1). Moreover, the resulting pH of both the inlet and outlet solutions was measured to be 7.9 ± 0.1 over time for all experiments, suggesting that each experiment was performed at a fixed saturation index. Overall, fluid chemical analyses ensured that all experiments were conducted under chemostatic conditions.

The calcite samples were taken out from the reactors after different durations over the course of the experiments for *ex situ* time-resolved surface topography measurements of the dissolving top faces with vertical scanning interferometry (VSI, Zygo NewView 9000). Right after

removal of the calcite chips from the reactors, the surfaces under study were gently cleaned with precision wipes soaked in pure ethanol, air dried, and placed under the VSI objective for topography measurements. As our previous study showed that the strongest evolution of the surface topography occurs in the first three days of dissolution, the acquisition frequency in this time interval was the highest, aiming to detail the short-term temporal evolution of the surface topography (Stigliano et al., 2021). After each VSI data acquisition, the calcite chips were placed back into the reactor to continue the experiments until completion.

4.2.1.3 VSI analyses and Data processing

Time-resolved VSI data were always collected at 50x magnification (lateral resolution of 0.17 μm) over an area of $\sim 1 \text{ mm}^2$ for all the studied surfaces. In order to characterize comprehensively the surface roughness associated with the planar areas under study, we identified several sub-windows (i.e., sampling windows), aiming to capture the statistical variability at play on each given crystal surface. Moreover, as surface roughness is a scale-dependent quantity (Fischer and Lutge, 2007), we selected sub-windows of two different sizes. Specifically, we worked with 30+ sub-windows of $80 \times 80 \mu\text{m}^2$ and 3 sub-windows of $400 \times 400 \mu\text{m}^2$. In broad terms, for a given lateral resolution, characterizations on smaller (but more numerous) sub-windows are better suited to describe the spatial heterogeneity along the crystal surface, whereas larger sub-windows (but less numerous) are more apt to characterize in detail the spatial dependency of the heights data within a given window. As a general approach, we tried to maximize the number of sub-windows, which were chosen randomly along the surface, while avoiding surface macro-defects (such as macrosteps or cracks) that would strongly bias the statistical analysis (Stigliano et al., 2021). Of note, the sub-windows sizes selected have been determined to be suitable for capturing the key roughness features, as R_a convergence is observed for both sub-windows sizes across all investigated conditions (see Figure B1, (Fischer and Lutge, 2007)). Once all the suitable sub-windows were selected for each experiment at a given time, the sub-windows corresponding to the same locations at all other times were also selected. To ensure precise localization of the same area for each subsequent analysis, we relied on cracks and visible imperfections on the surface, which remained at the same locations during dissolution, as reference points. Afterwards, the ensuing raw surface topography data were post-processed. To study the actual surface roughness, it was necessary to minimize the biases originated by the imperfect parallel alignment between the VSI objective and the studied surface, and by the waviness of the sample surface resulting from the polishing process (Stigliano et al., 2021). For this purpose, for each sub-window and at each observation time,

the topography data were detrended by removing the best-fitting surface from all data points (Table B2 and Table B3). In addition, the height values corresponding to VSI-related optical artifacts (i.e., pixels for which the VSI failed to acquire a height value or artificial spikes resulting from a sharp height transition between two adjacent pixels) were replaced by the arithmetic mean of the height values of the surrounding pixels. For all the selected sub-windows and at all times, the amount of replaced pixels was negligible (<0.1%) compared to the total number of pixels of each given window.

4.2.2 Statistical Approaches

To describe comprehensively the calcite surface topography resulting from dissolution at different saturation states, we relied on a variety of statistical tools, each addressing specific traits of the corresponding surface roughness. In particular, we targeted two main aspects of surface roughness: (i) its spatial heterogeneity along the surface, targeted through the analysis of smaller but more numerous sub-windows and (ii) the spatial dependency of the heights values within a given sub-window, targeted through the analysis of larger but less numerous sub-windows. For the ‘smaller sub-windows analysis’, we employed a simple unidimensional statistical descriptor, the average surface roughness parameter (R_a), whereas for the ‘larger observation windows analysis’, we adopted semi-variograms and power spectral density (PSD) analyses.

4.2.2.1 Average surface roughness R_a

We recall that the average roughness parameter (R_a) for a given sampling window is defined as:

$$R_a = \frac{1}{N} \sum_{i=1}^N |Z(x_i) - \langle Z \rangle| \quad (4.1)$$

where $Z(x_i)$ is the height value of the pixel in the i^{th} position on the grid, and $\langle Z \rangle$ is the arithmetic mean evaluated on all data points (N) within the sampling area. For surface roughness characterizations on smaller windows, it is more convenient to adopt a single-value expression (such as R_a) as it makes it easier to evaluate the degree of spatial heterogeneity across-windows and across-times for each given crystal surface. It allows to visually compare, within a single plot, the temporal evolution of the surface roughness (and its heterogeneity) resulting from dissolution at different Ω values. Conversely, for surface roughness characterizations on larger windows, a higher level of descriptive detail is required.

4.2.2.2 Experimental and Theoretical semi-variogram

As in our previous study ((Stigliano et al., 2021)), the degree of spatial correlation of the surface topography resulting from dissolution was quantified using the experimental semi-variogram $\gamma(h)$, which is defined as:

$$\gamma(h) = \frac{1}{2n(h)} \sum_{i=1}^{n(h)} [Z(x_i) - Z(x_i + h)]^2 \quad (4.2)$$

where $n(h)$ is the number of data pairs separated by a given distance (or lag), h (evaluated in all directions). Conceptually, the experimental semi-variogram quantifies the notion that data pairs of spatial quantities (such as the topography field, Z) exhibit a certain degree of similarity as a function of distance. It is indeed a measure of the ‘dissimilarity’ of the spatial field. In general, closer data pairs tend to be more similar than more distant ones. As a consequence, the experimental semi-variogram shows lower values at short lags and increasingly higher values as the separation distance increases. If stationarity conditions are met (i.e., statistical properties of the height values do not vary significantly over the region being analyzed) and if the underlying trends / biases have been properly removed, the experimental semi-variogram eventually reaches a plateau (Figure B2). Different topography maps are characterized by different degrees of spatial correlation and thus by different experimental semi-variogram curves. We take advantage of this property to quantitatively differentiate the surface roughness resulting from dissolution at different saturation states. Theoretical models are generally applied to interpret the experimental semi-variograms (Gringarten and Deutsch, 2001). Fitting experimental semi-variograms with theoretical semi-variograms allows one to encapsulate all the information regarding the degree of spatial correlation within the model parameters alone. In this study, a simple (two-parameters) semi-variogram exponential model proved capable of satisfactorily interpreting its experimental counterpart. The exponential model $\gamma(h)$ is defined as:

$$\gamma(h) = \gamma(0) + (C - \gamma(0)) \left(1 - \exp\left(-\frac{h}{a}\right)\right) \quad (4.3)$$

where: (i) $\gamma(0)$ is the nugget, a parameter that accounts for the short-scale random noise that is due to measurement error and uncontrolled environmental oscillations, (ii) C is the total sill (i.e., the semi-variogram plateau value) and (iii) a is a parameter related to the correlation length, or effective range (i.e., the separation distance above which data pairs are no longer spatially autocorrelated) (Figure B2). The difference between the total sill and the nugget, $(C - \gamma(0))$, is the partial sill, which represents the remaining variance of the height values after removing the contribution of random noise. The exponential semi-variogram model is unbounded, which means that the plateau value is only reached asymptotically. Therefore, the

correlation length is defined as the separation distance at which the semi-variogram equals a given percentage of the partial sill. If a percentage of 95% is selected, the correlation length is given by $\sim 3*a$. These model parameters can then be calibrated against the experimental semi-variogram computed on the surface topography data and plotted as a function of Ω .

4.2.2.3 Power spectral density (PSD)

To fully describe surface roughness, it is crucial to also consider the general notion that surfaces are characterized by different degrees of roughness at different spatial scales. In this regard, the power spectral density (PSD) enables one to quantify the surface roughness at different length scales by breaking it down into its individual frequency components.

In simple terms, surface topography data can be conceptualized as the ensemble of several 1-D height profiles evaluated along the radial direction from the center point of a given observation window. By applying the Fourier transform to these 1-D height profiles, we can decompose them into a series of sine and cosine waves, each characterized by a given frequency (i.e., the number of oscillations per unit length) and amplitude (i.e., the height of the wave). For all waves with each given frequency, the average value of the square of the amplitude is calculated. The power spectral density, or PSD, is the plot of the average amplitude squared as a function of the spatial frequency, or wavenumber (Jacobs et al.; Mellott et al., 2002; Persson et al., 2005). This enables one to quantify, within a single plot, the ‘low-frequency’ and the ‘high-frequency’ components of the surface roughness. Here we used the PSD to quantify the ‘surface roughness at different length scales’ that originated from dissolution at different saturation states.

4.2.3 Modeling of calcite dissolution using stochastic approaches

We attempted to identify the atomic-scale factors that may play a role in explaining the roughness- Ω trend that we observed experimentally at the VSI scale. To do so, we developed stochastic models of calcite dissolution applied with different values of fluid saturation state.

4.2.3.1 Classical kinetic Monte Carlo dissolution modeling of Kossel crystal structure

Kinetic Monte Carlo (kMC) modeling of mineral growth (Gilmer, 1980) and dissolution (Wehrli, 1989) aims to describe, within a probabilistic framework, the kinetics of the interactions of chemical elements transitioning from a solid state (in a crystal) to a dissolved state (in a fluid), and vice versa. Within this framework, it has been shown that a reasonable approximation for the calcite structure is given by the so-called Kossel crystal (Kossel, 1927b), a simple cubic lattice in which a site represents one CaCO_3 molecule (Ackerer et al., 2021; Carrasco et al., 2021). Additionally, adopting such an approximation in the present study

enabled us to investigate to what extent the atomic-scale mechanisms reproducing qualitatively the roughness- Ω trend observed experimentally at the meso-scale are fundamental to mineral dissolution (i.e., a result of the dynamic interaction between surface reactivity and fluid undersaturation). Therefore, we applied kMC simulations to model the dissolution of a Kossel crystal at different saturation states, aiming to investigate variations in the evolution of the resulting surface topography. For a Kossel crystal, the reactivity of each site is determined by the number of its nearest-neighbors (NNs), which equals the number of existing bonds. For a given site, the higher the number of NNs , the higher the number of existing bonds, hence, the lower its tendency to dissolve. Following this concept, the general expression for the dissolution probability $P_{d,N}$ of a site with N nearest-neighbors is given by the following (Kurganskaya and Lutttge, 2013):

$$P_{d,N} = \exp\left(-\frac{NE_a}{RT}\right) = P_b^N \quad (4.4)$$

where P_b is the bond-breaking probability (i.e. probability of breaking a single bond), E_a [kJ/mol] is the corresponding activation energy, T [K] is temperature and R [kJ/mol/K] is the universal gas constant. With this expression, it is implicitly assumed that all bonds are equivalent and that, for a given site, the cleavage of different bonds are independent events. To investigate the impact of the saturation state, back-precipitation events need to be included in the kMC model (Kurganskaya and Lutttge, 2021). The microscopic reversibility principle implies that, at equilibrium between dissolution and precipitation, the activation energy required to break a single bond is the same as the activation energy required for the same bond type to be formed. It follows that, at equilibrium, the generic expression for the precipitation probability $P_{p,N}$ of a site forming N bonds when adsorbed to the surface has to be identical to $P_{d,N}$. The driving force of precipitation processes is the difference in chemical potential $\Delta\mu$ [kJ/mol] between a given site in the aqueous solution and a given site at the crystal surface. Whereas the chemical potential of the bulk fluid is univocally determined by macroscopic thermodynamic parameters, the nonequivalence of surface sites poses a definitional problem regarding the expression of the ‘surface chemical potential’ (Kurganskaya and Lutttge, 2021). However, based on statistical mechanics considerations (Mutaftschiev, 2001), the kink site (i.e., the site type for which the coordination is half that of the bulk crystal; (Lutttge et al., 2019)) can be considered as representative of the whole crystal surface from a thermodynamics perspective, as first proposed by Kossel (Kossel, 1927b). Thus, the difference in chemical potential $\Delta\mu$ uniquely depends on the saturation state of the fluid. Adopting the conventional approach first introduced by Gilmer et al. (Gilmer, 1980; Gilmer and Bennema, 1972) and

recently used by Kurganskaya et al. for calcite (Kurganskaya and Lutge, 2021), we consider that precipitation events can only occur at kink sites ($N = 3$ in a Kossel crystal), according to the following precipitation probability:

$$P_{p,3} = \exp\left(\frac{\Delta\mu}{RT}\right) \exp\left(-\frac{3E_a}{RT}\right) \quad (4.5)$$

Note that when $\Delta\mu=0$, $P_{p,3} = P_{d,3}$, which implies that, at the microscopic scale, equilibrium between dissolution and precipitation is maintained at kink sites. Conversely, at far-from-equilibrium conditions (i.e., $\Delta\mu \rightarrow -\infty$), the precipitation probability becomes negligible. As in state of the art kMC modeling, we consider that the dissolution tendency is intrinsic to the mineral itself, hence independent of $\Delta\mu$ (Briese et al., 2017; Kurganskaya and Lutge, 2013; Kurganskaya and Lutge, 2016; Lasaga and Lutge, 2001b; Meakin and Rosso, 2008), whereas the frequency of precipitation events is a function of the distance from equilibrium (Kurganskaya and Lutge, 2021). Lastly, the time increment (Δt) after each iteration is defined as in Equation 4.6, which observes the concept that, for a surface configuration in which less likely events are prevalent (compared with a case in which more likely events are prevalent), on average, more time is needed before any event can occur, and therefore Δt is higher (e.g., Δt is maximum for a flat surface configuration). Moreover, Δt is inversely proportional to the ‘frequency factor’, ν [s^{-1}], which is an estimation of the expected attachment/detachment reaction attempts in one-unit time at the mesoscale (Ackerer2021).

$$\Delta t = \frac{1}{\nu(\sum_{N=1}^5 n_{d,N} P_{d,N} + n_{p,3} P_{p,3})} \quad (4.6)$$

4.2.3.2 Calcite dissolution simulations following the Ising model

In addition to exploring classical kMC modeling, we investigated the potential of the Ising model in reproducing the Ω -roughness relationship observed experimentally. The Ising model was first applied by Bandstra and Brantley (2008) to study the dissolution of a regular 2-D lattice (i.e., a surface profile, see their Figure 3, (Bandstra and Brantley, 2008)). In their model, the reaction mechanisms were defined in terms of nearest neighbor interactions, with dissolution and precipitation probabilities, respectively, decreasing and increasing with the number of nearest neighbors, according to a power law expression. In the present study, we generalized their model to investigate the dissolution of a regular 3-D lattice in which only ‘surface sites’ can react, as described in section 4.2.3.3. Therefore, the general expressions used in this study for the dissolution probability $P_{d,N}$ and precipitation probability $P_{p,N}$ of a site with N nearest-neighbors ($1 \leq N \leq 5$) are given, respectively, by the following equations:

$$P_{d,N} = \left(1 - \frac{N}{6}\right)^\gamma \quad (4.7)$$

$$P_{p,N} = \exp\left(\frac{\Delta\mu}{RT}\right) \left(\frac{N}{6}\right)^\eta \quad (4.8)$$

with γ and η being adjustable parameters.

4.2.3.3 Algorithmic details

A Kossel crystal can be conceptualized as a volume composed of identical sites, each one on top of and next to the other. The edge length of a single site was chosen as $a = 0.394$ nm to match the molar volume of calcite at ambient temperature and pressure (Carrasco and Aarão Reis, 2021). We considered an initially flat top surface with periodic boundary conditions, hence, all surface sites, i.e., sites at the very top in the (x,y) plane, initially have $NNs = 5$. As in Carrasco et al., 2021, we allowed detachment of the surface sites only. This reduces the overall computational effort as it makes it possible to simulate the dissolution dynamics of a crystal volume by only keeping track of a single topography map and the corresponding neighbors map specific to surface sites only ((Carrasco et al., 2021)).

For both the kMC and the Ising models, we adopted the ‘divide and conquer’ approach, for which one iteration step corresponds to one (dissolution or precipitation) event (Meakin and Rosso, 2008). At each iteration, the single event taking place is established based on the current surface configuration, i.e., number of sites of each given type, and the values of the elementary probabilities, $P_{d,i}$ and $P_{p,j}$ (with $j=3$ for the kMC model). This is done by computing the relative probabilities, $P_{d,i}^*$ and $P_{p,j}^*$, defined and piled up as in Figure 4.1 (Kurganskaya and Lutge, 2013). A random number between 0 and 1 is generated. If the random number falls within a specific relative probability class, the event corresponding to that category will occur (see example in Figure 4.1). Once the event type has been determined, one of the sites belonging to that class is randomly selected and the event executed.

Crystal defects are typically conceptualized as pre-determined sites, in the case of point defects, or group of sites, in the case of screw dislocations, within the crystal volume, which are associated with much higher reactivity (regardless of the site coordination) due to the strain field generated. For the kMC model, this can be implemented by reducing the activation energy associated with the bond-breaking probability, P_b , related to the impacted sites, as a function of the induced strain field, by defining dislocation parameters, such as core radius, strain energy and dislocation length (Kurganskaya and Lutge, 2016). However, Meakin and Rosso (2008) showed that equivalent simulation results can be achieved by implementing ‘instantaneous’

detachment of the sites at the affected locations, i.e., missing sites for point defects and pre-opened nanotubes for screw dislocations, without explicitly defining the strain field at core regions (Meakin and Rosso, 2008). Here we followed the latter approach, by implementing screw dislocations as pre-opened hollow cores of lattice sites with diameters of 4x4 for the kMC model and 1x1 for the Ising model. The pre-opened hollow cores were as deep as the whole simulated crystal to exclude the impact of the dislocation depth (Kurganskaya and Lutge, 2021). One single pre-opened hollow core was implemented for each simulated crystal and the window size was adjusted to match a reasonable value of dislocation density for calcite. Hence, we selected a window size of 200x200 sites. The resulting dislocation density was on the order of magnitude of 10^{10} cm^{-2} , which was in the upper end of the range found for real minerals ($10^3 - 10^{11} \text{ cm}^{-2}$), as representative of a strained calcite crystal (MacInnis and Brantley, 1992; Meakin and Rosso, 2008). The simulations were run for a number of iterations sufficient to reach a steady-state configuration of the surface roughness, as quantified through R_a . All the outputs of the simulations represent the average values evaluated over 10 simulation runs for each set of parameters tested.

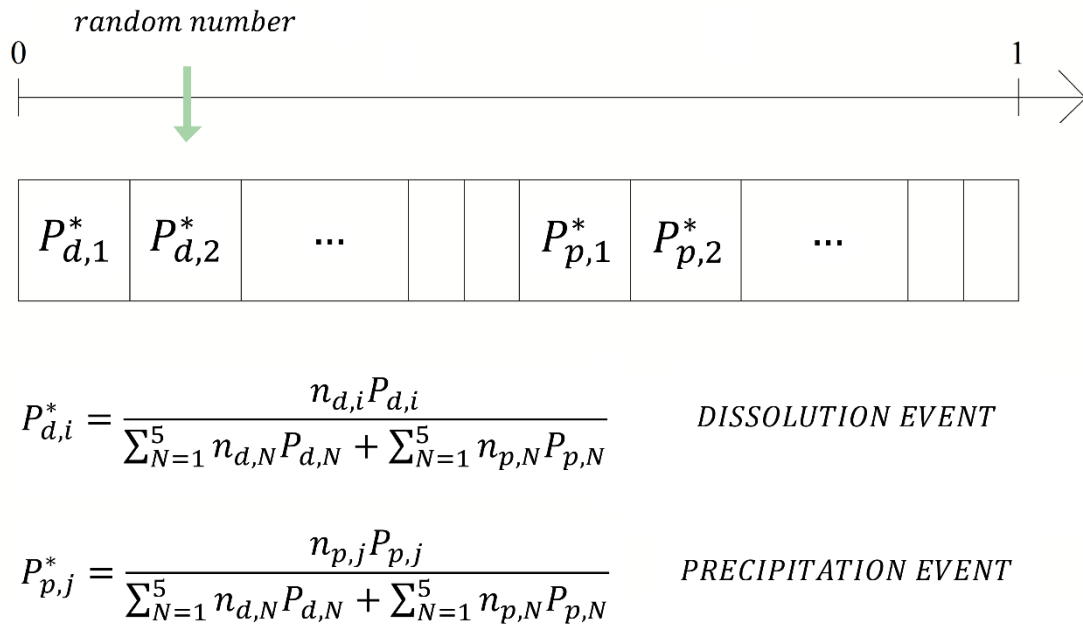


Figure 4.1 Example of (dissolution or precipitation) event selection and expression of the relative probabilities, $P_{d,i}^*$ (i.e., the probability that any site with i neighbors detaches from the surface) and $P_{p,j}^*$ (i.e., the probability of attachment events at any site for which j bonds would be formed), for a given surface configuration at a given iteration step. For the kMC model, $j =$

3. The expression of all relative probabilities (hence, the length of all event classes) changes at each iteration step as the surface configuration changes upon each event execution.

4.3 Results

4.3.1 Time-resolved small-windows statistical analyses

The key results of the time-resolved analysis of the surface topography, Z , for the 6 calcite surfaces reacted at different Ω are depicted in Figure 4.2. The figure shows, for all samples, the temporal evolution of the median (and corresponding interquartile range, IQR) of R_a values computed, for each surface, over at least 30 sub-windows of $80 \times 80 \mu\text{m}^2$ (Table B2). Steady-state dissolution rates as a function of Ω derived from Bouissonnié et al. (2018) are also included ((Bouissonnié et al., 2018)). Because for most of the samples, at $t > 0$ h, the 30+ R_a values were positively skewed (i.e., skewed towards high values of R_a , and, hence, non-normally distributed), we used the median (instead of the mean) to represent the central tendency of the data. As a measure of the dispersion of the data around the median, we adopted the IQR, which includes 50% of the central values.

Consistent with our previous findings at $\Omega=0.6$ (Stigliano et al., 2021), the biggest increase in surface roughness occurred, for all saturation states, at early times of dissolution, as evidenced from the first VSI acquisitions at ~ 15 hours. The sharpness of the increase in R_a showed inverse proportionality with respect to Ω : more aggressive conditions of the fluid (i.e., lower Ω) resulted in higher alteration of the calcite surface, whereas progressively higher Ω led to lower surface roughness development. After this initial increase, the temporal evolutions of R_a at different saturation states tended to reach mostly non-overlapping plateau values, with $R_{a, \Omega=0} = 90.4 \pm 5.2$ nm, $R_{a, \Omega=0.1} = 72.0 \pm 4.9$ nm, $R_{a, \Omega=0.3} = 28.1 \pm 3.7$ nm, $R_{a, \Omega=0.55} = 5.4 \pm 0.5$ nm, $R_{a, \Omega=0.65} = 3.2 \pm 0.4$ nm, and $R_{a, \Omega=0.8} = 1.0 \pm 0.3$ nm (computed as averages of the median values over the 3 final temporal acquisitions, with the \pm symbol indicating the range of variability in the median values). This indicates the achievement of a steady-state configuration of the surface roughness at all Ω . We therefore focused our statistical analysis on R_a values at the final time, as representative of the steady-state configurations. Figure 4.3 depicts the box plots computed on the 30+ R_a values for all Ω , showing a linear relationship in semi log-scale. To assess the statistical significance of the $R_a - \Omega$ trend at the final time, we performed one-tailed Wilcoxon rank-sum tests, specifically to check if the median value of R_a corresponding to each Ω value was significantly lower than the median value of R_a corresponding to the closest smaller Ω

value (i.e., $R_{a, \Omega=0.8} < R_{a, \Omega=0.65}$). The null hypothesis was that the median of the first dataset was greater than or equal to the median of the second dataset, and the alternative hypothesis was that the median of the first dataset was less than the median of the second dataset. For all datasets with $\Omega \geq 0.3$, the null hypothesis could be rejected with a p-value $\ll 0.005$, whereas the null hypothesis $R_{a, \Omega=0.1} \geq R_{a, \Omega=0}$ could be rejected only if the p-value threshold was set to 0.05. We therefore concluded that the $R_a - \Omega$ trend at the final time was statistically significant at all saturation states, and highly statistically significant for $\Omega \geq 0.3$. Note that, at all times, for $\Omega = 0$ and $\Omega = 0.1$, the dispersion-to-median ratio was higher than for all other saturation states, as clearly visible in Figure 4.3 at the final times. The higher dispersion of R_a values for these two saturation states can be explained by the fact that these are the only two experimental conditions producing well-developed etch pits (see Figure 4.7), which resulted into an overall more heterogeneous surface topography. Moreover, as the size of the sampling window was smaller than the size of the larger etch pits, the R_a measurement varied significantly if the specific sub-window was located at the bottom of the pit or if corners / edges were partially included. This effect also contributed to additionally skewing the datasets.

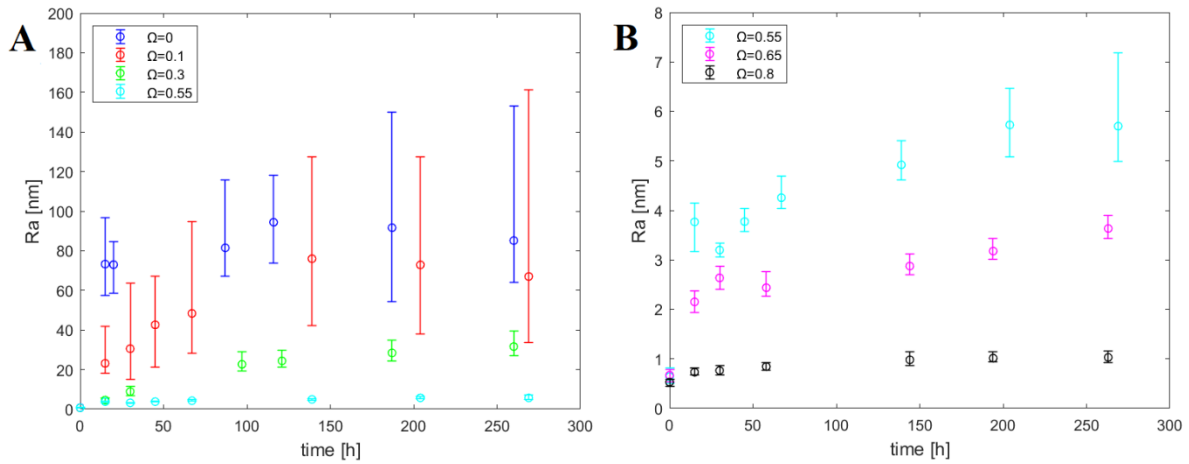


Figure 4.2 Comparison of the temporal evolution of R_a evaluated over 30+ sub-windows of $80 \times 80 \mu\text{m}^2$ for all saturation states: A) $\Omega=0, 0.1, 0.3, 0.55$; B) $\Omega=0.55, 0.65, 0.8$. The circles and the associated bars represent the median values and the corresponding interquartile intervals.

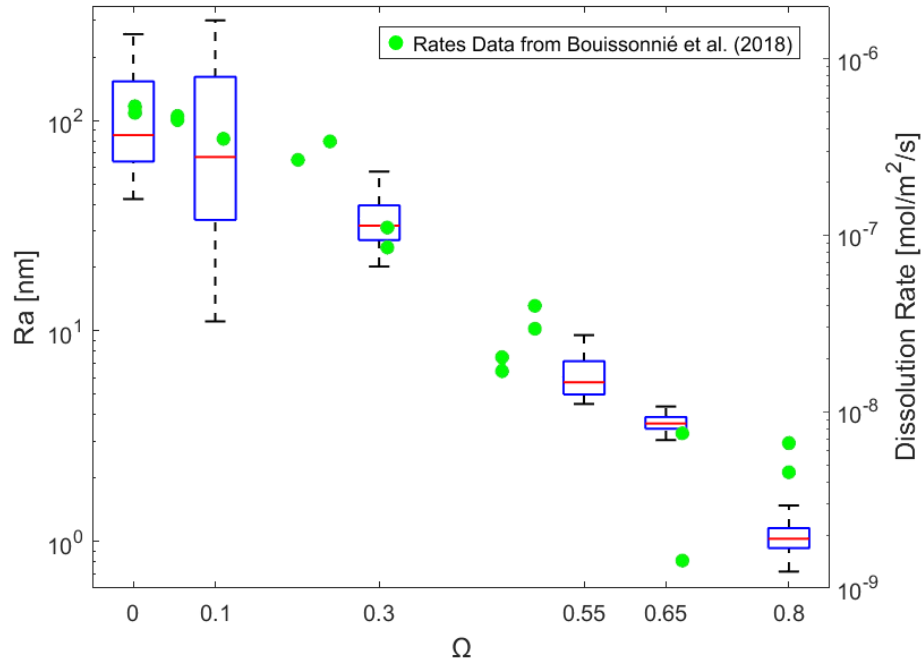


Figure 4.3 Box plots of R_a evaluated over 30+ sub-windows of $80 \times 80 \mu\text{m}^2$ at the final time as a function of Ω . Steady-state dissolution rates as a function of Ω derived from Bouissonnié et al (2018) in similar experimental conditions are also included. In such a semi log-scale representation, steady-state dissolution rates are thus shown to be strongly correlated to steady-state R_a values.

4.3.2 Time-resolved large-windows statistical analyses

4.3.2.1 Topography evolution as described by PSD and variograms

Figure 4.4 and Figure 4.5 show the power spectral density and experimental semi-variograms of the surface topography, Z , evaluated, for all saturation states, as a function of time ($t = 0$ hours, early, mid, and late times) across a given sub-window of $400 \times 400 \mu\text{m}^2$. Examples of VSI images showing the final surface topography for the various Ω values can be found in Figure 4.7. Consistent with the time-resolved R_a analysis on small-windows, for all saturation states, the largest development in surface roughness was detected at early stages of dissolution ($t = 15$ hours) (Figure 4.4 and Figure 4.5). Subsequently, the increase in surface roughness due to dissolution gradually diminished from early-to-mid and from mid-to-late times, pointing towards the achievement of a steady-state configuration of the surface. In general, for all saturation states, the PSD and the semi-variogram move towards higher values with time, until the curves evaluated at mid and late times quasi-overlap (Figure 4.4 and Figure 4.5), indicating a temporal stabilization of the surface in all cases. This increase in values reflected an increase

in surface roughness at all frequencies for the PSD and an overall increase in spatial variability for the semi-variogram. However, it is important to note that the increase was not constant across all frequencies and separation distances. Properly characterizing in detail this evolution over the full range of frequencies and lags can provide valuable insights into the dissolution processes at different Ω . At $\Omega = 0.8$, for low wavevector values (i.e., lower than $\sim 0.06 \mu\text{m}^{-1}$), the PSD, over time, remained mostly identical to those evaluated at $t = 0$ hours, whereas it convincingly increased in the mid-to-high interval (i.e., between ~ 0.06 and $10 \mu\text{m}^{-1}$), indicating a change in surface texture at small scales. Additionally, the semi-variogram structure was conserved from $t = 0$ h to $t > 0$ h (i.e., the semi-variogram plateau was reached at approximately the same lag), while moving towards higher semi-variogram values. When combined, these two pieces of information suggested that, upon dissolution, the large-scale surface texture mostly remained unaltered, while small-scale surface features either emerged (i.e., become detectable at the VSI-scale) or became more pronounced. This reflected the slight deepening of the polishing scratches that were already detectable at $t = 0$ h, along with the concomitant appearance of additional scratches, presumably occurring as a result of the preferential dissolution caused by the strain field induced by the polishing process (Figure B3). Similarly, at $\Omega = 0.65$, dissolution led to the deepening of pre-existing polishing scratches (Figure B4). Differently from what can be observed at $\Omega = 0.8$, the PSD evaluated at $\Omega = 0.65$ evolved in time towards higher values at all frequencies, reflecting a more uniform deepening of the polishing scratches due to dissolution. Differently from what we observed at $\Omega = 0.8$ and $\Omega = 0.65$, for $\Omega \leq 0.55$, the surface topographies resulting from dissolution did not inherit any pre-existing topographic features from the initial surface. Nevertheless, upon dissolution, the general trend of the PSD and semi-variogram moving towards higher values at all frequencies and lags was preserved, suggesting that the increase in surface roughness may be induced by a fundamental underlying dissolution mechanism over the whole Ω range. Lastly, we point out how, for $\Omega = 0.1$ and $\Omega = 0$, the semi-variogram from early to mid/late times moved towards higher values while reaching its plateau value at larger separation distances, mirroring the gradual development of etch pits in terms of both planar and vertical growth. Overall, for all saturation states, PSD and semi-variogram provided consistent pieces of information, showing mutually compatible temporal evolution. Note that the PSD and semi-variogram curves evaluated for $\Omega \leq 0.3$ at early time were higher than those evaluated for $\Omega \geq 0.65$ at steady-state, indicating that 15 hours of dissolution at far from equilibrium conditions were sufficient to produce a degree of surface roughness significantly higher than the maximum attainable at close-to-equilibrium. As in the previous section, we then focused our statistical analysis on

surface topography data acquired at the final time, as they are representative of the steady-state configuration of the surfaces.

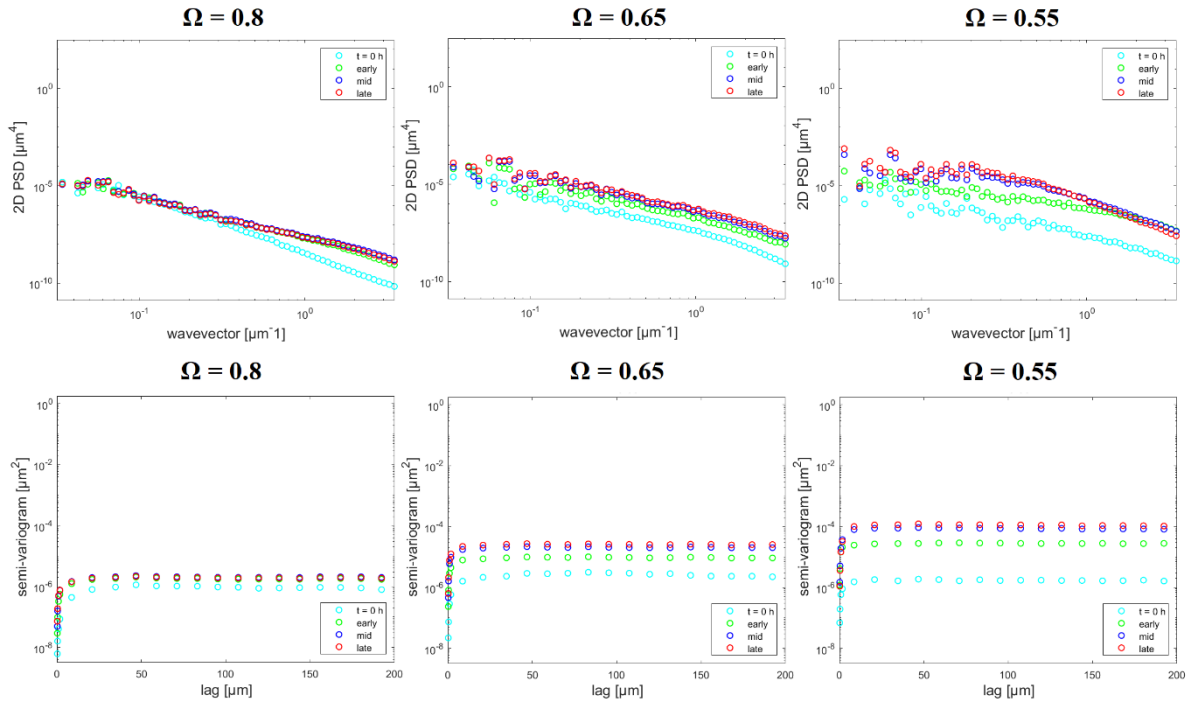


Figure 4.4 Comparison of the temporal evolution of PSD (top row) and semi-variogram (bottom row) evaluated on a given observation window of $400 \times 400 \mu\text{m}^2$ for $\Omega = 0.8, 0.65, 0.55$.

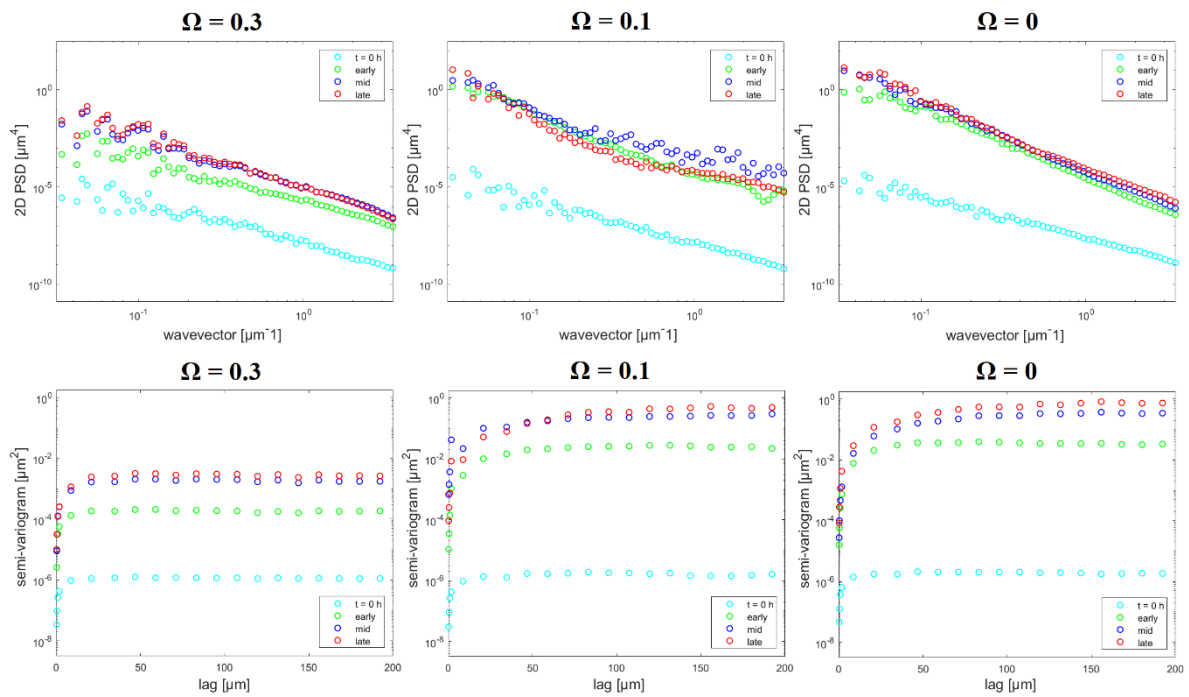


Figure 4.5 Comparison of the temporal evolution of PSD (top row) and semi-variogram (bottom row) evaluated on a given observation window of $400 \times 400 \mu\text{m}^2$ for $\Omega = 0.3, 0.1, 0$.

4.3.2.2 Steady-state PSD and variograms

Figure 4.6 shows the PSD and (experimental and theoretical) semi-variograms of the surface topography Z evaluated, for each Ω , over 3 sub-windows of $400 \times 400 \mu\text{m}^2$, at the final time (as described in the Materials and Methods section). Evaluations of PSD and semi-variograms at different Ω resulted in curves that were, at least partially, non-overlapping, even when considering the variability introduced by the 3 different observation windows. This indicated that the surface topographies resulting from dissolution at different Ω were statistically distinguishable, based on PSD and semi-variogram characterizations. When plotted on a log-log scale, the PSD exhibited a non-linear behavior over the whole range of wavevector values for all Ω , indicating a complex roughness pattern over multiple scales. However, some common features could be identified across all Ω . For instance, in all cases, there was an important drop in the power signal detected at high wavevector values, which indicated an important decrease in surface roughness at small-scale. It should be noted how, at close-to-equilibrium conditions (i.e., $\Omega = 0.8, 0.65, 0.55$), the PSD-curves partially overlapped at low and high wavevector values, while being clearly differentiable from the curves evaluated at $\Omega \leq 0.3$ over the whole wavevector range. This suggests that, at close-to-equilibrium conditions, the specific imprints left on surfaces by fluids with different degrees of undersaturation could only be detected at the intermediate-scale. In contrast, highly undersaturated fluids (i.e., far-from-equilibrium) resulted in surfaces with textures that were significantly different at all scales compared to close-to-equilibrium dissolution, which is in line with the switch in the dissolution mechanism. Notably, the PSD curve at $\Omega = 0.55$ exhibits a slightly distinct behavior compared to the other curves at close-to-equilibrium conditions. It stands apart by displaying a plateau for low wavevector values, suggesting that the surface topography at this particular condition is predominantly characterized by long-wavelength patterns. Similarly, the PSD curve at $\Omega = 0.3$ departs from the other curves at far-from-equilibrium for low wavevector values, reflecting a lower development of etch pits compared to $\Omega = 0.1$ and $\Omega = 0$. Interpretations of high vector values (i.e., very-high-frequency region) should be cautious. As the VSI lateral resolution is approached, the PSD sampling rate for a specific wavevector decreases, and the signal-to-noise ratio deteriorates. However, a plateau can be observed at far-from-equilibrium for wavevector values larger than $10 \mu\text{m}^{-1}$, particularly evident at $\Omega = 0$. The presence of such ‘very-high-frequency plateau’ can be interpreted as the remnant of roughness induced by the dominant topographical features (e.g., large etch pits at $\Omega = 0$ and $\Omega = 0.1$). Nevertheless, the observation that such a plateau value tends to be consistently higher at $\Omega = 0$ compared to $\Omega = 0.1$ suggests that there is also a concomitant increase in high-frequency roughness that is not directly related

to etch pits development as Ω decreases. This also explains why the plateau values are higher at far-from-equilibrium compared to close-to-equilibrium. The PSD analysis also revealed that the level of heterogeneity amongst the three different sub-windows, for a given Ω , was considerably higher at far-from-equilibrium (particularly noticeable at $\Omega = 0.1$ and $\Omega = 0$) compared to close-to-equilibrium conditions. Specifically, under close-to-equilibrium conditions, the three PSD curves obtained from the three different sub-windows almost overlapped, indicating a relatively low degree of heterogeneity at the crystal surface. In contrast, at far-from-equilibrium conditions, some variations emerged, especially at $\Omega = 0.1$ and $\Omega = 0$, the conditions for which well-developed etch pits were observed. The increased level of heterogeneity at the crystal surface arose from variations in the spatial distribution of etch pits, both in terms of density and size, which reflects distinct spatial distributions of crystal defects at various locations along the calcite surface.

For final time semi-variogram comparisons at different saturation states, we relied on evaluations of the exponential model parameters (i.e., correlation length ($3*a$), and partial sill ($C - \gamma(0)$), as depicted in Figure 4.8. The parameters C and a were derived using the least squares regression method with a prescribed nugget value of $5.2 \times 10^{-8} \mu\text{m}^2$ (Table 1). The nugget value was estimated based on 30 repeated VSI acquisitions at 50x magnification over an area of $400 \times 400 \mu\text{m}^2$ of a mechanically-polished calcite surface, as representative of the lowest level of roughness considered in this study. It was calculated as the average of the variance values evaluated across repeated height measurements for each given pixel. The repeated measurements have been conducted in environmental conditions (e.g., vibration level) comparable to those present during the acquisitions of the experimental topography data, and with identical VSI settings. The graph shows the two model parameters as a function of Ω in semi log-scale, both exhibiting an approximately linear trend with negative slope. The correlation length (i.e., the separation distance above which the height values are no longer spatially correlated) tended to decrease as the saturation state increased. At $\Omega = 0$ and $\Omega = 0.1$, the larger correlation length can be explained by the presence of well-developed etch pits, whereas, at $\Omega = 0.65$ and $\Omega = 0.8$, the lower correlation length is primarily determined by the polishing scratches (deepened by preferential dissolution), which dominate the overall topography (see Figure 4.7). In general, far-from-equilibrium conditions resulted in surfaces with more persistent autocorrelation over a greater distance, whereas surfaces reacted at closer-to-equilibrium conditions gradually exhibited a more rapid decline in spatial autocorrelation over shorter distances. Data points at $\Omega \geq 0.55$ deviated from this linear trend (when plotted in semi log-scale), presumably due to the impact of residual features from the initial topography

(as in Figure B3 and Figure B4). Similarly, the partial sill (i.e., the semi-variogram plateau value minus the nugget) convincingly decreased as Ω increased. This indicates that conditions of higher undersaturation of the fluid (i.e., low Ω) progressively led to surface structures with higher variance of the height values. Overall, the semi-variogram analysis at the final time suggested that, as the saturation state decreased, the surface became more variable over larger separation distances and the differences between the height values became more pronounced.

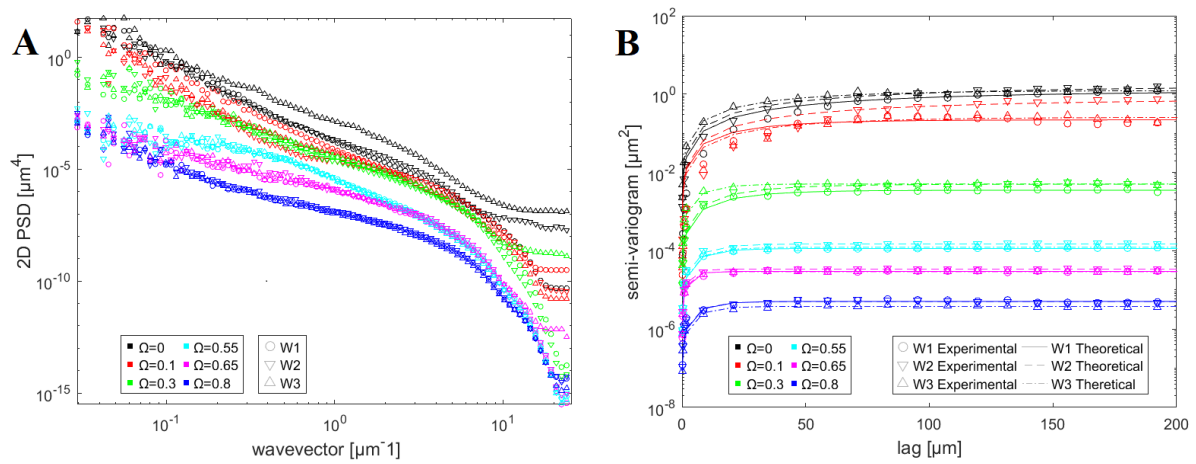


Figure 4.6 A) PSD and B) semi-variogram evaluated over 3 windows of $400 \times 400 \mu\text{m}^2$ for all Ω , at the final time. The semi-variogram plot displays for all sub-windows the experimental semi-variograms as symbols (i.e., circles, downward triangles, and upward triangles), with their model counterparts shown as lines (i.e., respectively, solid, dashed, and dashed-dot lines).

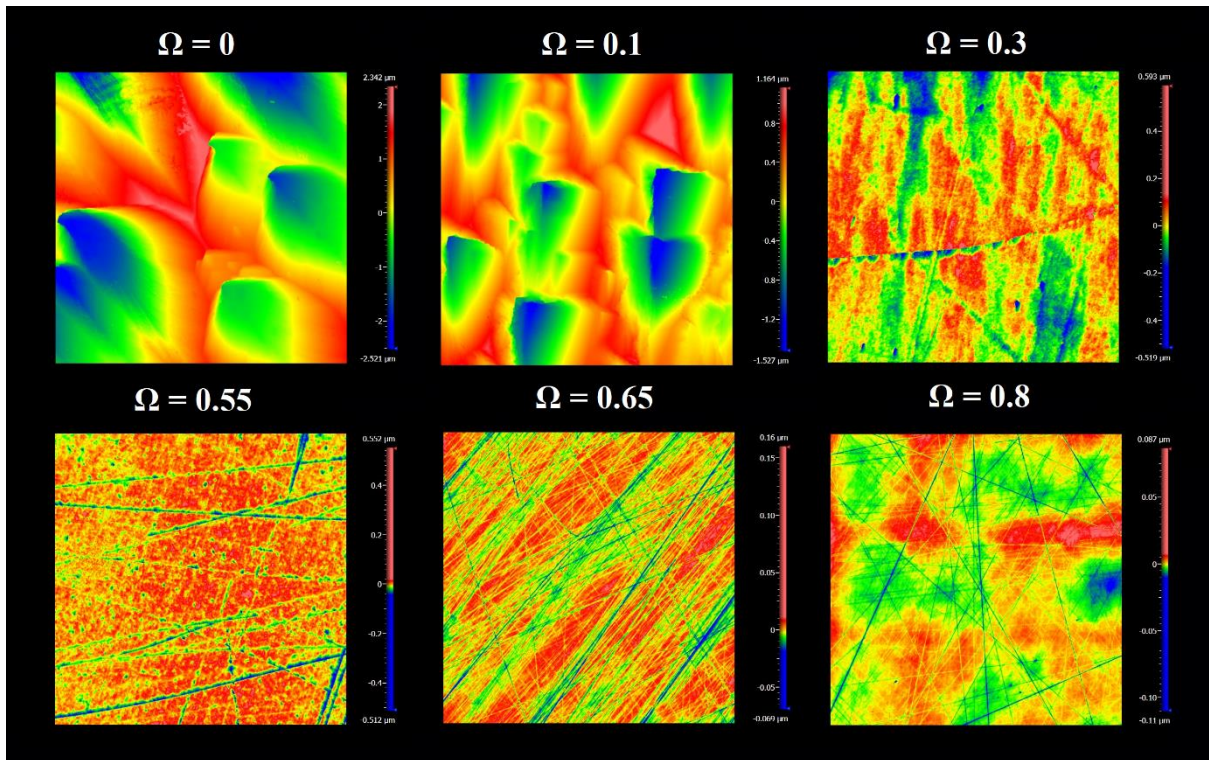


Figure 4.7 Images of surface topography data acquired with VSI at 50x magnification over a given observation window of $400 \times 400 \mu\text{m}^2$ for all Ω , at the final time.

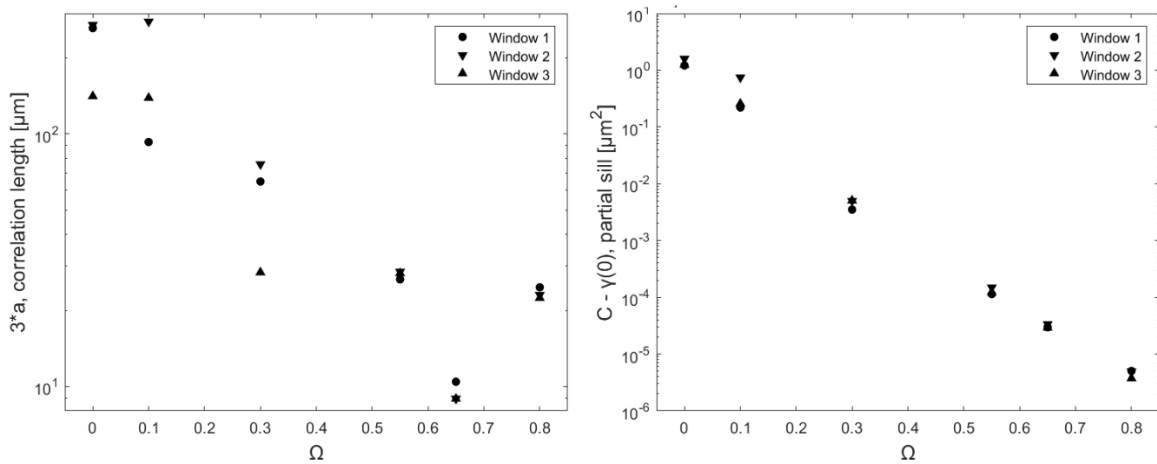


Figure 4.8 Semi-variogram model parameters (correlation length, $3*a$, and partial sill, $(C - \gamma(0))$ evaluated, for each saturation state, over 3 sub-windows of $400 \times 400 \mu\text{m}^2$, at the final time, plotted as a function of Ω .

Ω	$3*a$ [μm]			C [μm^2]			R^2		
	W1	W2	W3	W1	W2	W3	W1	W2	W3
0.00	262.53	270.27	141.00	1.21E+00	1.59E+00	1.24E+00	0.97	0.98	0.97
0.10	92.85	278.40	138.87	2.20E-01	7.45E-01	2.57E-01	0.87	0.95	0.89
0.30	64.77	75.81	28.29	3.51E-03	4.99E-03	5.06E-03	0.98	0.98	0.98
0.55	26.55	28.47	28.08	1.14E-04	1.49E-04	1.23E-04	0.99	0.99	0.98
0.65	10.44	8.94	8.94	2.97E-05	3.38E-05	2.92E-05	0.97	0.98	0.99
0.80	24.69	23.04	22.41	5.10E-06	5.04E-06	3.80E-06	0.94	0.96	0.96

Table 4.1 Table of semi-variogram model parameters (correlation length, $3*a$, and total sill, C) evaluated, for each saturation state, over 3 sub-windows of $400 \times 400 \mu\text{m}^2$, at the final time, corresponding to data displayed in Figure 4.8. A prescribed nugget value of $5.2\text{E-}8$ was used for the semi-variogram fitting. Corresponding R-squared values are also included.

4.4 Discussion

Our results suggest that, under the investigated experimental conditions, the steady-state configuration of calcite surfaces undergoing dissolution at different saturation states are statistically distinguishable. Below, we first describe the results of numerical simulations based on previously published stochastic dissolution models at the atomic-scale to ascertain the key processes that are required to support these results from a theoretical perspective. The combination of the outputs of statistical characterizations and numerical modeling is then used to discuss whether the steady-state surface topography of minerals resulting from dissolution at different Ω values can be used as a proxy of the saturation state of the fluid under which dissolution occurred.

4.4.1 Stochastic simulations of calcite dissolution as a function of Ω

4.4.1.1 Classical kMC modeling

Standard kMC modeling was applied as described in the Materials and Methods section. The parameter values used in the simulations were: $E_b = 16 \text{ kJ/mol}$, $T = 22 \text{ }^\circ\text{C}$ and $\nu = 10^{12} \text{ s}^{-1}$. The values for the bond-breaking activation energy, E_b , and frequency factor, ν , were selected from the range of possible values compatible with *ab initio* calculations (see (Ackerer et al., 2021; Carrasco et al., 2021)). The surface topographies resulting from simulations at different saturation states ($\Omega=0$, $\Omega=0.4$ and $\Omega=0.8$) are depicted in Figure 4.9 (2D representation) and in Figure B5 (3D representation). In contrast to our experimental observations, the long-term simulated dissolution led to the opening of hollow cores to form etch pits over the whole range

of Ω values investigated, which in turn resulted in the achievement of a similar Ra value at steady-state (Figure B6). The only observable difference in the steady-state surface topography could be detected at $\Omega=0.8$, with the etch pit showing more rounded steps and corners than those obtained at lower saturation states, as a result of more frequent re-precipitation events. Extending such simulations over windows of size equivalent to the VSI-scale would lead to the formation of micro-scale etch-pits, which are not observable experimentally for $\Omega > \Omega_{\text{critical}}$ (i.e., the saturation state threshold above which the formation of etch pits is no longer thermodynamically favored, which is ~ 0.45 for calcite; e.g., (Bouissonnié et al., 2018), and references therein). With these simulation settings, the presence of a constant source of highly reactive sites around the pre-opened hollow core eventually leads to the formation of an etch pit, regardless of the saturation state. The saturation state only controls the number of iterations required to achieve a steady-state configuration of the etch pit, with larger saturation states implying more iterations (Figure B6). Therefore, with the standard settings adopted for the investigated conditions, the kMC model fails to reproduce the evolution of the surface topography resulting from dissolution as a function of the saturation state that we observed experimentally.

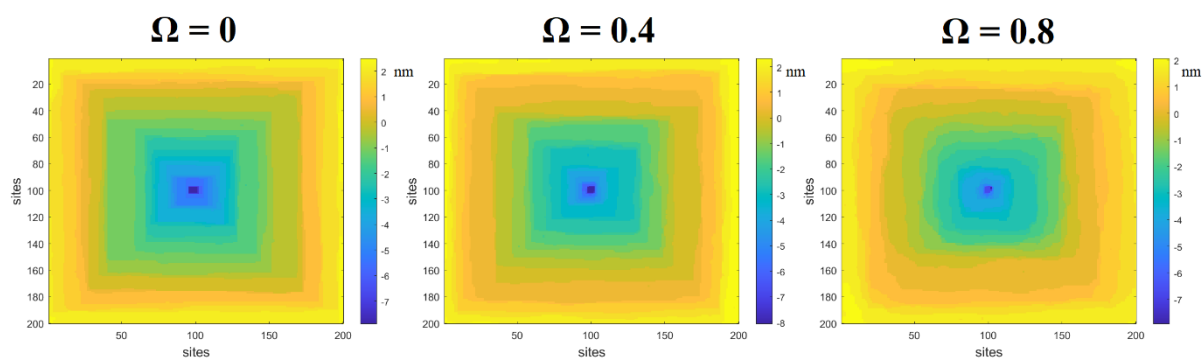


Figure 4.9 Comparison of steady-state surface configurations after dissolution at $\Omega=0$, $\Omega=0.4$ and $\Omega=0.8$, resulting from simulations with standard kMC modeling. The screw dislocations were implemented as pre-opened hollow cores of diameter 4×4 lattice sites and as deep as the whole simulated crystal.

4.4.1.2 Ising modeling

The Ising model was applied with parameter values arbitrarily set to: $\gamma = \eta = 3$. The surface topographies resulting from simulations at different saturation states ($\Omega=0$, $\Omega=0.4$ and $\Omega=0.8$) are depicted in Figure 4.10 (2D representation) and Figure B7 (3D representation). Consistent with our experimental observations and contrary to the output of classical kMC modeling, the

long-term simulated dissolution does not lead to the opening of hollow cores to form etch pits at close-to-equilibrium conditions ($\Omega=0.8$), despite the presence of a pre-opened hollow core. Moreover, at far-from-equilibrium, the pre-opened hollow core opens up to form etch pits that vary in depth as a function of Ω , which stems from the general expression of dissolution and precipitation probabilities. Overall, this allows one to reproduce the Ω -roughness trend observed experimentally over the whole range of saturation states (Figure 4.11).

The reason why the Ising model successfully reproduces this behaviour can be summarized in a few conceptual features that any potential model possibly needs to capture the surface roughness dynamics observed experimentally. Both the kMC and Ising models express the dissolution and precipitation probability of a given site as a function of the number of nearest neighbors. However, the Ising model produces ‘rougher surfaces’ because the relative differences in dissolution probability between differently coordinated sites is much lower than in the kMC model: $P_{d,i+1}/P_{d,i} < 1$ for Ising model, whereas $P_{d,i+1}/P_{d,i} \lll 1$ for kMC model, with $i = 1, 2, 3, 4$. In other words, while in the kMC model the layer-by-layer dissolution is mostly driven by kink sites only, in the Ising model, all sites participate more significantly to the global dissolution rate. To satisfy this feature with the kMC model, unrealistically lower values of the bond-breaking activation energy would need to be chosen.

The other key model feature is the relative importance of the precipitation probabilities of the sites with 4 and 5 nearest neighbors with respect to the dissolution probabilities of the sites with 1 and 2 nearest neighbors. In the Ising model, the precipitation events of sites forming 4 or 5 bonds play a significant role in compensating the roughness generated by the dissolution events. Additionally, this makes the surface roughness evolution more sensitive to the saturation state, which eventually is key to establish the Ω -roughness trend observed experimentally. Of note, the shape of etch pits, which is more rounded compared to simulations conducted with kMC modeling (see Figure B5 for kMC model and Figure B7 for Ising model), could still be refined by changing the values of γ and η . Here we did not try to find the combination that best reproduces the etch pit shape, as it was not the main goal of the modeling.

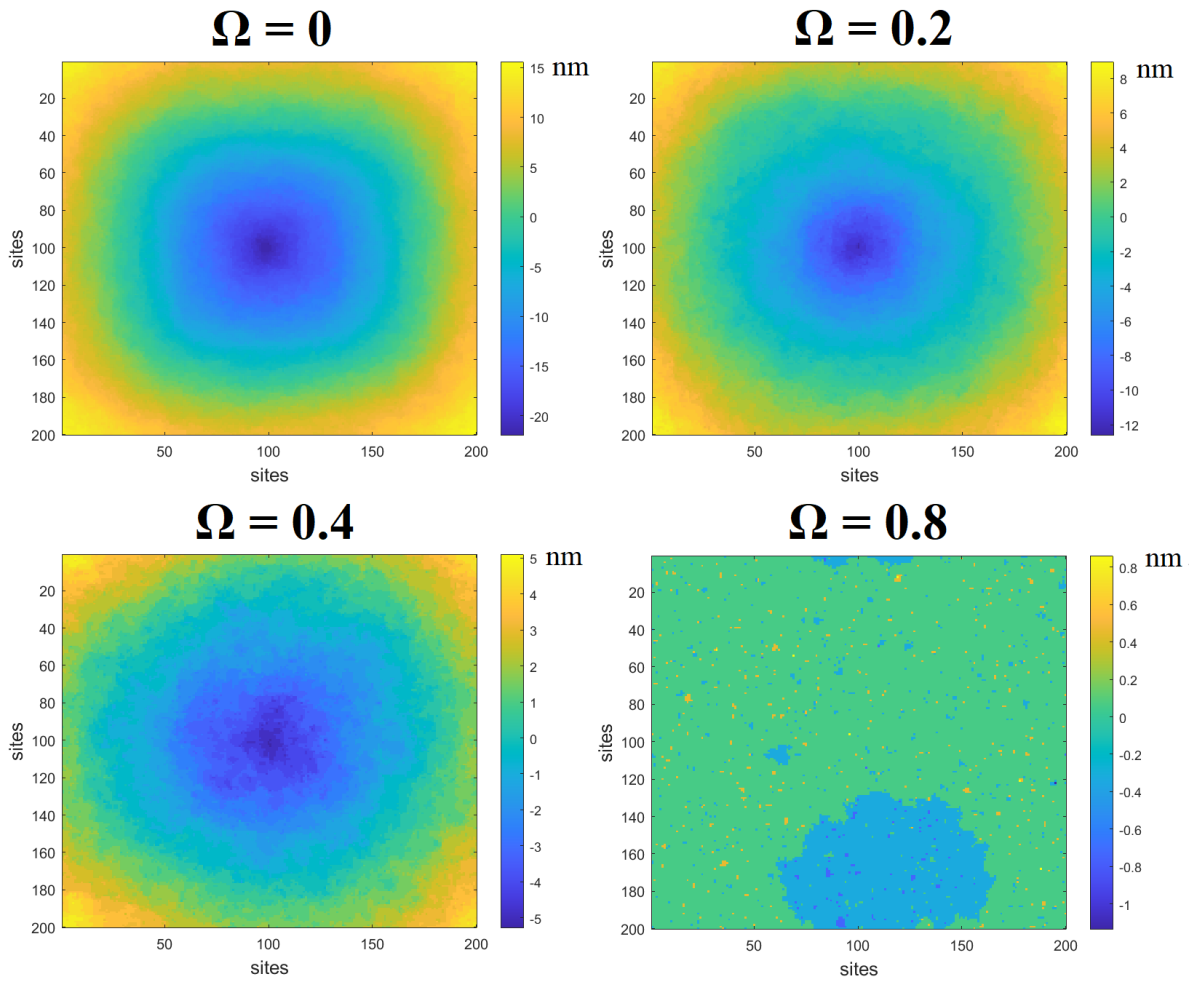


Figure 4.10 Comparison of steady-state surface configurations after dissolution at $\Omega=0$, $\Omega=0.2$, $\Omega=0.4$ and $\Omega=0.8$, resulting from simulations with Ising modeling. The screw dislocations were implemented as pre-opened hollow cores of diameter 1×1 lattice sites at the center of the simulation window in all cases. Despite the presence of a pre-opened hollow core, the Ising model does not form an etch pit at $\Omega=0.8$.

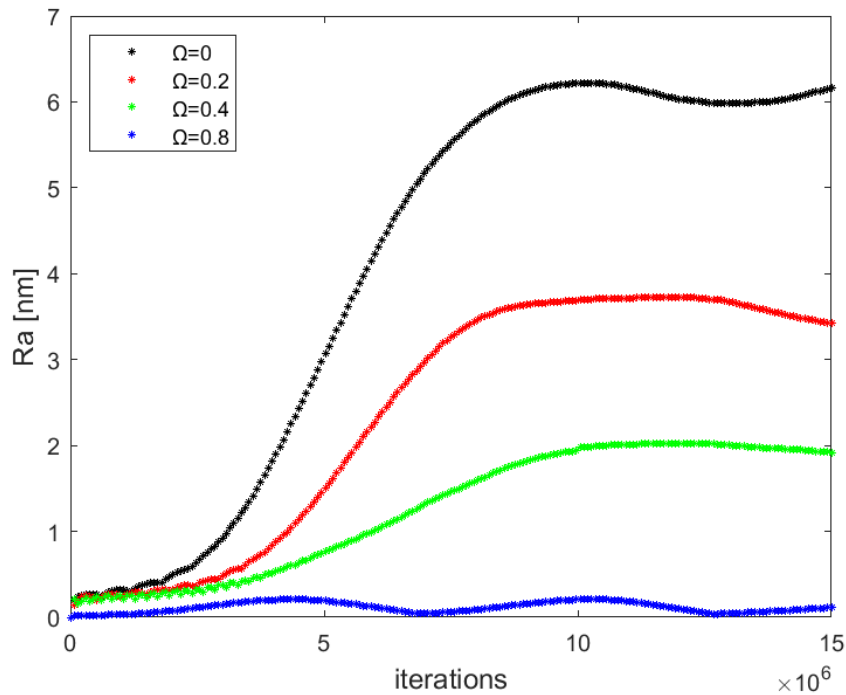


Figure 4.11 Comparison of R_a evaluated over the steady-state surface configurations resulting from dissolution at $\Omega=0$, $\Omega=0.2$, $\Omega=0.4$ and $\Omega=0.8$, simulated with Ising modeling. The pre-opened hollow core was excluded from the calculation of R_a . The different plateau values of R_a indicate the achievement of different steady-state configurations of the surface as a function of the saturation state.

4.4.2 Surface roughness: a relevant proxy for back-tracking past water-rock interaction conditions?

Several pre-requisites must be fulfilled for surface roughness to be a relevant proxy of past water-rock interactions: (i) surface roughness must reach a steady-state value for a given fluid composition; (ii) the roughness- Ω relationship must be bijective, (iii) the roughness- Ω relationship must not be impacted by the starting topographic configuration, while the transient period during which the surface topography evolves from one configuration to another must remain short compared to the duration of the water-rock interaction event that is tracked. These three aspects are discussed in the three subsections below.

4.4.2.1 Evidence for a temporal stabilization of the roughness towards a steady-state configuration: a pre-requisite to infer the solution composition

The dynamic nature of a dissolving crystal surface has long raised the question of the existence of a steady-state microtopographic configuration that would no longer depend on time and/or the reaction progress. Intimately related to this question, the recognition that mineral reactivity

decreased with time following a power law (Maher et al., 2004; Vance et al., 2009; White and Brantley, 2003) and references therein) has fuelled this debate and raised the question of the time required for a steady-state to develop, or even the existence of such a steady-state (Köhler et al., 2005; Weissbart and Rimstidt, 2000).

From an experimental standpoint, few studies have reported time-resolved statistical analyses of the roughness of crystal surfaces undergoing dissolution, with contrasted results. Regarding experiments conducted with mineral powders, most of them focused on the relationship between the temporal evolution of the surface area typically quantified through BET and geometric surface area measurements, which are related through the so-called ‘roughness factor’ (roughness factor = BET surface area / geometric surface area). The BET surface area measurement is based on the Brunauer-Emmett-Teller (BET) theory, which relates the amount of gas adsorbed by a given material to its total surface area. In contrast, the geometric surface area measurement refers to the total surface area of a material based solely on its geometric properties, such as shape and size. The ‘roughness factor’, therefore, quantifies the deviations of the actual surface from a hypothetical smooth surface (Anbeek, 1992). Although several studies reported a temporal increase in the roughness factor with time (e.g. (Gautier et al., 2001)), the use of BET surface area as a criterion to decipher the evolution of the roughness of the crystalline surface has been subsequently questioned for silicate minerals, since post-dissolution specific surface areas can be altered by interference from porous altered surface layers that are not representative of the surface area of the dissolving crystalline surface ((Daval et al., 2010) and references therein).

In the light of such shortcomings, the link between surface morphology and mineral reactivity has also been extensively studied on single crystal surfaces, specifically by looking at the evolution of the mineral surface microtopography during dissolution with high-resolution techniques, such as atomic force microscopy (AFM) or high-resolution optical microscopies (e.g., confocal profilometry, phase-shift interferometry, VSI, (Saldi et al., 2017)) and references therein). For instance, Pollet-Villard et al. (2016) evaluated the evolution of the experimental semi-variogram over the AFM surface topography of a (001) orthoclase surface after far-from-equilibrium dissolution at $T = 180\text{ °C}$ and $\text{pH} = 9$ (Pollet-Villard et al., 2016b). Over the short duration of their experiments (< 5 days), the variance of the surface topography observed a continuous increasing trend. Similarly, Saldi et al. (2017) investigated the surface topography evolution of different cleavage $\{10\bar{1}4\}$ faces and miscut surfaces parallel to the $\{0001\}$ crystallographic plane of dolomite single crystals during dissolution at $T = 50\text{ °C}$ and pH of \sim

4.7 (Saldi et al., 2017). An increasing trend of the RMS surface roughness with time was reported, suggesting that a morphological steady state may not be reached at the surface of dolomite under the investigated conditions. Godinho et al. (2014) investigated the temporal evolution of the Ra surface roughness of different fluorite faces subjected to dissolution at $T = 21\text{ }^{\circ}\text{C}$ and pH of ~ 3.6 , showing that a steady-state configuration was reached for the (115), (334), (104) and (245) faces (with distinguishable plateau values), whereas it was not achieved for the (102) and (110) faces (Godinho et al., 2014). Conversely, the achievement of a steady-state configuration of the surface roughness was reported by Li et al. (2021) for the (010) olivine face after dissolution at room temperature and pH of ~ 1.0 (Li et al., 2021). Together with the experimental results of the present work, these previous studies suggest that the steady-state configuration of the surface roughness resulting from dissolution is both crystallographically- and fluid-controlled, and that a critical reaction progress needs to be observed prior to possibly reaching a steady-state.

The impact of different thermodynamic and kinetic parameters on the evolution of the surface area and reactivity of minerals was also explored through numerical modeling. Several studies based on kMC modeling of far-from-equilibrium dissolution investigated the evolution of nanosized grains with different size and shape (e.g., (Carrasco et al., 2021) and references therein) and of mineral surfaces at different temperatures and for different values of activation energy for molecular detachment (Carrasco et al., 2021). For instance, Carrasco et al. (2021) showed that for a bond-breaking activation energy of $E = 16.0 \pm 0.7\text{ kJ/mol}$ and fixed temperature, the dissolution of an initially flat surface of a defect-free Kossel crystal results into a steady-state configuration of the surface roughness, which reflects the achievement of a constant number of kink sites at the surface (Carrasco et al., 2021). Moreover, sensitivity analyses revealed that higher temperatures and / or lower values of the bond-breaking activation energy result in rougher surfaces at steady-state. Interestingly, Ackerer et al. (2021) reached comparable conclusions in their modeling work, following similar approaches (Ackerer et al., 2021). Finally, several stochastic and deterministic modeling exercises aimed at investigating the dynamics of defect-driven crystal reactivity concluded that etch pit coalescence played a key role in the attainment of steady-state roughness and associated crystal dissolution rate at far-from-equilibrium conditions ((Lasaga and Lutge, 2001a; Pollet-Villard et al., 2016b) and references therein).

In the present study, all experiments and simulations converge towards the conclusion that the mechanically-polished calcite surface microtopography reaches a steady-state on timeframes of

the order of tens of hours at most, which is consistent with previous studies (MacInnis and Brantley, 1992; Stigliano et al., 2021). From an experimental standpoint, the steady-state roughness is apparently controlled by the fluid saturation state, with higher roughness corresponding to lower fluid saturation states. Only the time required to reach a steady-state differs from experiment to experiment. As a first approximation, it appears that the difference between the initial and final roughness is the parameter that primarily controls the duration of the transient period. From a numerical standpoint, a common point in all simulations, regardless of the considered model, is the existence of a steady-state surface roughness for all Ω values considered. Note that, for all Ω values, this transient time may vary for different initial surfaces depending on the difference in surface roughness between the initial surface and the final equilibrium configuration, as further discussed in Section 4.4.2.3. The reason for the achievement of a steady-state configuration relies on the fact that both kMC and Ising models fundamentally link the sites reactivity to the number of nearest neighbours. Consequently, while a certain degree of surface roughness is necessary for dissolution to occur, its evolution is limited by the fact that isolated sites (i.e., sites with only one neighbour) are associated with much higher reactivity compared to the rest of the surface and therefore dissolve preferentially. This inevitably leads to a stabilization of the surface roughness that, otherwise, could potentially increase indefinitely. Such a balance between more reactive and less reactive sites is reflected by the stabilization of kink sites at the surface over time (see, e.g., (Ackerer et al., 2021; Bouissonnié et al., 2020a; Bouissonnié et al., 2020b)), which testifies the achievement of a mean steady-state that energetically integrates over all different surface sites.

In summary, and to the best of our knowledge, this study is the first of its kind that demonstrates both from experimental and theoretical standpoints that the surface roughness of a crystalline surface subjected to dissolution eventually reaches a steady-state value for all fluid saturation states. This is a strong pre-requisite to possibly use this relation as a proxy for back-estimating fluid composition for past water-rock interactions. Future efforts should focus on enhancing the statistical characterization of the steady-state surface roughness resulting from dissolution and extending it to various conditions. For instance, VSI Power Spectral Density characterizations of the steady-state configuration could be expanded to higher frequencies through the complementary use of AFM, in accordance with the methodology outlined by Gong et al. (2016) ((Gong et al., 2016)). These approaches have the potential to identify on weathered mineral surfaces additional imprints of the fluid composition. Below, we briefly discuss the second pre-

requisite that needs to be observed for roughness to be a relevant indicator of the fluid composition, that is, the uniqueness of such a relation.

4.4.2.2 Is the Ω -roughness relation bijective?

A striking aspect of the experimental work described in Section 4.3 is the seemingly bijective nature of the relation between roughness and Ω , which seems to be an intrinsic property of crystal dissolution. To the best of our knowledge, very few studies have addressed this question, either experimentally or numerically. From an experimental standpoint, as emphasized in the introduction section, our current knowledge is basically limited to the description of etch pit formation at far-from-equilibrium conditions, corresponding to higher surface roughness compared to closer-to-equilibrium conditions, where etch pit nucleation is no longer spontaneous. Strikingly, modeling studies have not reached much more detailed conclusions, as the characterization of surface roughness was not central to these previous works, which were primarily aimed at investigating rate- Ω relations (e.g., (Kurganskaya and Lutge, 2021; Martin et al., 2020; Martin et al., 2019)). When combined with the numerical simulations conducted in the present study (see Section 4.4.1), two important conclusions can be drawn from kMC simulations run with a simple Kossel crystal structure and bond-breaking probabilities consistent with *ab initio* calculations:

(i) the steady-state roughness of a dissolving defect-free surface (which can be seen as an ideal surface for which no dislocation etch pits are formed, corresponding to close-to-equilibrium conditions) remains independent of Ω and systematically very low. This is consistent with the fact that the low reactivity of terrace sites limits the topography to 2-3 atomic layers only (as observed in this work over the whole Ω -range and from (Carrasco et al., 2021) for far-from-equilibrium dissolution at room temperature);

(ii) for simulations run with surfaces including outcropping dislocations, the steady-state surface roughness is much higher and does not depend on Ω .

As a consequence, kMC simulations run with a simple Kossel crystal structure and a bond-breaking activation energy larger than ~ 5 -10 kJ/mol (defined as the threshold for kink-dominated surfaces; see (Ackerer et al., 2021)) cannot predict the bijective relation observed experimentally. Therefore, either the input parameters need to be adjusted (and will thus depart from their theoretical values estimated from first principles), or a higher level of freedom needs to be allowed to the model for it to be successful.

The sensitivity analyses that we ran while developing the model that best captures the roughness- Ω trend observed experimentally highlighted two important results: (i) decreasing the gap between the dissolution probability of terrace sites and that of other sites having fewer number of bonds tends to increase the overall surface roughness, while limiting the contribution of dislocation etch pits to the overall roughness at close-to-equilibrium conditions; (ii) allowing for the precipitation at sites other than kink sites, with a precipitation probability that increases with the connectivity of the site, makes the surface roughness evolution more sensitive to the saturation state. Of note, the Ising model proposed by Bandstra and Brantley (2008) meets both requirements, explaining why it is successful in this regard (Bandstra and Brantley, 2008).

Importantly, while the Ising model provided the best agreement between simulations and observations, this does not fully rule out the possibility that simulations based on the classical kMC formalism (i.e., based on bond-breaking and bond-forming activation energies, as described by Equation 4.4 and Equation 4.5) may satisfactorily reproduce the experimentally observed roughness- Ω trend. For instance, Martin et al (2019) suggested that if the bond-forming activation energy was significantly higher than the bond-breaking activation energy, spontaneous terrace vacancies can be created and pit opening can be more favorable than adatom removal (Martin et al., 2019). This would result in increased surface roughness over the whole Ω range, which is a prerequisite to obtain a bijective roughness- Ω relation. Secondly, more sophisticated formulations can be proposed for the bond-breaking activation energy reflecting the existence of nonequivalent kink sites for calcite as proposed by Kurganskaya and Lutge (2021) (Kurganskaya and Lutge, 2021). This results in a modification of the apparent bond-breaking activation energy at those sites. If this modification goes in the direction of a decrease in the apparent activation energy, this would in turn decrease the gap between the reactivity of terrace and kink sites, which represents another prerequisite to obtain a bijective roughness- Ω relation.

Finally, comparing the outputs of all those models to the experimental measurements assumes that the trends revealed numerically at the atomic-level faithfully reflect the trends observed experimentally at the nanometer-level. While this assumption was implicitly followed in previous studies (e.g., (Bandstra and Brantley, 2008)), it is important to recall that surface roughness is a scale-dependent parameter, so that the transfer of information from one scale to another is not trivial (see the extensive work by Fischer and Lutge (2007), (Fischer and Lutge, 2007)). Alternative approaches using mesoscale models could then represent a promising

avenue of research (e.g., (Stigliano et al., 2021)), although to the best of our knowledge, such models would only be empirical at this stage.

4.4.2.3 Promises and obstacles for the use of Ω -roughness relations as a proxy to infer past weathering conditions

In our previous study (Stigliano et al., 2021), we suggested that mineral surfaces exhibiting left-skewed, leptokurtic topography distribution might be a distinctive feature of minerals that have been subjected to dissolution. Here, we further argue that when the reaction occurs under ideal, well-controlled conditions (i.e., starting with statistically identical mineral surfaces and reacted in solutions of fixed chemical composition differing only in their saturation state), negative correlations between steady-state roughness configuration and solution saturation state represent an emerging intrinsic feature of mineral dissolution. Comparing these results with rates data from (Bouissonnié et al., 2018), it can be noted how both the steady-state R_a values and the steady-state dissolution rates decrease linearly in semi log-scale as a function of Ω (see Figure 4.3. Such correlation suggests that, after a transient phase in which roughness and reactivity are dictated by the interaction between the fluid and the ‘current surface configuration’ (e.g., (Bose et al., 2008; Fischer et al., 2018; Kurganskaya and Luttge, 2021)), the interaction between the bulk solution and the surface eventually leads towards a minimization of the surface energy, whose configuration is strictly dependent on the saturation state. However, prior to using such a new tool to back-estimate the conditions under which fluid-mineral reactions occurred, e.g., for paleoenvironmental reconstructions, several issues would need to be tackled. This includes knowledge of the impact of: (i) the initial surface microtopography; (ii) possible fluctuations in fluid composition on steady-state surface roughness; and (iii) whether these results apply to calcite only, or whether they might be extended to other rock-forming minerals. We will now examine these three issues in detail.

(i) The rationale for examining the impact of the starting surface microtopography on steady-state roughness is two-fold. First, it is frequently argued that mineral grinding and/or polishing result in an increase in high energy sites and associated transient dissolution regimes that are not representative of long-term weathering (e.g., (Eggleston et al., 1989) and references therein). Consequently, one might argue that the results described above might be an artifact of the methods followed to conduct the study. Second, the breakdown of minerals which occurs along cleavage planes both in the field and in the laboratory usually results in heavily stepped surfaces, even on fields of view as small as a few 10s of microns on a side, similar to those used in the present study (see microphotographs in (Ruiz-Agudo et al., 2009) as an example).

As further explained below, it is challenging to address this point from an experimental perspective, as the time required to erase a given starting topographic configuration may not be compatible with reasonable experimental timescales. Conversely, numerical modeling appears well suited to tackle this question, as it allows one to run a wide variety of sensitivity tests over short timescales. As a consequence, here we tested the impact of initial surface roughness configuration using the Ising model that was shown to best reproduce the roughness- Ω relations revealed experimentally. The following initial configurations have been tested: (i) a perfectly flat surface with $R_a = 0$ nm; (ii) a surface composed of normally distributed height values, with mean = 0 nm and standard deviation = 15 nm, resulting in $R_a = 4.8$ nm; and (iii) a stepped surface containing 2 steps with height of 20 nm and 40 nm, overall resulting in $R_a = 15$ nm. The simulations were run for two Ω values ($\Omega = 0.2$ and $\Omega = 0.8$) representative of far-from and close-to-equilibrium conditions, respectively. As can be seen in Figure 4.12, after a transient phase of variable duration that depends both on the roughness of the initial surface and Ω , the relaxation of the surface converges towards a unique final roughness that depends only on the saturation state at which the simulations were run. In addition, by using the simulated surface retreat as a function of the number of iterations to calculate a conversion factor between iterations and elapsed time, it is possible to estimate the relaxation time for the different initial surface configurations. By doing so, we found that if the difference in surface roughness between the initial and the equilibrium configuration is sufficiently large (or, in other words, if the initial surface is sufficiently rough), the higher the saturation state, the longer the transient phase. This seems a reasonable result, since lower Ω values correspond to higher dissolution rates. Of note, starting from a surface with a step of a few microns (e.g., a cleaved surface), the estimated elapsed time to reach steady-state at $\Omega = 0.8$ is in the order of months. This sensitivity analysis highlights two important results: first, investigating the impact of initial roughness on steady-state surface roughness experimentally would have required durations that are hardly compatible with laboratory constraints for close-to-equilibrium conditions. Second, and more importantly, such durations remain short compared to geologic timescales, suggesting that calcite surface microtopography might preserve imprints related to the composition of the latest aqueous fluid that contacted calcite surface.

(ii) The rationale for examining the impact of possible fluctuations in fluid composition on steady-state surface roughness is also two-fold: first, in the field, the reaction conditions are rarely buffered to well-constrained physicochemical conditions, but are rather impacted at various frequencies by environmental fluctuations such as rainfall or temperature (e.g., see the

calculations of the impact of seasonal variations on the saturation state of pore water in a soil profile conducted by (Wild et al., 2019a)). Second, it has been previously observed experimentally and theoretically that the nucleation of etch pits inherited from fluid-mineral interactions at far-from-equilibrium conditions could keep on driving mineral reactivity at close-to-equilibrium conditions, where the nucleation of etch pits is no longer spontaneous (Arvidson and Luttge, 2010; Beig and Luttge, 2006; Kurganskaya and Luttge, 2021), resulted in so-called ‘non-steady state dissolution rates’. In other words, the reactivity of crystalline materials is inherited from the reaction history, as underlined by the modeling work of Fischer et al (2018) (Fischer et al., 2018).

To test for the consequences of oscillations in the fluid composition, we used the Ising model to simulate the impact of a sudden switch in solution saturation from $\Omega = 0.8$ to $\Omega = 0.2$ and then back to 0.8 on calcite surface microtopography, starting from an initially perfectly flat surface. Note that such a switch can be considered as an extreme and most likely unrealistic scenario in natural settings, except for anthropic perturbations such as subsurface CO₂ injection, which may result in a dramatic drop of the pore water by several pH units within time frames of a few days (e.g., (Kampman et al., 2014) and references therein). As can be seen in Figure 4.13, the surface roughness evolves from a steady-state value representative of $\Omega = 0.8$ to ultimately stabilize to a new value that is characteristic to the Ω value at which the simulation was run. Similarly, after the second switch in Ω , the surface roughness gradually decreases to reach a value that is indistinguishable from the roughness calculated before the first switch in Ω . This latter result is consistent with the results shown Figure 4.12: the roughness of the surface ultimately stabilizes to a value that is representative of the ongoing fluid saturation state, irrespective of the starting roughness of the surface. Note that the characteristic time to reach this new steady-state value is, again, intimately related to the starting roughness value and dissolution rate, itself dictated by the fluid saturation state.

Lastly, it should be noted how variations in fluid composition caused by the presence of both framework and impurity ions can also potentially modify the calcite surface roughness resulting from dissolution. For instance, the presence of given free ions in the aqueous solution, such as Mg²⁺ or SO₄²⁻, has been shown to alter the density and depth of etch pits on calcite surfaces ((Ruiz-Agudo et al., 2009)) and the corresponding etch pits morphology ((Gao et al., 2010)). This can potentially modify the surface roughness resulting from dissolution and should, therefore, be taken into consideration when interpreting Ω -roughness relationships.

(iii) Overall, the results above pinpoint that calcite represents a good candidate to potentially preserve imprints representative of the latest fluid composition of the waters that interacted with this mineral. As emphasized in previous studies, the time required to reach steady-state dissolution rate – and correspondingly, steady-state surface topography – is short, with estimates ranging from minutes ((Bandstra and Brantley, 2008)) to hours ((MacInnis and Brantley, 1992) and this study) at far-from-equilibrium, and from hours to months at close-to-equilibrium ((Stigliano et al., 2021) and this study) at room temperature. Moreover, Bose et al. (2018) introduced the concept of ‘topographic relaxation time’, which refers to the processes associated with time-dependent alterations in dissolution kinetics and surface morphology that occur following a sudden change in solution chemistry ((Bose et al., 2008)). Based on their theoretical formulation, estimates of the relaxation time for calcite can range from a few hours to a few days. This intrinsically high reactivity is key to ensure that the surface topography measured at a given time does not represent an integrated, transient state that is not representative of steady-state conditions. Conversely, Bandstra et al. (2008) suggested that the time required to reach steady-state for silicate minerals could be 2 to 5 orders of magnitude larger than that for calcite (in agreement with the much lower reactivity of silicates), which would require that the fluid composition remain stable over up to tens of thousands of years under close-to-equilibrium conditions to preserve imprints of the latest fluid composition interacting with the minerals (Bandstra and Brantley, 2008). This is the first clear limitation of the extension to silicate minerals of surface roughness measurements as a proxy for fluid composition. But more importantly, the weathering of silicate minerals is also characterized by the build-up of submicron-thick silica layers, both in the field and in laboratory (Daval et al., 2011; Hellmann et al., 2012; Nugent et al., 1998), the roughness of which is completely beyond crystallographic control (Jordan et al., 1999; Wild et al., 2019b). In addition to the complicating factor represented by the attachment of secondary phases to the surface of primary minerals (for which sonication is not always sufficient to reveal the altered surface of primary minerals), such aspects need to be addressed in dedicated studies to reach definitive conclusions regarding the use of surface roughness as a proxy for the conditions under which fluid-rock interactions occurred.

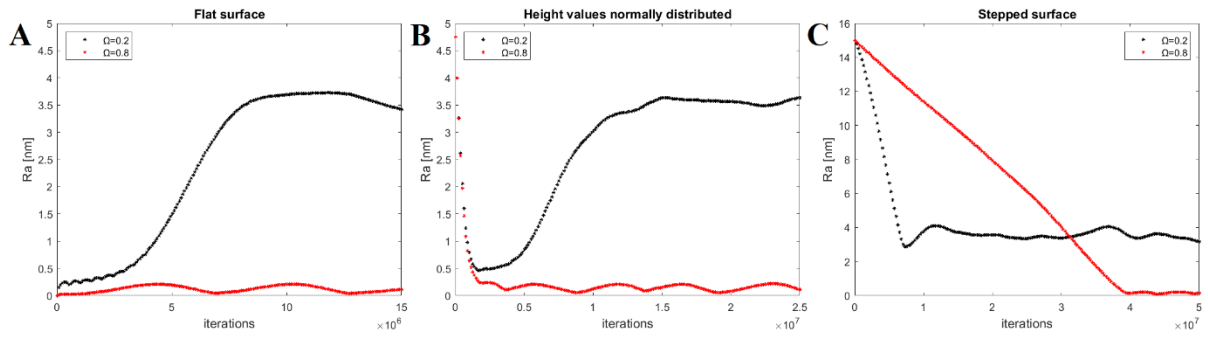


Figure 4.12 Comparison of the R_a evolution as a function of the number of iterations at $\Omega = 0.2$ and $\Omega = 0.8$ for systems with different initial surface configurations, as described in 4.2.3: (A) a perfectly flat surface; (B) a surface composed of normally distributed height values, (C) a stepped surface. Note that the steady-state roughness for a given Ω is the same, regardless of the initial surface configuration.

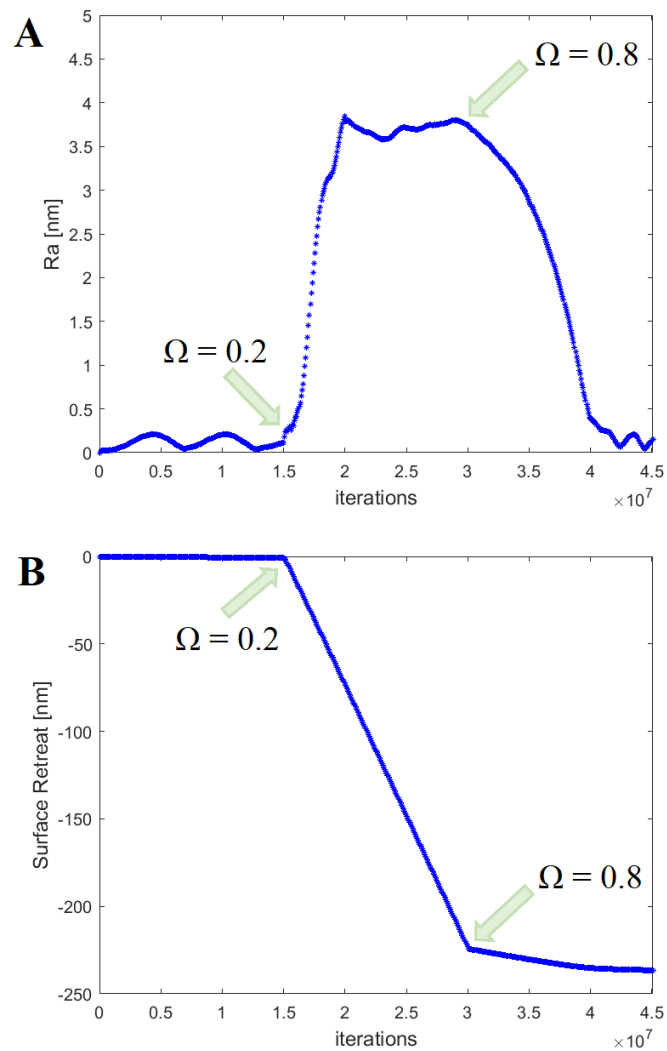


Figure 4.13 R_a evolution as a function of the number of iterations for a system undergoing a sudden switch in solution saturation from $\Omega = 0.8$ to $\Omega = 0.2$ and then back to $\Omega = 0.8$. After a transient time, the surface always reaches a steady-state configuration that is only indicative of the saturation state of the fluid, while erasing the imprints left on the surface by the saturation state visited previously. Note the asymmetry in the transient times: overwriting the smoother surface resulting from dissolution at $\Omega = 0.8$ with the rougher surface resulting from dissolution at $\Omega = 0.2$ requires less time than what is needed for the opposite pathway.

4.5 Conclusions

We investigated the potential of the calcite surface microtopography (as quantified through surface roughness characterizations) to be quantitatively informative of past weathering conditions. Two main pre-conditions have to be met to achieve this purpose: (i) the calcite surface needs to evolve towards a steady-state configuration that is determined by the fluid saturation state, Ω , and (ii) the steady-state configurations obtained at different Ω values must be statistically distinguishable from each other. In the present study, we provided experimental evidence and theoretical validation that both conditions apply under the investigated conditions. In particular, based on a combination of unidimensional descriptors (R_a) and spatial statistics metrics (PSD and semi-variogram) analyses, we derived experimentally a seemingly bijective Ω -roughness relation for which larger roughness evaluations correspond to lower Ω values. The validity of this empirical relation was corroborated by Ising dissolution modeling of a Kossel crystal, suggesting that the behavior observed experimentally might be an intrinsic property of crystal dissolution.

Additionally, we used the Ising model to investigate the impact of the initial surface topography and of Ω fluctuations on the steady-state configuration of the crystal surface. We showed that, in a timeframe negligible compared to geological timescales (i.e., \sim in the order of months at most), the crystal surface reaches a new steady-state configuration that only depends on the fluid saturation state most recently visited. Therefore, the present study suggests that information related to the fluid chemistry can be retrieved from the fine analysis of surface roughness of calcite, which is a prerequisite to possibly extend this finding to carbonate minerals altered in natural settings, including extraterrestrial contexts (for the record, a similar approach has been used with the Mars lander Phoenix, which carried an AFM among the instruments onboard to possibly evidence etching features at the surface of grains (see (Velbel

and Losiak, 2010)). Finally, one of the main challenges that needs to be overcome is to identify natural settings that exhibit the most suitable conditions of preservation (i.e., minerals that ceased to be in contact with a fluid while remaining protected from erosion mechanisms).

Further research should also focus on the identification of Ω -signals on naturally weathered minerals to confirm the generality of our findings. However, as far as carbonate minerals are concerned, promising targets could be buried geological formations, fossilized organisms and cave formations, with potential relevance to terrestrial and Martian contexts.

References

- Ackerer, P., Bouissonni e, A., di Chiara Roupert, R., Daval, D., 2021. Estimating the activation energy of bond hydrolysis by time-resolved weighing of dissolving crystals. *npj Mater. Degrad.* 5 (1), 48.
- Anbeek, C., 1992. Surface roughness of minerals and implications for dissolution studies. *Geochim. Cosmochim. Acta* 56 (4), 1461–1469.
- Arvidson, R.S., Luttge, A., 2010. Mineral dissolution kinetics as a function of distance from equilibrium - New experimental results. *Chem. Geol.* 269 (1–2), 79–88.
- Arvidson, R.S., Collier, M., Davis, K.J., Vinson, M.D., Amonette, J.E., Luttge, A., 2006. Magnesium inhibition of calcite dissolution kinetics. *Geochim. Cosmochim. Acta* 70, 583–594.
- Bandstra, J.Z., Brantley, S.L., 2008. Surface evolution of dissolving minerals investigated with a kinetic Ising model. *Geochim. Cosmochim. Acta* 72 (11), 2587–2600.
- Beig, M.S., Luttge, A., 2006. Albite dissolution kinetics as a function of distance from equilibrium: Implications for natural feldspar weathering. *Geochim. Cosmochim. Acta* 70, 1402–1420.
- Berner, R.A., Sjoberg, E.L., Velbel, M.A., Krom, M.D., 1980. Dissolution of pyroxenes and amphiboles during weathering. *Science* 207 (4436), 1205–1206.
- Bose, S., Hu, X.M., Higgins, S.R., 2008. Dissolution kinetics and topographic relaxation on celestite (001) surfaces: the effect of solution saturation state studied using atomic force microscopy. *Geochim. Cosmochim. Acta* 72 (3), 759–770.
- Bouissonni e, A., Daval, D., Marinoni, M., Ackerer, P., 2018. From mixed flow reactor to column experiments and modeling: upscaling of calcite dissolution rate. *Chem. Geol.* 487, 63–75.
- Bouissonni e, A., Daval, D., Ackerer, P., 2020a. Dissolution anisotropy of pyroxenes: a surrogate model for steady-state enstatite dissolution resulting from stochastic simulations of the hydrolysis process. *J. Phys. Chem. C* 124 (24), 13113–13126.
- Bouissonni e, A., Daval, D., Guyot, F., Ackerer, P., 2020b. The dissolution anisotropy of pyroxenes: experimental validation of a stochastic dissolution model based on enstatite dissolution. *J. Phys. Chem. C* 124 (5), 3122–3140.
- Brantley, S.L., Crane, S.R., Crerar, D.A., Hellmann, R., Stallard, R., 1986. Dissolution at dislocation etch pits in quartz. *Geochim. Cosmochim. Acta* 50 (10), 2349–2361.
- Briese, L., Arvidson, R.S., Luttge, A., 2017. The effect of crystal size variation on the rate of dissolution – a kinetic Monte Carlo study. *Geochim. Cosmochim. Acta* 212, 167–175.
- Carrasco, I.S.S., Aar ao Reis, F.D.A., 2021. Modeling the kinetics of calcite dissolution in neutral and alkaline solutions. *Geochim. Cosmochim. Acta* 292, 271–284.
- Carrasco, I.S.S., Machado, E.A., Reis, F.D.A.A., 2021. Simulations of dissolution of initially flat calcite surfaces: retreat velocity control and surface roughness scaling.

- ACS Earth Space Chem. 5 (10), 2755–2767. Daval, D., Sissmann, O., Corvisier, J., Garcia, B., Martinez, I., Guyot, F., Hellmann, R., 2010. The Effect of Silica Coatings on the Weathering Rates of Wollastonite (CaSiO₃) and Forsterite (Mg₂SiO₄): An Apparent Paradox.
- Daval, D., Sissmann, O., Menguy, N., Saldi, G.D., Guyot, F., Martinez, I., Corvisier, Garcia, B., Machouk, I., Knauss, K.G., Hellmann, R., 2011. Influence of amorphous silica layer formation on the dissolution rate of olivine at 90 degrees C and elevated pCO₂. Chem. Geol. 284 (1–2), 193–209.
- Daval, D., Hellmann, R., Saldi, G.D., Wirth, R., Knauss, K.G., 2013. Linking nm-scale measurements of the anisotropy of silicate surface reactivity to macroscopic dissolution rate laws: new insights based on diopside. Geochim. Cosmochim. Acta 107 (0), 121–134.
- Daval, D., Calvaruso, C., Guyot, F., Turpault, M.-P., 2018. Time-dependent feldspar dissolution rates resulting from surface passivation: experimental evidence and geochemical implications. Earth Planet. Sci. Lett. 498, 226–236.
- Duckworth, O.W., Martin, S.T., 2004. Role of molecular oxygen in the dissolution of siderite and rhodochrosite. Geochim. Cosmochim. Acta 68 (3), 607–621.
- Eggleston, C.M., Hochella, M.F., Parks, G.A., 1989. Sample preparation and aging effects on the dissolution rate and surface-composition of diopside. Geochim. Cosmochim. Acta 53 (4), 797–804.
- Emmanuel, S., 2014. Mechanisms influencing micron and nanometer-scale reaction rate patterns during dolostone dissolution. Chem. Geol. 363, 262–269.
- Fischer, C., Luttge, A., 2007. Converged surface roughness parameters – a new tool to quantify rock surface morphology and reactive alteration. Am. J. Sci. 307.
- Fischer, C., Arvidson, R.S., Lüttge, A., 2012. How predictable are dissolution rates of crystalline material? Geochim. Cosmochim. Acta 98 (0), 177–185.
- Fischer, C., Kurganskaya, I., Luttge, A., 2018. Inherited control of crystal surface reactivity. Appl. Geochem. 91, 140–148.
- Fisk, M.R., Giovannoni, S.J., Thorseth, I.H., 1998. Alteration of oceanic volcanic glass: textural evidence of microbial activity. Science 281 (5379), 978–980.
- Gao, P., Wang, Z., Fu, W., Liao, Z., Liu, K., Wang, W., Bai, X., Wang, E., 2010. In situ TEM studies of oxygen vacancy migration for electrically induced resistance change effect in cerium oxides. Micron 41 (4), 301–305.
- Gautier, J.M., Oelkers, E.H., Schott, J., 2001. Are quartz dissolution rates proportional to BET surface areas? Geochim. Cosmochim. Acta 65 (7), 1059–1070.
- Gilmer, G.H., 1980. Computer Models of Crystal Growth, 208, pp. 355–363 (4442).
- Gilmer, G.H., Bennema, P., 1972. Simulation of Crystal Growth with Surface Diffusion, 43, pp. 1347–1360.
- Godinho, J.R.A., Piazzolo, S., Balic-Zunic, T., 2014. Importance of surface structure on dissolution of fluorite: implications for surface dynamics and dissolution rates. Geochim. Cosmochim. Acta 126, 398–410.

- Gong, Y., Misture, S.T., Gao, P., Mellott, N.P., 2016. Surface roughness measurements using power spectrum density analysis with enhanced spatial correlation length. *J. Phys. Chem. C* 120 (39), 22358–22364.
- Gringarten, E., Deutsch, C.V., 2001. Teacher's aide variogram interpretation and modeling. *Math. Geol.* 33 (4), 507–534.
- Guinoiseau, D., Fekiacova, Z., Allard, T., Druhan, J.L., Balan, E., Bouchez, J., 2021. Tropical weathering history recorded in the silicon isotopes of lateritic weathering profiles, 48 (19) e2021GL092957.
- Hellmann, R., Wirth, R., Daval, D., Barnes, J.-P., Penisson, J.-M., Tisserand, D., Epicier, T., Florin, B., Hervig, R.L., 2012. Unifying natural and laboratory chemical weathering with interfacial dissolution–reprecipitation: a study based on the nanometer-scale chemistry of fluid–silicate interfaces. *Chem. Geol.* 294–295 (0), 203–216.
- Jacobs, T.D.B., Junge, T., Pastewka, L., 2017. Quantitative characterization of surface topography using spectral analysis. *Surf. Topogr. Metrol. Prop.* 5 (1), 013001.
- Jordan, G., Higgins, S.R., Eggleston, C.M., Swapp, S.M., Janney, D.E., Knauss, K.G., 1999. Acidic dissolution of plagioclase: In-situ observations by hydrothermal atomic force microscopy. *Geochim. Cosmochim. Acta* 63 (19–20), 3183–3191.
- Kampman, N., Bickle, M., Wigley, M., Dubacq, B., 2014. Fluid flow and CO₂–fluid–mineral interactions during CO₂-storage in sedimentary basins. *Chem. Geol.* 369 (0), 22–50.
- Köhler, S.J., Bosbach, D., Oelkers, E.H., 2005. Do clay mineral dissolution rates reach steady state? *Geochim. Cosmochim. Acta* 69 (8), 1997–2006.
- Kontakiotis, G., Mortyn, P.G., Antonarakou, A., Martínez-Botí, M.A., Triantaphyllou, M. V., 2011. Field-based validation of a diagenetic effect on *G. ruber* Mg/Ca paleothermometry: core top results from the Aegean Sea (eastern Mediterranean), 12 (9).
- Kossel, W., 1927. *Mathematisch-Physikalische Klasse. Zur theorie des kristallwachstums 1927*, 135–143.
- Kurganskaya, I., Luttge, A., 2013. A comprehensive stochastic model of phyllosilicate dissolution: structure and kinematics of etch pits formed on muscovite basal face. *Geochim. Cosmochim. Acta* 120 (0), 545–560.
- Kurganskaya, I., Luttge, A., 2016. Kinetic Monte Carlo approach to study carbonate dissolution. *J. Phys. Chem. C* 120 (12), 6482–6492.
- Kurganskaya, I., Luttge, A., 2021. Mineral dissolution kinetics: pathways to equilibrium. *ACS Earth Space Chem.* 5 (7), 1657–1673.
- Lasaga, A.C., Blum, A.E., 1986. Surface chemistry, etch pits and mineral-water reactions. *Geochim. Cosmochim. Acta* 50 (10), 2363–2379.
- Lasaga, A.C., Luttge, A., 2001a. Variation of crystal dissolution rate based on a dissolution stepwave model, 291 (5512), 2400–2404.
- Lasaga, A.C., Luttge, A., 2001b. Variation of crystal dissolution rate based on a dissolution stepwave model. *Science* 291, 2400–2404.

- Lemarchand, D., Cividini, D., Turpault, M.P., Chabaux, F., 2012. Boron isotopes in different grain size fractions: exploring past and present water–rock interactions from two soil profiles (Strengbach, Vosges Mountains). *Geochim. Cosmochim. Acta* 98, 78–93.
- Li, X., Wang, Q., Shen, X., Pedrosa, E.T., Luttge, A., 2021. Multiscale investigation of olivine (010) face dissolution from a surface control perspective. *Appl. Surf. Sci.* 549, 149317.
- Luttge, A., Arvidson, R.S., Fischer, C., Kurganskaya, I., 2019. Kinetic concepts for quantitative prediction of fluid-solid interactions. *Chem. Geol.* 504, 216–235.
- MacInnis, I.N., Brantley, S.L., 1992. The role of dislocations and surface morphology in calcite dissolution. *Geochim. Cosmochim. Acta* 56 (3), 1113–1126.
- Maher, K., DePaolo, D.J., Lin, J.C.F., 2004. Rates of silicate dissolution in deep-sea sediment: in situ measurement using U-234/U-238 of pore fluids. *Geochim. Cosmochim. Acta* 68 (22), 4629–4648.
- Martin, P., Manzano, H., Dolado, J.S., 2019. Mechanisms and dynamics of mineral dissolution: a new kinetic Monte Carlo model, 2 (10), 1900114.
- Martin, P., Gaitero, J.J., Dolado, J.S., Manzano, H., 2020. KIMERA: a kinetic Montecarlo code for mineral dissolution, 10 (9), 825.
- McCave, I.N., Hall, I.R., 2006. Size sorting in marine muds: processes, pitfalls, and prospects for paleoflow-speed proxies, 7 (10).
- Meakin, P., Rosso, K.M., 2008. Simple kinetic Monte Carlo models for dissolution pitting induced by crystal defects. *J. Chem. Phys.* 129 (20), 204106.
- Mellott, N.P., Brantley, S.L., Pantano, C.G., 2002. Topography of Polished Plates of Albite Crystal and Glass during Dissolution.
- Mutaftschiev, B., 2001. The Atomistic Nature of Crystal Growth.
- Nugent, M.A., Brantley, S.L., Pantano, C.G., Maurice, P.A., 1998. The influence of natural mineral coatings on feldspar weathering. *Nature* 395 (6702), 588–591.
- Persson, B.N.J., Albohr, O., Tartaglino, U., Volokitin, A.I., Tosatti, E., 2005. On the nature of surface roughness with application to contact mechanics, sealing, rubber friction and adhesion. *J. Phys. Condens. Matter* 17 (1), R1.
- Phillips-Lander, C.M., Legett, C., Madden, A.S.E., Madden, M.E.E., 2017. Can we use pyroxene weathering textures to interpret aqueous alteration conditions? Yes and No 102 (9), 1915–1921.
- Pollet-Villard, M., Daval, D., Fritz, B., Knauss, K.G., Schäfer, G., Ackerer, P., 2016. Influence of etch pit development on the surface area and dissolution kinetics of the orthoclase (001) surface. *Chem. Geol.* 447, 79–92.
- Ruiz-Agudo, E., Putnis, C., Jimenez-López, C., Rodriguez-Navarro, C., 2009. An atomic force microscopy study of calcite dissolution in saline solutions: the role of magnesium ions. *Geochim. Cosmochim. Acta* 73 (11), 3201–3217.
- Saldi, G.D., Voltolini, M., Knauss, K.G., 2017. Effects of surface orientation, fluid chemistry and mechanical polishing on the variability of dolomite dissolution rates. *Geochim. Cosmochim. Acta* 206, 94–111.

- Sheldon, N.D., Tabor, N.J., 2009. Quantitative paleoenvironmental and paleoclimatic reconstruction using paleosols. *Earth Sci. Rev.* 95 (1), 1–52.
- Siena, M., Guadagnini, A., Bouissonni'e, A., Ackerer, P., Daval, D., Riva, M., 2020. Generalized sub-Gaussian processes: theory and application to hydrogeological and geochemical data. *Water Resour. Res.* 56 (8) e2020WR027436.
- Siena, M., Bussetti, G., Recalcati, C., Riva, M., Du`o, L., Guadagnini, A., 2021. Statistical characterization of heterogeneous dissolution rates of calcite from in situ and realtime AFM imaging. *Transp. Porous Media* 140 (1), 291–312.
- Smith, M.E., Knauss, K.G., Higgins, S.R., 2013. Effects of crystal orientation on the dissolution of calcite by chemical and microscopic analysis. *Chem. Geol.* 360–361 (0), 10–21.
- Stigliano, L., Siena, M., Ackerer, P., Guadagnini, A., Daval, D., 2021. Statistical description of calcite surface roughness resulting from dissolution at close-to-equilibrium conditions. *ACS Earth Space Chem.* 5 (11), 3115–3129.
- Teng, H.H., 2004. Controls by saturation state on etch pit formation during calcite dissolution. *Geochim. Cosmochim. Acta* 68 (2), 253–262.
- van der Lee, J., De Windt, L., 2002. CHESSTutorial and Cookbook. Updated for version 3.0., Manual Nr. LHM/RD/02/13, Paris, 116 pp.
- Vance, D., Teagle, D.A.H., Foster, G.L., 2009. Variable Quaternary chemical weathering fluxes and imbalances in marine geochemical budgets. *Nature* 458 (7237), 493–496.
- Velbel, M.A., Losiak, A.I., 2010. Denticles on chain silicate grain surfaces and their utility as indicators of weathering conditions on Earth and Mars. *J. Sediment. Res.* 80 (9), 771–780.
- Wehrli, B., 1989. Monte Carlo simulations of surface morphologies during mineral dissolution. *J. Colloid Interface Sci.* 132 (1), 230–242.
- Weissbart, E.J., Rimstidt, D.J., 2000. Wollastonite: incongruent dissolution and leached layer formation. *Geochim. Cosmochim. Acta* 64 (23), 4007–4016.
- White, A.F., Brantley, S.L., 2003. The effect of time on the weathering of silicate minerals: why do weathering rates differ in the laboratory and field? *Chem. Geol.* 202 (3–4), 479–506.
- Wild, B., Daval, D., Guyot, F., Knauss, K.G., Pollet-Villard, M., Imfeld, G., 2016. pH-dependent control of feldspar dissolution rate by altered surface layers. *Chem. Geol.* 442, 148–159.
- Wild, B., Daval, D., Beaulieu, E., Pierret, M.-C., Viville, D., Imfeld, G., 2019a. In-situ dissolution rates of silicate minerals and associated bacterial communities in the critical zone (Strengbach catchment, France). *Geochim. Cosmochim. Acta* 249, 95–120.
- Wild, B., Daval, D., Micha, J.-S., Bourg, I.C., White, C.E., Fernandez-Martinez, A., 2019b. Physical properties of interfacial layers developed on weathered silicates: a case study based on labradorite feldspar. *J. Phys. Chem. C* 123 (40), 24520–24532.
- Wilkin, R.T., Barnes, H.L., Brantley, S.L., 1996. The size distribution of framboidal pyrite in modern sediments: an indicator of redox conditions. *Geochim. Cosmochim. Acta* 60 (20), 3897–3912.
- Wille, M., Babechuk, M.G., Kleinhanns, I.C., Stegmaier, J., Suhr, N., Widdowson, M., Kamber, B.S., Schoenberg, R., 2018. Silicon and chromium stable isotopic systematics during basalt

weathering and lateritisation: a comparison of variably weathered basalt profiles in the Deccan Traps, India. *Geoderma* 314, 190–204.

Chapter 5 : Surface imprints of microbial weathering as potential biosignatures

Introduction

The previous chapter documented the existence, under abiotic conditions, of a one-to-one relationship between the steady-state calcite surface roughness resulting from dissolution and the saturation state of the fluid. This suggests that fluid imprints left on weathered minerals can be quantitatively informative of past weathering conditions. In this context, investigating the impact of microorganisms on the Ω -roughness relationship developed abiotically can offer valuable insights into the second fundamental question at the core of this thesis: does microbial weathering result in specific *imprints* at the mineral surface that could be *quantitatively* attributable to the action of life?

To address this question, flow-through dissolution experiments were conducted targeting the same conditions as in the previous study (i.e., $T = 22\text{ }^{\circ}\text{C}$, $\text{pH} = 7.9$, and various saturation states, $\Omega = 0.00, 0.10, 0.30, 0.55, 0.65, 0.80$). However, in this case the calcite surface undergoing dissolution was covered with a biofilm of the cyanobacterium *Chroococcidiopsis thermalis* PCC 7203. Experiments were conducted under continuous light exposure, for a total duration of ~ 4 days (i.e., the relaxation time after which a steady-state surface roughness is attained for all saturation states investigated, under abiotic conditions). The calcite surface topography data resulting from microbially-mediated dissolution at different saturation states were analysed with semi-variogram and PSD analyses, evaluated over regions of $600 \times 600\ \mu\text{m}^2$, and compared with the abiotic counterparts.

The main experimental results showed that, under far-from-equilibrium conditions, biofilm-mediated dissolution produced high-elevation regions (i.e., regions that dissolved less compared to the rest of the surface) at locations where clusters of cells were still sticking to the surface at the end of the experiments. After removal of the cells, these regions could be *quantitatively* detected by the spatial statistical metrics adopted. In contrast, under close-to-equilibrium conditions, abiotically and biotically weathered surfaces were statistically undistinguishable.

Furthermore, the dissolution mechanism behind the formation of these ‘topographic highs’ was further investigated through kMC modeling at far-from-equilibrium conditions. This suggested that the formation of these ‘less dissolved regions’ might be caused by the generation of a

microenvironment at the mineral-biofilm interface in which the saturation state is locally higher compared to that of the bulk solution. Of note, kMC modeling was preferred over Ising models and other empirical models because it is mechanistically supported, being based on *ab initio* calculations. Moreover, while kMC modeling fails to reproduce the evolution of the surface topography observed in abiotic experiments at close-to-equilibrium conditions, it satisfactorily reproduces its evolution at far-from-equilibrium conditions, so that both Ising model or classic kMC model can be used indistinguishably.

Overall, this study offers a novel *mechanistically-supported* methodology to *quantitatively* differentiate abiotically and biotically weathered surfaces, providing an innovative tool for the identification of biosignatures based on the microtopography of naturally weathered samples.

In addition, an unprecedented experiment was conducted using an original flow cell that was designed to monitor *in situ* calcite dissolution with VSI. This experiment was conducted at $\Omega = 0.00$, aiming to closely monitor the dynamics of cyanobacteria cells attachment/detachment and the corresponding contribution to the dissolution process. Preliminary results confirmed that, at far-from-equilibrium conditions, high-elevation-regions are formed at the locations where the cells agglomerate. Furthermore, the VSI *in situ* acquisition setup allowed to generate a ‘bacteria residence time map’, that is a visual representation of the duration of coverage by bacteria of specific areas on the calcite surface during dissolution. This residence time map was found to be positively correlated with the calcite microtopography resulting from dissolution acquired after physically removing all residual cells from the surface. In other words, cells that stuck to the calcite surface for longer times tended to have a larger inhibitory impact of substrate dissolution, strengthening the conclusion that the calcite microtopography may preserve a record of the history of biofilm coverage.

This chapter is divided into two main sub-sections, one dedicated to the findings of the *ex situ* experiments (section 5.1), and the other one dedicated to preliminary results from the *in situ* experiments (section 5.2). Section 5.1 is presented as a research article that will be submitted to *PNAS*.

5.1 Imprints of microbial contribution to mineral weathering detected by statistical characterizations of surface microtopography

Imprints of microbial contribution to mineral weathering detected by statistical characterizations of surface microtopography

Luca Stigliano^{1,2,3}*, Karim Benzerara², Philippe Ackerer³, Nicolas Menguy², Stephan Borensztajn⁴,
Cynthia Travert², Fériel Skouri-Panet², Damien Daval¹

¹ Univ. Grenoble Alpes, Univ. Savoie Mont Blanc, CNRS, IRD, Univ. G. Eiffel, ISTerre, 38000 Grenoble, France

² Sorbonne Université, Museum National d'Histoire Naturelle, UMR CNRS 7590, Institut de Minéralogie, de Physique des Matériaux et de Cosmochimie (IMPMC), 75005 Paris, France

³ ITES Institut Terre et Environnement de Strasbourg - CNRS/Université de Strasbourg, 5 rue Descartes, 67000 Strasbourg, France

⁴ Institut de Physique du Globe de Paris (IPGP) - CNRS - Université Paris Cité, 1 Rue Jussieu, 75005 Paris

* Corresponding author: Luca Stigliano

Classification: PHYSICAL SCIENCES: Earth, Atmospheric, and Planetary Sciences

Keywords: microbial weathering, biosignatures, microtopography, calcite dissolution

Significance statement

The identification of biosignatures resulting from microbe-mineral interactions represents a cornerstone for the search for traces of life in rocks. Current criteria used to assess the biogenicity of mineral alteration rely on qualitative, thus subject to debate, considerations. Traditional approaches have primarily focused on surface etching features morphologically resembling microbes, overlooking other potential imprints of biotic activity. This study shows that biofilm-mediated calcite dissolution generates high-elevation regions on the surface due to localized reduction in dissolution rate, resulting from the formation of a micro-environment at the calcite-biofilm interface. While state-of-the-art analytical methods failed to detect distinctive biogenicity features, statistical characterizations of the microtopography succeeded to unambiguously detect these biotic imprints. Overall, this study offers a novel approach for the non-destructive and unequivocal identification of bioweathering signatures.

Abstract

The absence of unambiguous criteria to define imprints of microbe-mineral interactions currently represents an obstacle to quantifying the contribution of microorganisms to chemical weathering on Earth and, more generally, to the search for traces of life in the geological record. Conventional methods based on qualitative descriptions of etching features supposedly induced by microorganisms have often proven equivocal. Shifting towards mechanistically supported quantitative criteria thus appears necessary to overcome such ambiguities. Here, calcite dissolution experiments were carried out at room temperature and various solution compositions, either under sterile conditions or with a cyanobacterial biofilm covering the calcite surface. None of the state-of-the-art methods usually used to evidence biosignatures (i.e., electron microscopy imaging, nanoscale chemical and crystallographic characterizations) succeeded in detecting any distinctive biogenicity feature. Conversely, high-elevation regions at the calcite surface were uniquely detected through statistical microtopography characterizations based on semi-variogram and power spectral density analyses, making microbially-weathered surfaces quantitatively distinguishable from their abiotic counterparts. Interestingly, these high-elevation regions formed beneath the microbial cells are at odds with the surface etching features resembling cell morphologies that are usually sought as bioweathering markers. Atomic-scale stochastic simulations of the dissolution process suggested that these regions resulted from a local increase in fluid saturation state at the biofilm-mineral

contact, leading to a localized reduction in dissolution rate. Overall, this study offers a new avenue for the non-destructive and unambiguous identification of the signatures of mineral bioweathering in natural settings.

5.1.1 Introduction

Microorganisms essentially occupy niches on Earth that are home to fluid-rock interactions (Flemming and Wuertz, 2019). While biology may significantly impact these interactions, there is some debate about the relative contribution of the biotic versus abiotic processes (Schwartzman and Volk, 1989). Determining the biosignatures associated with fluid-mineral-microorganisms interactions has thus long been a challenge in Earth and planetary sciences, especially for the quantification of the contribution of microbes to chemical weathering in natural settings (Wild et al., 2022; Wild et al., 2021) or the search for traces of life (Santelli et al., 2001).

Micron-scale morphological features, such as tubular microchannels or etch pits developed in altered glass or mineral samples have been repeatedly interpreted as imprints of bioweathering left by microorganisms in modern as well as ancient samples as old as 3.8 Gyr (Bennett et al., 1996; Fisk et al., 1998; Jongmans et al., 1997; McLoughlin et al., 2007; Thorseth et al., 1995). In particular, etching features resembling microorganisms “in size and shape”, consequently interpreted as resulting from enhanced dissolution beneath the attached cells, are among the conventional criteria used to suggest past or ongoing interactions between microbial cells and minerals (Fisk et al., 1998; Thorseth et al., 1995). However, although a few studies provided direct compelling evidence for so-called ‘bacterial entrenchment’ (Davis et al., 2007; Lüttge et al., 2003), biosignatures based on the microtopography of naturally weathered samples has often proven equivocal, as etch pits and tubular features could equally be formed abiotically (Fisk et al., 2013; Santelli et al., 2001).

In that respect, the advent of non-destructive surface sensitive microtopography measurement techniques, such as atomic force microscopy (AFM) or vertical scanning interferometry (VSI), has shown promise as means to provide microtopography characterizations that go beyond simple qualitative observations. Recently, these techniques allowed to quantify the impact of fungal attachment to mineral substrate in the field (Wild et al., 2022), but this required some pre-assessment of the starting topography of the mineral surface and identification of the

location of fungal hyphae. Conversely, detecting the univocal impact of past bacterial attachment has proven elusive so far, unless individual living cells and/or biofilm remains were concurrently identified.

Here, we hypothesize that the interactions between microorganisms and minerals may leave traces in the microtopography of the mineral surface. The use of surface microtopography as an unambiguous parameter in the search for bacterial imprints requires the simultaneous fulfillment of three conditions yet to be met to date: (i) any metrics derived from microtopography measurements proposed as a biogenicity criterion must be defined without the need to make assumptions regarding the starting microtopography of the mineral and the physicochemical environment in which the microbe-mineral contact has occurred; (ii) microtopography analyses must go beyond local, qualitative and/or subjective observations, and have to be considered at a scale large enough to derive quantitative statistical criteria; (iii) a mechanistic understanding that supports the observations must be offered to confirm that any possible correlation between surface microtopography and the presence of microorganisms actually results from a causal relationship.

For this purpose, calcite is a mineral substrate of particular interest. Indeed, (i) it is ubiquitous on Earth, representing a dominant phase in limestones and marine sediments (Morse et al., 2007); (ii) its reactivity is almost unaffected by pH in the pH range typical of fluid-limestone interactions (Brantley and Olsen, 2014) (i.e., for pH ranging from ~5 to ~11, no assumption has to be made regarding the fluid composition apart from the fluid saturation state), and, (iii) under abiotic conditions, the high dissolution rate of calcite ensures that any transient starting topographic feature is erased from the surface in a matter of a few months at most, reaching a steady-state configuration (Bandstra and Brantley, 2008; Stigliano et al., 2023). We recently showed that, under abiotic conditions, the steady-state calcite surface microtopography varies with the saturation state of the fluid (Ω) at which the dissolution reaction occurred, according to a bijective relationship (Stigliano et al., 2023). In other words, the surface topography of any calcite crystal reacted under stable conditions over durations as large as a few months is representative of the Ω value at which the reaction took place.

In the present study, we tested if and how this relation could be impacted by bacteria. If this is the case, this may provide a direct biosignature of microbe-mineral interactions. We used *Chroococcidiopsis thermalis* PCC 7203, a soil cyanobacterium known for its resistance to desiccation (Murik et al., 2017; Waterbury and Stanier, 1978), and particularly targeted as a

model strain in astrobiology (Billi et al., 2011). Several *Chroococcidiopsis* strains have been shown to be endolithic and to inhabit calcite rocks (Casero et al., 2021; Wierzchos et al., 2018). Combining biotic and abiotic calcite dissolution experiments with statistical characterizations of the surface microtopography, we found a specific signature of dissolution mediated by cyanobacteria. No other specific chemical or crystallographic signature could be detected at the surface of calcite using nanoscale microscopy and spectroscopy techniques. We further developed stochastic dissolution modeling at the atomic-scale to support the observed feature, providing, to the best of our knowledge, the first direct evidence that the impact of bacteria on mineral surface microtopography goes much beyond the classical criterion of etching features resembling single microbial cells “in size and shape”. Such an unexpected finding thus offers a new tool for the search of traces of microbe-mineral interactions in the geological record.

5.1.2 Results

5.1.2.1 Abiotic vs. microbially-influenced calcite dissolution rates

Dissolution rates evaluated through surface retreat measurements were determined under biotic conditions using vertical scanning interferometry (VSI) and compared with the values determined abiotically under similar conditions (both in terms of fluid chemistry, i.e., pH, alkalinity and ionic strength, and experimental settings) from Bouissonnié et al. (2018) over the same Ω range here investigated (Figure C1) (Bouissonnié et al., 2018). The saturation state of the fluid (Ω) was varied between 0 (far-from-equilibrium conditions) and 0.8 (close-to-equilibrium conditions). With the only exception of $\Omega = 0.00$ and $\Omega = 0.30$, for which the biotic dissolution rate was higher than the value expected abiotically under the same conditions or very close to it, respectively, an overall decrease in calcite reactivity was observed under biotic conditions for all saturation states investigated.

5.1.2.2 Statistical characterization of calcite surface microtopography

VSI and scanning electron microscopy (SEM) images of the calcite surfaces reacted with solutions at different saturation states under biotic conditions revealed no etching features that could be associated with microbial activity according to conventional criteria: no etch pits resembling microorganisms in terms of “size and shape” were observed (see Figure 5.1.1, Figure C2 and Figure C3). Therefore, we investigated whether the microtopography resulting from biotic dissolution at various saturation states exhibits distinctive statistical traits when compared with its abiotic counterparts (Figure 5.1.2; see Materials and Methods section for an explanation of the different statistical measurements).

The power spectral density (PSD) curves obtained at close-to-equilibrium at $\Omega = 0.55$ and $\Omega = 0.65$ under biotic conditions exhibit a shift towards lower values compared with their abiotic counterparts across all spatial frequencies, and they mostly align with the PSD curve obtained abiotically at $\Omega = 0.80$. This reflects a decrease in surface roughness at all spatial scales. The curve obtained biotically at $\Omega = 0.8$ is indistinguishable from its abiotic counterpart. Consistently, the semi-variogram sill values obtained biotically at $\Omega = 0.55$, 0.65 and 0.80 show a similar trend, approximately matching the value obtained abiotically at $\Omega = 0.80$. However, overall, both PSD and semi-variogram analyses indicate that, at close-to-equilibrium conditions, abiotically and biotically weathered calcite surfaces are not statistically distinguishable. Conversely, some significant distinctions can be observed at far-from-equilibrium (i.e., $\Omega = 0.30$, 0.10 and 0.00). At $\Omega = 0.30$, although the PSD curve and the sill value showed only minimal differentiation between biotic and abiotic conditions, the higher correlation length evaluated for biotic conditions can be interpreted as a subtle distinctive trait of biotic weathering. However, this feature in itself cannot be used as a distinctive biogenicity criterion without knowledge of the fluid saturation state, since comparable or even larger correlation lengths were also recorded abiotically at lower saturation states.

In contrast, at $\Omega = 0.10$ and $\Omega = 0.00$, multiple metrics point towards a statistical differentiation between biotically and abiotically weathered surfaces. Specifically, at $\Omega = 0.10$, the biotic PSD decreases more steeply compared to the abiotic counterpart as wavevector values increase, indicating that the surface roughness exhibits less high-frequency features. Moreover, the sharp drop in the PSD signal notable in the very-high-frequency region (i.e., wavevector values higher than $\sim 10 \mu\text{m}^{-1}$) indicates a minimal degree of small-scale irregularities. Overall, this suggests that the biofilm-mediated dissolution at $\Omega = 0.10$ produces smoother surfaces in terms of high-frequency components compared with abiotic conditions. A similar behavior can also be observed at $\Omega = 0.00$, with the biotic PSD deviating from its abiotic counterpart in the high-frequency region (i.e., wavevector values higher than $\sim 1.5 \mu\text{m}^{-1}$). Regarding semi-variogram characterizations, the biotic sill value at $\Omega = 0.00$ is almost identical to its corresponding abiotic value, whereas at $\Omega = 0.10$ it is slightly lower, indicating that biofilm-mediated dissolution produces surfaces with height values more clustered around the mean plane compared to abiotic conditions. Furthermore, the strongest statistical differentiation between biotically and abiotically weathered surfaces at $\Omega = 0.00$ and at $\Omega = 0.10$ is given by the correlation length. Indeed, in both cases the values obtained biotically largely exceed those obtained abiotically across all explored saturation states. Therefore, this appears as a distinctive trait of microbially-

mediated calcite dissolution. Overall, both PSD and semi-variogram analyses indicate that, at far-from-equilibrium conditions, abiotically and biotically weathered calcite surfaces are statistically distinguishable, especially at $\Omega = 0.00$ and $\Omega = 0.10$.

In practical terms, the main factor explaining the biotic statistical imprints observed under far-from-equilibrium conditions is the presence of distinct regions that display more pronounced topographical elevation compared to the rest of the surface (Figure 5.1.1B and C). Overall, the presence of these regions makes the height values correlated on average over larger distances across the surface (Figure C4), concomitantly reducing the high frequency components of surface roughness.

The emergence of these topographical variations results from lower local dissolution rates (Figure C5; discussion section). These regions were further characterized by correlating VSI images before and after removal of the cells from the surface. Specifically, these regions represent areas that retained clusters of cells at the end of the experiments (Figure 5.1.1 a, e vs. b, f). This correlation suggests a causal link between biofilm coverage and a localized reduction in dissolution rate. None of these regions with heightened elevation were detected at $\Omega = 0.55$, 0.65, and 0.80 (Figure C2 and Figure C3).

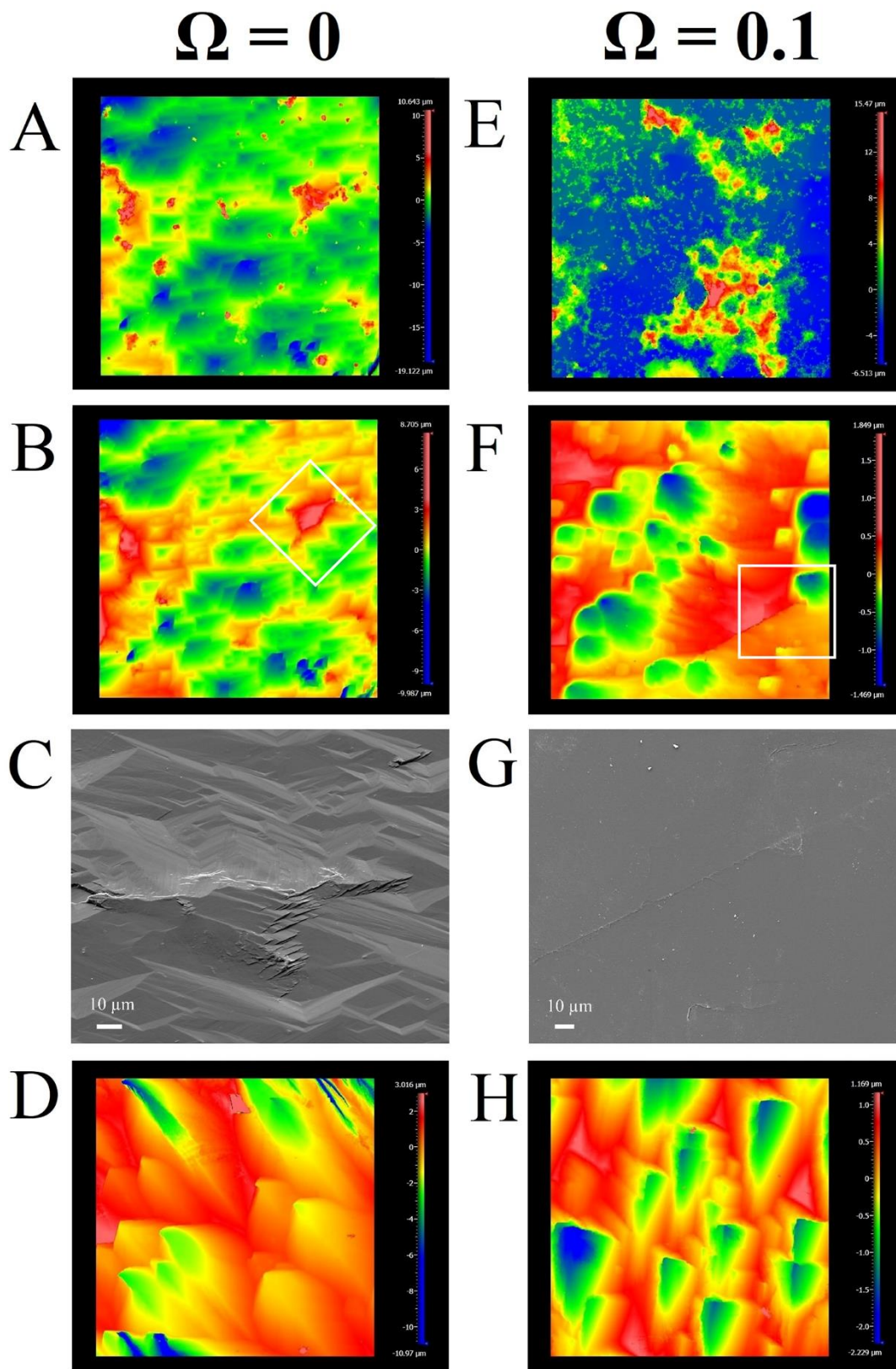


Figure 5.1.1 Panels showing the calcite surface topography resulting from biotic and abiotic dissolution at $\Omega = 0$ (left-hand side, A-D) and $\Omega = 0.1$ (right-hand side, E-H). A and E show VSI images acquired before removal of the cells, at $\Omega = 0$ and at $\Omega = 0.1$, respectively. B and F

show corresponding VSI images acquired after removal of the cells. C and G show an SEM close-up of the areas outlined in B and F, respectively. These areas were targeted for FIB milled thin foils extraction, as shown in Figure C6. VSI abiotic counterparts are shown in D ($\Omega = 0$) and H ($\Omega = 0.1$). The size of all VSI images is $600 \times 600 \mu\text{m}^2$.

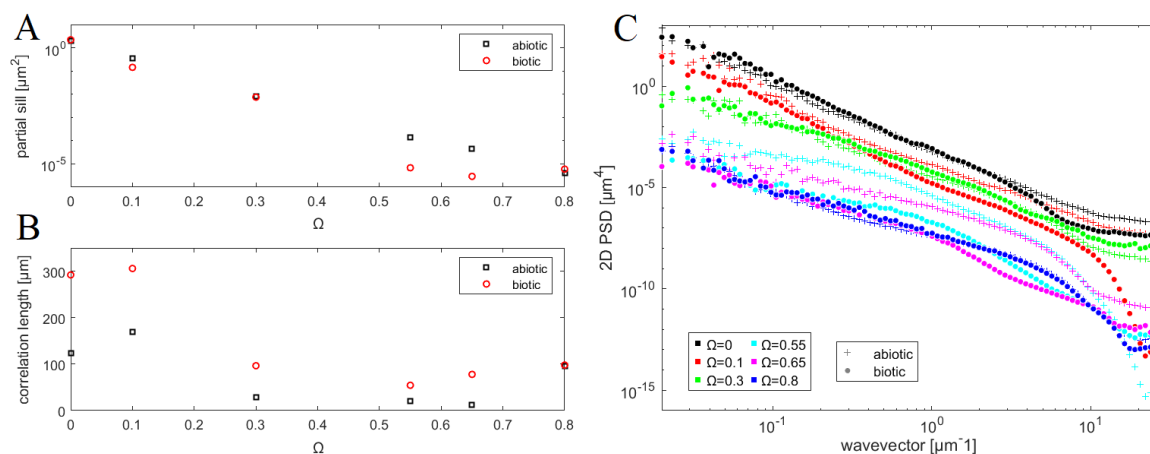


Figure 5.1.2 A, B) Semi-variogram model parameters as a function of Ω in abiotic (black squares) and biotic (red circles) conditions. C) PSD at different saturation states in abiotic (+ signs) and biotic (full circles) conditions. Semi-variogram and PSD curves have been evaluated over sub-windows of $600 \times 600 \mu\text{m}^2$.

5.1.2.3 Crystallographic and chemical characterizations of calcite regions populated with cyanobacteria

We further inspected the regions populated with cyanobacteria in experiments carried out at $\Omega = 0.10$ and $\Omega = 0.00$ using transmission electron microscopy (TEM) characterizations conducted on focused ion beam (FIB) milled thin foils, attempting to identify any potential chemical and / or crystallographic imprint left at the surface of these locations at a submicron scale (Figure 5.1.1 and Figure C6). X-ray energy dispersive spectroscopy (XEDS) analyses showed no chemical difference between the first 10s of nm underneath calcite surface and the rest of the calcite, with a uniform distribution of Ca along the foils (Figure 5.1.3B, Figure C7 and Figure C8). Moreover, the crystalline homogeneity was confirmed using high resolution transmission electron microscopy (HRTEM) revealing no significant alteration of the crystal structure at the very surface of calcite. Last, no other phase -amorphous or crystalline- was observed up to the very surface.

Overall, under the investigated conditions, the statistical characterization of the surface microtopography appeared as the only tool able to quantitatively differentiate between biotically and abiotically weathered surfaces.

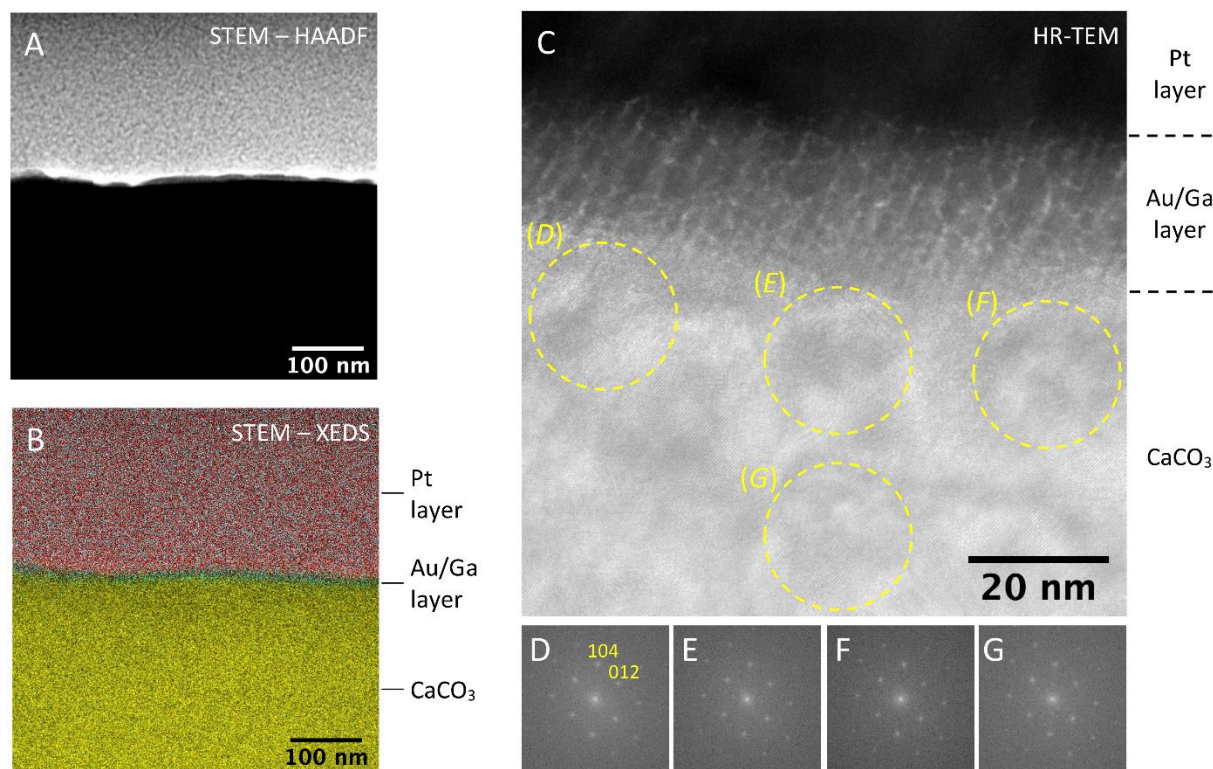


Figure 5.1.3 (A) STEM-HAADF image of a FIB thin foil of the calcite crystal reacted at $\Omega = 0$ extracted from the high-elevation region displayed in Figure 1.B and corresponding STEM-XEDS elemental map (B) acquired using Pt-M α , Ga-K α and Ca-K α lines. (C) High resolution TEM image of the same area. (D – E) Fast Fourier transforms of labelled areas in (C) showing the crystalline homogeneity of the calcite: each FFT corresponds to calcite with the same $[-4 - 2 1]$ zone axis. The indexing is relative to the calcite cell parameters (R-3c, $a = 4.989 \text{ \AA}$, $c = 17.061 \text{ \AA}$).

5.1.3 Discussion

Comparisons of the surface microtopography limited to qualitative considerations (e.g., changes in etch pits morphology) and physicochemical characterizations at the atomic scale have proven ineffective in differentiating between abiotically and biotically weathered calcite surfaces under the investigated conditions. Conversely, a thorough statistical characterization

of the calcite surface microtopography involving power spectral density and semi-variogram analyses quantitatively differentiated between those processes, at least at far-from-equilibrium conditions. Such a differentiation requires microtopography analyses over a relatively broad field of view ($\sim 600 \times 600 \mu\text{m}^2$). This is possible using VSI, which provides observation windows large enough to conduct statistical analyses able to capture the impact of the high-elevation regions, whose influence extends far beyond the size of a single cell. Below, we explore whether such results can be supported by independent modeling of the dissolution process at the atomic-scale, using parameters derived from independent *ab initio* quantum mechanical studies. As stated above, this step represents a prerequisite to assert that statistical analyses of surface microtopography represent a reliable tool to detect microbially-influenced mineral weathering. We then conclude with a discussion of the promises and limitations of this new approach.

5.1.3.1 Microbially-mediated generation of topographic highs

The overall decrease in calcite reactivity and the specific occurrence of elevated topographical areas observed beneath microbial cells argue in favor of a local change in the dissolution mechanism, whereby the biofilm restricts the propagation of dissolution stepwaves (Lasaga and Luttge, 2001a). Such a dissolution-inhibiting process can be mechanistically explained in various non-exclusive ways: (i) creation of a micro-environment at the calcite-biofilm interface chemically different from that of the bulk solution due to metabolic activity ((Ahmed and Holmström, 2014; Barker et al., 1998) and references therein); (ii) diffusion limitation of ions between the surface and the bulk solution by the biofilm (Davit et al., 2013); (iii) mechanical obstruction caused by the presence of the biofilm that physically hinders the calcite-water contact (Luttge and Conrad, 2004).

While these are all plausible explanations, complete hindering of the calcite-water contact can be excluded based on surface retreat measurements. In all cases, the relative height of the high-elevation regions was always lower than the global surface retreat, Δh (Figure C5). This implies that dissolution did occur beneath the biofilm (albeit at a lower rate compared to the rest of the surface), suggesting that the biofilm did not hinder direct contact between the crystal surface and the bulk fluid. Therefore, a reasonable explanation for the reduced dissolution rates observed beneath biofilm patches rather stems from the dynamic interplay between the formation of a micro-environment caused by cells metabolic activity and the diffusion-limiting impact of the porous biofilm. At a bulk scale, the addition of *C. thermalis* PCC 7203 cells to the aqueous solution in our experiments under light exposure increased the solution pH (Figure C9), primarily because of photosynthetic activity (e.g., (Dittrich and Sibling, 2010)). Thus, it can

be expected that the local pH of the microenvironment beneath cells would be higher compared to that of bulk solution. Moreover, it is reasonable to expect that the diffusion-limiting impact of the biofilm would lead to a concentration of dissolved Ca^{2+} and CO_3^{2-} that is higher in the microenvironment solution compared to the surrounding bulk solution. When combined, both considerations point towards a microenvironment with a higher saturation state compared to that of the bulk solution. Specifically, to be able to obtain a dissolution rate that is lower (but not null) than the rest of the surface, the microenvironment saturation state, Ω , should be higher (but lower than 1).

We tested this hypothesis through kinetic Monte Carlo (kMC) modeling of Kossel crystal dissolution (see Materials and Methods). The model successfully reproduced the high-elevation regions observed experimentally (Figure 5.1.4), which are responsible for the observed statistical signatures described above. Specifically, a good agreement was achieved with the surface feature displayed in Figure 5.1.1c, both in terms of its stepped structure and overall shape.

From a mechanistic perspective, the key for such a feature to emerge is to locate the sub-window with higher Ω somewhere in-between various dislocation centers. In this way, the coalescence of the dissolution stepwaves propagating from the pre-opened hollow cores is slowed down by more frequent re-precipitation events within the microenvironment, eventually leading to the emergence of elevated stepped regions as dissolution progresses. This specific configuration also possibly explains why such features are not observed all over the surface, as they result from the peculiar combination of etch pits (and therefore, dislocations) distribution and the location of biofilm attachment at the calcite surface.

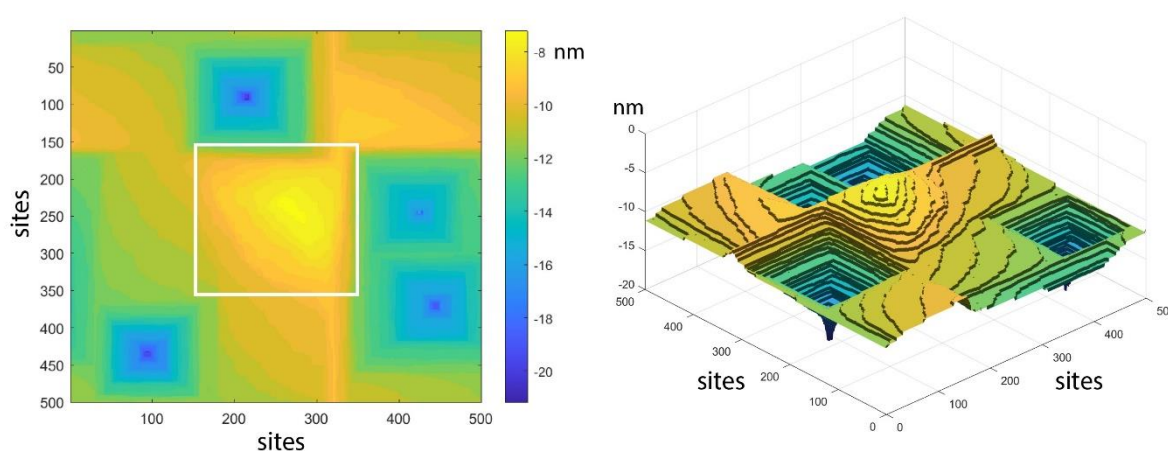


Figure 5.1.4 Surface topography (left-hand side, 2D representation; right-hand side, 3D

representation) resulting from kMC modeling of biofilm-mediated Kossel crystal dissolution at $\Omega_{\text{bulk}} = 0$. The white square delimits the area in which a higher saturation state (i.e., $\Omega_{\text{biofilm}} = 0.6$) was set. Corresponding abiotic kMC modeling outcomes are displayed in Figure C10.

5.1.3.2 Promises and limitations for the use of statistical characterizations of mineral microtopography as a proxy to infer imprints of microbial activity

The kMC simulations carried out using parameters derived from independent *ab initio* quantum mechanical studies suggest that the interaction between the calcite surface and a microenvironment with locally higher Ω values is a likely explanation for the observed topographic highs revealed through statistical characterizations of surface microtopography. These findings contrast with the conventional (and oftentimes controversial) criteria that associate tubular and/or granular etching features observed on naturally weathered samples to fungal and/or bacterial imprints (e.g., (Staudigel et al., 2008; Van Breemen et al., 2000)). To the best of our knowledge, topographic highs are not among the distinctive features that are searched for, and their unambiguous evidence through statistical characterizations is absent from the list of biogenicity criteria associated to microbially-influenced mineral weathering (McLoughlin et al., 2007).

Importantly, our findings verify all criteria recalled previously for the search of imprints of microbe-mineral interactions: (i) no need for strong assumptions regarding the reaction conditions apart from the saturation state of the fluid, which is obvious to constrain based on the bijective relationship existing between etch pit nucleation and far-from-equilibrium conditions, as demonstrated theoretically and experimentally for decades (e.g., (Brantley et al., 1986; Lasaga and Blum, 1986) for quartz (Bouissonnié et al., 2018) for calcite); (ii) the derivation of quantitative statistical parameters and (iii) an independent mechanistic support. Therefore, we hypothesize that such biotic imprints could potentially be identified on a variety of microbially-mediated weathered minerals, provided that the biofilm generates a microenvironment (above the underlying substrate) characterized by a saturation state that is higher compared with that of the bulk solution. Such a mechanism is likely to be commonplace, as testified by the growing number of studies that point out the ability of microbial biofilms to mitigate the impact of extensive chemical weathering (Carter, 2005; Elert et al., 2021), which might eventually contribute to a sustained attachment of the biofilms.

Among the main limitations of this approach, it can be questioned whether biofilm attachment is the only mechanism that can lead to the development of topographic highs on a pitted mineral surface. Arguably, the attachment of secondary minerals resulting from chemical weathering is

also known to act as a protective layer that can eventually inhibit the reactivity of the underlying dissolving minerals (Daval et al., 2009a; Velbel, 1993). However, unlike biofilm attachment, such layers are rarely discontinuous and often adhere firmly to the substrate, so that they can hardly be removed even by sonication techniques (Zhu et al., 2006). In addition, they overall have a much stronger resistance to aging than biofilms, so that they are likely to be detected on naturally weathered samples.

To conclude, we therefore suggest that statistical approaches targeted to quantitatively describe microtopographic biotic imprints on weathered mineral surfaces can be adopted as additional independent methods for detecting potential biosignatures following a non-destructive / non-invasive approach.

5.1.4 Materials and methods

5.1.4.1 Starting materials and experimental protocol

Starting from a natural calcite sample, 12 smaller fragments of $\sim 100 \text{ mm}^3$ were obtained through cleavage along the natural $\{104\}$ calcite plane, as verified with X-ray diffraction (XRD) analyses conducted with a Siemens D5000 diffractometer. The chemical analyses of the original natural calcite reported in (Bouissonnié et al., 2018) revealed that the major impurities were Mg ($\sim 0.1 \text{ wt.}\%$), Sr (475 ppm) and Mn (60 ppm). For each fragment, one of the resulting $\{104\}$ faces was processed through a sequence of mechanical polishing steps, with a final grit size of $0.25 \mu\text{m}$.

The flow-through system for each dissolution experiment consisted of a tank open to the atmosphere, a peristaltic pump and a perfluoroalkoxy alkane (PFA) reactor. The aqueous solution was continuously transferred from the tank into the reactor containing the calcite chip and subsequently either discarded or sampled for chemical solution analysis using Varian 720 ICP-AES (see Table C1 for fluid analyses). The solution inside the reactor was continuously stirred to ensure uniform chemical conditions. The reactor was positioned within an incubator operating at a controlled temperature of $T = 22.0 \pm 0.1 \text{ }^\circ\text{C}$, while the measured pCO_2 of the room was found to be $500 \pm 50 \text{ ppm}$ during all experiments.

The aqueous solution composition was: $\text{NaCl} = 5.8 \text{ g/L}$, $\text{NaHCO}_3 = 0.086 \text{ g/L}$. $\text{CaCl}_2 \cdot 2\text{H}_2\text{O}$ was added in different amounts (i.e., 0 g/L , 0.0485 g/L , 0.1425 g/L , 0.2685 g/L , 0.3205 g/L , 0.405 g/L) to target 6 different saturation states (i.e., $\Omega = 0.00, 0.10, 0.30, 0.55, 0.65, 0.80$).

The outputs of abiotic experiments carried out in our previous study (Stigliano et al., 2023) were used to provide a baseline for comparison with biotic experiments. In brief, for each

experiment, a calcite chip was positioned on a Teflon tripod in the reactor with the polished face facing upwards. At various time intervals throughout the experiments, the calcite samples were removed from the reactors for ex-situ time-resolved surface topography measurements of the dissolving top faces with VSI (Zygo NewView 9000) at 50x magnification over an area of $\sim 1 \text{ mm}^2$. The experiments lasted for a total duration of ~ 11 days.

For the biotic experiments, a similar setup was adopted, with a few adjustments outlined below. All the experimental equipment directly in contact with the aqueous solution was sterilized (either autoclaved or rinsed and bathed in an aqueous solution of ethanol at 70%) prior to the start of the experiments and left to dry out in a sterile laminar flow cabinet. The aqueous solution was pre-filtered at $0.2 \text{ }\mu\text{m}$. To establish a non-reacting reference surface, a small portion ($\sim 1 \text{ mm}^2$) of the crystal surfaces was covered with room temperature vulcanized (RTV) glue and left to dry out before the sample being bathed overnight in absolute ethanol. At the end of the experiments, the glue mask was removed, and the average height difference between the reacted and non-reacted areas (referred to as surface retreat, Δh) was used to estimate the dissolution rate of calcite (e.g., (Stigliano et al., 2021)). Right before the start of each biotic experiment, the reactor was pre-filled with sterile aqueous solution and the calcite chip submerged and placed on the Teflon holder, with the polished face facing upwards. During this stage, $160 \text{ }\mu\text{L}$ of pre-filtered tank solution, enriched with *Chroococidiopsis thermalis* PCC 7203 cells, was injected onto the polished calcite face to create a biofilm on the mineral substrate. To obtain the cell suspension, 20 mL of a pure culture in exponential growth, grown in a BG-11 medium (Rippka et al., 1979), was centrifuged at 1200 rpm . After discarding the supernatant, the cell pellet was resuspended in $160 \text{ }\mu\text{L}$ of pre-filtered tank solution and then injected onto the calcite surface. The biotic experiments lasted for ~ 4 days as the abiotic experiments showed that this duration exceeds the time required to achieve a steady-state configuration of the calcite surface resulting from dissolution (~ 60 hours; (Stigliano et al., 2023)). Lastly, to prevent a pH increase in the bulk solution inside the reactor as a result of photosynthetic activity and to uphold saturation states similar to those targeted in the abiotic experiments, the flow rate was increased from 0.15 mL/min to 1.15 mL/min (Figure C9).

5.1.4.2 Analytical characterizations

Topography images of the calcite surface were acquired with VSI over an area of $\sim 1 \text{ mm}^2$ at 50x at the final time. The images were acquired before and after physically removing the biofilm from the surface using an aqueous solution of sodium dodecyl sulfate (SDS) at 2% (Buss et al., 2003) and saturated with respect to calcite to prevent dissolution during this

cleaning step. Subsequently, the calcite surface topographies resulting from biofilm-mediated dissolution at various saturation states were quantitatively compared to the steady-state configurations of the corresponding abiotic experiments. This comparative approach involved semi-variogram and PSD analyses conducted over areas of 600x600 μm^2 . In brief, the experimental semi-variogram provides a measure of the degree of spatial correlation of the heights data, whereas the PSD quantifies the surface roughness at different length scales by deconstructing it into its individual frequency components. More details can be found in (Stigliano et al., 2023).

Additionally, the calcite surfaces were characterized with SEM, attempting to identify specific surface features that might be diagnostic of microbial presence and / or activity. Based on VSI pictures acquired before and after removing the biofilm, two locations that exhibited higher density of cells sticking to the calcite substrate at the end of the experiments have been identified as of potential interest, one at $\Omega = 0.00$ and one at $\Omega = 0.10$ (Figure 5.1.1 and Figure C6). These locations have been targeted for FIB-milling and TEM characterization (Figure C11), to look for chemical and / or crystallographic ‘anomalies’ that might be associated with the presence of the cells.

Ultrathin electron transparent cross sections were prepared by FIB Ga^+ milling with the Auriga® 40 FIB-SEM (Carl Zeiss NTS GmbH) dual-beam operated at IPGP (Paris, France). HRTEM and scanning transmission electron microscopy (STEM) observations were performed on FIB foils using a 200 kV JEOL 2100F microscope operated at IMPMC (Paris, France) equipped with a field emission gun. XEDS spectra were acquired in STEM mode to probe the chemical composition of the reacted calcite samples, with a focused electron beam (1 nm) and a detection limit close to 0.1 wt%.

5.1.4.3 Stochastic simulations of calcite dissolution

Standard kMC modeling of far-from-equilibrium dissolution of a Kossel crystal has been applied to assess whether stochastic dissolution simulations parameterized following results from *ab initio* studies can successfully reproduce specific surface features resulting from biotic dissolution. We recall that, in classical kMC modeling (e.g., (Kurganskaya and Lutge, 2021)), the dissolution probability, $P_{d,N}$, of a surface site having N neighbors is given by Equation 5.1.1, where E_a [kJ/mol] is the activation energy associated with the breakdown (and formation) of a single bond, R [kJ/mol/K] is the universal gas constant and T [K] is temperature. Precipitation is allowed at kink sites only (i.e., $N = 3$), with the corresponding precipitation probability being provided in Equation 5.1.2, where $\Delta\mu$ [kJ/mol] is the difference in chemical potential between

a given site in the aqueous solution and a given site at the crystal surface. The parameter values used in the simulations were: $E_a = 15.5$ kJ/mol and $T = 295.15$ K, where the activation energy value was selected from the range of possible values compatible with ab initio calculations (Carrasco and Reis, 2021). Simulations were conducted using the ‘divide and conquer’ approach ((Meakin and Rosso, 2008)). More algorithmic details can be found in (Stigliano et al., 2023). Lastly, the contribution of the microbes to the dissolution dynamics has been taken into account by implementing locally an arbitrary higher Ω (i.e., $\Omega_{\text{biofilm}} = 0.6$ vs $\Omega_{\text{bulk}} = 0$), which simulated a micro-environment at the mineral-biofilm interface characterized by a higher fluid saturation.

$$P_{d,N} = \exp\left(-\frac{NE_a}{RT}\right) \quad (5.1.1)$$

$$P_{p,3} = \exp\left(\frac{\Delta\mu}{RT}\right) \exp\left(-\frac{3E_a}{RT}\right) \quad (5.1.2)$$

5.2 *In situ* VSI investigations of microbial weathering signatures

5.2.1 Introduction

In order to further investigate the mechanism underlying the formation of the high-elevation regions observed *ex situ* at far-from-equilibrium conditions, an *in situ* VSI calcite dissolution experiment was conducted at $\Omega = 0.00$.

The development of such a flow cell was one of the objectives of the ERC Mobidic project that funded most of this PhD work. It has been conducted by Dr. Bastien Wild during his postdoctoral fellowship in parallel with this PhD work. A stable version of the flow cell has been ready in July 2023, making it possible to run a first preliminary experiment aimed at better characterizing the interplay between microbial attachment and calcite dissolution.

The main advantage of the *in situ* VSI setup is the possibility to observe simultaneously the dynamics of cells attachment/detachment to the calcite substrate and the concurrent dissolution process. Nonetheless, there are a few technical challenges associated with in-situ VSI imaging of solid materials through a liquid medium and with the *in vivo* imaging of bacteria.

As previously mentioned in sub-section 1.5.2, since water has a different refractive index compared to air, the presence of a water medium in between the VSI objective and the solid sample affects the optical path of the beam reflected from the sample surface. This needs to be addressed by adding an ad-hoc designed filter in the path of the beam reflected from the reference mirror to compensate for the presence of water (and, in some configurations, of a transparent reactor cup). Moreover, the presence of bacterial cells on the sample surface, with their own distinct refractive index, can further disrupt the optical path of the beam. This can lead to the generation of artifacts in the acquired topography data, which must be corrected in the data processing stage. However, if these technical and post-processing challenges can be successfully overcome, the in-situ approach has the unique potential of providing valuable mechanistic insights into biofilm-mediated dissolution that are beyond the reach of *ex situ* experimental configurations.

5.2.2 Materials and methods

The VSI *in situ* experimental setup adopted in this work consisted of: (i) a commercially available glass compensated objective, which allows to acquire image through a glass window, by putting a same glass slide in the prism slider assembly, after the beam splitter, before the

internal reference of the objective; (ii) a flow-through fluid cell placed under the VSI objective, containing a calcite sample with a mechanically-polished top {104} face; (iii) a transparent glass at the top of the fluid cell, functioning as a see-through reactor cup that allows the VSI light beam to reach the calcite surface; (iv) a tank reservoir connected upstream to the flow-through fluid cell, containing an aqueous solution with the same solution composition as in the previous experiments conducted at $\Omega = 0.00$ ($\text{NaCl} = 5.8 \text{ g/L}$ and $\text{NaHCO}_3 = 0.086 \text{ g/L}$); (v) a conical 15 mL centrifuge tube containing an aqueous solution saturated with respect to calcite enriched with a pellet of PCC 7203 cells that were obtained from a culture in the exponential growth phase. The temperature of the room was maintained at $T = 22 \pm 0.5 \text{ }^\circ\text{C}$ and the solution pH was measured to be $\text{pH} = 7.5 \pm 0.1$ all over the progress of the experiments, both in the tank solution and at the outlet of the fluid cell. All aqueous solutions employed in the experiment were pre-filtered at $0.2 \text{ }\mu\text{m}$.

The aqueous solution containing the PCC 7203 pellet was injected into the fluid cell with a flow rate of 15 mL/h set by a peristaltic pump placed downstream. The fluid cell had previously been filled with an aqueous solution saturated with respect to calcite. The pump was then stopped for ~ 2 minutes to allow the cells to stick to the calcite surface. Then, an aqueous solution saturated with respect to calcite was run through the fluid cells for ~ 5 minutes to free the fluid cell from all bacteria cells that did not stick to any solid substrate. Subsequently, the aqueous solution at $\Omega = 0.00$ was run into the fluid cell with a constant flow rate of 15 mL/min. VSI topography images of a given area of $400 \times 400 \text{ }\mu\text{m}^2$ of the calcite surface undergoing dissolution were acquired every 3 minutes, for a total duration of 22 hours. Every ~ 5 hours, the flow rate was increased by a ~ 100 -fold factor for ~ 1 minute to evacuate air bubbles that formed inside the fluid cell over time, due to the imperfect sealing of the system.

VSI in-situ topography images were acquired at $20\times$ (lateral resolution, $dl = 0.4 \text{ }\mu\text{m}$) with an objective equipped with an ad-hoc designed filter able to compensate for the equivalent refractive index of the water and of the see-through reactor cup located in between the objective and the calcite surface. Subsequently, the time-resolved topography data were processed to gain insights into the interplay between the real-time bacteria coverage and calcite surface topography evolution. This involved: (i) estimating the rate of detachment of bacterial cells from the calcite surface undergoing dissolution; (ii) comparing the evolution of regions that were never covered with areas that were partially covered by bacteria; (iii) generating a 'bacteria residence time map', which provided an estimate of the duration of bacteria coverage for each pixel in the topography data of the analysed region.

The light reflected from the bacterial cells was consistently interpreted by the VSI as negative height values relative to the calcite surface beneath, seemingly appearing as depressions in the surface. This was likely due to a different refractive index of the bacterial cells compared to the surrounding water medium. Of note, similar VSI artifacts were also observed by (Waters et al., 2009) under dry conditions when imaging bacteria on reflective solid materials. By taking advantage of this conflicting interferometric information, it was possible to locate the bacterial cells present on the surface by applying a cutoff value at the lower end of the histogram of the height values. Importantly, this allowed to monitor the bacteria coverage over time, while enabling to observe the surface progressively exposed to the fluid as bacteria detached from the surface.

At the end of the experiment, the residual cells sticking to the calcite surface were physically removed using an aqueous solution of sodium dodecyl sulfate (SDS) at 2% and saturated with respect to calcite, according to the same protocol followed in the previous study. VSI topography data of the calcite surface were subsequently acquired in dry conditions with a different objective at 20× (lateral resolution, $dl = 0.45 \mu\text{m}$).

5.2.3 Results and discussion

5.2.3.1 Detachment rate of bacterial cells and surface roughness evolution

An example of how the location of individual bacterial cells could be detected on the surface at different times during dissolution is provided in Figure 5.2.1. When comparing the optical images of a given area with the corresponding topography images, it was observed that the VSI interpreted individual cells as depressions in the surface. Therefore, at each given time, applying a lower-end cutoff value allowed the counting of the number of bacterial cells projected on the horizontal plane adhering to the surface and the identification of the portions of the calcite surface that were not covered by bacteria.

The detachment rate of bacterial cells was determined by plotting the number of pixels associated with bacterial cells as a function of time, calculated using a cutoff value of $-0.38 \mu\text{m}$ (Figure 5.2.2). The cutoff value was chosen as the highest value that would allow to detect the highest number of individual cells at the surface, while simultaneously excluding all negative height values originated from the portion of the surface that was not covered by bacteria. This is particularly critical for rougher surfaces. The sharp decrease in slope that is observed for times larger than 10.8 hours is largely a consequence of the protocol followed to counting individual cells. Indeed, as the calcite surface roughness increased over time during dissolution,

it became progressively more difficult to differentiate negative height values associated with bacteria from height values originated from the uncover portion of the surface. As a result, the derived plot can only be considered reliable within the time interval between $t = 0$ hours and $t = 10.8$ hours. Thus, the slope of the regression line determined in that specific time interval was used to derive the detachment rate. This was done by assuming an average coverage of 25 pixels (pixel width of $0.4 \mu\text{m}$) for each individual cell, which resulted in a detachment rate of ~ 159 cells / hour.

Additionally, this cutoff approach enabled to analyse the evolution of the surface topography evaluated over areas of $80 \times 80 \mu\text{m}^2$ of a region that was entirely devoid of bacteria throughout the entire duration of the experiment (Figure 5.2.3) and of a region that was consistently partially covered by bacteria (Figure 5.2.4). This made possible to compare the temporal evolution of the corresponding surface mean height values and average surface roughness parameters, R_a (Figure 5.2.5). Calculations were performed only based on surface height values, excluding the regions covered by cells at any given time. Notably, the gradual detachment of bacterial cells from the surface progressively revealed surface height values that were previously inaccessible. Overall, this analysis showed that, while the uncovered area tended to maintain overtime approximately the same relative average height with respect to the average mean plane of the total surface, the partially covered area tended to increase its relative average height. In other words, this indicates that the presence of cells in that specific location led to the generation of a region with higher elevation compared to the rest of the surface. Furthermore, the R_a analysis revealed that while the uncovered area reached a steady-state configuration of surface roughness after a relaxation time of ~ 18 hours, the average surface roughness parameter evaluated over the partially covered area exhibited a consistent increasing trend. This further indicates that the localized presence of agglomerates of cells significantly affected the evolution of the surface topography.

Of note, quite unexpectedly, despite conducting the experiments under far-from-equilibrium conditions ($\Omega = 0.00$), etch pits were not observed anywhere on the surface. Several factors might explain this observation. One possibility is that the duration of the experiments was not long enough to allow etch pits to fully develop and/or or the VSI resolution was insufficient to detect early-stage etch pits. Additionally, this could also be due to the presence of EPS coatings on the surface, which might have hindered the nucleation of etch pits, preventing their formation, as observed *ex situ* in some areas covered by agglomerates of cells. These hypotheses will be further investigated in future experiments.

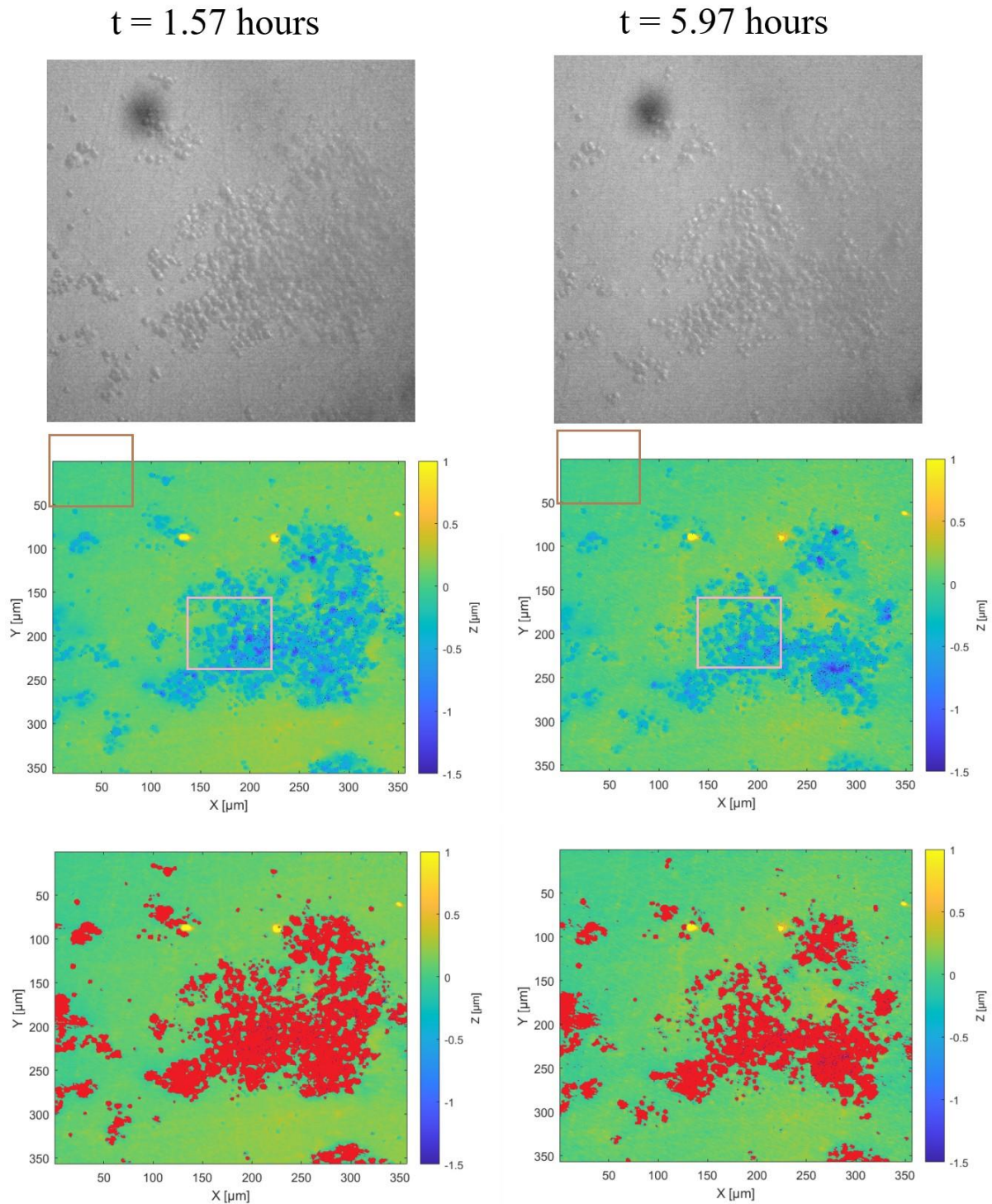


Figure 5.2.1 Panel displaying a sub-window of $350 \times 350 \mu\text{m}^2$ at two different times: $t = 1.57$ hours (left-hand side column) and $t = 5.97$ hours (right-hand side column). The first row displays optical images, whereas the second row displays the corresponding topography images acquired in-situ with VSI at $20\times$ ($dl = 0.4 \mu\text{m}$). The brown and pink squares of $80 \times 80 \mu\text{m}^2$ outlined in the topography maps represent the locations that were targeted in Figure 5.2.3 and Figure 5.2.4 respectively. Comparing the optical images in the first row with the corresponding

topography in the second row revealed that individual cells were interpreted by the VSI as negative height values after a first-order surface detrending. By applying a cutoff value of $-0.1 \mu\text{m}$, it was possible to identify most of the cells present on the surface at a given time, without significantly including any real height value originated from the calcite surface. All values lower than the cutoff are displayed in red in the topography images in the last row.

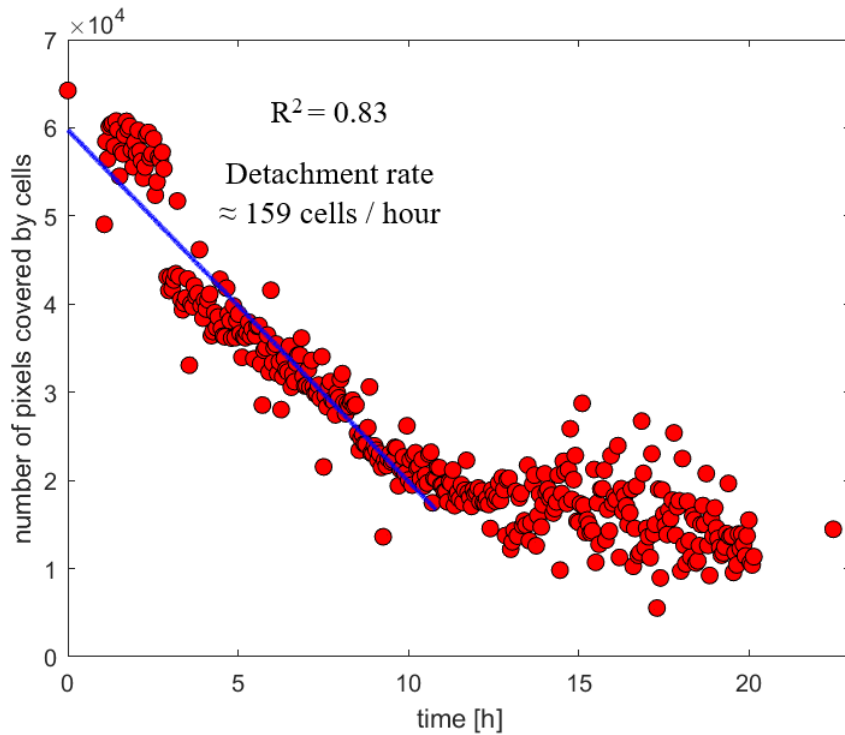


Figure 5.2.2 Number of pixels covered by cells as a function of time, evaluated over the area of $350 \times 350 \mu\text{m}^2$ displayed in Figure 5.2.1. The detachment rate was estimated based on the slope of the regression line evaluated between $t = 0$ h and $t = 10.8$ h, assuming an average of 25 pixels covered by each bacterial cell (diameter $\sim 2 \mu\text{m}$). The cutoff value used throughout the analysis was set at $-0.38 \mu\text{m}$.

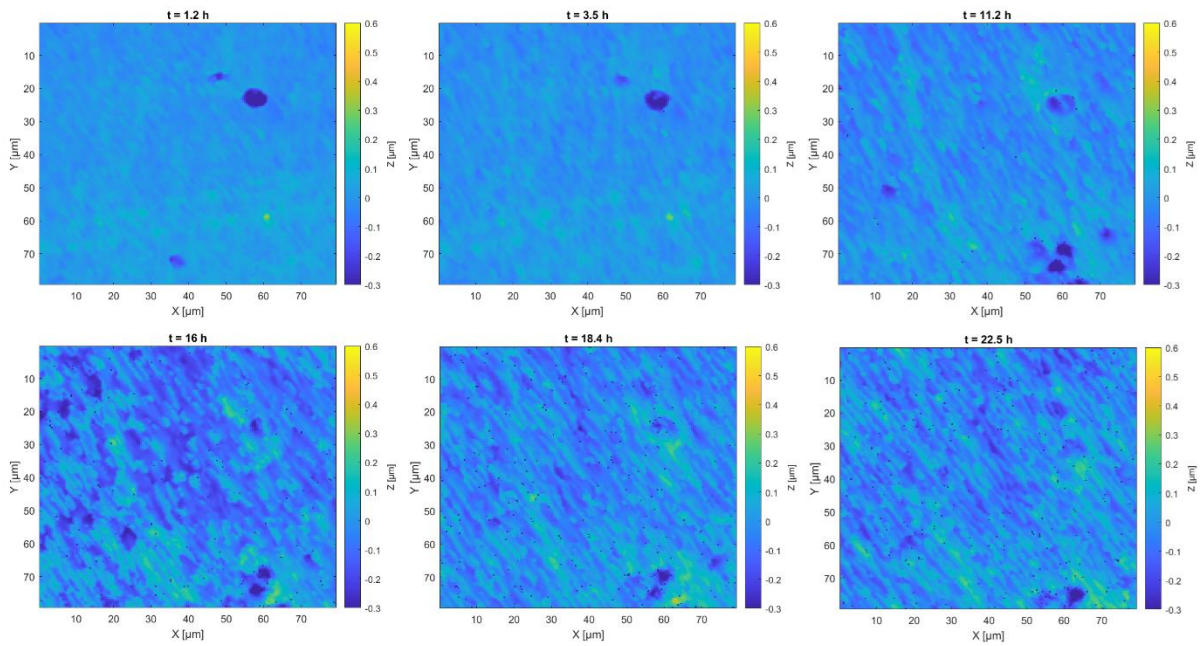


Figure 5.2.3 Surface topography images obtained at different times over the area of $80 \times 80 \mu\text{m}^2$ delineated in brown in Figure 5.2.1. This provides a visual representation of an area that was entirely devoid of bacteria throughout the entire duration of the experiment.

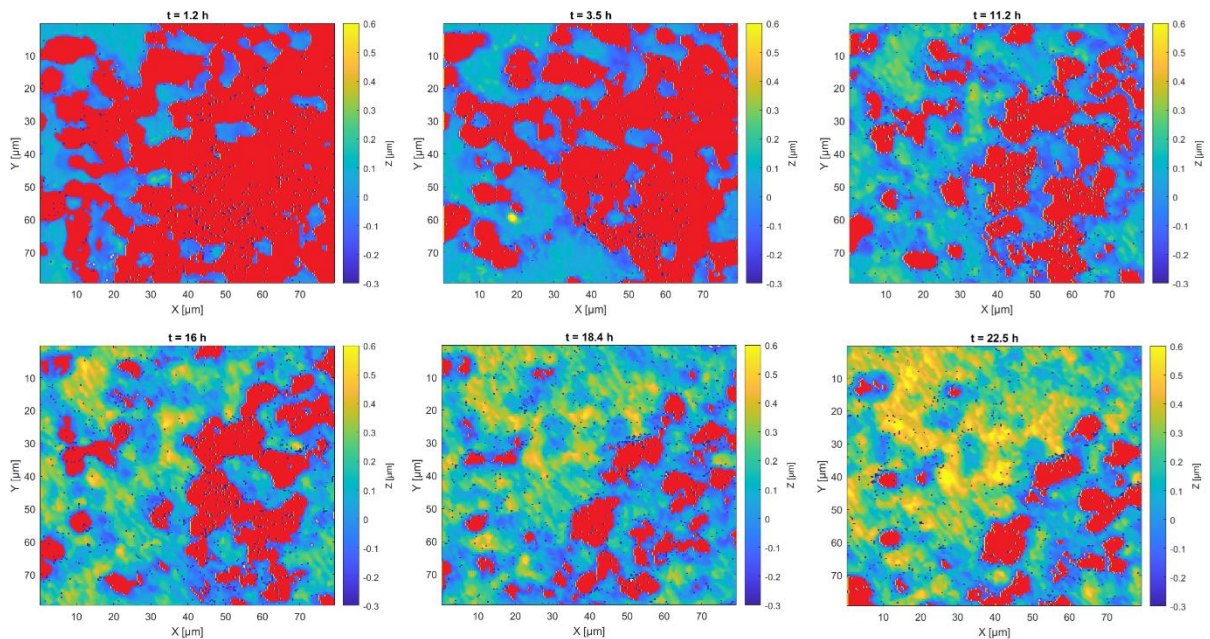


Figure 5.2.4 Surface topography images obtained at different times over the area of $80 \times 80 \mu\text{m}^2$ delineated in pink in Figure 5.2.1. This provides a visual representation of an area that was partially covered by bacteria during the experiment, displaying the cells detachment dynamics. Note that the colour scale used for the height values is the same as the one used in Figure 5.2.3.

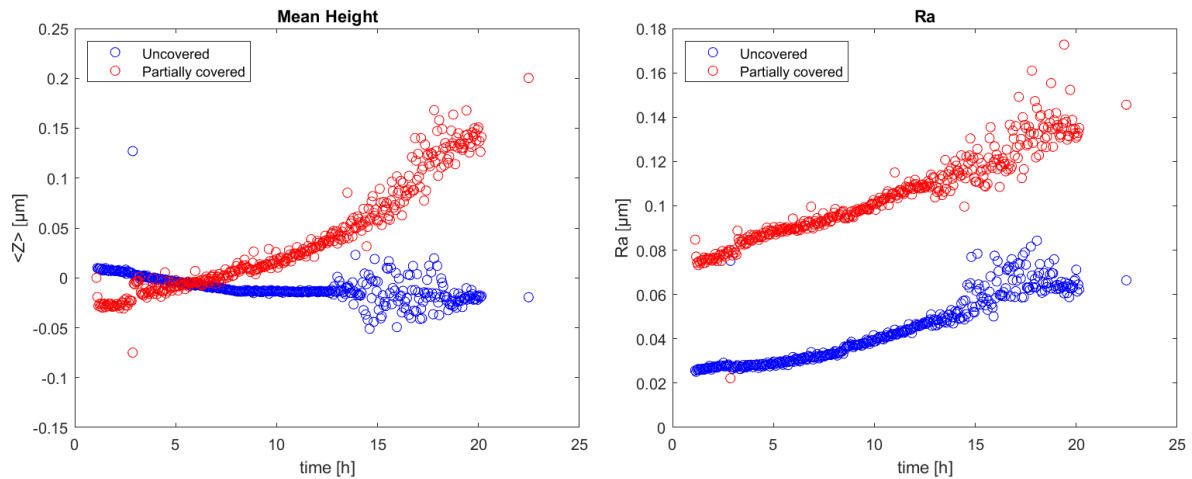


Figure 5.2.5 Plots of the temporal evolution of the average mean height (left-hand side) and average surface roughness parameter, R_a (right-hand side), evaluated over areas of $80 \times 80 \mu\text{m}^2$. The ‘Uncovered’ (blue) curves were evaluated over the area delineated in brown in Figure 5.2.1, whereas the ‘Partially covered’ (red) curves were evaluated over the area delineated in pink in Figure 5.2.1.

5.2.3.2 Bacteria residence time

Figure 5.2.6 provides a visual comparison of the ‘bacteria residence time map’ calculated based on *in situ* acquisitions with the corresponding surface topography acquired *ex-situ* at the final time, after removing the residual biofilm from the calcite surface. The ‘bacteria residence time map’ was calculated by categorizing each pixel of the surface topography acquired *in-situ* at any given time as ‘covered’ or ‘uncovered’. At each time step, if the considered pixel considered was categorized as ‘covered’ (based on a cutoff value of $-0.38 \mu\text{m}$), the ‘residence time map’ was incremented by the time interval between two consecutive acquisitions. Thus, the final residence time map represents the cumulative duration during which each pixel was covered by bacterial cells. As previously mentioned, the automatic detection of individual cells at various times over field of views as large as $350 \times 350 \mu\text{m}^2$ with a cutoff value of value of $-0.38 \mu\text{m}$ can only be considered reliable within the time interval between $t = 0$ hours and $t = 10.8$ hours. Therefore, the ‘bacteria residence time map’ was calculated only based on the *in-situ* topography data acquired over that time period. Furthermore, since the *ex situ* topography data were acquired over the same field of view but with a lower resolution compared to the *in situ* acquisitions (because of the use of a traditional Mirau objective instead of the glass compensated objective used for the *in situ* acquisition), in order to have a one-to-one

correspondence between pixels, the ‘bacteria residence time map’ was rescaled with a bilinear interpolation to match the resolution of the *ex situ* surface topography.

The residence time map and final surface topography were then compared by plotting the height values corresponding to all pixels with a given residence time as a function of all residence time values, averaged over time intervals of one hour (Figure 5.2.7). The resulting plot shows that, while the average of all height values associated with pixels that were never covered by bacteria (i.e., residence time equal to zero) was slightly negative, the average height values associated with pixels that were covered by bacteria for a given time was consistently positive, which means that all pixels that have been covered by bacteria tended to be more elevated compared to the surface mean plane (and to the ‘uncovered’ counterparts). Moreover, the average height values associated with pixels that were covered by bacteria for a given time show an upward trend as the residence time intervals increase, with a notable sharp increase for the 2-hour residence time interval and according to a seemingly linear trend for larger time intervals. This suggests that locations that were covered by bacteria for longer times dissolved less compared to the rest of the surface, which ultimately resulted in the formation of a so-called ‘high-elevation region’, with relative height of $\sim 0.34 \mu\text{m}$ after ~ 22 hours.

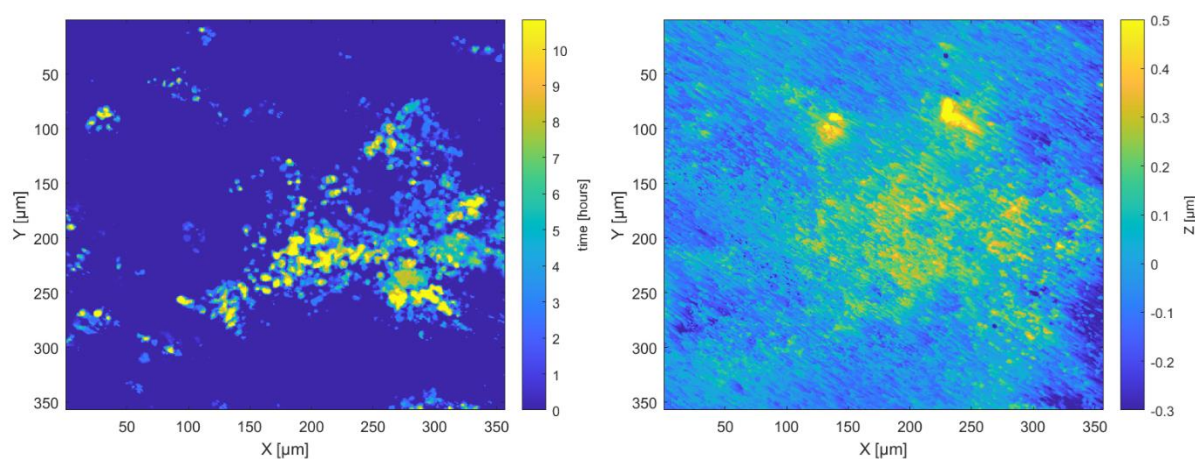


Figure 5.2.6 Comparison of the ‘bacteria residence time map’ based on in-situ acquisitions (left-hand side) with the corresponding surface topography acquired *ex-situ* in dry conditions after physically removing the residual cells from the calcite surface (right-hand side). The size of the images is $357 \times 357 \mu\text{m}^2$.

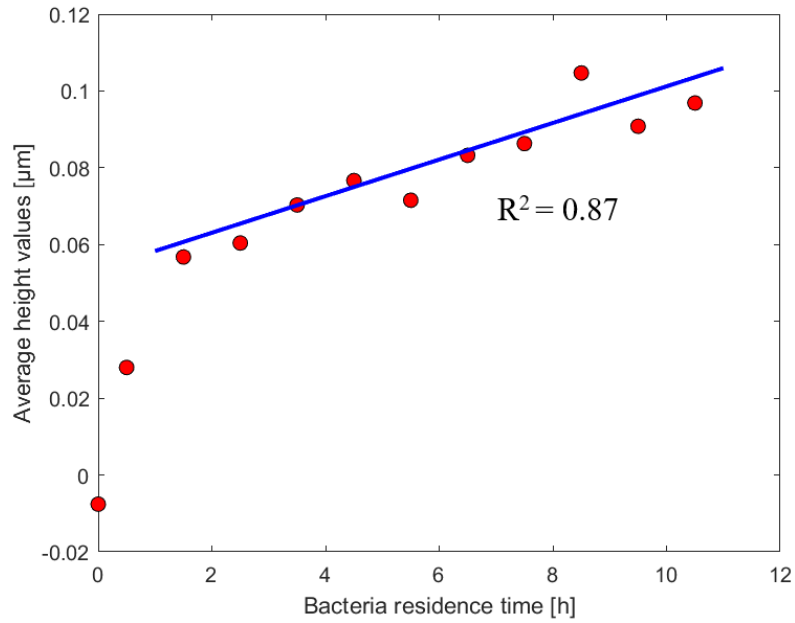


Figure 5.2.7 Plot of the average height values associated with various bacteria residence time values as a function of different residence time intervals. Each plotted value represents the average of all height values corresponding to pixels for which the residence time interval falls within one hour interval. It provides an average estimate of the correlation between the ‘final surface topography’ and the ‘bacteria residence time map’ displayed in Figure 5.2.6.

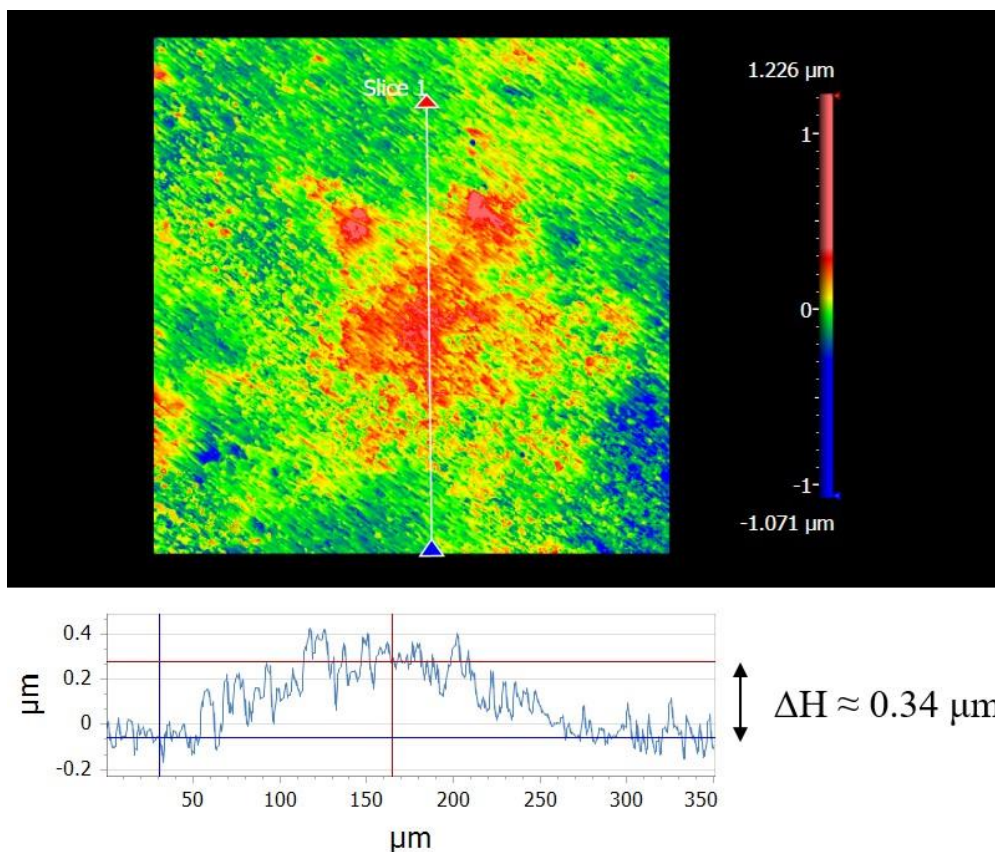


Figure 5.2.8 Surface profile of the ‘high-elevation-region’ generated at the location where the bacterial cells sticked for longer times, with relative height of $\sim 0.34 \mu\text{m}$ with respect to the rest of the surface after ~ 22 hours of dissolution.

5.2.4 Conclusions

The results presented in this second sub-section of Chapter 5 are preliminary and part of an ongoing research. An outline of future experimental and processing efforts is provided in Chapter 6, where methods to address the current limitations are also discussed. Nonetheless, these preliminary findings can already provide some valuable additional insights into the interplay between biofilm dynamics and mineral dissolution. First, the *in situ* VSI setup shed light into the dynamics of cells detachment during dissolution, thereby enabling the estimation of the detachment rate of bacterial cells from the calcite surface. Secondly, the analysis of surface topography in areas devoid of bacteria and in areas consistently partially covered by bacteria revealed that biofilm coverage has a distinct impact on the surface topography evolution, specifically leading to the generation of regions with higher elevations compared to the rest of the surface and exhibiting a distinct evolution of surface roughness. Lastly, the

comparison between the ‘bacteria residence time map’ and the final surface topography revealed that areas covered by bacteria for longer periods tended to dissolve less compared to the rest of the surface, thereby resulting in the formation of ‘high-elevation-regions’. Overall, this further confirms the existence of the bio-weathering signatures formed under far-from-equilibrium conditions that were documented for the first time in sub-section 5.1 and clarifies that these signatures are formed at the locations covered by agglomerates of cells for durations as short as a few hours. Furthermore, the correlation between bacteria residence time map and the final surface topography suggests that the calcite microtopography resulting from dissolution may preserve signatures of the history of biofilm coverage, thus providing additional clues about past bio-weathering conditions.

References

- Ahmed, E., Holmström, S.J.J.M.b., 2014. Siderophores in environmental research: roles and applications. 7(3): 196-208.
- Bandstra, J.Z., Brantley, S.L., 2008. Surface evolution of dissolving minerals investigated with a kinetic Ising model. *Geochimica Et Cosmochimica Acta*, 72(11): 2587-2600.
- Barker, W.W., Welch, S.A., Chu, S., Banfield, J.F., 1998. Experimental observations of the effects of bacteria on aluminosilicate weathering. *American Mineralogist*, 83(11-12 Part 2): 1551-1563.
- Bennett, P.C., Hiebert, F.K., Choi, W.J., 1996. Microbial colonization and weathering of silicates in a petroleum-contaminated groundwater. *Chemical Geology*, 132(1): 45-53.
- Billi, D. et al., 2011. Damage Escape and Repair in Dried *Chroococidiopsis* spp. from Hot and Cold Deserts Exposed to Simulated Space and Martian Conditions. *Astrobiology*, 11(1): 65-73.
- Bouissonnié, A., Daval, D., Marinoni, M., Ackerer, P., 2018. From mixed flow reactor to column experiments and modeling: Upscaling of calcite dissolution rate. *Chemical Geology*, 487: 63-75.
- Brantley, S.L., Crane, S.R., Crerar, D.A., Hellmann, R., Stallard, R., 1986. Dissolution at dislocation etch pits in quartz. *Geochimica et Cosmochimica Acta*, 50(10): 2349-2361.
- Brantley, S.L., Olsen, A.A., 2014. 7.3 - Reaction Kinetics of Primary Rock-Forming Minerals under Ambient Conditions A2 - Holland, Heinrich D. In: Turekian, K.K. (Ed.), *Treatise on Geochemistry (Second Edition)*. Elsevier, Oxford, pp. 69-113.
- Buss, H.L., Brantley, S.L., Liermann, L.J.J.G.J., 2003. Nondestructive methods for removal of bacteria from silicate surfaces. 20(1): 25-42.
- Carrasco, I.S., Reis, F.D.A., 2021. Modeling the kinetics of calcite dissolution in neutral and alkaline solutions. *Geochimica Et Cosmochimica Acta*, 292: 271-284.
- Carter, E.L.W., 2005. Carbon cycling and mineral weathering in temperate forested watersheds: an integrated study of solution and soil chemistries. University of Michigan.

- Casero, M.C., Ascaso, C., Quesada, A., Mazur-Marzec, H., Wierzchos, J., 2021. Response of Endolithic Chroococciopsis Strains From the Polyextreme Atacama Desert to Light Radiation. 11.
- Daval, D. et al., 2009. Carbonation of Ca-bearing silicates, the case of wollastonite: Experimental investigations and kinetic modeling. *Chemical Geology*, 265(1-2): 63-78.
- Davis, K., Neelson, K., Lüttge, A., 2007. Calcite and dolomite dissolution rates in the context of microbe–mineral surface interactions. *Geobiology*, 5(2): 191-205.
- Davit, Y. et al., 2013. Hydrodynamic dispersion within porous biofilms. *Physical Review E*, 87(1): 012718.
- Dittrich, M., Sibling, S.J.G.S., London, Special Publications, 2010. Calcium carbonate precipitation by cyanobacterial polysaccharides. 336(1): 51-63.
- Elert, K. et al., 2021. Degradation of ancient Maya carved tuff stone at Copan and its bacterial bioconservation. *npj Materials Degradation*, 5(1): 44.
- Fisk, M.R., Crovisier, J.-L., Honnorez, J., 2013. Experimental abiotic alteration of igneous and manufactured glasses. *Comptes Rendus Geoscience*, 345(4): 176-184.
- Fisk, M.R., Giovannoni, S.J., Thorseth, I.H., 1998. Alteration of Oceanic Volcanic Glass: Textural Evidence of Microbial Activity. *Science*, 281(5379): 978-980.
- Flemming, H.-C., Wuertz, S., 2019. Bacteria and archaea on Earth and their abundance in biofilms. *Nature reviews microbiology*, 17(4): 247-260.
- Jongmans, A.G. et al., 1997. Rock-eating fungi. *Nature*, 389: 682.
- Kurganskaya, I., Luttge, A., 2021. Mineral Dissolution Kinetics: Pathways to Equilibrium. *ACS Earth and Space Chemistry*, 5(7): 1657-1673.
- Lasaga, A.C., Blum, A.E., 1986. Surface chemistry, etch pits and mineral-water reactions. *Geochimica et Cosmochimica Acta*, 50(10): 2363-2379.
- Lasaga, A.C., Luttge, A., 2001. Variation of Crystal Dissolution Rate Based on a Dissolution Stepwave Model. *Science*, 291: 2400-2404.
- Luttge, A., Conrad, P.G., 2004. Direct observation of microbial inhibition of calcite dissolution. *Applied and Environmental Microbiology*, 70(3): 1627-1632.
- Lüttge, A., Zhang, L., Neelson, K.H.J.A.J.o.S., 2003. Mineral surfaces and their implications for microbial attachment: Results from Monte Carlo simulations and direct surface observations. 305: 766-790.
- McLoughlin, N., Brasier, M.D., Wacey, D., Green, O.R., Perry, R.S., 2007. On biogenicity criteria for endolithic microborings on early Earth and beyond. *Astrobiology*, 7(1): 10-26.
- Meakin, P., Rosso, K.M., 2008. Simple kinetic Monte Carlo models for dissolution pitting induced by crystal defects. *The Journal of Chemical Physics*, 129(20): 204106.
- Morse, J.W., Arvidson, R.S., A., L., 2007. Calcium carbonate formation and dissolution. *Chemical Reviews*, 107(2): 342-381.
- Murik, O. et al., 2017. What distinguishes cyanobacteria able to revive after desiccation from those that cannot: the genome aspect. 19(2): 535-550.

- Rippka, R., Deruelles, J., Waterbury, J.B., Herdman, M., Stanier, R.Y., 1979. Generic Assignments, Strain Histories and Properties of Pure Cultures of Cyanobacteria. *111*(1): 1-61.
- Santelli, C.M., Welch, S.A., Westrich, H.R., Banfield, J.F., 2001. The effect of Fe-oxidizing bacteria on Fe-silicate mineral dissolution. *Chemical Geology*, *180*(1-4): 99-115.
- Schwartzman, D.W., Volk, T., 1989. Biotic enhancement of weathering and the habitability of Earth. *Nature*, *340*(6233): 457.
- Staudigel, H. et al., 2008. 3.5 billion years of glass bioalteration: Volcanic rocks as a basis for microbial life? *Earth-Science Reviews*, *89*(3-4): 156-176.
- Stigliano, L., Ackerer, P., Benzerara, K., Daval, D., 2023. Linking calcite surface roughness resulting from dissolution to the saturation state of the bulk solution. *Chemical Geology*, *637*: 121680.
- Stigliano, L., Siena, M., Ackerer, P., Guadagnini, A., Daval, D., 2021. Statistical Description of Calcite Surface Roughness Resulting from Dissolution at Close-to-Equilibrium Conditions. *ACS Earth and Space Chemistry*, *5*(11): 3115-3129.
- Thorseth, I.H., Furnes, H., Tumyr, O., 1995. Textural and chemical effects of bacterial activity on basaltic glass: an experimental approach. *Chemical Geology*, *119*(1): 139-160.
- Van Breemen, N. et al., 2000. Mycorrhizal weathering: a true case of mineral plant nutrition? , *49*: 53-67.
- Velbel, M.A., 1993. Formation of protective surface layers during silicate-mineral weathering under well-leached, oxidizing conditions. *American Mineralogist*, *78*(3-4): 405-414.
- Waterbury, J.B., Stanier, R.Y., 1978. Patterns of growth and development in pleurocapsalean cyanobacteria. *Microbiol Rev*, *42*(1): 2-44.
- Waters, M.S. et al., 2009. Simultaneous Interferometric Measurement of Corrosive or Demineralizing Bacteria and Their Mineral Interfaces. *75*(5): 1445-1449.
- Wierzchos, J., Casero, M.C., Artieda, O., Ascaso, C., 2018. Endolithic microbial habitats as refuges for life in polyextreme environment of the Atacama Desert. *Curr Opin Microbiol*, *43*: 124-131.
- Wild, B., Gerrits, R., Bonneville, S., 2022. The contribution of living organisms to rock weathering in the critical zone. *npj Materials Degradation*, *6*(1): 98.
- Wild, B., Imfeld, G., Daval, D., 2021. Direct measurement of fungal contribution to silicate weathering rates in soil. *Geology*.
- Zhu, C., Veblen, D.R., Blum, A.E., Chipera, S.J., 2006. Naturally weathered feldspar surfaces in the Navajo Sandstone aquifer, Black Mesa, Arizona: Electron microscopic characterization. *Geochimica Et Cosmochimica Acta*, *70*(18): 4600-4616.

Chapter 6 : Conclusions and perspectives

6.1 Key findings, limitations, and generalizability

Overall, this PhD work contributed to the fundamental understanding of the informative content embedded within weathered mineral surfaces. Through a combination of experimental and modeling approaches, this study showed that the steady-state calcite surface roughness resulting from dissolution can be used as a proxy to back-estimate the saturation state of the fluid and that the calcite surface microtopography may preserve imprints of microbial weathering that can be quantitatively detected.

More specifically, under abiotic conditions, an empirical relationship was established between a statistical characterization of the steady-state surface roughness of calcite resulting from dissolution and the saturation state of the fluid under which the reaction occurred. Stochastic modeling investigations suggested that the steady-state surface roughness configurations resulting from dissolution at different Ω do not depend on the reaction history and that the relaxation time required for calcite to achieve a microtopography steady-state is in the order of several months at most, which is negligible compared to geological timescales. The statistical characterizations associated with each saturation state investigated can therefore be used as reference values to back-estimate the saturation state of the fluid for weathered calcite surfaces reacted under unknown conditions.

Furthermore, dissolution experiments conducted upon covering the calcite surface with a biofilm of cyanobacteria revealed that, under the investigated conditions, biofilm-mediated dissolution did not produce etching features resembling microorganisms in 'size, shape and distribution'. In contrast, biofilm mediation produced high-elevation regions across the calcite surface at the locations where the cells agglomerated, with the size of such regions extending far beyond the size of individual cells. Such results were independently confirmed by preliminary observations conducted *in situ*. Atomic-scale stochastic simulations of the dissolution process suggested that these distinctive bio-weathering features arose from a localized increase in the fluid saturation state at the biofilm-mineral interface. This increase in saturation state could be attributed to a local increase in pH likely induced by photosynthetic activity, which, in turn, led to a localized reduction in the calcite dissolution rate. Importantly, the presence of these distinctive microbial weathering signatures could be quantitatively detected through the statistical characterizations developed in this study. These tools, therefore,

may provide a novel, non-destructive means to quantitatively, thus less ambiguously, identify biosignatures on naturally weathered minerals.

Before discussing the generalizability and potential applications of these findings to natural settings, it is important to emphasize that these outcomes were obtained within well-controlled laboratory settings. It is therefore crucial to thoroughly investigate any disparities between the investigated conditions and the complexities of natural settings, as such differences could potentially reduce the signals-to-noise ratio observed in this work.

6.1.1 Limitations

First, the laboratory experimental setup adopted, which consisted in a continuously stirred flow-through system in which physico-chemical conditions were maintained constant over the progress of the calcite dissolution experiments, does not fully capture the dynamic and fluctuating nature of natural systems. The primary discrepancies between the laboratory settings employed in this study and natural settings can be summarized as follows: (i) the laboratory setup maximizes mineral-water contact, unlike natural settings where fluid-mineral interactions occur within porous media or involve mineral surfaces partially covered by sediments, organic matter, and biofilms, thereby reducing the available reactive surface area; (ii) the laboratory settings maintained turbulent flow and homogeneous chemical conditions within the reactor through continuous stirring, which contrast with the laminar and/or discontinuous flows that are observed, for instance, in soils, where a gradient in the fluid saturation state can be generated at the fluid-mineral interface along the direction of the water flow; (iii) the controlled temperature conditions maintained in the lab stand in contrast to the diurnal and seasonal temperature variations prevalent in many natural environments ; (iv) the use of a simplified medium in the lab, devoid of chelating agents, organic matter, and other compounds commonly found in natural environments may not fully capture the complexity of interactions that occur in natural settings. Notably, none of these discrepancies inherently implies that the Ω -roughness signal observed in this laboratory study would not be convincingly recognized in natural environments as well. However, it is plausible that the reference Ω -roughness curves derived here may need recalibration in more realistic settings. Specifically designed incubation experiments can address this question, as discussed in sub-section 6.3.2.

Secondly, the experiments were conducted with mm-size mechanically-polished natural calcite crystals. In natural settings, the size of calcite crystals can vary widely from one location to another, depending on the specific geological and environmental conditions. In this study, the attainment of a steady state surface roughness configuration indicative of the fluid saturation

state was only demonstrated for calcite single crystals with {104} surfaces larger than 4-5 mm, which can be conceptualized as ‘infinite surfaces’. For smaller crystals, the contribution of corners and edges to the dissolution process and to the corresponding microtopography evolution becomes more significant (Noiriel et al., 2020). This increased influence of corners and edges may potentially impact the achievement of a steady-state configuration and/or the establishment of a bijective Ω -roughness relationship. Moreover, it is well-established that mechanical polishing increases the dislocation density (MacInnis and Brantley, 1992), which, in turn, affects the crystal reactivity and the corresponding surface microtopography evolution. While employing crystals with different dislocations densities (e.g., naturally cleaved samples and/or samples subject to various degrees of mechanical and thermal stress), under the same physico-chemical conditions of the fluid, is unlikely to hinder the establishment of a bijective of Ω -roughness relationship, it is plausible that the time required to achieve a steady-state configuration of the surface and the surface roughness reference values might differ. As a consequence, further experimental and modeling work is needed to explore how the Ω -roughness relationship developed in this study changes for calcite crystals with varying defect distributions, fluid impurities, and framework impurity ion, as well as to explore the existence of a Ω -roughness relationship for smaller calcite crystals. On a similar note, different fluid compositions, pH levels, temperature conditions, and the presence of fluid impurities would also need to be investigated. In parallel, improving the fundamental understanding of the underlying mechanisms may help narrowing down the parameters that would need to be investigated. Ultimately, a comprehensive library of Ω -roughness relationships obtained under a variety of fluid-mineral conditions relevant for natural environments would need to be generated.

Lastly, with regards to the biotic experiments, it is important to note that this study employed a single bacterial strain, with one specific metabolism. In natural settings, biofilm-forming microbial communities often consist of diverse bacteria, as well as consortia of archaea and microbial eukaryotes, with a wide array of metabolic pathways. Such diversity in microbial populations and metabolisms in nature may lead to variations in the bio-weathering features produced and potentially limit the clarity of the microbial weathering signal that was detected experimentally in this work with a single bacteria strain. Future work should therefore explore the impact of more complex and realistic biofilm-forming microbial communities.

6.1.2 Generalizability

Considering the limitations posed by the experimental approach adopted in this study, it becomes possible to explore the potential applicability of these findings to other mineral-microbe systems.

At the core of the empirical Ω -roughness relationship that was developed in this work under abiotic conditions, there is the difference in surface microtopography resulting from dissolution that is observed at far-from-equilibrium versus close-to-equilibrium conditions for all minerals with a framework structure, as discussed in section 1.2.5. Therefore, all minerals for which a critical value of Gibbs free energy can be clearly identified (i.e., a critical value that distinctly separates far-from-equilibrium conditions, for which the opening of hollow cores to form etch pits is thermodynamically favoured, from close-to-equilibrium conditions, for which crystallographic etch pits are not formed), have the potential to exhibit a more general relationship between the saturation state and the surface topography arising from dissolution. However, for such Ω -roughness relationships to be used as a proxy for reconstructing past weathering conditions, the surface topography associated with distinct saturation states must also achieve a steady-state configuration over relatively short timescales. The attainment of a steady-state configuration of the crystal surface is likely to be the most challenging requirement to be met. For instance, Anbeek, (1992) showed that the surface roughness factors of naturally-weathered feldspars vary by more than one order of magnitude, suggesting that a steady-state configuration of the surface might not exist. In contrast, the attainment of a steady-state of surface roughness was documented under laboratory conditions for the (115), (334), (104) and (245) faces of fluorite (Godinho et al., 2014) and for the (010) olivine face (Li et al., 2021), under far-from-equilibrium conditions. Hence, fluorite and olivine emerge as promising candidates to work, along with calcite, as proxies for back-estimating the fluid saturation state in natural settings.

Furthermore, additional experimental work is needed to explore the existence of a bijective relationship between Ω and the steady-state surface roughness of calcite under pH conditions that were not explored in this work. However, since the calcite dissolution rate is approximately constant between pH=5.5 and pH=8.5 (Sjoberg and Rickard, 1984) and given the distinct link that exists between surface roughness and dissolution rate at pH~7.9, as documented in this study, it is plausible that the Ω -roughness relationship here developed would extend at least to this entire pH range.

Lastly, regarding the bio-weathering signatures documented in this study, similar high-elevation regions can potentially be identified on a variety of microbially-mediated weathered minerals, provided that the biofilm creates a microenvironment with a higher saturation state compared to the bulk solution. This potential includes a wide spectrum of microbial species, with various metabolisms, and a diverse range of mineral substrates.

Taking into account the discussed constraints and prospects for generalization, the natural settings most relevant to the findings of this work are detailed in the following section.

6.2 Applications to natural settings

6.2.1 Estimation of the fluid saturation state in natural environments

With regards to the Ω -roughness proxy relationship developed in this study, given the constraints provided by the laboratory conditions adopted and discussed in the previous subsection, natural settings that could be relevant for these findings include water-dominated environments with relatively stable chemical conditions and environments that ceased to be in contact with aqueous fluids. These include aquatic environments, such as lakes, rivers and oceans, where minerals interact with water over extended periods, but also arid deserts, caves and planetary surfaces, where minerals might have ceased to interact with water.

In natural settings where calcite crystals (or other minerals with a similar Ω -roughness relationship) are no longer in contact with aqueous fluids, the utility of the Ω -roughness proxy relationship becomes straightforward. By comparing the statistical metrics associated with a naturally weathered calcite sample to the reference values established in this study, it would become possible to estimate the last fluid saturation state experienced by that surface, offering valuable insights into the chemical history of these surfaces that would be otherwise inaccessible.

With regard to aquatic environments with relatively stable chemical conditions, the utility of the Ω -roughness proxy relationship becomes less straightforward. This is because, in such settings, it is often feasible to collect both mineral and aqueous samples. Analysing the chemistry of the collected aqueous samples would provide a direct method for estimating the fluid saturation state based on solution chemistry analyses. Therefore, for these settings, the Ω -roughness proxy relationship becomes beneficial only when the fluid saturation state cannot be reliably estimated based on solution chemistry analyses. These include settings where

measuring the concentrations of all dissolved elements is straightforward, but the estimation of the corresponding activity coefficients becomes challenging due to the presence of complexing agents in the solution. This challenge introduces significant uncertainty when estimating the fluid saturation state. In this context, an example of practical application would be the use of the Ω -roughness proxy to estimate the saturation state of seawater with respect to calcite, where the abundant presence of dissolved organic compounds may hinder the accurate estimate of $[\text{Ca}^{2+}]$ activity. Indirect estimations of seawater saturation state with respect to calcite, based on *in situ* derived dissolution rates, have been suggested in previous studies (Naviaux et al., 2019). On a similar basis, the Ω -roughness proxy relationship developed in this study could be used to estimate the seawater saturation state more reliably at different depths of the ocean, as well as to identify shifts in the saturation state of seawater due to ocean acidification.

6.2.2 Determination of biosignatures on naturally weathered minerals

The tool developed in this work for the determination of biosignatures based on the surface microtopography resulting from dissolution has the potential to be valuable in a wide range of natural settings, including the search for life on other planets.

As previously mentioned, the bioweathering imprints (i.e., high-elevation regions) documented in this work can potentially be identified on a variety of microbially-mediated weathered minerals, provided that the biofilm creates a microenvironment with a higher saturation state compared to the bulk solution. When considering CaCO_3 -minerals, these include microbes whose metabolism results in a net increase of the solution pH, such as phototrophic, nitrifying and ammonia-oxidizing bacteria. As a consequence, the identification of these high-elevation regions in natural settings on Earth can provide insights into past presence of life in extreme environments as well as providing clues about the specific microbial populations that might have been present in the past in a given environment.

6.3 Future perspectives

Building upon the findings of this work, there are several promising avenues for future research and exploration, along with potential methodological improvements. These include conducting additional *in situ* dissolution experiments, which are currently ongoing, as well as designing incubation and preservation experiments aimed at investigating the 'surface signals' achievable under conditions more closely resembling natural settings.

6.3.1 Microbial weathering in-situ experiments

The sub-section 5.2 was centred around the in-situ cyanobacteria-mediated calcite dissolution experiment conducted at $\Omega = 0.00$, which provided initial insights into the potential of this experimental configuration. In this framework, additional *in situ* dissolution experiments will be performed, exploring a wider range of saturation states and initial surface conditions, with the ultimate goal of broadening the mechanistic understanding of the interplay between biofilm dynamics, mineral substrate dissolution, and corresponding surface microtopography evolution.

The study presented in the sub-section 5.1, which was based on *ex situ* dissolution experiments, revealed that close-to-equilibrium conditions resulted in a larger biofilm coverage of the calcite surface at the end of the experiments compared to far-from-equilibrium conditions. This can be explained either as a consequence of the larger surface retreat obtained at far-from-equilibrium (due to higher reactivity) or as a consequence of inconsistent initial biofilm coverage, which could not be monitored with the experimental configuration adopted. To address this question, targeted *in situ* experiments for which the dynamics of biofilm coverage can be monitored in real-time can provide additional insights that could support either explanation.

Notably, the different biofilm coverage observed at the end of the ex-situ experiments at far-from-equilibrium compared to close-to-equilibrium conditions can, in principle, also be explained by different metabolic activity of the cyanobacteria, resulting from different solution concentrations of $[\text{Ca}^{2+}]$. If *in situ* experiments will confirm that the final biofilm coverage is consistently higher at far-from-equilibrium compared to close-to-equilibrium conditions (with the initial biofilm coverage being approximately the same), additional *in situ* experiments can be designed to explore whether this is a consequence of the larger surface retreat (due to higher reactivity) or of a different metabolic activity (due to different concentrations of $[\text{Ca}^{2+}]$). One possibility to explore this aspect is to conduct two dissolution experiments with the same Ω , where one experiment is run with a pre-etched surface (e.g., pretreated in mQ water so that etch pits develop on the surface) and one with an untreated mechanically-polished surface. The pre-etched surface would (transiently) have higher reactivity compared to the untreated surface, even if the fluid saturation state is the same in both cases (Beig and Luttge, 2006). If the pretreated surface exhibits a higher cell detachment rate compared to the untreated surface, then it would be possible to conclude that the material loss controls the biofilm detachment rather than the concentration of $[\text{Ca}^{2+}]$, suggesting that Ω might only indirectly control the biofilm detachment by modulating the mineral substrate reactivity.

In general, the detachment of bacterial cells from the surface is controlled by two main parameters: the fluid-dynamics conditions (i.e., the flow rate in the *in situ* setup and the rotational speed of the stir bar in the *ex situ* setup) and the material loss from the calcite substrate due to dissolution. The *in situ* setup enables to targetedly explore the control of bacterial detachment by conducting specific experiments with different flow rate and with conditions that lead to higher reactivity of calcite, in terms of fluid chemistry (e.g., pH lower than 5.5) and/or using more reactive samples (e.g., calcite crystals with larger dislocation density and/or pre-etched). Ongoing in-situ experiments will attempt to address this question.

In parallel, potential methodological improvements of data processing will also be investigated. In particular, the protocol for identifying individual cells across the calcite surface, which is at the core of all analyses presented in the sub-section 5.2, currently show some limitations that could potentially be overcome. The current protocol, which involves establishing a given cutoff value (kept constant at different times) leads to an underestimation of the bacteria coverage at any given time. One possibility of improvement involves partitioning the area investigated into various sub-windows for which distinct time-varying cutoff values can be assigned. Moreover, when it comes to study the evolution of the surface roughness of partially covered areas as in section 5.2.3.1, one current limitation involves that individual cells identified by the cutoff-based approach erroneously appear to be surrounded by negative height values (Figure 5.2.4). As these supposedly negative height values disappear as cells detach from the surface, these can be interpreted as VSI artifacts and should, therefore, be excluded. Indeed, including such negative height values in the surface analyses leads to observable inconsistencies. For instance, as displayed in Figure 5.2.5, the presence of these ‘artificial’ negative height values shifts the mean height value of the partially covered surface at $t = 0$ h towards a lower value compared to the uncovered counterpart, when they should both be centred approximately in zero. Additionally, this results in a consistently higher R_a , even at early times, which is likely to be a processing artifact. To address this limitation, one potential solution is to identify the locations of individual cells using cutoff-based approaches and then expand the zones to be excluded by a few pixels in all directions around these locations. This approach would ensure the removal of all 'artificial' negative height values from the analysis, thus improving the accuracy of the surface analysis.

Overall, the prospects of conducting additional *in situ* experiments and enhancing the associated data processing hold promise for advancing the fundamental understanding of the informative

content embedded into bio-weathered mineral samples, a question central to this manuscript work.

6.3.2 Incubation weathering experiments and field studies

While methodological improvements and additional laboratory experimental studies can provide further insights into the fundamental understanding of the informative content of biotically and abiotically weathered surfaces, it is also crucial to conduct experiments and field studies specifically designed to explore the presence and persistence of (bio-)weathering signatures on mineral samples across natural settings.

To this end, it is essential to investigate the existence of detectable 'microtopography signals' in natural environments. To address this question, incubation experiments involving calcite samples should be conducted across various natural settings, spanning from soils to aqueous environments, targeting different saturation states with respect to calcite of the bulk solution. Comparisons of the statistical characterizations of the resulting microtopographies with the reference values developed in this work would potentially allow to understand the extent to which these findings can directly be applied to natural settings. On the same note, the naturally-occurring coverage of the calcite samples from complex biofilms, and the resulting potential distinctive surface features, would also need to be targetedely investigated, in order to explore the relevance for natural environments of the microbial signatures identified in this study.

The second necessary step would involve examining the extent to which these 'microtopography signals' can be preserved over time and under varying physicochemical conditions. While some of these questions were addressed in this study from a modeling perspective, direct observations are also required.

Overall, conducting these incubation experiments in natural environments can provide insights into the types of natural settings where the findings of this research hold the most promise and relevance. Once potential natural environments are identified, field studies aimed at exploring the existence of detectable 'microtopography signals' on naturally weathered mineral samples collected from these settings will be essential. Hopefully, this will confirm the results of this PhD work, which suggested that naturally-weathered minerals may serve as a proxy to back-estimate the fluid saturation state, and that microbial weathering does result in specific imprints at the mineral surface that could be quantitatively attributable to the action of life.

6.4 Concluding remarks

Collectively, this PhD work contributed to advance the fundamental understanding of the informative content embedded within weathered mineral surfaces. Through a combination of laboratory experiments and modeling approaches, this research showed that, under the conditions investigated in the lab, the calcite steady-state surface roughness resulting from dissolution can be used as a proxy to back-estimate the saturation state of the fluid. Additionally, this study revealed that the calcite surface microtopography resulting from biofilm-mediated dissolution can preserve imprints of microbial weathering, which can be quantitatively, thus less ambiguously, detected. Moving ahead, it is essential to conduct additional extensive research, both in laboratory and in the field, to evaluate the applicability of these findings to natural settings. Overall, the novel, mechanistically-supported quantitative criteria developed in this PhD work represent a first step forward in the capability to reconstruct past weathering conditions and identify mineral bio-weathering signatures in natural settings, both on Earth and in the broader context of astrobiology.

References

- Anbeek, C., 1992. Surface roughness of minerals and implications for dissolution studies. *Geochimica et Cosmochimica Acta*, 56(4): 1461-1469.
- Beig, M.S., Luttge, A., 2006. Albite dissolution kinetics as a function of distance from equilibrium: Implications for natural feldspar weathering. *Geochimica et Cosmochimica Acta*, 70: 1402-1420.
- Godinho, J.R.A., Piazzolo, S., Balic-Zunic, T., 2014. Importance of surface structure on dissolution of fluorite: Implications for surface dynamics and dissolution rates. *Geochimica Et Cosmochimica Acta*, 126: 398-410.
- Li, X., Wang, Q., Shen, X., Pedrosa, E.T., Luttge, A., 2021. Multiscale investigation of olivine (010) face dissolution from a surface control perspective. *Applied Surface Science*, 549: 149317.
- MacInnis, I.N., Brantley, S.L., 1992. The role of dislocations and surface morphology in calcite dissolution. *Geochimica et Cosmochimica Acta*, 56(3): 1113-1126.
- Naviaux, J.D. et al., 2019. Calcite dissolution rates in seawater: Lab vs. in-situ measurements and inhibition by organic matter. *Marine Chemistry*, 215: 103684.
- Noiriel, C., Oursin, M., Daval, D., 2020. Examination of crystal dissolution in 3D: A way to reconcile dissolution rates in the laboratory? *Geochimica Et Cosmochimica Acta*, 273: 1-25.
- Sjoeberg, E.L., Rickard, D.T.J.C.G., 1984. Calcite dissolution kinetics: surface speciation and the origin of the variable pH dependence. 42(1-4): 119-136.

Appendices

Appendix A

Step	Grit (Eu) Number	μm
1	P120	127
2	P400	35
3	P800	21.8
4	P2500	8.4
5	-	6
6	-	3
7	-	0.25

Table A1 Grit sizes of the multi-step grinding and polishing sequence.

Detection Limits	0.002	0.001	0.003	0.007	0.001	0.001	0.003	0.02	0.04	0.002
time [h]	Si	Al	Mg	Ca	Fe	Mn	Ti	Na	K	P
0	-	-	-	54.3	0.003	-	-	s	1.75	-
23	-	0.004	-	53.8	0.003	-	-	s	1.88	-
46	-	0.001	-	53.7	0.003	-	-	s	1.91	-
69	0.003	-	-	54.0	0.004	-	-	s	1.87	-
92	-	-	-	54.1	0.002	-	-	s	1.88	-
116	-	0.001	-	54.2	0.002	-	-	s	1.90	-
141	-	0.001	-	54.3	0.002	-	-	s	1.91	-
164	-	-	-	54.4	0.002	-	-	s	1.94	-
188	-	-	-	54.6	0.002	-	-	s	1.87	-

Table A2 ICP-AES analyses of the aqueous solution at different times. Concentrations are expressed in ppm.

Appendix B

$\Omega = 0$

time [h]	Ca [ppm]
0.00	0.06
15.00	1.01
20.00	0.96
87.00	1.03
116.00	0.98
187.00	1.02
260.00	0.98

$\Omega = 0.1$

time [h]	Ca [ppm]
0.00	13.31
15.00	13.87
30.00	13.95
45.00	13.86
67.00	14.01
139.00	13.95
204.00	13.90
269.00	13.91

$\Omega = 0.3$

time [h]	Ca [ppm]
0.00	38.94
15.00	39.09
30.00	39.11
97.00	39.04
121.00	39.18
187.00	39.07
260.00	39.05

$\Omega = 0.55$

time [h]	Ca [ppm]
0.00	73.16
15.00	74.10
30.00	73.25
45.00	73.81
67.00	73.33
139.00	73.31
204.00	73.78
269.00	73.23

$\Omega = 0.65$

time [h]	Ca [ppm]
0.00	87.51
15.00	88.03
30.00	87.70
58.00	87.49
144.00	88.00
194.00	88.08
263.00	87.81

$\Omega = 0.8$

time [h]	Ca [ppm]
0.00	110.65
15.00	110.58
30.00	111.02
58.00	110.89
144.00	111.58
194.00	110.69
263.00	110.72

Table B1 ICP-AES measurements of the inlet vs outlet solutions for all saturation states over the progress of the experiments.

	$\Omega = 0$	$\Omega = 0.1$	$\Omega = 0.3$	$\Omega = 0.55$	$\Omega = 0.65$	$\Omega = 0.8$
Number of sub-windows	30	37	35	50	45	39
Surface detrending	1st order	1st order	1st order	1st order	2nd order	2nd order

Table B2 The table indicates, for all saturation states, the number of sampling windows of $80 \times 80 \mu\text{m}^2$ used in the small-windows statistical analysis and the specific surface detrending adopted. As described in the Materials and Methods section, the sampling windows were identified randomly along the surface, while avoiding surface macro-defects, and only selected if available at all times. Moreover, in general, a second-order surface detrending was applied to correct for the imperfect parallel alignment between the surface and the VSI objective and by the waviness of the sample surface resulting from the polishing process. However, at $\Omega_{\text{calcite}} \leq 0.55$, the effects of the polishing process on the surface were no longer visible after dissolution.

Hence, a first-order surface detrending was applied to correct for the imperfect VSI-surface parallel alignment, while preserving the actual shape of dissolution surface features, such as etch pits.

	$\Omega = 0$	$\Omega = 0.1$	$\Omega = 0.3$	$\Omega = 0.55$	$\Omega = 0.65$	$\Omega = 0.8$
Early times [h]	15	15	15	15	15	15
Mid times [h]	116	139	121	139	144	144
Late times [h]	260	269	260	269	263	263
Surface detrending	1st order	1st order	1st order	1st order	4th order	4th order

Table B3 The table indicates, for all saturation states, the precise times referred to as ‘early’, ‘mid’ and ‘late’ times in the text and the specific surface detrending adopted on sub-windows of $400 \times 400 \mu\text{m}^2$. For $\Omega_{\text{calcite}} = 0.65$ and $\Omega_{\text{calcite}} = 0.8$, to correct for the waviness of the sample generated by the polishing process and still present after dissolution, a 4th order surface detrending was adopted. Compared to the small-window analysis, for which a 2nd order detrending was adopted on $80 \times 80 \mu\text{m}^2$ sub-windows, the waviness of the sample detected with a $400 \times 400 \mu\text{m}^2$ observation window was more complex, and hence required an higher order detrending. Otherwise, for $\Omega_{\text{calcite}} \leq 0.55$, the effects of the polishing process on the surface were no longer visible after dissolution, and a 1st order degree surface detrending was adopted.

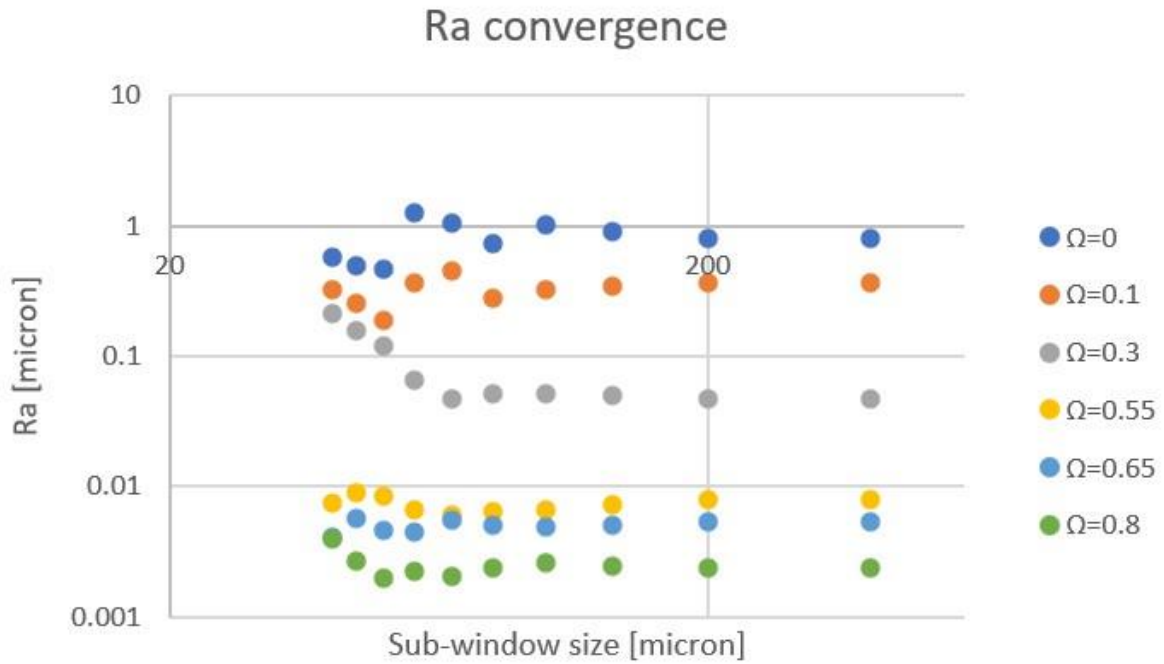


Figure B1 Analysis of R_a convergence as a function of sub-window size. In this analysis, the different sub-windows were generated by progressively dividing the field of view, starting from the largest window used in the study (i.e., $400 \times 400 \mu\text{m}^2$), into smaller sizes, by a factor of 2 at each step. The R_a values showed in the plot represent the average values evaluated across all sub-windows with a given size.

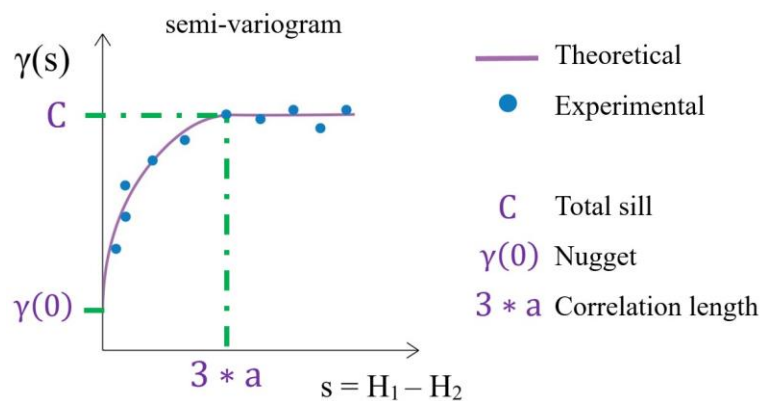


Figure B2 Figure showing the graphical relationships between experimental and theoretical semi-variogram, including model parameters: total sill, nugget and correlation length.

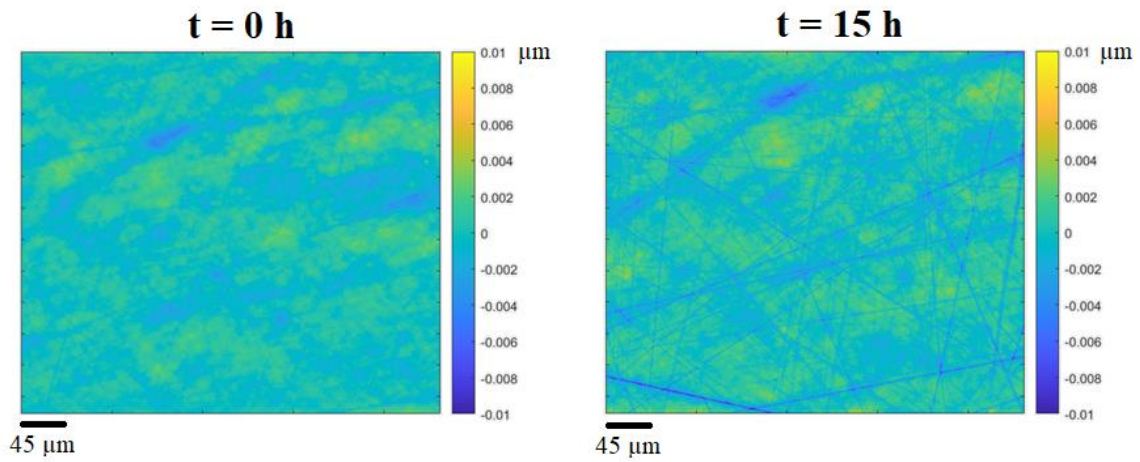


Figure B3 Surface topography comparison of a $400 \times 400 \mu\text{m}^2$ observation window at $t = 0 \text{ h}$ and $t = 15 \text{ h}$, for $\Omega_{\text{calcite}} = 0.8$. The increase in depth of the polishing scratches due to preferential dissolution is evident when comparing the two time lapses at fixed colour scale.

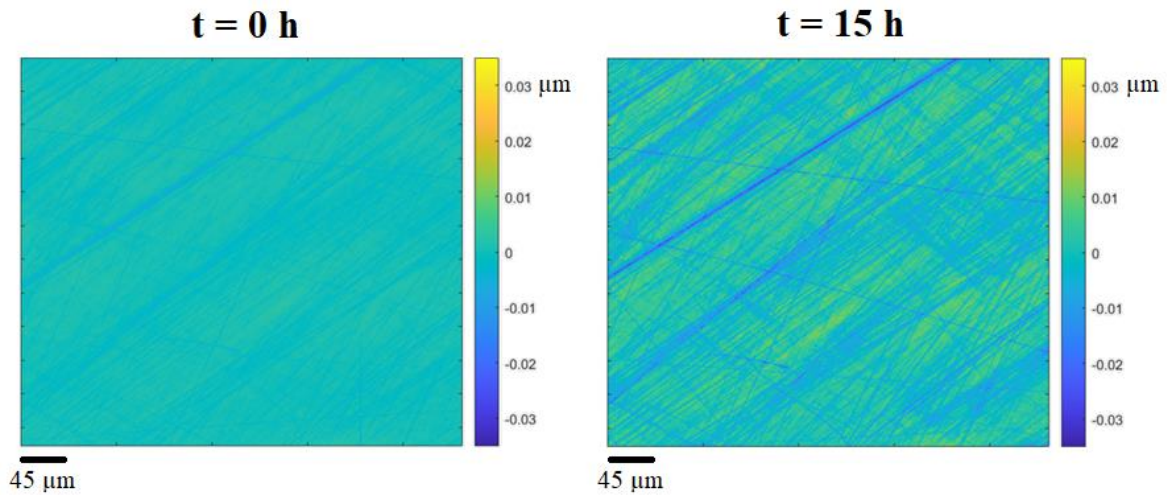


Figure B4 Surface topography comparison of a $400 \times 400 \mu\text{m}^2$ observation window at $t = 0 \text{ h}$ and $t = 15 \text{ h}$, for $\Omega_{\text{calcite}} = 0.65$. The increase in depth of the polishing scratches due to preferential dissolution is evident when comparing the two time lapses at fixed colour scale.

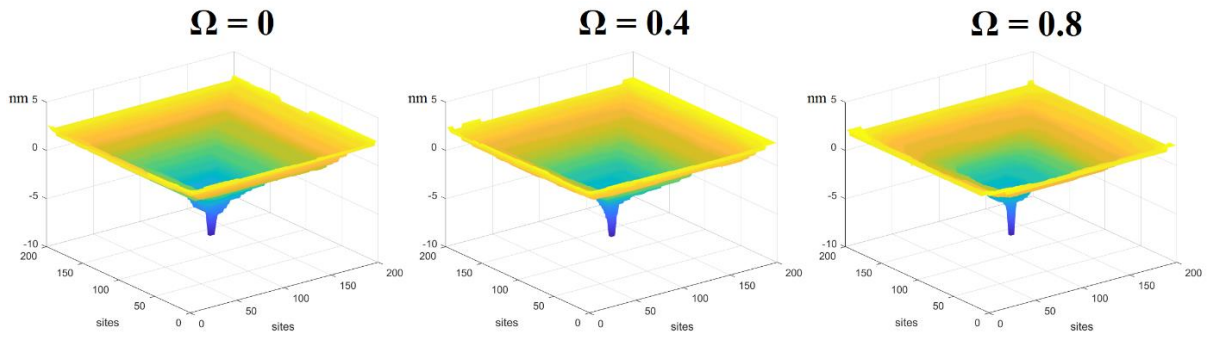


Figure B5 Comparison of steady-state surface configurations after dissolution at $\Omega=0$, $\Omega=0.4$, and $\Omega=0.8$, resulting from simulations with classical kMC modeling, in 3D representation.

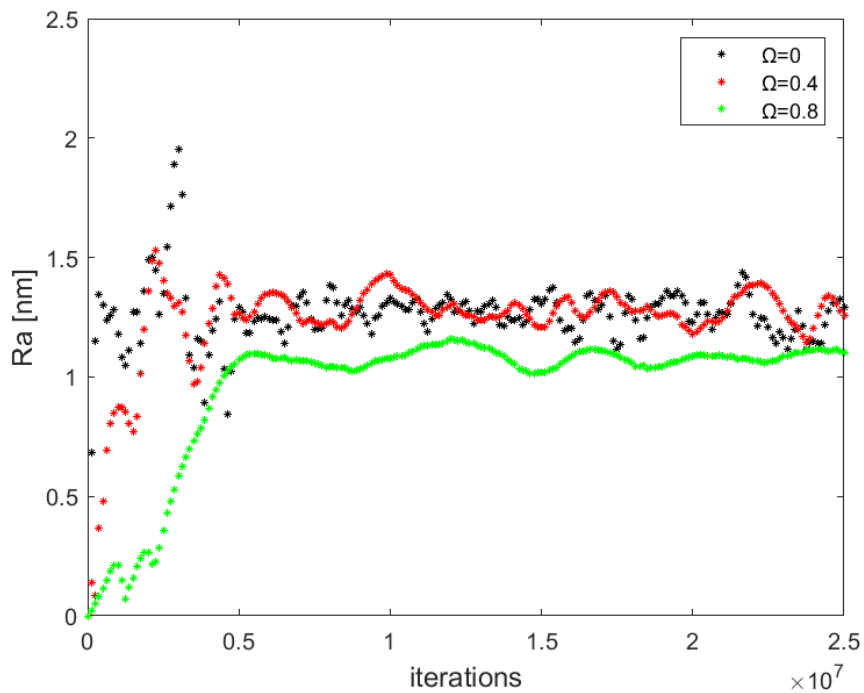


Figure B6 Comparison of R_a evaluated for the steady-state surface configurations resulting from dissolution at $\Omega=0$, $\Omega=0.4$ and $\Omega=0.8$, simulated with standard kMC modeling. The pre-opened hollow cores of 4×4 lattice sites were excluded from the calculation of R_a . The plateau values of R_a indicate the achievement of a steady-state configuration of the surface.

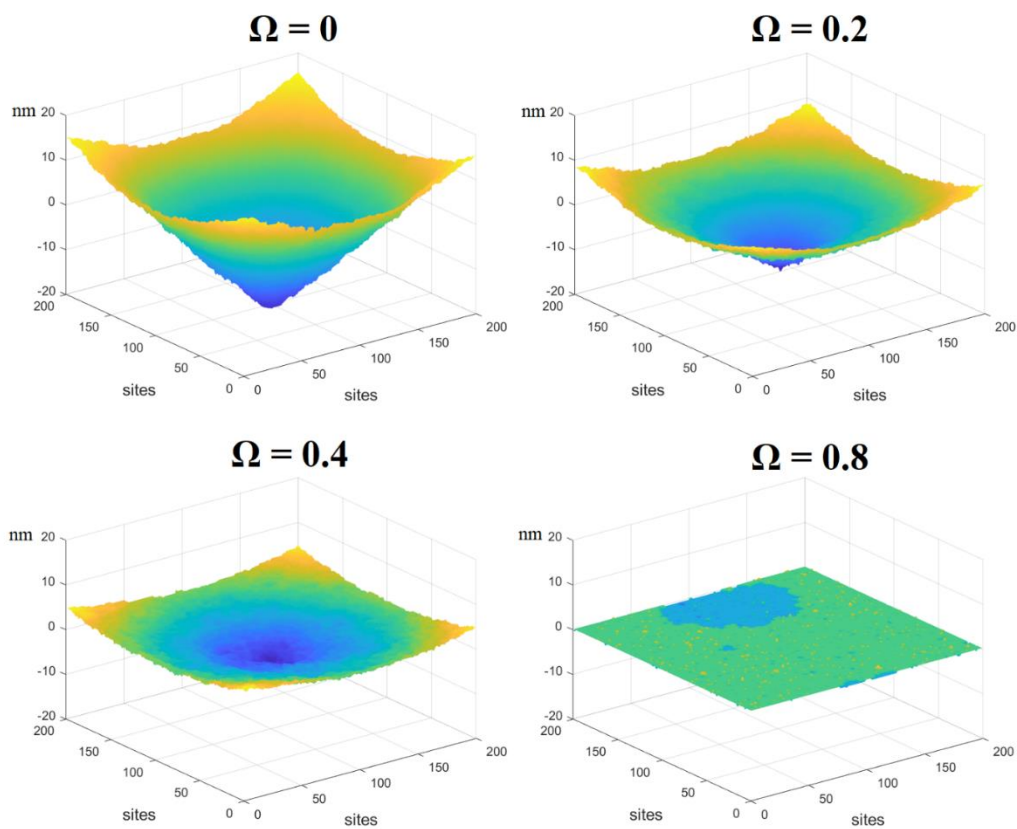


Figure B7 Comparison of steady-state surface configurations after dissolution at $\Omega=0$, $\Omega=0.2$, $\Omega=0.4$ and $\Omega=0.8$, resulting from simulations with Ising modeling, in 3D representation.

Appendix C

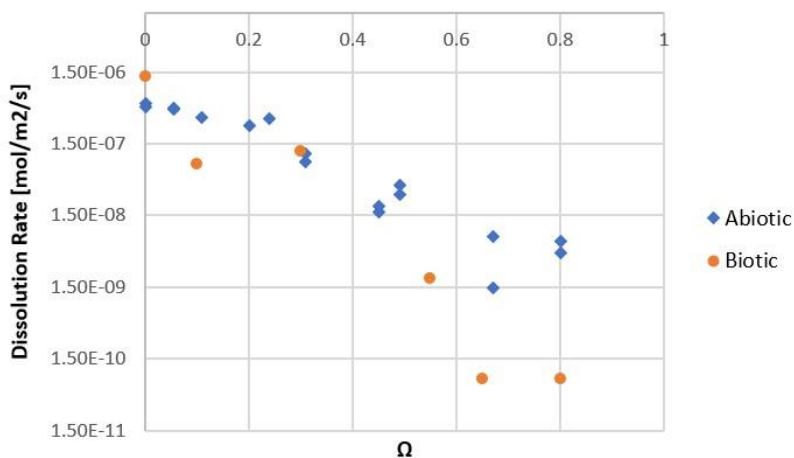


Figure C1 Calcite dissolution rates as a function of Ω obtained in abiotic and biotic conditions. Abiotic rates data were derived from Bouissonnié et al. (2018) in similar conditions.

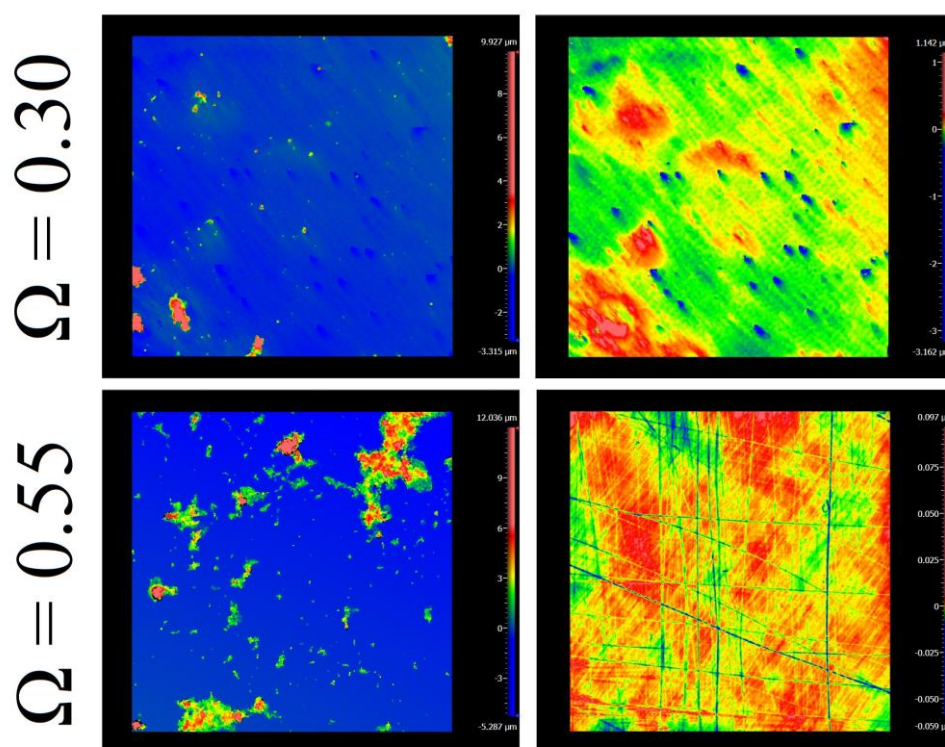


Figure C2 Panels showing the calcite surface topography resulting from calcite biotic dissolution at $\Omega = 0.30$ and $\Omega = 0.55$, before (left-hand side) and after (right-hand side) removal of the PCC 7203 cells. The size of all VSI images is $600 \times 600 \mu\text{m}^2$.

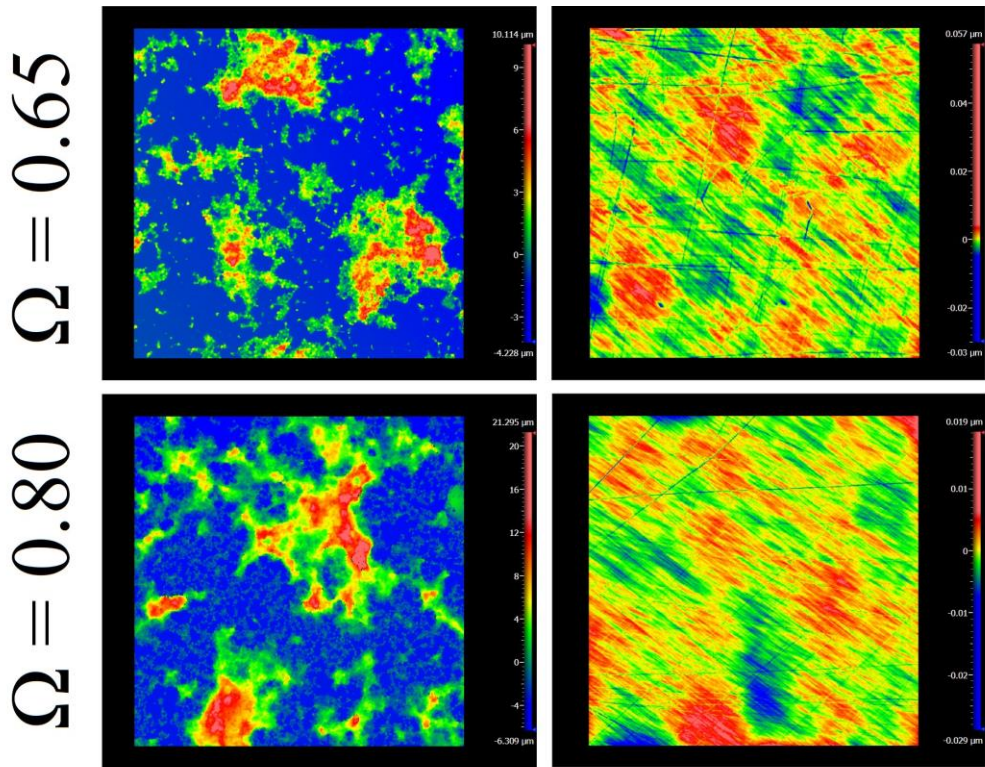


Figure C3 Panels showing the calcite surface topography resulting from calcite biotic dissolution at $\Omega = 0.65$ and $\Omega = 0.80$, before (left-hand side) and after (right-hand side) removal of the PCC 7203 cells. The size of all VSI images is $600 \times 600 \mu\text{m}^2$.

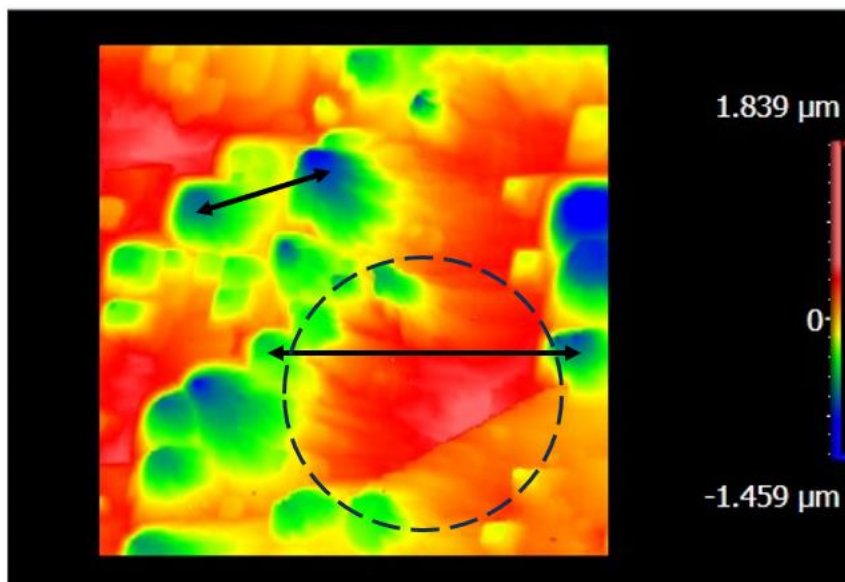


Figure C4 Close-up of Figure 5.1.1F. This sketch schematically illustrates how the presence of high-elevation regions affects the semi-variogram correlation length. If the high-elevation areas (see, e.g., dashed circle) were absent, the correlation length would be determined by the average distance between the centers of etch pits (see shorter double arrow). However, due to the presence of these areas, the surface heights values become correlated on average over larger distances (see longer double arrow), thus leading to a higher correlation length compared to abiotic dissolution. The size of the VSI image is 400x400 μm^2 .

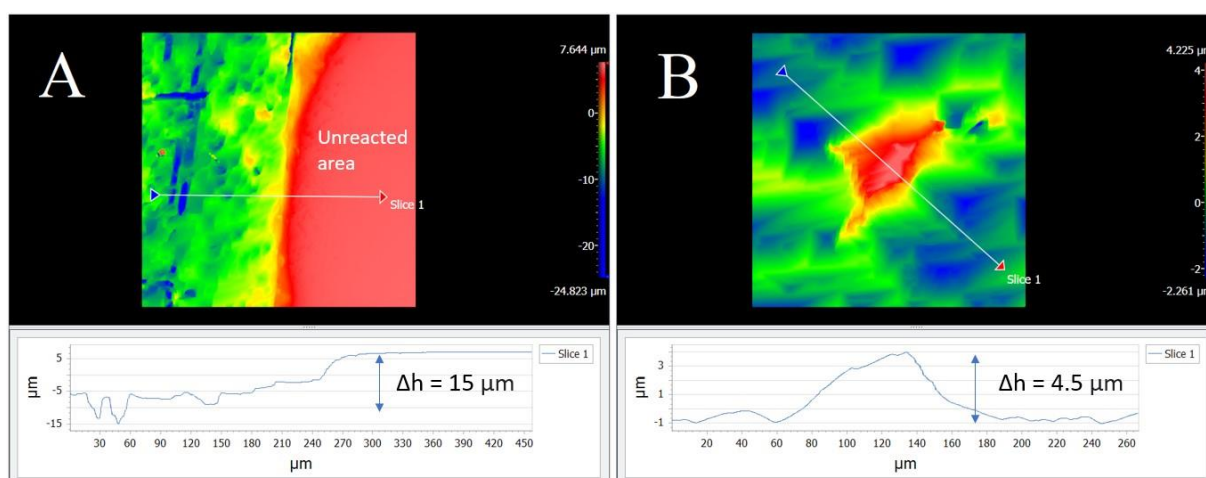


Figure C5 A) Global surface retreat, Δh , evaluated as the average height difference between the reacted and non-reacted area. The size of the VSI image is 500x500 μm^2 . B) Relative height of the high-elevation region displayed in Figure 5.1.1 B, C. The size of the VSI image is 250x250 μm^2 . A, B) Overall, comparing the relative height of the high-elevation region to the global surface retreat reveals that dissolution was only limited by the biofilm presence, not inhibited.

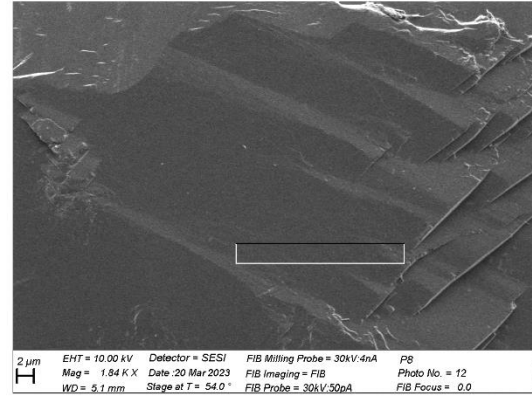
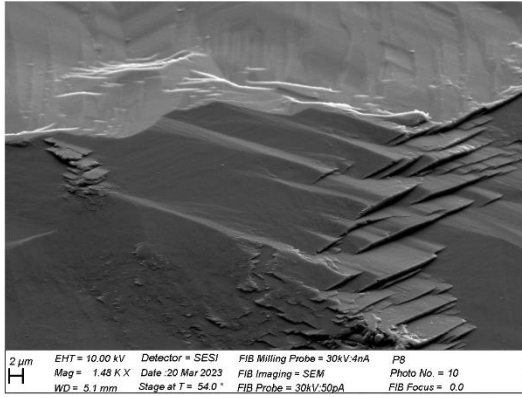
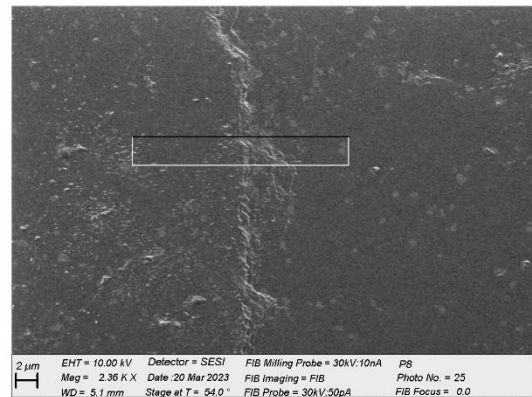
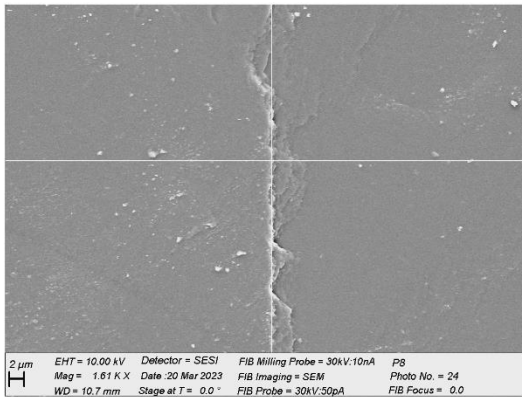
$\Omega = 0.00$  $\Omega = 0.10$ 

Figure C6 Locations targeted for FIB foil extraction. SEM (left-hand side) and FIB (right-hand side) images close-up of the high-elevation regions displayed in Figure 5.1.1C and Figure 5.1.1G. These areas were targeted as they exhibited higher density of cells sticking to the calcite substrate at the end of the experiments (see Figure 5.1.1).

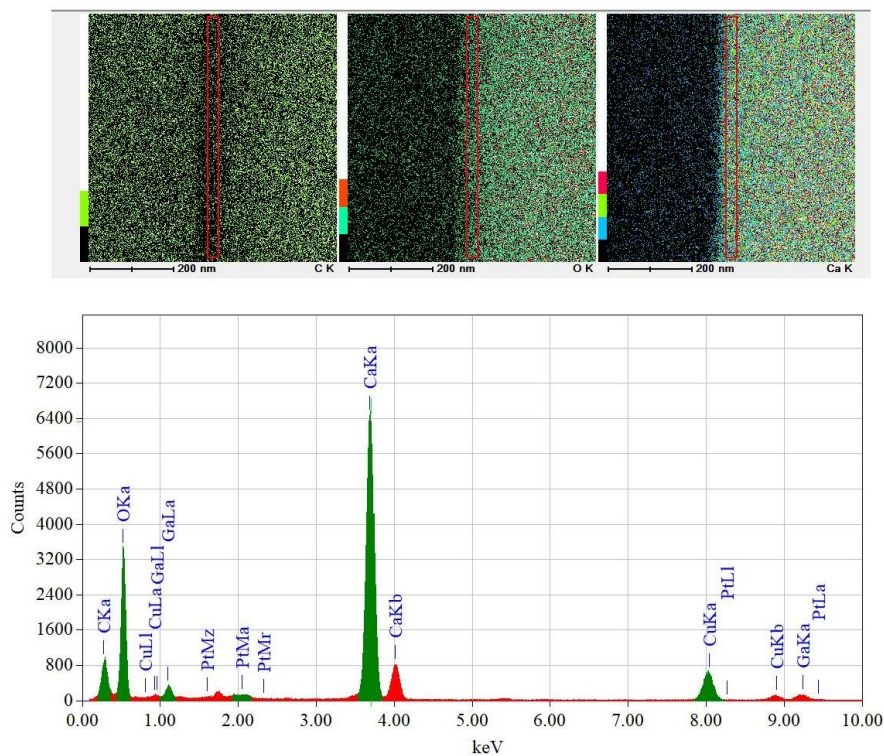


Figure C7 EDXS analyses conducted on the uppermost nanometers beneath the calcite surface (see red area) reacted at $\Omega = 0.00$ did not reveal any discernible peaks indicative of elements other than Ca, C, O. The absence of foreign element signals implies that there were no additions of external elements into the crystal due to interactions between the biofilm and the calcite.

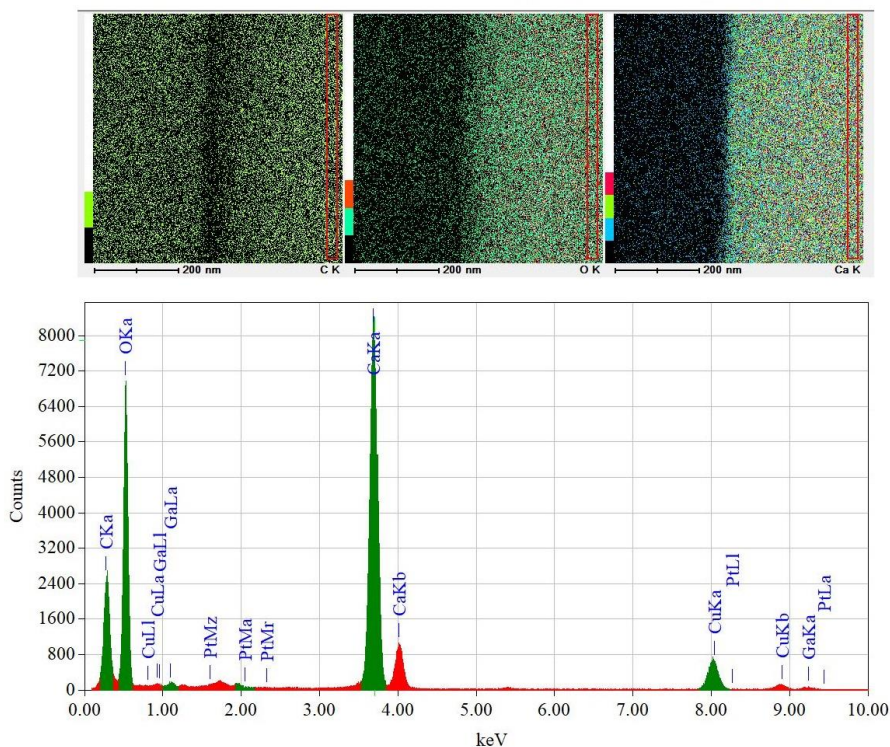


Figure C8 EDXS analyses conducted over an area contained in the same region depicted in Figure C7, but situated a few tens of nm deeper beneath the surface. EDXS analyses over this area also did not reveal the presence of any discernible peaks indicative of elements other than Ca, C, O.

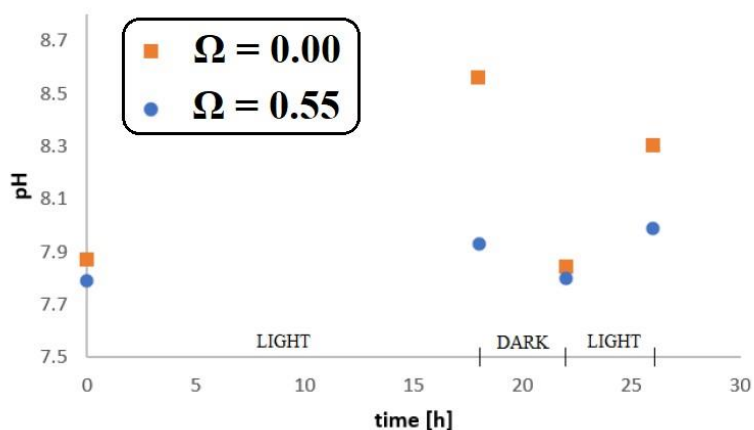


Figure C9 Solution pH evolution as a function of time, under intermittent light exposure, evaluated in batch tests for two of the solution employed in our experiments (i.e., $\Omega = 0$, with $\text{NaCl}=5.8 \text{ g/L}$, $\text{NaHCO}_3=0.086 \text{ g/L}$, $\text{CaCl}_2=0 \text{ g/L}$; $\Omega = 0.55$, with $\text{NaCl}=5.8 \text{ g/L}$,

$\text{NaHCO}_3=0.086$ g/L, $\text{CaCl}_2=0$ g/L), upon enrichment with PCC 7203 cells. These tests demonstrate that the overall impact of adding PCC 7203 cells, subjected to light exposure, to the experimental solutions (when the fluid is not continuously replenished as in flow-through systems at a sufficiently fast rate) is an increase of the bulk solution pH, likely due to photosynthetic activity. In flow-through tests, a pH increase was observed under light exposure for flow rates lower than ~ 0.6 mL/min.

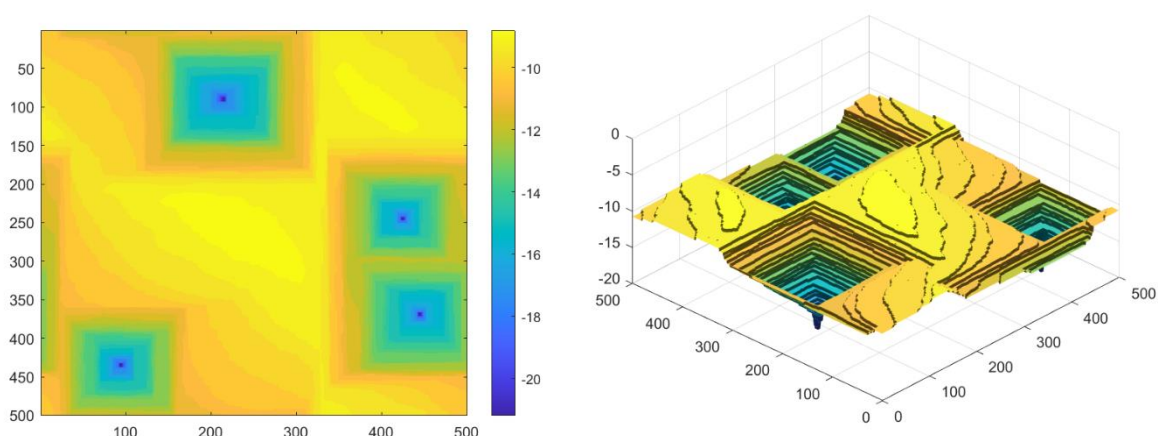


Figure C10 Surface topography (left-hand side, 2D representation; right-hand side, 3D representation) resulting from kMC modeling of abiotic Kossel crystal dissolution at $\Omega_{\text{bulk}} = 0$, conducted using the same simulations settings employed for Figure 5.1.4, with the exception that no sub-window with higher Ω value was introduced.

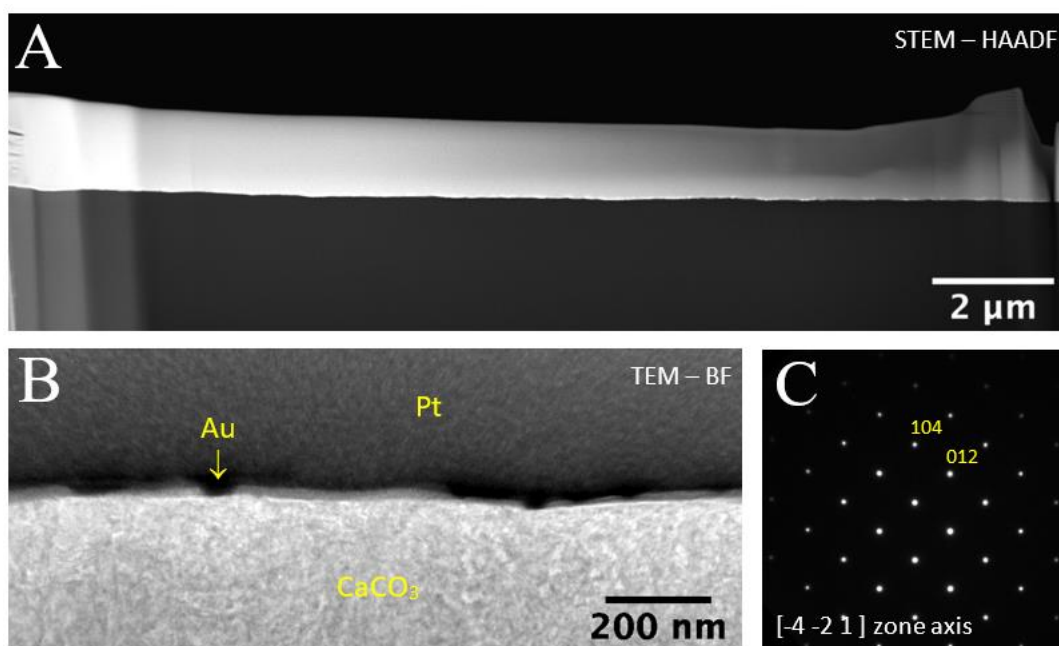


Figure C11 A) High-angle annular dark-field scanning transmission electron microscopy (STEM - HAADF) of the FIB foil used for TEM analysis, showing the Pt support. B) Bright field transmission electron microscopy (TEM – BF) close-up of the FIB foil, showing the Au-coating applied to the calcite surface prior to FIB milling. C) Calcite diffraction pattern.

ICP-AES	Ca [ppm] ($\Omega=0.00$)	Ca [ppm] ($\Omega=0.10$)	Ca [ppm] ($\Omega=0.30$)	Ca [ppm] ($\Omega=0.55$)	Ca [ppm] ($\Omega=0.65$)	Ca [ppm] ($\Omega=0.80$)
t = 0 h	0.83	14.23	39.32	72.71	88.79	104.27
t = 3 h	0.85	14.71	39.34	71.34	91.70	104.91
t = 16 h	0.87	14.58	38.75	71.73	90.30	102.92
t = 48 h	0.84	14.72	38.43	73.09	90.84	104.28
t = 61 h	0.87	14.06	39.71	73.15	88.81	103.47
t = 95 h	0.86	14.28	39.02	73.29	88.90	106.11

Table S1 ICP-AES measurements of the aqueous solution for all saturation states, sampled at different time points during the biotic experiments. Samples collected at $t > 0$ h were collected from the reactor outlet, while the samples at $t = 0$ h were obtained directly from the tank solution. Solution pH of both the tank and the outlet solutions was measured to be 7.9 ± 0.1 over time, as for the abiotic experiments (see Stigliano et al. (2023)).

List of publications

Stigliano L, Ackerer P, Benzerara K, Daval D (2023), Linking calcite surface roughness resulting from dissolution to the saturation state of the bulk solution. *Chemical Geology*.
DOI: <https://doi.org/10.1016/j.chemgeo.2023.121680>

Stigliano L, Caumartin J, Benzerara K, 2023, Micro- and nanoscale techniques for studying biofilm-mineral interactions. *Methods in Microbiology*.
DOI: <https://doi.org/10.1016/bs.mim.2023.04.001>

Stigliano L, Siena M, Ackerer P, Guadagnini A, Daval D (2021), Statistical Description of Calcite Surface Roughness Resulting from Dissolution at Close-to-Equilibrium Conditions. *ACS Earth and Space Chemistry*.
DOI: <https://doi.org/10.1021/acsearthspacechem.1c00226>